Investigations of the Neural Mechanisms of Cardiac Stability

Stefan van Duijvenboden

Submitted in accordance with the requirements for the degree of

Doctor of Philosophy

Department of Mechanical Engineering

UCL

I, Stefan van Duijvenboden, confirm that the work presented in this thesis is my own. Where information has been derived from other sources, I confirm that this has been indicated in the work.

Abstract

Electrical instability of the heart is known to precede the onset of lethal arrhythmias and the autonomic nervous system (ANS) is a primary factor in this process. However, the exact mechanisms of failure remain poorly understood. This work aims to better understand how ANS activity affects the electrical properties of the heart by investigating the effect of autonomic rhythms on the ventricular action potential duration (APD) recorded at tissue level using unipolar electrograms (UEGs).

Studying dynamic behaviour of APD was associated with large data-sets of UEGs. Methods were developed to improve accuracy of automatic detection of APD, like narrow search windows and correlation filters to detect ambiguous activity. A simulation study was conducted to generate realistic UEG recordings to examine the effect of signal quality and filtering on tracking of APD dynamics. New insights were provided in how signal quality and filtering affect the accuracy of APD tracking. The proposed improvements were found to reduce the detection error substantially.

The effect of autonomic rhythms on ventricular APD was explored using existing clinical data. By employing techniques to determine causality and time-frequency coherence, evidence was found that the ANS modulates ventricular electrophysiology: (1) with respiratory behaviour via a direct causal pathway, and (2) at a lower frequency and related to signs of enhanced sympathetic activity in blood pressure observed during mental stress.

Further investigations were undertaken by designing and conducting a clinical experiment to study the effect of baroreceptor control on APD. Novel methodologies to determine the statistical significance of response curves were used to demonstrate for the first time that ventricular APD can be influenced by baroreceptor stimulation independent of heart rate.

Identification of the neural mechanisms controlling cardiac stability may ultimately contribute to the development of new diagnostic tools and treatments to prevent thousands of deaths each year.

Acknowledgements

Out of many people who have helped me in brining this thesis together, I would like to thank my supervisor, Ben Hanson, first. It was a great pleasure working with him throughout this project. He repeatedly went out of his way to act my interest and has always been generous with his time. His insightful criticism helped me to gain confidence in my own ideas during this project. Thank you, Ben.

Next, I would like to thank Peter Taggart and Michele Orini. Peter's guidance in physiological and Michele's guidance in methodological matters were invaluable for this project. It was a great pleasure to work with you, and I enjoyed our vibrant discussions. Special thanks also to Richard Ang, Neil Srinivasan, and to Michele again, for helping me carrying out the experiment in the time pressured environment of the Bart's Heart Centre. Thank you to James Fisher for borrowing me his experimental equipment and for sharing his expertise. I am grateful to Vanessa Diaz, my second supervisor, for contributing her perspective when needed and taking the time for sharing ideas and giving constructive criticism. Thank you to Nick Child, Pier Lambiase, Jas Gill for all the enjoyable and useful discussion along the way. Thank you to Andrew Redfearn for helping me with the pressure sensors.

I would never have been able to peruse this project without the funding provided by my UCL Impact Studentship supported by my philanthropic donor. Also the funding towards conference expenses awarded by the UCL Department of Mechanical Engineering was much appreciated, and I am grateful for choosing to award that funding to me.

Thank you to everyone who ever shared a lunch-time crossword with me at 132 Hampstead Road. That routine disruption of my work so often turned out be what I really needed.

Thank you to Mum, Dad, Nickel, Gwenneth, Imre, Thomas, Sofia and Ester and to my friends in London and Holland for their distractions, support and perspective. A special thank you to Ester as well for giving feedback on a draft of this thesis.

Contents

List of Figures

List of Tables

Nomenclature

$d\vec{S}$	Outward normal vector to an infinitesimal surface element, with magnitude equal to the element's area.
L	The local component of a UEG.
t_r	The steepest downward slope during phase 3 of the action potential, used as an index of repolarisation.
T_{up}	The steepest up-stroke of the UEG T-wave, used as an index of the timing of local repolarisation.
v_m	Transmembrane electrical potential.
$\dot{V}_{down}$	The steepest downward slope of an activation wave in the UEG, used as an index of local depolarisation.
R	The remote component of a UEG.
σ_e	Extracellular conductivity.
σ_i	Intracellular conductivity.
∇Z	Lead Field.

Abbreviations

ABP	Arterial Blood Pressure.
ANS	Autonomic Nerve System.
APD	Action Potential Duration.
AR	Auto Regressive (model).
ARI	Activation Recovery Interval.
ARP	Absolute Refractory Period.
AT	Activation Time.
AV-node	Atrioventricular node.
BEG	Bipolar Electrogram.
CNS	Central Nerve System.
CWT	Continuous Wavlet Transform.
DC	Directed Coherence.
ECG	Electro Cardiogram.
ERP	Effective Refractory Period.
FFT	Fast Fourier Transform.
GUI	Graphical User Interface.
HRV	Heart Rate Variability.
IHD	Ischemic Heart Disease.
LV	Left Ventricle.
MAP	Monophasic Action Potential.
MAP90	MAP recovers for 90%.
MVAR	Multi Variate Auto Regressive.
MSNA	Muscular Sympathetic Nerve Activity.
NCP	Neck Chamber Pressure.

NP	Neck Pressure.
NS	Neck Suction.
PSD	Power Spectral Density.
QT	QT interval: the time between the Q-wave and T-wave in a single beat of the ECG.
RESP	Respiration.
RR	RR interval: the time between two consecutive R-waves in the ECG.
RT	Recovery Time.
RV	Right Ventricle.
SA node	Sino Atrial node.
SBP	Systolic Blood Pressure.
SPWVD	Smoothed Pseudo Wigner Ville Distribution.
STFT	Short-Time Fourier Transform.
TAP	Transmembrane Action Potential.
TFC	Time-Frequency Coherence.
TMP	Transmembrane Potential.
VF	Ventricular Fibrillation.
UEG	Unipolar Electrogram.
VF	Ventricular Fibrillation
VNS	Vagal Nerve Stimulation.
WVD	Wigner Ville Distribution.

Related Publications

The following publications were generated from this project:

Journal Papers

- Hanson, Ben, Nick Child, Stefan Van Duijvenboden, Michele Orini, Zhong Chen, Ruben Coronel, Christopher A. Rinaldi, Jaspal S. Gill, Jaswinder S. Gill, and Peter Taggart. "Oscillatory behavior of ventricular action potential duration in heart failure patients at respiratory rate and low frequency." Frontiers in physiology 5 (2014): 414.

- van Duijvenboden, Stefan, Ben Hanson, Nick Child, Michele Orini, Christopher A. Rinaldi, Jaswinder S. Gill, and Peter Taggart. "Effect of autonomic blocking agents on the respiratory-related oscillations of ventricular action potential duration in humans." American Journal of Physiology-Heart and Circulatory Physiology 309, no. 12 (2015): H2108-H2117.

- Taggart, Peter, Hugo Critchley, Stefan van Duijvendoden, and Pier D. Lambiase. "Significance of neuro-cardiac control mechanisms governed by higher regions of the brain." Autonomic Neuroscience 199 (2016): 54-65.

Conference Papers

- van Duijvenboden, Stefan, Michele Orini, Peter Taggart, and Ben Hanson. "Accuracy of measurements derived from intracardiac unipolar electrograms: A simulation study." In Engineering in Medicine and Biology Society (EMBC), 2015 37th Annual International Conference of the IEEE, pp. 76-79. IEEE, 2015.

- van Duijvenboden, S., M. Orini, N. Child, J. S. Gill, P. Taggart, and B. Hanson. "Investigation of causal interactions between ventricular action potential duration, blood pressure and respiration." In Computing in Cardiology Conference (CinC), 2015, pp. 621-624. IEEE, 2015.

Chapter 1

Introduction

1.1 Background

Cardiac arrhythmia - irregular electrical activity of the heart - is an important cause of premature death in the industrialised world, killing more than 25,000 people per year in the UK alone [1]. Electrical instability of the heart is known to precede the onset of these catastrophic events and it has become increasingly evident that the nervous system can be a primary factor in this process [2–4]. Under normal conditions, each contraction of the heart is generated by an electrical impulse that spreads through the cardiac tissue. The orchestrated progression of this signal is crucial to efficient propulsion of blood around the body. Both regional and temporal differences in cardiac activity have shown to increase the vulnerability to arrhythmias [5–8]. Understanding the mechanisms by which the nervous system regulates local cardiac activity is therefore an important research problem.

Oscillatory behaviour is a ubiquitous property of many biological systems including the cardiovascular system [9]. Oscillations in blood pressure at approximately 0.1 Hz frequency have been observed for over a century. Oscillations in blood pressure with breathing have also long been known. Since both oscillations are known to interact with the nervous system, research and clinical attention has been directed towards characterising the influence of these oscillatory processes on regional and temporal activity of cardiac tissue [10, 11]. Recent advances in computing technology have made it possible to gather and analyse physiological data and their interactions at both frequencies in greater quantities and detail than before [11].

1.2 Overall aim and hypotheses

Since the ventricular myocardium receives autonomic input from both vagal and sympathetic branches, this thesis is driven by the hypothesis that neural related periodicities may also influence the heart's excitable properties locally. Characterisation of the influences of respiratory and Mayer wave rhythms on local cardiac electrophysiology could offer new insights in the nature of autonomic control of the heart.

The aim of the work described in this thesis was therefore to characterise the effect of autonomic rhythms on the ventricular action potential duration (APD). To that end, new analytical methodologies were developed and modified to characterise the mechanisms by which the autonomic nervous system (ANS) regulates the heart's local activity. These techniques were applied on existing *in-vivo* experimental data, yielding novel insights about the nervous interactions with the heart. The neural interactions were further investigated by designing and conducting a clinical experiment to expose the effects of periodic autonomic stimulation on the action potential duration (APD).

The work carried out in this thesis focusses specifically on:

- Design, testing & validation of novel analytical tools to improve estimation of dynamic behaviour of APD using simulated electrogram recordings.
- Application and development of advanced analytical tools to investigate the presence and origin of oscillatory behaviour of ventricular APD using invasive electrocardiographic recordings in humans *in-vivo* data during pharmacological manipulation of the ANS and psychological stress.
- Design and creation of a physiological experiment to investigate the effect of periodic autonomic stimulation on ventricular APD in humans.

1.3 Structure of the report

This thesis is structured as follows: first, an overview is provided of the fundamental working of the heart and the means by which its behaviour is controlled by the nervous system in Chapter 2. This chapter then focuses on reviewing relevant published literature to derive the current understanding of the neural mechanisms involved in modulating local cardiac activity. The final part of this chapter discusses available techniques to measure and anal-

yse dynamical behaviour of the local electrical properties of the heart and underlying the interactions with other physiological signals.

Chapter 3 describes the design and implementation of novel signal processing tools for automatic analysis of unipolar electrograms (UEGs) to obtain measures of localised electrical behaviour in cardiac electrophysiology. A numerical study using a large quantity of simulated physiological signals is presented to investigate how the reliability of the computed markers varies with noise and filtering which is commonly used in clinical practice. The developed tools were used in Chapter 4 combined with new advanced analytical techniques to investigate the (causal) interrelationship between APD, respiration and blood pressure during controlled respiration and mental stress from existing experimental data. The validity of the results was further explored in Chapter 5 by exploring the effect of neural stimulation on APD. To that end, this chapter describes a time and a spectral analysis technique combined with the design and assessment of a physiological test-bed for periodic stimulation of the autonomic nervous system.

Finally, Chapter 6, draws together the work, discussing the impact and clinical relevance. Some opportunities for future investigation based on these novel methods and results are highlighted. Appendices are included which provide further technical details and copies of peer-reviewed publications which have been created in the course of this research.

Chapter 2

Literature review

This chapter reviews the present understanding of the neural control mechanisms of the heart, and existing techniques for measuring and characterising cardiac electrical behaviour.

Sections 2.1 & 2.2 explain the fundamentals of the mechanical and electrical working of the heart to orient readers who are not yet familiar with cardiac (electro)physiology. An awareness of the basic electrophysiology of the heart is necessary to appreciate the relevance of the novel analytical and experimental tools described later in this thesis. Readers who are already familiar with cardiac electrophysiology may therefore choose to begin at section 2.3, page 45. Sections 2.3 - 2.5 review the major contributions and current challenges in understanding of the neural cardiac control mechanisms, including recording and analytical techniques to study the neural influences on the electrical properties of the heart in more detail.

Sections included in the literature review:

- 2.1 **Fundamentals of the heart's function**

- 2.2 **Cellular mechanisms underlying cardiac electrical activity**

- 2.3 **Electrical measurements of local cardiac activity** This section focusses on the recording technique to explore localised cardiac activity.

- 2.4 **Neural control of cardiac function:** This section explains how the autonomic nervous system controls cardiac behaviour. Special emphasis is put on two neurally induced cardiovascular rhythms.

- 2.5 **Methods for characterising short-term variability and interactions:** The novel analytical techniques implemented in this thesis were specifically designed to characterise short-term variability, dynamic interactions, and causality.

2.1 Fundamentals of the heart's function

The heart is a muscular structure that is in continuous operation to drive the blood around the body's circulatory system. Its operation is maintained by a regular cycle of mechanical and electrical events, called the cardiac cycle. The phases of a complete cardiac cycle are illustrated in Figure 2.1. During the cycle, the atria first contract to fill the ventricles, then the ventricles contract to propel the blood into the pulmonary and systemic circulation. The state of contraction is referred to as systole, and relaxation is referred to as diastole. Although the output generated by both ventricles of the heart is equal, the left ventricle has considerably more muscular mass to generate a higher pressure: typically, the pressure in the systemic circulation varies between 80 and 120 mmHg at the aorta (10.7-16.0 kPa) and roughly 10-25 mmHg (1.3-3.3 kPa) at the pulmonary artery. The contraction mechanisms differ between ventricles: the right ventricle moves the outer wall towards the intraventricular septum, whereas the left ventricle contracts by reducing both diameter and length. This asymmetry requires a fine degree of coordination between cardiac cells to ensure efficiency of the mechanical contraction.

The contraction of the heart is initiated by an electrical signal that spreads through the cardiac muscle tissue, called myocardium. As shown in Figure 2.1, the electrical signal originates in a group of specialised cells high in the right atrium, known as the sinoatrial (SA) node. The signal then spreads then throughout the atrial muscle resulting in contraction of the atria. A layer of fibrous tissue prevents the impulse from spreading directly from into the ventricles. The only electrical pathway between atria and ventricles is the atrioventricular (AV) node, which has an important function to slow down the conduction. This allows the atria to contract and empty before the ventricles become activated. Once past the AV node, the signal is guided further down to the ventricular muscles via a network of specialised conducting cells, called the Purkinje fibre system. This network ensures that the ventricles are activated in an apex to base manner to make the contraction mechanically efficient.

Coordination of the transmission of this signal and the response of cardiac cells to

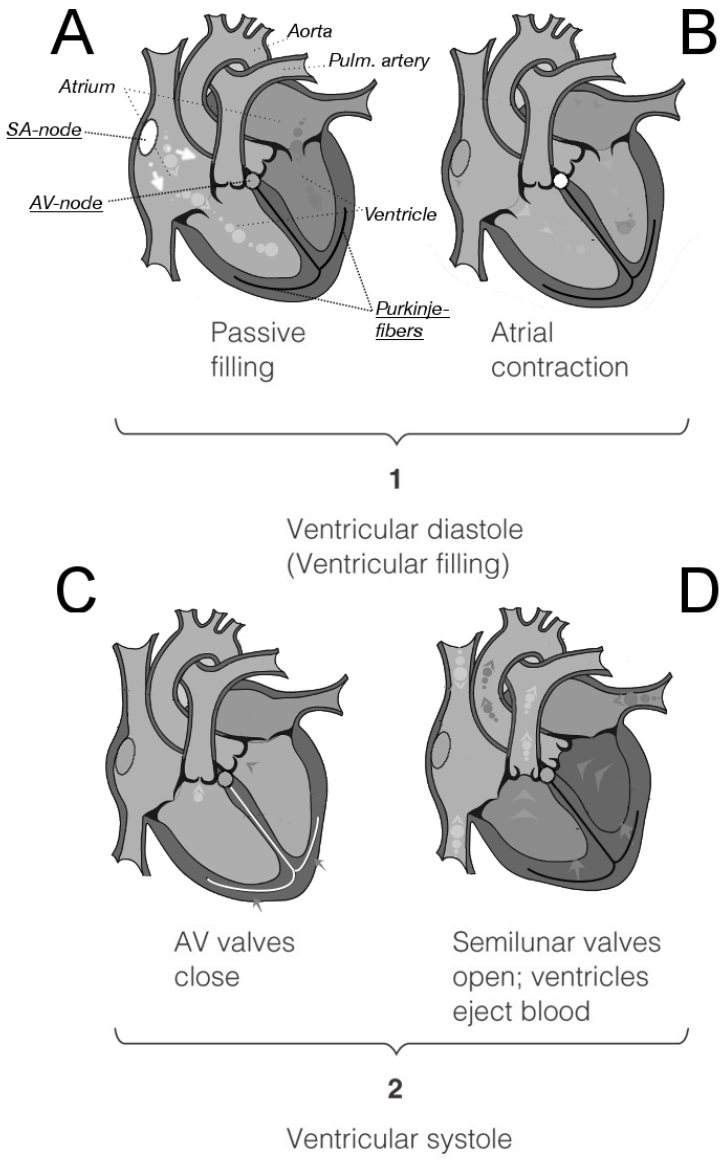

Figure 2.1: Schematic illustration of the cardiac cycle. An electrical signal that activates the cardiac muscle originates in the sinoatrial (SA) node (panel A) and spreads through both atria initiating the atrial systole (panel B). The signal then travels into the ventricles via the atrioventricular (AV) node and Purkinje-fibres carry the signal quickly to the ventricular muscle cells (panel C) resulting in the ventricular systole (panel D).

it are important contributors to the efficiency and stability of the heart. Both aspects are controlled by a complex network of control mechanisms, including the autonomic nervous system.

2.1.1 Cardiac electrical activity

The cardiac conduction system is the component that initiates and coordinates the heart's electrical activities and is vital for maintenance of cardiac stability. An important property of most cardiac cells is that they are electrically excitable and linked to each other. This allows a signal to spread from cell to cell in a chain-reactive manner. The work presented in this thesis focusses on the electrical properties of the cardiac muscle cells (myocytes) that are responsible for the contraction of the ventricle. While 'at rest', they maintain an electrical potential between their interior and the surrounding medium: the interior of the cell is more negatively charged than the exterior resulting in a transmembrane potential close to -90 mV. In response to a sufficient deflection of the transmembrane potential in positive sense, the cell undergoes a series of ion currents (discussed in Section 2.2) which initially causes a rapid depolarisation of the membrane potential to around +30 mv. The cell will remain depolarised for a brief period before it repolarises again to its rest-potential of about -90 mV. This depolarisation-repolarisation pattern is referred to as the action potential and is a typical electrical feature of cardiac myocytes. As illustrated in Figure 2.2, contraction of a myocyte is initiated by the action potential.

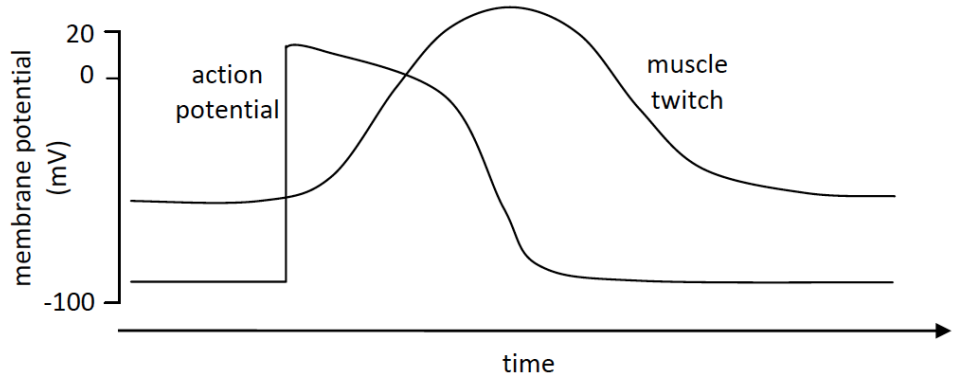

Figure 2.2: Timing of the action potential and the resultant mechanical contraction in cardiac myocytes.

Once the myocyte is depolarised, the cell remains unresponsive (refractory) for new stimuli. This refractory period represents an important safety feature of the heart as it ensures that the signal can only progress in forward direction. However, due to the chain-reaction nature of the impulse propagation, spurious activity in a localised region of the heart can still lead to unwanted activity of a more global nature. Such disruptions of the normal progression, termed arrhythmias, can be fatal and arise from problems in either the initiation or conduction of the heart's signal.

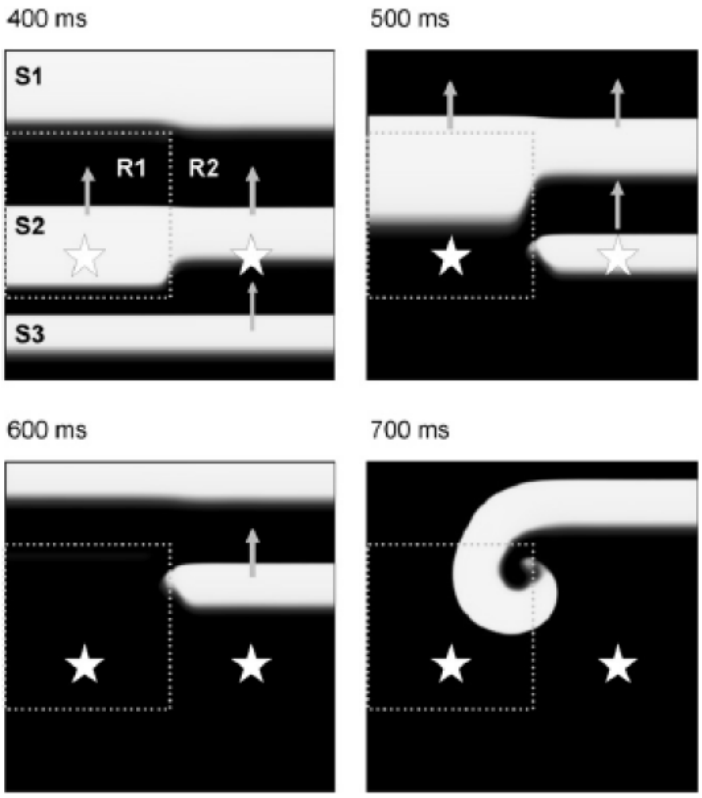

Figure 2.3: Computer modelling of re-entry due to regional differences in refractoriness. The refractory period in R1 is longer than R2. Reproduced from [12]. Permission not required.

The importance of the refractory period in maintaining cardiac stability is demonstrated Figure 2.3. In this example, the progression of the activation wave is shown in two adjacent regions of the heart (R1 and R2). Under normal conditions, the wave of activation travels upwards and R1 and R2 should have approximately the same refractory period. However, in this model, the refractory period in R1 is prolonged due to differences in the tissue properties and when activation wavefront S3 arrives, R1 is still refractory. As a re-

sult, S3 is blocked in R1 and can only travel further upwards via R2, as shown in the lower left panel of the figure. At 700 ms, R1 recovers from its refractory period which allows the activation wave to progress from R2 into R1. Because the cells in R1 have recovered from their refractory period, the activation wave can now freely spread into R1 and also travel back in opposite direction of S3. As the wave travels downwards, it will eventually reach cells in R2 and below that have just recovered from their refractoriness from S3. Via this route, the wave can then travel upwards again, allowing the wave front to travel in an endless circle. This phenomenon is known as re-entry and can lead to circular patterns of excitation that pre-empts the signal from the SA node and disrupts the healthy filling and emptying phase of the healthy cardiac cycle.

This simple example demonstrates that spatial and temporal variations of APD and the refractory period are of crucial importance to cardiac stability. Hence, to study cardiac stability, it is important to measure the properties of the myocardium locally.

2.2 Cellular mechanisms underlying cardiac electrical activity

In the previous section, the problem of re-entry was explained in terms of the spatiotemporal relationship between excitation and refractoriness. This section briefly describes the cellular mechanisms underlying the generation of the normal cardiac action potential, which are important for a correct interpretation of electrical measurements taken from the heart.

The changes in membrane potential during the action potential of cardiac cells are caused by a sequence of ion fluxes through specialised channels in the cell membrane. The observed electrical changes are dominated by movement of sodium (Na^+), potassium (K^+) and calcium (Ca^{2+}) ions. Control mechanisms can selectively modify corresponding channels to modulate ion flows and cardiac behaviour.

The two main forces that drive ions across the cell membrane are the electrical and chemical potential. The electrical potential refers to the voltage difference across the cell membrane: Positively charged ions are attracted towards areas of more negative electrical potential. On the other hand, ions also tend to diffuse from high concentration areas to low concentration areas, referred to as the chemical potential. If ions were allowed to move freely, they would tend to move towards an equilibrium states in which the electrical poten-

tial opposes the chemical potential, resulting in zero net flow. This equilibrium potential is known as the Nernst potential. The Nernst equilibrium potentials for Na^+, K^+ and Ca^{2+} ions are shown in Figure 2.4.

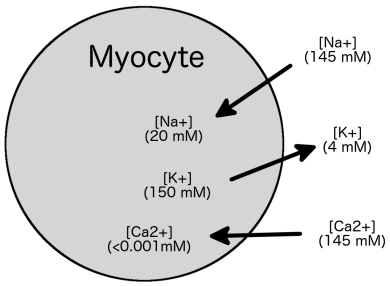

Equilibrium potentials	
E_{Na}	+52 mV
E_K	-96 mV
E_{Ca}	+134 mV

Figure 2.4: Left panel: Differences in ion concentrations between the inside and outside of a myocyte during rest. Right panel: The corresponding equilibrium potentials.

The movement of ions across the cell membrane of myocytes is restricted because they need to pass through ion-specific channels that change their conductance in response to variations in membrane potential. If a channel opens, the resultant ion flow causes the membrane potential to shift towards the Nernst potential for that ion. To maintain the chemical potential, the cell consists of ion exchangers that actively pump K^+ in the cell and Na^+ and Ca^{2+} out. During rest, the interior of the cell contains relatively high concentration of K^+ and low concentrations of Na^+ and Ca^{2+} with respect to outside. The chemical potential corresponds to a negative membrane potential of about -90 mV, close the Nernst potential of K^+ (Figure 2.4).

The action potential is generated by a typical sequence of selectively opening and closing of ion channels generating the corresponding changes in membrane voltage. A general description of identified ion channels is provided in [13]. Their variety is still relevant to this thesis in that it illustrates the complexity of mechanisms available to adjust the myocyte's behaviour.

For ventricular myocytes, the action potential consists of five distinctive phases, which are described in Figure 2.5. Myocytes are activated in response to a sufficient stimulus that can raise the membrane potential over the threshold of about -50 mV. After the depolarisation, Na^+ channels will close, regardless of the membrane potential using a time and voltage

dependent mechanisms that prevents it from re-opening until the myocyte has repolarised beyond about -70 mV. The cell will remain refractory and cannot be activated again before it has reached this point. Under normal conditions, there is a close relationship between refractoriness and action potential duration (APD) [14].

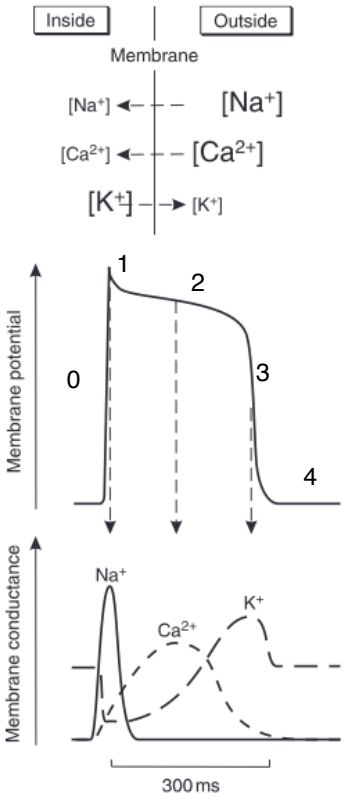

- **Phase 0**: A fast upstroke of the membrane potential mainly due to rapid opening of Na^+ channels causing an inward current and change of the Na^+ concentration inside the cell. The membrane potential rises from -90 mV to approximately+30 mV.
- **Phase 1**: Rapid but small repolarisation component caused by total inactivation of the Na^+ channels and opening of K^+ channels allowing K^+ to exit the cell.
- **Phase 2**: Opening of Ca^2+ channels causes an influx of positive current which approximately matches the remaining positive efflux of K^+ through a few open K^+ channels.
- **Phase 3**: Repolarisation component of the action potential, caused by closing of the Ca^{2+} channels and opening of more K^+ channels decreasing the membrane potential.
- **Phase 4**: Corresponds to the resting membrane potential.

Figure 2.5: Phases of the myocyte action potential.

High-level control mechanisms like the nervous system act on different ion channels to modulate cardiac behaviour and the action potential. Corresponding changes in membrane potential caused during the action potential can be measured extra-cellularly, offering a convenient window to study local cardiac behaviour.

2.3 Neural control of cardiac function

The heart is innervated at various points by the autonomic nervous system (ANS) to ensure that cardiac output constantly adapts to changing demands [15]. This section focusses on the innervation of the heart by the ANS and how it affects cardiac electrical behaviour.

2.3.1 Overall structure and function

Neural regulation of the heart is established by two major autonomic divisions: the sympathetic and parasympathetic. The sympathetic division is said to preside over the use of metabolic resources and emergency responses, whereas the parasympathetic division presides over the restoration of the body's reserves. In most physiological conditions, the activation of one division is accompanied by the inhibition of the other. For example, increased firing of sympathetic nerves results in simultaneous decreased firing of parasympathetic (vagal) nerves, which results in increased heart rate.

Both divisions of the ANS modulate the heart's behaviour by releasing neurotransmitters that bind to specific receptors on the membrane of cardiac cells. As shown in Figure 2.6, sympathetic activation causes release of norepinephrine (NE). Acetylcholine (ACh) is the neurotransmitter of the parasympathetic system. Control of the heart rate is dominated by parasympathetic activity that affects the SA and AV node where acetylcholine binds to muscarinic receptors. Parasympathetic activation in these node results in lowering of firing rate in the SA node and a slower conduction in the AV node. In contrast, control of the contractile force is only minimally affected by parasympathetic influence and primarily modulated by the sympathetic nerves. In contrast to the SA and AV node, the ventricular muscle is only sparsely innervated by parasympathetic nerve fibres. Regional patterns of innervation might impose regional differences on timing and strength of contraction that could increase inhomogeneity of the ventricular substrate potentially leading to re-entry of the type demonstrated *in-silico* in Figure 2.3 [12, 16]. This emphasises the importance of gaining an understanding of the local aspects of autonomic interactions with the heart. With this motivation, the work presented in this thesis was designed to improve the general understanding of physiological mechanisms that have not previously been linked by evidence to the emergence of arrhythmia.

An important example that demonstrates how cardiac functioning is controlled by the autonomic limbs is the baroreflex. This reflex represents a negative feedback loop to keep blood pressure in balance. Pressure receptors in the vascular system continuously monitor blood pressure and based on this information the brain modulates parasympathetic and sympathetic activity neural outflow to the heart. For example, if the blood pressure is too low, sympathetic outflow to the heart will be enhanced and parasympathic outflow will be

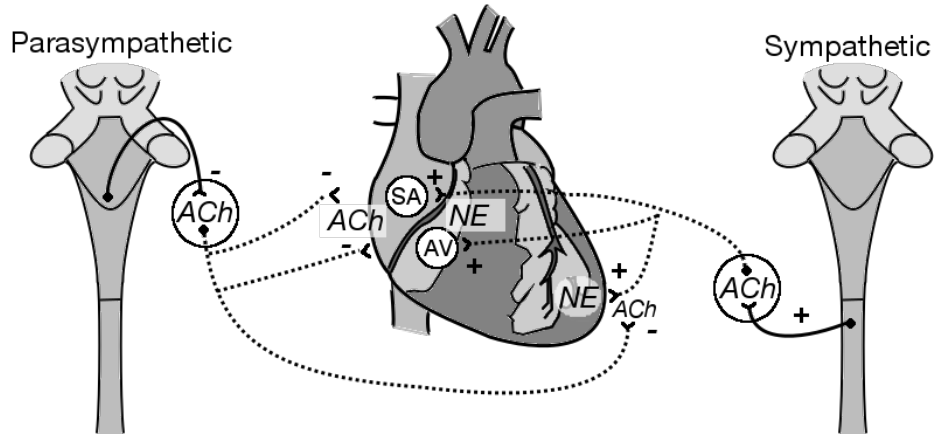

Figure 2.6: Autonomic innervation of the heart. ACh = acetylcholine, NE = Norepinephrine.

inhibited. As a result, heart rate and contraction force increase in an attempt to increase blood pressure.

Studying heart rate and blood pressure responses to altered baroreceptor input has gained important insights into the autonomic regulation of the heart and circulation. For this reason, it was hypothesised that studying the response of localised electrical behaviour of the heart to altered baroreceptor input could reveal important undiscovered information about the nature of autonomic control of the heart local properties. This approach underlies experimental work carried out in Chapter 5, in which APD behaviour in humans was investigated in response to autonomic stimuli. The next subsection will focus in more detail on the neural modulation of the ventricular myocytes, because the neural related changes occurring in the electrical properties of these cells are thought to play a key role in the genesis of lethal arrhythmias and are therefore of key interest in this thesis [4].

2.3.2 Modulation of electrical activity by neurotransmitters

Sympathetic activity leads to release of NE, which binds to β-receptors located on the membrane of the myocytes. Stimulation of β-receptors leads to a number of reactions which causes shortening of the APD. Most prominent is the increased duration and probability of the Ca^{2+} channels opening. This causes an increased Ca^{2+} influx during the action potential which affects the contractile machinery of the cell. As shown in Figure 2.5, Ca^{2+} influx is responsible for the plateau phase of the action potential, but although the increased influx will have an increased depolarising effect, this is overcompensated by an increased outward K^{+} current. The latter current increases the slope of phase 4 depolarisation. As a result, the net effect of sympathetic activation is a shortening of the APD and refractory

period [17]. The effects of β-receptor stimulation on APD are shown in Figure 2.7.

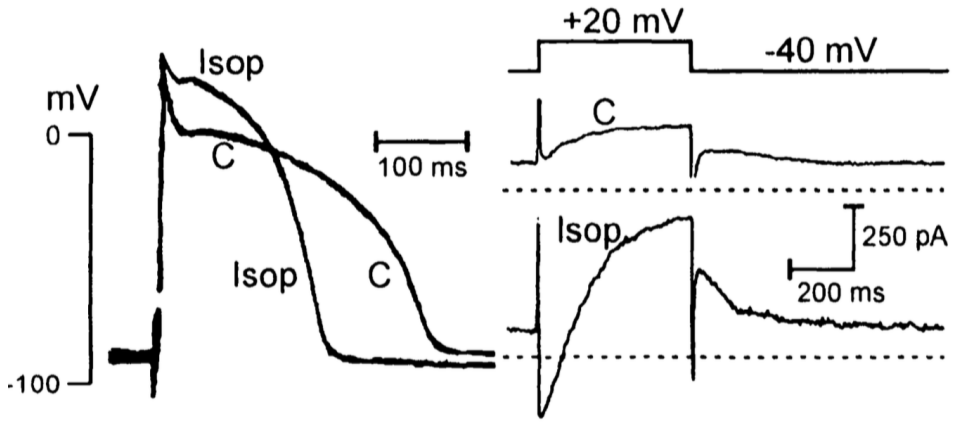

Figure 2.7: Effect of stimulation of β-receptors with isoproterenol (Isop) on the action potential (left) and Ca^{2+} and K^{+} currents (right) in a canine ventricular myocyte. The plateau phase (phase 2 of the action potential) is shifted in the positive direction and shortened. Using voltage clamp records, it was shown that inward Ca^{2+} and outward K^{+}currents are increased. C = control. Modified from [18]. Permission not required.

The effects of acetylcholine on the ventricular myocytes are relatively small due to the limited parasympathetic innervation. However, at the prejunctional level, the sympathetic and parasympathetic neurones are interconnected, with each system exerting a negative effect on the other. Specifically, there is a β-muscarinic interaction referred to as "accentuated antagonism" that antagonises β-receptor actions [19, 20]. Parasympathetic stimulation can antagonise, both presynaptically and postsynaptically, inhibiting Ca^{2+} and K^{+} currents causing prolongation of the APD and refractory period.

It should be mentioned that studies that look specifically at the effects of neurotransmitters (e.g. [18]) are often performed based on *ex-vivo* measurements in which cells or tissues were isolated. In the functioning heart, cells and tissues may respond differently due to their interconnection. An experiment aiming to investigate the electrophysiological effects of vagal actvitiy in the *in-vivo* was conducted by Yamakawa et al. [21], who performed vagal nerve stimulation in pigs. As expected, a significant prolongation of ARI was found. However, an important caveat when studying APD changes is that APD is a function of heart rate, i.e. APD shortens with increasing heart rate and vice versa. The experimental design did not count for this, as heart rate was not clamped. Consequently, the observed

changes in electrophysiolgy could actually be caused by the decrease in heart rate. Based on their experimental setup, it is not possible to evaluate direct (heart rate independent) effects on APD. Another important consideration is that the vagal nerve was stimulated artificially. This might be useful to investigate the direct effect of the nerve, but for studying the neural control system it is less useful as electrical stimulation of nerves does not mimic normal physiological behaviour.

In general, increased sympathetic activation has been associated with an increased risk of ventricular arrhythmias and fibrillation, whereas parasympathetic activation is considered to be cardioprotective [3, 22]. The experiments described in this work particularly focus on the subtle aspects of autonomic innervation on the heart to investigate the mechanisms of control of the nervous system on cardiac stability.

2.3.3 Responses to emotional stress

The ANS is not only involved in facilitating haemostasis, it also responds to commands from higher brain centres. For example, the ANS mediates the cardiac fight or flight response when the body has to be prepared for forecast requirements. However, mental stress has also been recognised as playing a significant role in the onset of arrhythmic events and sudden cardiac death [4, 23]. For example, previous studies have confirmed that psychological stress can cause a profound reduction of the cardiac threshold for arrhythmias, like ventricular fibrillation [24]. While the fatal consequences of autonomic response are not exaggerated, the mechanisms are still incompletely understood, they are presumably caused by the influence of sympathetic activity on the myocardium through changes in perfusion and/or electrophysiology [4].

2.3.4 Cardiovascular rhythms and repolarisation

Oscillatory behaviour is a ubiquitous property of many biological systems including the cardiovascular system [9]. Blood pressure and heart rate are known to exhibit oscillatory behaviour at approximately 0.1 Hz and (Mayer waves) and at the respiratory frequency (approximately 0.25 Hz); both rhythms have been associated with ANS activity. Quantification of this variation has provide insight into the neural regulation of the heart. The two frequencies and their relation to autonomic regulation of the heart are discussed in this subsection.

2.3.4.1 Respiratory oscillations

Heart and blood pressure variations at the respiratory frequency are widely held as a parasympathetic (vagal) phenomenon, and this theory is supported by substantial published data [25, 26]. An important finding that supports this explanation is the enhanced amplitude of the variation at the respiratory frequency following inhibition of sympathetic activity using cardioselective blockers of the β-receptors. This assumes that sympathetic outflow opposes parasympathetic mediated oscillations and that sympathetic blockade removes this effect.

Since ANS input is also known to affect the cardiac action potential, Hanson et al. hypothesised that ventricular APD might also exhibit cyclical behaviour with respiration [10]. To test the existence of such a mechanism, they measured ARIs from UEGs recorded at tissue level inside the heart ventricles (endocardium) in patients with healthy ventricles. The heart rate was clamped during the experiment by electrical pacing of the right ventricle and subjects were instructed to breathe at fixed frequencies. Using autoregressive spectral analysis, it was found that ARI exhibited respiratory-related oscillations. Examples of this behaviour are shown in Figure 2.8. Although these observations were consistent with autonomic oscillation, there remained other possible explanations attributable to external factors. Three possible scenarios are: (1) chest movements associated with breathing changes the distance between the recording and reference electrodes which induces changes in the signal morphology; (2) as the lungs fill with air, their effective conductivity decreases, which can alter the lead field; and (3), the exploring electrodes may have moved with respect to the myocardial wall. The latter explanation was ruled out using X-ray video feed, which confirmed good contact. The other two explanations cannot be ruled out completely, but are estimated to be unlikely. In the first place because persisting oscillations were found just after the onset of breath holding. Secondly, sympathetic blocking agents were found to reduce the ARI oscillations in a small subcohort of 5 patients. These observations seem to support that at least some of the oscillations, did indeed reflect modulation of cardiac electrophysiology. The autonomic blockade test should be repeated in a larger group to confirm the results.

More information about respiratory-related ARI oscillations could be obtained by characterising the relationships between the observed ARI oscillations, respiration and blood

pressure. For example by measuring the strength of the link (coupling) between ARI, respiration and blood pressure. Although both signals exhibited oscillations at the same frequency, phase lag between ARI and respiration was reported to be different by Hanson et al. [10]. The study did, however, not confirm whether both signals were significantly coupled, necessary to prove the relationship. Tools that allow can quantify the strength of interrelationships are described in Section 2.5.1 and have recently been employed to study heart rate variations during spontaneous breathing, so this is a key priority for research which will be addressed in this thesis [27].

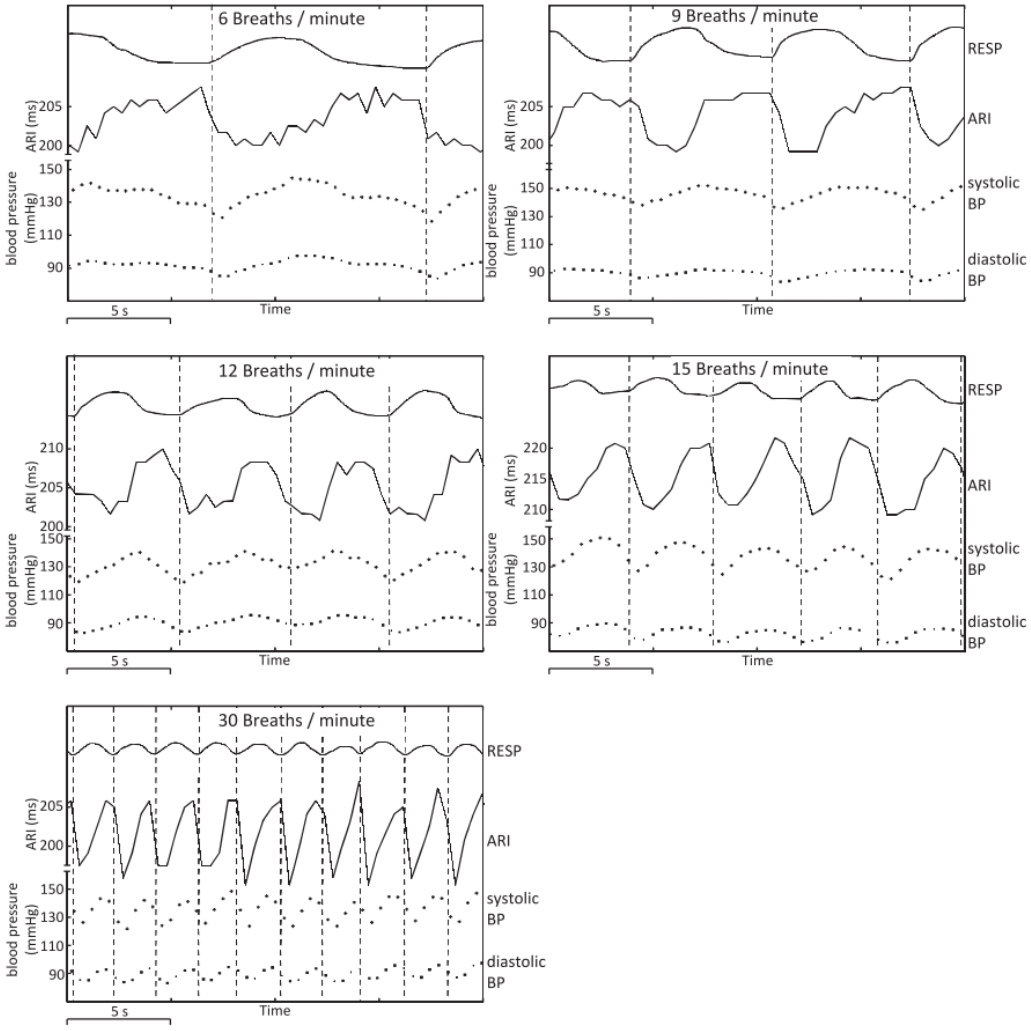

Figure 2.8: Cyclical variation of ARI and arterial blood pressure: Example plots showing respiration, ARI, and arterial blood pressure at respiratory frequencies of 6,9,12,15 and 30 breaths/min. Adapted from [10]. Permission not required.

Finally, regarding the study of Hanson et al. [10], it should be noted as well that a substantial number of recording sites did not exhibit significant oscillatory behaviour with

respiration. Although the authors do not specifically address this point, it raises the question whether this means that there were actually no oscillation in local APD or whether it was related to the signal quality affecting estimation of activation and recovery times. The development of new techniques to assess the significance of oscillatory behaviour and coupling is therefore implemented in this thesis to improve the interpretation of the observations.

2.3.4.2 Low frequency oscillations

Low frequency oscillations in blood pressure and heart rate at a frequency between 0.04-0.15 Hz are observed during enhanced sympathetic activation and often termed Mayer waves. Mayer waves are closely coupled with oscillations in sympathetic outflow [28]. The substratum of Mayer waves is generally assumed to be neural by waxing and waning of sympathetic output. The exact mechanisms underlying these oscillations are still unclear, but the haemodynamic basis is believed to result from oscillatory behaviour of the vasomotor tone resulting in cyclic variation of vascular resistance [25, 29, 30]. As Mayer waves have shown to modulate the behaviour of the autonomic nervous system, it would be of great importance to identify whether Mayer wave oscillations are affecting local electrophysiology directly. This is especially of interest as Mayer waves are enhanced sympathetic activity, like mental stress, which is known to increase the vulnerability to arrhythmias and sudden cardiac death.

Regarding low frequency oscillations of repolarisation, some evidence has been provided by measuring the QT interval in the ECG, which is sometimes used as an indirect and very rough measurement of the global ventricular repolarisation. Negoescu and colleagues analysed the spectral content of the QT interval series, and observed that the power at the Mayer wave frequency band (0.05-0.15Hz) was significant increased during several tasks that are associated with a higher sympathetic tone, like emotional stress [31]. However, in this study heart rate was not clamped and low-frequency oscillations were observed in heart rate as well. It is therefore possible that the observed changes in QT were actually due to changes in heart rate and do not represent independent modulation of global APD.

Based on these literature findings, it is hypothesised that Mayer waves may indeed occur in APD given the profound influence of sympathetic activation. Using clamped

heart rate and UEG recordings to measure ARIs would help to further validate the low-frequency variability of the APD as a control mechanism of cardiac electrophysiology. Time-frequency methods seem to be best suited, given the fact that Mayer waves can occur and disappear spontaneously.

To summarise this subsection, autonomic modulation of cardiac electrical activity is a richly complex subject. The heart is innervated by two limbs of the autonomic nervous system at various sites. Awareness of the dynamic variations of ANS output to the heart are essential when investigating the nervous control systems of the heart. Two important rhythms that are known to cause temporal variation in the autonomic outflow to the heart are respiratory behaviour and low-frequency Mayer waves. Both dynamics have been well studied on the global properties of the heart (e.g. heart rate), but less is known about their influence on the local properties of the heart. As mentioned previously, differences in local activity can increase the vulnerability of arrhythmias, combined with the fact that both rhythms are associated with pro-arrhythmic conditions (e.g. sleep apnea and mental stress), makes it highly interesting to study their influence on local electrophsyiology [4, 23, 32]. In addition, the baroreflex input can be used to actively modulate the autonomic activity to the heart, and stimulation could be useful to study the effect of neural control on localised cardiac activity.

2.4 Electrical measurements of local cardiac activity

Contraction of the heart's chambers is characterised by activation of large collections of myocytes. The resulting potential difference across the heart is large enough to be measured by placing electrodes on the skin. This recording technique is called the electrocardiogram (ECG). Figure 2.9a displays the basic electrode configuration for the ECG. Each pair of ECG electrodes is referred to as a lead and each lead shows a characteristic waveform during the cardiac cycle. For example, Figure 2.9b shows the waveform recorded during the depolarisation of the ventricle which repeats for each cardiac cycle. This salient detail makes the ECG a convenient non-invasive instrument that has been intensively used for studying the global effects of the nervous system on the heart.

The nature of the ECG interpretation involved in this thesis does not require a detailed theoretical analysis. It is sufficient to consider a single cardiac dipole which act across the

boundary between polarised and depolarised regions. This dipole can be represented as a vector that changes magnitude and direction when a wave of electrical activity spreads through the heart, for instance during the depolarisation of the myocardium as shown Figure 2.9b.

A typical ECG pattern recorded during the cardiac cycle is shown in Figure 2.10. The fluctuations, or waves, are named: The P wave corresponds to the depolarisation of the atrium. This wave is followed by a QRS complex, which represents depolarisation of the ventricles and the T-wave represents the repolarisation of the ventricles. Note that both the T-wave and the QRS complex both produce upward deflections when considering that they represent opposite effects. The generally accepted explanation for this is that repolarisation occurs in the reverse direction to depolarisation, thus the last regions to depolarise are

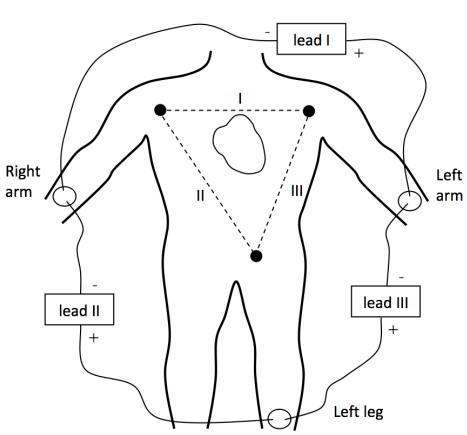

(a) Configuration of the ECG leads.

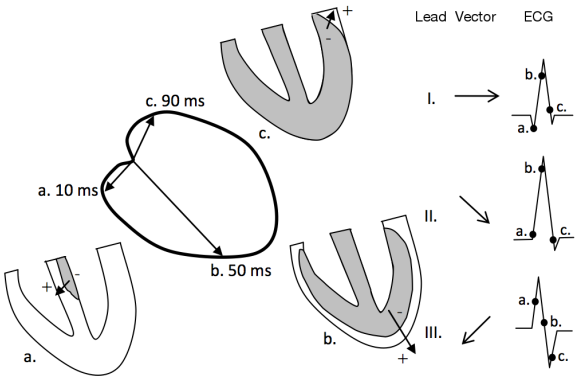

(b) ECG vector representation describing the activation (depolarisation) of the ventricles at three time stages.

Figure 2.9: The configuration and genesis of the ECG.

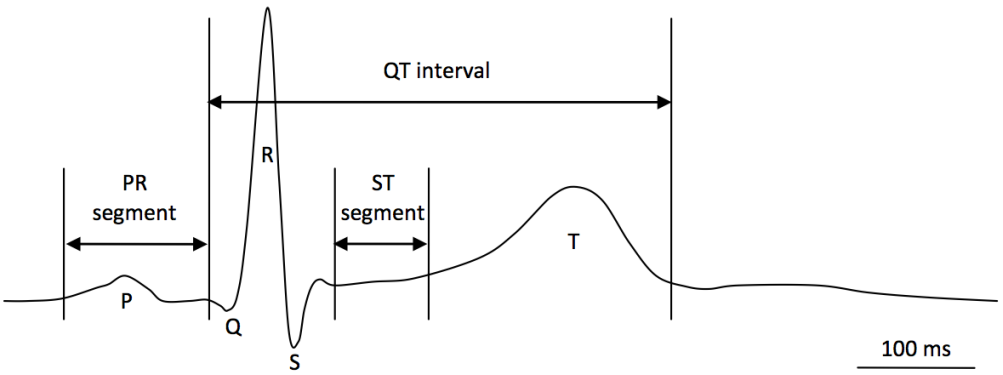

Figure 2.10: A typical ECG recordings trace and its features.

commonly known to be the first to repolarise [33].

2.4.1 Limitations of the ECG

The ECG can be used to characterise normal cardiac electrical activity and is used extensively in clinic to identify a wide range of pathologies. As an investigative tool, it is particularly useful because measurements can be made non-invasively. However, the ECG is measured throughout the body, which limits its spatial specificity.

Neural control of the heart is anatomically and functionally heterogeneous to maintain overall stability and efficiency of cardiac behaviour during varying physiological scenarios. Consequently, a more complete impression of the nature of nervous control of the heart can be achieved from recordings measured inside the heart. Intracardiac measurements can differentiate between activities from different regions of myocardium with greater spatial specificity than is available from the ECG, making them useful for detecting subtitle changes in electrophysiology during neural activation.

2.4.2 Intracardiac unipolar electrograms

Western reviewed several (intracardiac) recording techniques with high spatial resolution to study the influences of the nervous system based on three criteria: (1) suitability for human *in vivo* studies, (2) ability to characterise local repolarisation as well as depolarisation, and (3) spatial specificity [11]. Based on these criteria, the UEG was found most useful and was employed by Western and colleagues to explore the nature the influence of respiratory behaviour on cardiac electrophysiology [10, 11]. This work is discussed later in Section 2.3.4.

The work presented in this thesis is an extension of Western's work in which novel signal processing method for UEGs were developed to expose the nature of the nervous control mechanisms in more detail. Assessment of the validity of these results requires a sound understanding of the genesis of the UEG and an awareness of the accuracy of the related markers. To that end, the UEG recording technique and related markers of local cardiac activity are briefly reviewed below.

UEGs are measured as the difference in electrical potential between an electrode in contact with the cardiac tissue and a reference electrode positioned outside the heart as illustrated in the left panel of Figure 2.11. In theory, the method assumes that only the po-

tential measured at the tip contributes to the UEG voltage and that the contribution of the remote reference is negligible. The commonly observed deflections in the UEG strongly resemble those in ECGs and therefore they are referred by the same lettering system, the QRS complex reflects depolarisations and the T-wave that follows represents repolarisation. Regarding the specificity of the recording, it should be mentioned that the body does not offer a reference that is stable enough to acquire an *in-vivo* recording that purely reflects activity at the tip, however, recordings can still be used to obtain important about the electrophysiological behaviour of the heart.

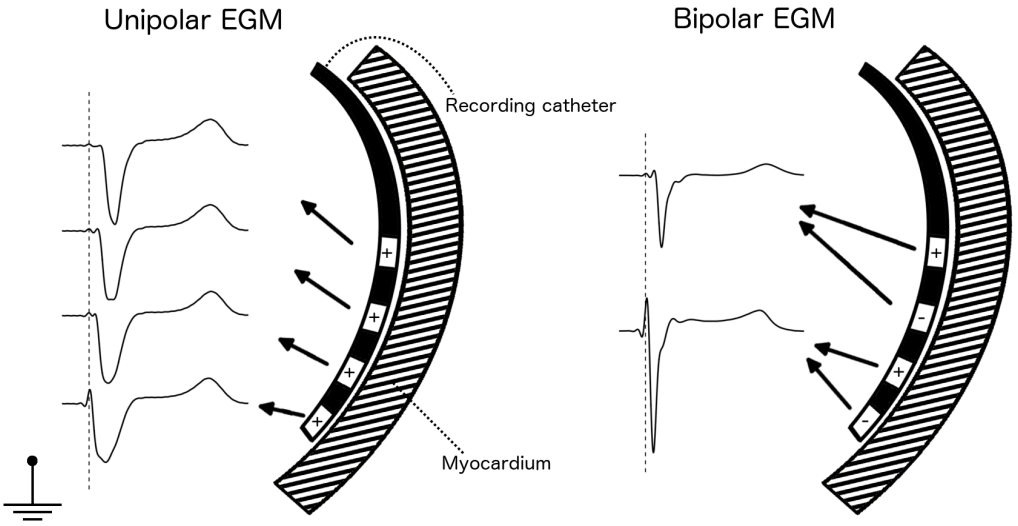

Figure 2.11: A schematic illustration of the arrangement of the UEG (left) and BEG (right) electrodes positioned against the inside of the myocardium, called endocardium. The arrows indicate the typical UEG waveform morphologies of such recordings. EGM = electrogram

The relationship between a monophasic action potential and a corresponding UEG waveform is illustrated in Figure 2.12. The upstroke of the action potential gives a negative deflection in the UEG. This is caused by Na^+ ions in the vicinity of the measuring electrode that move from the extra cellular matrix into the cell, decreasing the local potential in the extra cellular matrix. The nominal time of local activation is at the time of the greatest downward slope of this negative deflection in the UEG [34]. In literature, this point is generally referred as $\dot{V}_{down}$. In a similar way, the rapid change in membrane potential during phase 3 of the action potential causes a deflection in the UEG, shown as the T-wave. The point in the T-wave with the maximum upstroke, T_{up}, has shown to be well correlated with the point of maximum downward slope in the action potential t_r in experimental and computation studies [35–38]. This method to determine repolarisation is often referred to as the

Wyatt method [35]. The interval between $\dot{V}_{down}$ and T_{up} is called the activation recovery interval (ARI) and a useful substitute for the APD [37, 38].

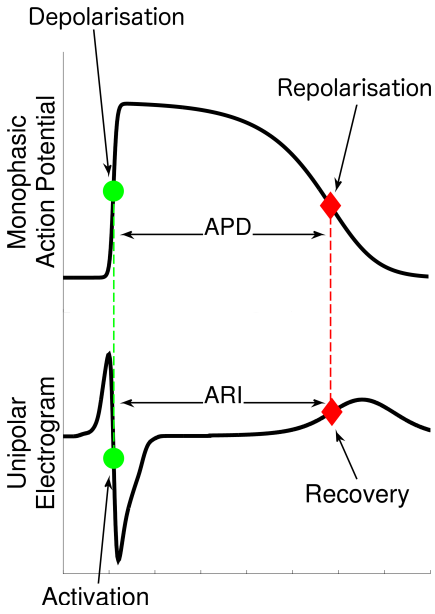

Figure 2.12: The relationship between the monophasic action potential (MAP) and the unipolar electrogram (UEG). Activation and recovery times are commonly used indices to estimate depolarisation and repolarisation.

2.4.2.1 Accuracy of activation-recovery intervals derived from the UEG

A potential confounding factor in the interpretation of the ARI, is that the interpretation of T_{up} is less straightforward than $\dot{V}_{down}$, because t_r does not correspond to any discrete event at cellular level as repolarisation is not an instantaneous process: By the time the action potential has depolarised to about -55mV, some of the fast Na^+ channels responsible for depolarisation have already returned into an excitable state [15]. This makes the cell, as a whole, partially excitable and this state is referred to as the relative or effective refractory period (ERP) to distinguish it from the absolute refractory period. As explained previously, the rate at which Na^+ channels return to excitability is voltage- and time-dependent. Consequently, the degree of refractoriness depends rather on the preceding time-course of repolarisation than on the timing of an instantaneous event. This ambiguity may seem to defy the use of a single point to differentiate between refractory and excitable. However, phase 3 of the action potential is sudden enough for such a simplification to be viable, especially in ventricular myocytes.

Studies have found a good correlation between the ARI and ERP, measured as the interval between depolarisation time and the time at which the cell is able to fire a new

action potential, in animals and humans [35, 36, 39, 40]. Figure 2.13 shows the strong correlation between ARI and refractory period found by Chinushi [40]. However, it should be emphasised that ARI is not a direct approximation of ERP, but given the correlation, it can be interpreted as a useful description of action potential duration (APD).

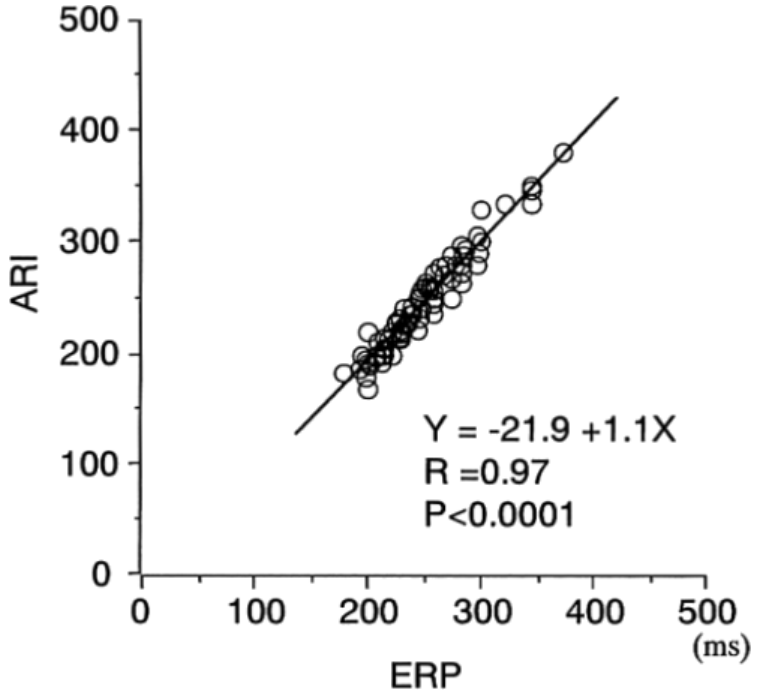

Figure 2.13: A high correlation was found between ARI and the (effective) refractory period (ERP) in humans. Data from Chinushi et al. [40] with permission.

More experimental validation of the ARI as an estimate of APD has been provided Coronel and colleagues using an experiment in which they regionally cooled tissue of porcine hearts to prolong the action potential locally [38]. ARI measures were compared to to Monophasic Action Potential (MAP) recordings. MAPs give a close approximation of the local action potential, allowing accurate estimation of APD. This technique is however more invasive and less practical compared to UEGs [11]. Also in this study some variability between ARI and APD was observed.

As shown in Figure 2.14, the polarity of the T-wave changes if the timing of repolarisation changes. The next subsection offers a more detailed interpretation of UEG signals and how they related to local cardiac behaviour.

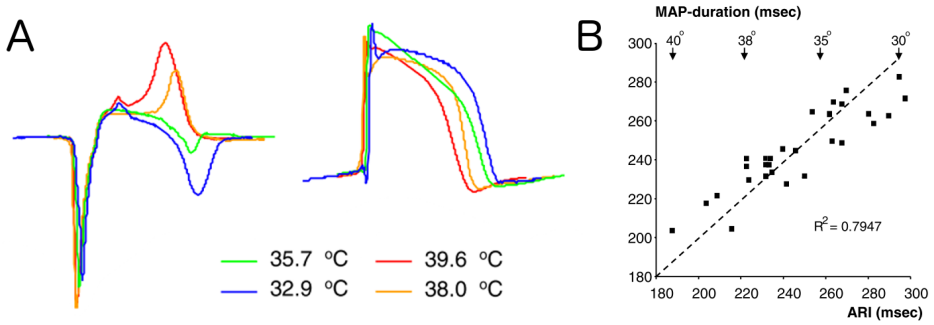

Figure 2.14: A: UEG waveforms recorded from the same site during local cooling of the tissue temperatures to modulate the APD locally at the recording site. There is a clear relation between the UEG T-wave and the corresponding position of T_{up}, and the APD. B: A strong correlation was found between ARI and APD (monophasic action potential (MAP) duration). Data from obtained from Coronel et al. [38] and reproduced with permission.

2.4.2.2 An intuitive model to predict the UEG morphology from the transmembrane potential

Potse and co-workers proposed and validated a simple and intuitive model to explain the UEG waveform as a function of time and position using the difference between a position-dependent local component $L(x,t)$ and a position independent remote component, $R(t)$:

$$UEG(x,t) = L(x,t) - R(t) \tag{2.1}$$

In this model, L is completely determined by local activity, recorded from the tip of the electrode at the cardiac source, whereas R is dominated by remote activity. The local component L can be estimated as the extracellular potential θ_e immediately outside the cardiac cell using the core-conductor model, defined as a scaled mirror image of the local membrane potential:

$$L = -\frac{\sigma_i}{\sigma_i + \sigma_e} v_m \tag{2.2}$$

where σ is the conductivity for the intracellular (i) and extracellular (e) domains, v_m represent the local membrane potential. The two domains interact by exchange of membrane current, as happens during the action potential. Conductivities were assumed to be isotropic to keep the model simple. The remote component (R) is the reference potential derived from Geselowitz [41]. This makes:

$$UEG(x,t) = -\frac{\sigma_i}{\sigma_i + \sigma_e} v_m - \int_H \sigma_i v_m \nabla Z \cdot d\vec{S} \tag{2.3}$$

where $d\vec{S}$ is an element of area on the heart's conductivity interface H, and ∇Z is a transfer impedance which relates these source elements to the reference potential (R).

Using this equation, one can explain the morphology of the T-wave in the UEG. As visualised in Figure 2.15, the remote component resembles an smoothed action potential. Based on 2.3, the UEG will be negative if the local component L is more positive than the remote component R. This happens when the cardiac cells at the electrode repolarise later compared to the rest of the myocardium. This explains why T-waves in 2.14A become negative following local cooling as this process only delayed repolarisation of cells around the UEG electrode, causing a positive T-wave (normal temperature) to change into a negative T-wave following cooling. Conversely, in early repolarising regions, the T wave is positive because the local membrane is still already repolarised, when most other cells are still depolarised. In agreement with experimental studies, biphasic waves always have a negative part followed by a positive part [38]. UEGs are plotted in Figure 2.15 for the full spectrum of T-wave morphologies (positive, biphasic, and negative).

2.4.2.3 Sources of error in measurements of unipolar electrograms

Western reviewed the implications of deviations from this ideal conditions on the reliability of ARI measurements and listed two important confounding factors that affect measurements of repolarisation [11]

Violation of theoretical assumptions: Deviation from the assumed action potential morphology : The action potential used in the simulation study of Potse (Figure 2.15) are characterised by a steep slope during repolarisation phase of the action potential [37]. During certain conditions, like ischemia and rapid pacing, the shape of the action potential may become more triangular. The timing of T_{up} is based on the assumption that the deflection of of the remote component during phase 3 is less steep compared to phase 3 of the local action potential, resulting in a clear T_{up}. If phase 3 of the action potential becomes less distinctive, then the UEG deflection during repolarisation becomes less sharp and T_{up} may become less meaningful or more easily corrupted by the behaviour of the remote component.

Violation of theoretical assumptions: Deviation from the idealised pattern of propagation : It has been shown in simulation and experimental studies that $\dot{V}_{down}$ and T_{up} can differ substantially from the associated membrane activities when the activation wave

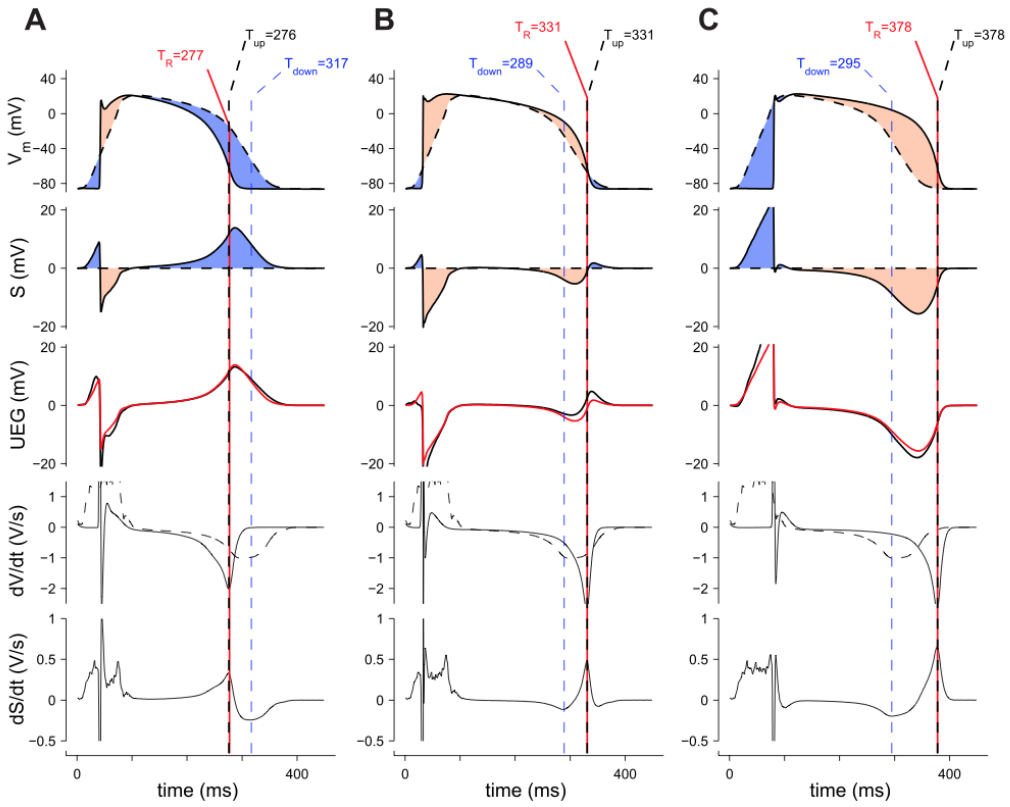

Figure 2.15: Simple intuitive model explaining the UEG waveform by subtracting a local component from a remote component. In the top row both components are drawn (solid = local component, dashed = remote component). If the local potential is more negative than remote potential, then the constructed electrogram is positive. This explains the relation between local repolarisation time and the T-wave morphology as shown in the second row. The third row shows the time derivative of the UEG with the local time of recovery T_{up} vs. the local time of repolarisation T_R. A: positive T-wave. B: biphasic T-wave. C: negative T-wave. Adapted from Potse et al [37]. Permission not required.

travels differently from the idealised pattern of propagation. Such an exception is likely to occur during fibrillation (chaotic activity), at sites where activity is initiated or terminated, and at site of discontinuous tissue properties (diseased or damaged tissue). The latter condition is thought to be most relevant for this project and would result in fractionated UEG waveforms that cannot reliably used for ARI estimation and should be omitted from analysis. Compared to normal sinus rhythm, the propagation pattern of the activation wave is changed when a pacing stimulus is used to artificially excite the heart during experiments. However, similar to normal sinus rhythm, the activation wave still spreads in an organised pattern through the myocardium.

Noise contamination Another important source of error that is independent of the theoretical basis on which ARI measurements rely is noise. Noise affect measurements of activation time (AT) and recovery time (RT). The latter index is especially vulnerable for noise since the upslope of the T-wave is not as steep as the and activation wave. Low-pass filtering can be used to attenuate noise and is incorporated into clinical hardware and is almost universally applied unless manually disabled. It can attenuate noise assuming the noise is present in higher frequencies than the signal, however all filtering distorts the underlying signal to some extent. At present, no studies have yet focussed particularly on how the accuracy of ARI detection depends on signal quality and filtering. Consequently, filter setting to manage noisy recordings remain empirical.

2.4.2.4 Measurement bias for positive T-waves

In spite of the reasoning and experimental evidence supporting the use of the Wyatt method, the fact remains that some studies have observed a substantial measurement bias in the sense that, at sites repolarising relatively early (yielding positive T waves), T_{up} tends to underestimate t_r. In recent computational work, Western et al. identified the electrode configuration as a possible cause of this bias [42]. It was found that a positive T-wave bias could emerge as a consequence of increased distance between the electrode and the underlying tissue. As a result, the signal becomes more smoothed which shifts T_{up} earlier in time as shown in Figure 2.16.

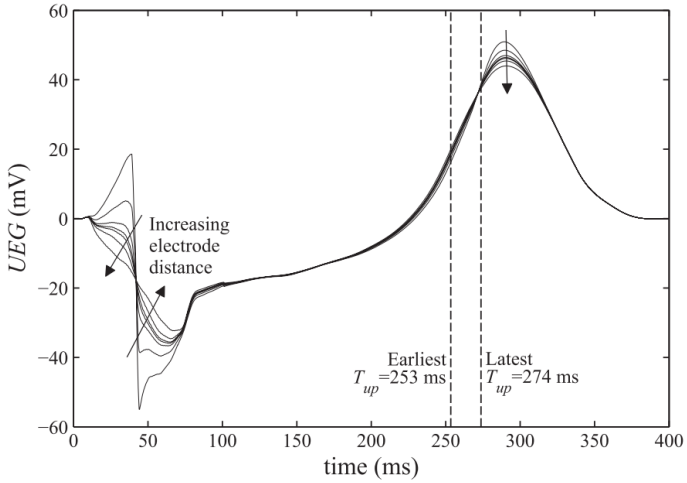

Figure 2.16: Reproduced from [42]. Calculated electrograms corresponding to large (16 mm) and small (0.004 mm) distances between the exploring electrode and the tissue. A measurements bias for T_{up} was identified with increasing the electrode distance. Permission not required.

2.5 Methods for characterising short-term variability and interactions

As outlined in the previous section, neural cardiovascular control is associated with oscillatory behaviour of heart rate and blood pressure. Identification of these periodic components in ventricular APD is required to characterise neural control regimes that modulate ventricular electrophysiology. An important aspect that should be taken into account when analysing these signals, is that oscillatory behaviour at the respiratory and Mayer frequency are not stationary under natural conditions. For example, the respiratory frequency varies during natural breathing and Mayer waves may spontaneously come and go. In addition, (temporal) coupling between APD and blood pressure Mayer waves could help to further understand the relationship between both processes and indicate that they are driven (at least in part) by a common mechanism. Thus, the methodology used to analyse APD variability should take into account the intrinsic non-stationarity nature of the processes, which means that the time-varying frequency characteristics should be measured.

Various methods exist for characterising time-frequency content and the choice depends on the specific nature of the signal to be examined. To determine the ideal method for characterising neural control of APD variability, two criteria were considered: (1) suitability for characterising time-varying spectral properties, and (2) temporal and frequency resolution.

- **Suitability for characterising time-varying spectral properties:** To track changes related to ANS activity, the method must be capable to characterise changes in frequency content accurately. For example, it was mentioned that Mayer waves may come and go. Localisation of such episodes is important for correct interpretation of temporal variability in electrophysiology. The effectiveness of the model is therefore heavily depended on method's capability to characterise short-term oscillatory behaviour.

- **Time and frequency resolution:** To characterise autonomic modulation, the frequency resolution must be fine enough to distinguish the spectral components of Mayer waves and respiration. For example, variation with respiration typically occurs around 0.25 Hz, while Mayer waves are known to occur between 0.05 - 0.15 Hz

[25]. At the same time, time resolution must be fine enough to follow quick variations, typically of the order of few seconds.

Broadly speaking, most of the time-frequency techniques that have been applied to cardiovascular signals can be divided in two categories: parametric and non-parametric.

2.5.0.1 Parametric autoregressive approach

The behaviour of a signal can be described as a realisation of a stochastic process. An autoregressive model uses this approach and approximates the signal's behaviour by predicting each successive point on its own previous values. The general relationship of a linear autoregressive model is described as:

$$y_n = -\sum_{k=1}^{p} a_k y_{n-k} + \varepsilon_n \tag{2.4}$$

In this expression, y_n is seen as the result of a linear combination of its own previous values, weighted by coefficients a_k. The model order is given by p, and represent the number of parameters a_k used to predict the next. Finally, ε_n is the error in predicting each nth point. Coefficients a_k are chosen such that the noise component is minimal and furthermore, noise should be white and uncorrelated. The model in 2.4 can be extended to capture the time-varying spectrum using time-varying coefficients:

$$y_n = -\sum_{k=1}^{p} a_{k,n} y_{n-k} + \varepsilon_n \tag{2.5}$$

where coefficients $a_{k,n}$ are the coefficients at time n, where n represents a time section of the signal to capture the time-varying properties of the coefficients. The corresponding time varying power spectrum of the model identified from a signal is defined as:

$$P(f,n) = \frac{\sigma^2}{\left(1 + \sum_{k=1}^{p} a_{k,n} e^{-i2\pi fk}\right)^2} \tag{2.6}$$

where σ is the standard deviation of the prediction error $\varepsilon(n)$ and f is the frequency. The time-varying frequencies of any oscillations in the signal are extracted by locating the peaks in $P(f,n)$. In general, auto-regressive spectra are preferable to non-parametric spectra for identifying spectral components when only a small number of data points are available, because the frequency resolution is not determined by the number of data points

used for calculation. However, correct selection of the model order is crucial, because false spectral peaks may be produced when an erroneous model order is chosen. Thus, the determination of the right model order is a significant issue and a major disadvantage of this method. Various methods were introduced to simplify this process. Most commonly being used is the Akaike information criterion, which evaluates the model order by measuring the trade off between accuracy and complexity [43]. Nonetheless, the fact that coefficients a_k need to be time-varying for capturing non-stationary behaviour, complicates the selection of the right model.

2.5.0.2 Non-parametric approaches

Short-Time Fourier Transform: The Fourier transform has served, and is of current use today, as a basis for a considerable amount of physiological experiments, because it is the most straightforward and accessible method available. Signal $y(t)$ admits a spectral decomposition in the form:

$$\hat{y}(f) = \int y(t) e^{-i2\pi ft} dt \tag{2.7}$$

where $\hat{y}(f)$ is a complex number that encodes both amplitude and phase of a sinusoidal component of signal $y(t)$. The traditional framework of the Fourier analysis assumes stationary, i.e. that the signal comprises variation at a number of frequencies, and that does not change over the duration of the signal. In order to track variations in frequency content with time, one can slice the signal into a number of short segments and perform the Fourier transform on each one of them: this method is known as the short time Fourier transform (STFT):

$$S(\tau, f) = \int y(t) \omega(t-\tau) e^{-i2\pi ft} dt \tag{2.8}$$

where $\omega(t-\tau)$ represents the symmetric window function and $S(\tau, f)$ is the Fourier transform of the windowed version of $y(t)$. For each segment (τ), the rule applies that the frequency resolution is $2/T$, where T is the window length. This relationship implicates an important trade off between time and frequency resolution: A narrow window offers good time resolution, but this comes at the expense of frequency resolution and vice versa.

Continuous Wavelet Transform: The basic method of the continuous wavelet transform (CWT) is to project the signal on a family of zero-mean functions, called wavelets. Wavelets are obtained by stretching or compressing an elementary wavelet (the mother wavelet) in time, allowing different frequencies to be examined. The CWT of signal $y(t)$ is defined as:

$$W(\tau,s) = \int_{-\infty}^{+\infty} y(t)\Psi^*_{s,\tau}(t)\,\mathrm{d}t. \tag{2.9}$$

where τ is the translation and s the scale factor and $*$ denotes the complex conjugated. Note that the CWT therefore forms a time-scale representation rather than a time-frequency representation. The basic wavelet $\Psi_{s,\tau}$ is calculated from the mother wavelet as:

$$\Psi_{\tau,s} = \frac{1}{\sqrt{s}}\Psi\left(\frac{t-\tau}{s}\right) \tag{2.10}$$

where s is the scaling function and τ is the translation factor. Time and frequency resolution are a function of the scale: High frequencies (small scales) are precisely located in time but this comes at the cost of the frequency resolution. The opposite is true for low frequency components, which are typically well characterized in frequency but less well-resolved in time. The difference between the uniform time-frequency representation of the STFT and to the non-uniform representation of the CWT is shown in Figure 2.17. The non uniform time-frequency grid makes the CWT particularly useful for detecting abrupt changes in continuous recordings, but the drawback is that the resolution is frequency dependent. Mager et al. has used the CWT to study beat-to-beat heart rate variability to expose the autonomic control on cardiovascular functionality [44]. A limitation of this method, is that the non-uniform time-frequency spectrum has also a more complicated appearance compared to the uniform time-frequency representation.

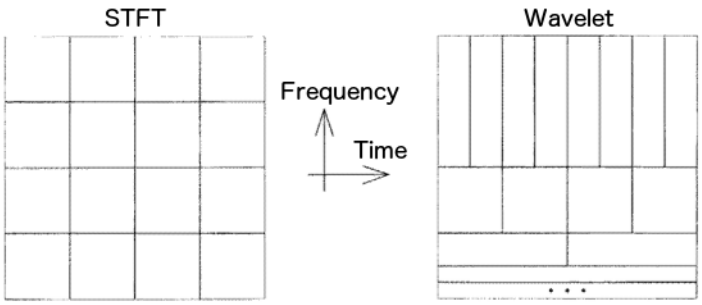

Figure 2.17: Time-frequency representations of CWT and STFT.

Smoothed Pseudo Wigner Ville Distribution: Both STFT and CWT perform a sort of 'localised' time-frequency transform since they rely on the analysis of a limited time window (ω or Ψ) that is translated along the whole time axis. In both cases this implies limitations in the time-frequency resolution. Bilinear time-frequency transforms overcome this limitation by distributing the energy of the signal in a more sophisticated way over the time-frequency plane. The Wigner-Ville distribution (WVD) is one of the most powerful bilinear time-frequency transforms and is given by:

$$W_y(t,f) = \int_{-\infty}^{+\infty} y\left(t+\frac{\tau}{2}\right) y^*\left(t-\frac{\tau}{2}\right) e^{-i2\pi f\tau} d\tau \tag{2.11}$$

In this equation the signal appears twice and is used in the form of analytic associate y^*, which is the complex conjugate of the real signal y. The WVD is computed by taking the Fourier transform of the signal's autocorrelation function with respect to the delay variable τ. One can think of this as a kind of STFT where the windowing function ω is a time-scaled, time-reversed copy of the original signal.

A desirable property of the WVD is that it produces instantaneous frequency and excellent localisation of temporal and spectral components resolution. However, an important problem that is inherent to this type of analysis is the appearance of strong cross-term interferences that complicate interpretation of the spectrum [45]]. Cross-term interference are manifested as oscillating features arising in the time-frequency plane halfway between each pairs of components, as shown in Figure 2.18A. These interferences are not due to spectral components of the signal but are due to their mutual interactions and should be removed in order to improve interpretation of the distribution.

Because interference terms are oscillatory, they can be attenuated by filtering the WVD. The smoothed pseudo Wigner-Ville distribution (SPWVD) is one of the most interesting approaches, since it provides an independent control over the time and frequency resolution. The SPWVD of signal $y(t)$ can be estimated in the time-lag domain (t,τ) by using a separable kernel $\phi(t,\tau) = \phi(t)\phi(\tau)$:

$$S_{xx}(t,f) = \int_{-\infty}^{+\infty} \phi_d(\tau) \left[\int_{-\infty}^{+\infty} \phi_t(t-\upsilon) y\left(\upsilon+\frac{\tau}{2}\right) y^*\left(\upsilon-\frac{\tau}{2}\right) d\upsilon \right] e^{-i2\pi f\tau} d\tau \tag{2.12}$$

where the term in the brackets represents a smoothed version of the auto-correlation

function. Functions $\phi_d(\tau)$ and $\phi_t(t-\upsilon)$ represent the smoothing kernels. The effect of time-frequency smoothing is illustrated in Figure 2.18 using a example signal composed of two frequencies whose amplitudes are modulated in time: panel A shows the unfiltered WVD of a signal, panel B shows a frequency filtered version of panel A, in which $\phi_d(\tau)$ is used to remove interference between signals not superimposed in time, called the Pseudo Wigner-Ville distribution, panel C shows the effect of smoothing in time performed by $\phi_t(t-\upsilon)$ removing the residual interferences. The kernel filtering has reduced the cross-terms contaminations substantially, but the time-frequency resolution is now clearly lowered.

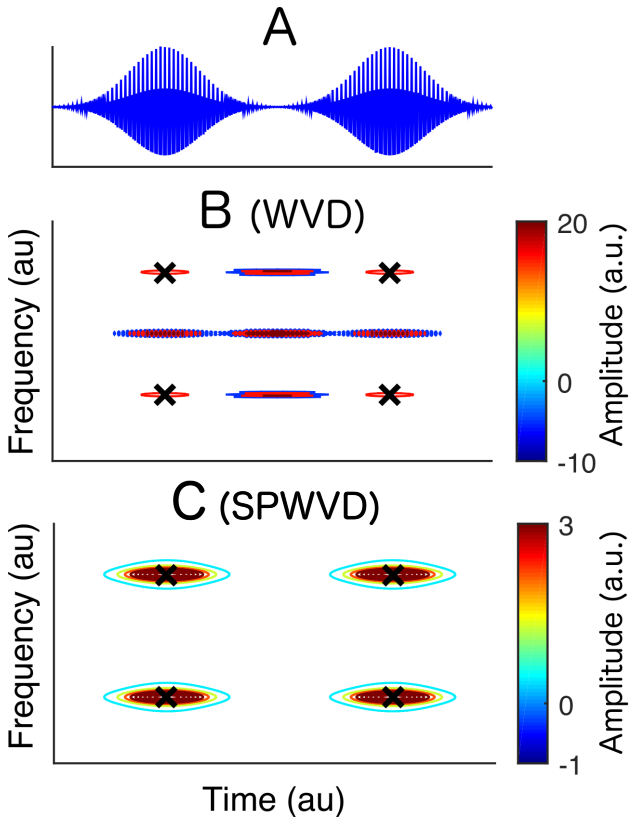

Figure 2.18: Effect of time-frequency smoothing of the Wigner-Ville Distribution (WVD) derived from a signal (A) composed of four time-frequency components. Panel (B): WVD distribution of the signal and containing interference terms. (C): WVD filtered in time and frequency to reduce interference terms: Smoothed pseudo Wigner-Ville distribution (SPWVD). The colour maps in B and C represent the amplitude of each time-frequency component. The frequencies of the four time-frequency components and their amplitude with respect to time can be clearly identified by the high amplitudes in C at the black crosses.

An important advantage of the SPWVD over STFT and CWT, is that it offers the

possibility of determining the shape of the smoothing function both in time and frequency, which in turn would allow more accurate localisation of APD dynamics related to neural activity. To assess the performance of the SPWVD in the analysis of non-stationary signals related to the autonomic modulation, Orini et al. generated stochastic signals that mimic real heart rate variability patterns. Signals were analysed using an exponential kernel with different settings [45]. It was observed that the correct smoothing function was particularly important for the estimation of the instantaneous power at respiratory frequencies, where the misdetection due to residual interference terms were more frequent [45]. The relationship between smoothing and time-frequency resolution depends on the shape and size of the smoothing kernel. Orini proposed two different parameters to quantify the resolution: 1) the width at half the maximum of the kernel (Δ_x^m), or 2) the width of the kernel at $a\%$ of the total area of the kernel ($\Delta_x^{a\%}$) [45]. The variable x in both parameters represents the time or frequency. Both parameters applying to a general kernel function are displayed in Figure 2.19.

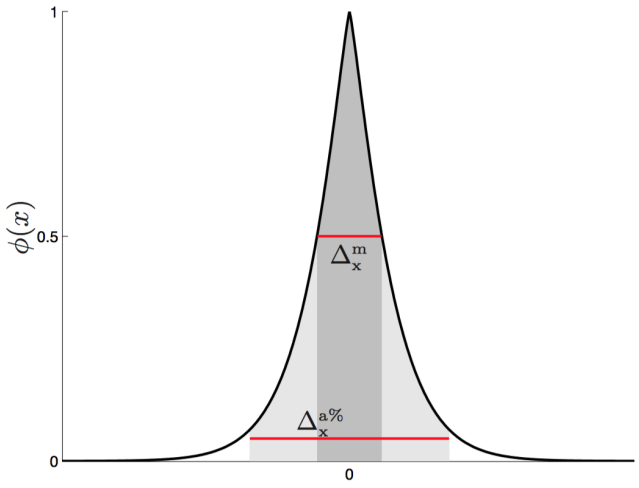

Figure 2.19: Two methods to quantify time-frequency resolution of the SPWVD based on the shape of the smoothing kernel $\phi(x)$, where x represents time or frequency. Parameter Δ_x^m represents the width of the kernel at half maximum, whereas, $\Delta_x^{a\%}$ represents $a\%$ of the total area of the kernel ($a = 95\%$).

2.5.1 Time-frequency coherence analysis

As explained in the previous subsection, time-frequency analysis is a useful method to track the time-varying spectral properties of ARI. The investigations of this thesis particularly seek to expose underlying dynamic interactions with other neural-controlled processes, like respiration and blood pressure. For example previous work by Hanson et al. demonstrated a relation between ARI and respiration, but the impact of this result is limited unless we also know whether ARI is indeed linked with respiratory behaviour [10]. Similarly, coupling of low-frequency oscillations in ARI with Mayer waves would provide important information

the mechanisms underlying these ARI oscillations.

Characterisation of the dynamic interactions between physiological signals using cross spectral analysis has been widely used in assessing the functioning of the cardiovascular system, i.e. heart period, arterial pressure and respiration [27]. The strength of the link between two non-stationary signals as a function of time can be measured using the time-frequency coherence (TFC):

$$\gamma(t,f) = \frac{|S_{xy}(t,f)|}{\sqrt{S_{xx}(t,f)S_{yy}(t,f)}} \quad \gamma(t,f) \;\; \varepsilon[0,1] \tag{2.13}$$

where $S_{xx}(t,f)$ and $S_{yy}(t,f)$ are the non-stationary auto spectra of $x(t)$ and $y(t)$, and $S_{xy}(t,f)$ represents the non-stationary cross spectrum. The TFC ranges between 0 (absence of correlation) and 1 (complete correlation). The auto spectra of $x(t)$ and $y(t)$ are estimated using Equation 2.12 which represents a smoothed version of the Fourier transform of the auto-correlation function. The cross spectrum $S_{xy}(t,f)$ is computed similar as the autospectra (Equation 2.12) by replacing x^* with y^* to compute the Fourier transform of the cross correlation:

$$S_{xy}(t,f) = \int_{-\infty}^{+\infty} \phi_d(\tau) \left[\int_{-\infty}^{+\infty} \phi_t(t-\upsilon) x\left(\upsilon + \frac{\tau}{2}\right) y^*\left(\upsilon - \frac{\tau}{2}\right) d\upsilon \right] e^{-i2\pi f\tau} d\tau \tag{2.14}$$

A important advantage of the TFC is that is allows the significance of coupling to be inspected as function of time. This valuable aspect was used in recent work of Orini et al., in which the SPWVD and the TFC have been used to characterise temporal evolution of coupling between heartbeat interval (RR-interval) and arterial blood pressure in subjects undergoing a tilt-table test [27]. The tilt-table test, which is a simple, noninvasive, test for stimulating the ANS. As shown in Figure 2.20, the protocol included an early supine position (T_{es}) followed by a head-up tilted (T_{ht}) and a later supine position (T_{ls}). The SPWVD clearly characterises the non-stationary dynamics of respiration in RR interval and blood pressure, which fluctuated between 0.15 and 0.25 Hz. Despite the non-stationary structure of the signals, the regions in which the local coupling was statistically significant were localised by the TFC analysis. Clearly, by using averaging in traditional spectral ranges, one would have estimated a much lower coherence for respiration and erroneously

detected abrupt changes in coupling between low-frequency oscillations (around 0.1 Hz) at t=240 and t=600s. This example demonstrates the ability of the SPWVD TFC to localise changes in the strength of the temporary coupling between both processes, for example the coupling at 0.1 Hz frequency which has been related to sympathetic nervous activity is clearly increased during tilting [25, 28]. TFC will be used in this thesis to characterise ARI behaviour and the interactions with blood pressure, since both are subject to similar conditions, like varying respiration during natural breathing or Mayer waves that may come and go.

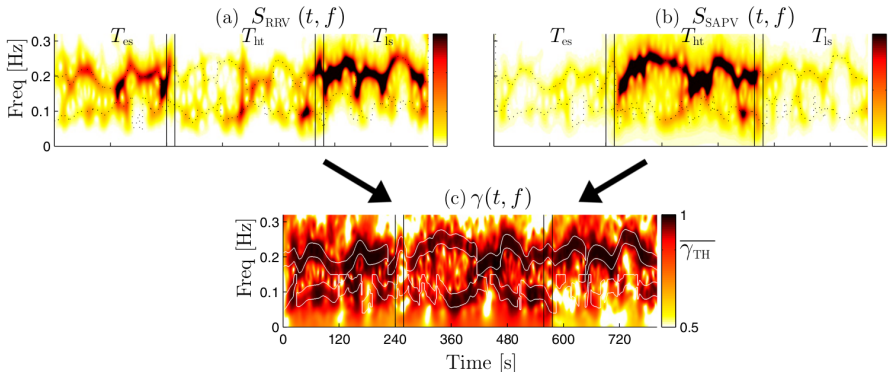

Figure 2.20: Characterisation of temporal evolution of coupling between heart rate and arterial pressure variability based on the SPWVD time-frequency coherence (TFC). Top row: SPWVD of heart rate variability (a) and arterial blood pressure (b). Bottom: corresponding TFC ($\gamma(t,f)$). Significant TFC was found with respiration (around 0.2 Hz) and temporary at a low frequency (around 0.1 Hz). low frequency, especially during head-up tilt position (T_{ht}), which has shown to increase sympathetic nervous activity. Reproduced from [46] with permission.

2.5.2 Characterisation of causal interactions using multivariate analysis

Coherence analysis offers a powerful method to extend upon previous physiological studies by demonstrating a link between oscillations in (for example) respiration and cardiac APD, beyond just illustrating that they are both oscillating. However, information provided by the coherence is limited to analysis between two signals and does not provide any information about the direction of the coupling. For example, coherence can demonstrate that three processes are coupled by comparing them pairwise, but is unable to disambiguate between the underlying connectivity patterns, like the two presented in Figure 2.21.

To overcome this problem, Faes and Nollo proposed a framework to assess the interactions based on a causality measure derived from linear time series analysis [47–49]. This framework decomposes frequency domain measures of coupling (coherence) into terms eliciting the directional information from one process to another, the so-called directed co-

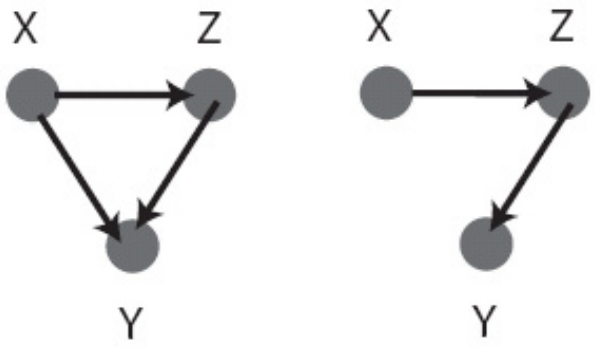

Figure 2.21: Two possible interactions cannot be distinguished by pairwise analysis, as we will find coupling between X and Y in both cases.

herence (DC). The DC $\gamma_{ij}(f)$ ($y_j \rightarrow y_i$) is defined as:

$$\gamma_{ij}(f) = \sqrt{\frac{S_{i|j}}{S_{ii}}} = \frac{\sigma_j H_{ij}(f)}{\sqrt{S_{ii}(f)}} = \frac{\sigma_j H_{ij}(f)}{\sqrt{\sum_{m=1}^{P} \sigma^2 |H_{im}(f)|^2}} \tag{2.15}$$

where H_{ij} is the directed transfer function from y_j to y_i, $S_{i|j}$ represents the part of spectrum of y_i (S_{ii}) due to y_j. Further interpretation of the DC in terms of coupling strength is achieved considering its normalisation properties:

$$0 \leq |\gamma_{ij}(f)|^2 \leq 1 \, , \; \sum_{m=1}^{P} |\gamma_{im}(f)|^2 = 1 \tag{2.16}$$

These properties indicate that the squared DC $|\gamma_{ij}(f)|^2$ measures a normalised coupling strength: 0 in the absence of directed coupling from $y_j \rightarrow y_i$ at the frequency f, and 1 in the presence of full coupling.

Where direct coupling suggests an interaction between two indices, DC indicates a direction of the coupling (albeit without providing information about the pathway of coupling). For example, if one can find DC from respiration to heart rate at the respiratory frequency, then this interaction could be the result from a direct pathway in which respiration directly affects heart rate, but also from an indirect pathway, e.g. respiration affecting blood pressure, which then in turn affects heart rate. Nonetheless, this technique has the potential to significantly extend the impact of previous studies. The full derivation of the DC formalised in the context of a multivariate autoregressive (MVAR) representation is given in Appendix A.

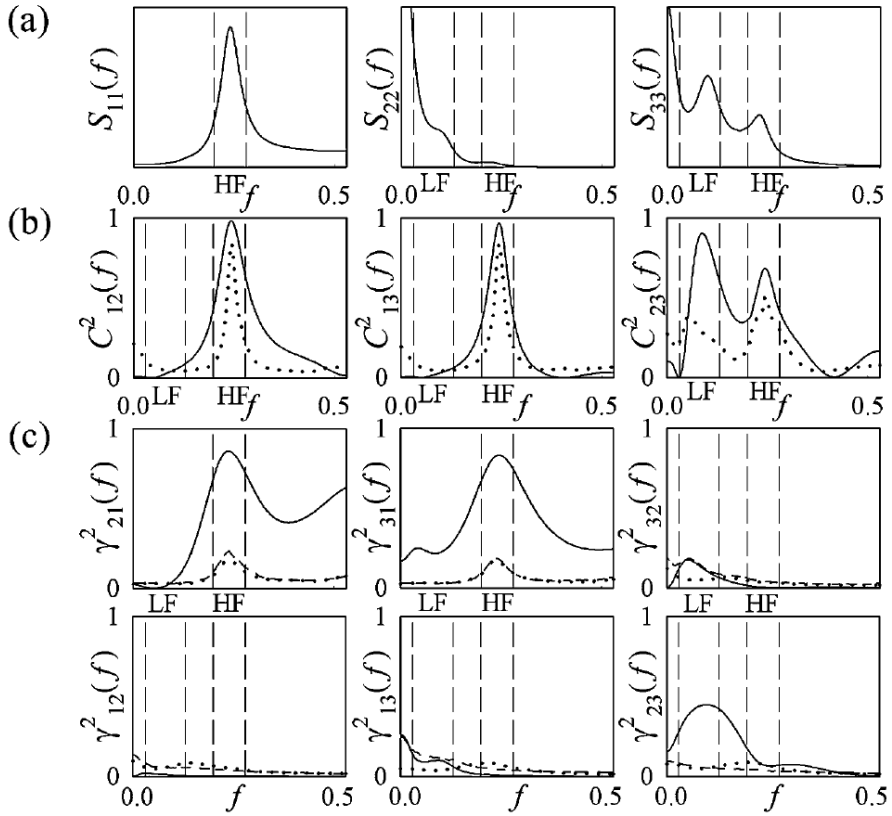

Figure 2.22: Example data showing frequency-domain measures of coupling and causality between respiratory flow (y_1), systolic blood pressure (y_2), and heart rate interval (y_3). Top row (a) shows the spectra of each process. A clear high frequency (HF) component related to respiration is present in y_1 and y_3. Row (b) shows pairwise analysis of the squared coherence. For example, C^2_{12} shows the squared coherence between y_1 and y_2. All processes show high coherence for the HF component. In addition, y_2 and y_3 are also correlated for the LF component. The squared directed coherence (γ^2_{ij}) is shown in (c) and shows the decomposition of the coherence. For example, γ^2_{21} and γ^2_{31} show that for HF oscillations information is flowing from $y_1 \rightarrow y_2$ and $y_1 \rightarrow y_3$, indicating causality from y_1 to the other signals. In addition, y_2 and y_3 show mutual causality for the LF component. As one may expect, there is no causality for $y_2 \rightarrow y_1$ and $y_3 \rightarrow y_1$ pathways, because y_1 is controlled voluntary. Data reproduced from [49]. Permission from publisher not required.

Faes and colleagues used DC to study short-term cardiovascular and cardiorespiratory interactions in young adults [49]. Beat-to-beat time series of heart period, systolic blood pressure, and respiratory flow were measured and tested for their underlying (causal) interactions. The spectra, squared coherence and squared DC of the signals from a representative subject are shown and explained in Figure 2.22. Regarding the low frequency (LF) component, the peaks in γ^2_{23} and γ^2_{32} suggests mutual interaction between heart-rate and blood pressure at the low frequency. The small peak in γ^2_{32} for the LF component may suggest

neural feedback driven by arterial blood pressure sensors that respond to the LF oscillations in blood pressure [50]. This is part of a negative feedback system that controls heart rate and cardiac contraction based on the blood pressure measures, known as the baroreflex.

Two important technical aspects need consideration regarding the interpretation of the results of this study. Firstly, blood pressure was measured continuous using a non-invasive finger cuff using the Finapres method. This method has two limitations: (1) Most importantly, Imholz et al. reported that this technique introduces an artificial time-lag of about 1.4s compared to (invasive) intra-arterial blood pressure measurements [51]. Given the fact that causal interactions are based on signal information of samples from the past, this could be an important confounding factor in the causality analysis. (2): another limitation is the accuracy of the non-invasive blood pressure measurements. Although these measurements show good correlation with invasive intra-arterial blood pressure measurements, Imholz et al. reported systolic deviations between both methods ranging from 10 to +11 mmHg, which is in the magnitude range of blood pressure oscillations related to respiration and Mayer waves [25, 52].

The second important problem is that because heart period fluctuates, the measurements are irregularly sampled. To overcome this problem signals have to be interpolated to infer a continuous-time measure which is not physiologically meaningful. Therefore although this work is very helpful in mapping physiological interaction mechanisms, there is potential to obtain a more robust model by studying human physiology with more invasive measures of blood pressure, with a fixed-paced heart rate and even with voluntarily controlled respiration rate, such as the clinical recording situation used successfully by Hanson et al. [10, 53].

2.6 Conclusions and objectives

This chapter has presented the current understanding of how the neural control regimes of the heart are organised and how they influence the heart's electrical behaviour. Oscillatory behaviour of blood pressure and heart rate is an important manifestation of ANS control. Recent work has reported that ventricular APD is also modulated cyclically with respiration independent of heart rate. More research is needed to elucidate the neural contribution to these oscillations and to find out whether APD also exhibits variability at the lower frequency. To that end, methods were discussed to investigate short-term variability and coupling, and the directionality of coupling. This chapter can be summarised as follows:

- Refractoriness is a critical determinant of cardiac stability and is related to the action potential duration (APD) and modulated by the nervous system.

- Unipolar electrograms (UEGs) can be used to estimate the APD with good correlation. However, at present there is some uncertainty about how these estimates are affected by signal quality and how that interference could affect tracking of APD dynamics.

- ANS control is manifested by oscillations at a low frequency and a high (respiratory) frequency. Cyclical modulation of ventricular APD has been observed with respiration, however the causality of interactions has not been demonstrated yet. In addition, the baroreflex has shown to play an important role in regulating the autonomic activity to the heart, but the response of APD to altered baroreceptor input has not been studied yet.

- Time-frequency and time-frequency coupling analysis using the smooth pseudo Wigner-Ville distribution (SPWVD) have proven to be useful in charactering non-stationary behaviour of the ANS associated periodicities in heart rate and blood pressure. In addition, the directed coherence (DC) is a useful analytical technique to determine directionality of coupling.

The conclusions of this literature review have led to the following objectives for this thesis:

- To investigate the effect of signal noise on ARI measurements and to develop and evaluate new methods to improve estimation of ARIs. Chapter 3 elaborates on this objective.

- To explore the origin of respiratory APD oscillations in more detail by: (1) studying the effect of autonomic blockade in a larger population allowing robust statistics to be applied, (2) quantifying the (causal) interrelationship between ARI, respiration and blood pressure, and (3) investigating the effect of spontaneous (non-stationary) breathing on ARI using time-frequency analysis. Research towards this objective is presented in Chapter 4.

- To characterise low-frequency modulation of ARI and the relationship with blood pressure Mayer waves. This work is also presented in Chapter 4.

- To characterise ARI behaviour in response to low-frequency stimulation of the baroreceptor. This approach underlies experimental work carried out in Chapter 5.

Chapter 3

Automatic assessment of cardiac repolarisation dynamics

Computational and experimental studies have shown that activation times (ATs) and recovery times (RTs) derived from the intracardiac unipolar electrogram (UEG) correlate well with local depolarisation and repolarisation times, making this technique useful for studying dynamics of local electrophysiology [10, 11, 35, 36, 38]. However, characterisation of action potential duration (APD) modulation related to autonomic nervous activity requires the recordings to be of sufficient length and preferably taken simultaneously from different sites of the heart to add a spatial dimension. This clearly results in large quantities of data that need to be studied. For example, even relatively short recordings of one minute using 20 electrodes at an average heart rate of 100 beats per minute will involve around 100 x 20 = 2000 beats to be examined. As a result, datasets involved in these studies are generally intractable without automated identification of ATs and RTs.

To improve the accessibility of such data, Western proposed and developed a system for semi-automatic identification of pacing spikes, ATs and RTs [11, 54]. The system has shown to be effective for its intended purpose and was used to characterise APD modulation related to respiration [10, 11]. However, further refinement is needed to replace elements of the algorithm which currently rely on a set of non-intuitive parameters, for example to detect activation waves and T-waves.

Although the relationship between APD and activation recovery interval (ARI) has been studied extensively, all measurements depend on the signal quality and since electrical

noise is ubiquitous in clinical recordings, there is concern about whether the derived ARI measures are sufficiently robust to study dynamics of APD. As explained in Section 2.4.2.3, signal noise can introduce ARI variability uncorrelated with APD behaviour, which would make ARIs less meaningful for studying APD behaviour. Low-pass filtering is a powerful solution to improve the signal-to-noise ratio (SNR), but it also unavoidably distorts the signal and the effect of this distortion has not been investigated to date.

The aim of the research presented in this chapter was to address those key issues in obtaining and analysing experimental electrophysiological data. To that end, in the first part of this chapter new analytical methods were proposed to improve identification of ARIs (Section 3.1). In the second part a study was designed and carried out using simulated electrograms to investigate the efficacy of these new methods and the effect of signal quality and filtering on ARI detection (Section 3.2. The improved analytical tools were applied in an attempt to resolve an interesting phenomenon described by Hanson et al. [10] in which the oscillation of ARI varied at different sites on the myocardium.

3.1 Automated identification of activation recovery intervals

The algorithm established by Western for automated recognition of ARIs from UEG signals relies on on a non-intuitive set of decision criteria to detect ATs and RTs. As a result, the reliability of this method heavily relies on a set of non-intuitive parameters, while UEGs manifest a wide range of waveforms. However, when considering a signal obtained from a single recording site, as shown in Figure 3.1, it can generally be observed that the waveform of each heartbeat is very similar and only subject to subtle changes in time. An important advantage of this behaviour is that it allows one to generate a template of the typical waveform morphology observed during each heartbeat. This template waveform can be used to detect the nominal event times. Since the changes observed in ARI are normally very small, it was hypothesised that the accuracy of automatic ARI identification could be improved by incorporating this *a priori* knowledge (i.e. that the signal waveform changes are relatively subtle over time in a single recording).

It was further hypothesised that the use of a template waveform could also help to discriminate between normal and ambiguous activity which would avoid analysis of unreliable or unidentifiable waveforms (e.g. an ectopic beat, or loss of signal connectivity) and hence prevent detection of unreliable ARI values.

This section describes the design of the new algorithm to improve automatic assessments of the ARI dynamics from UEG signals.

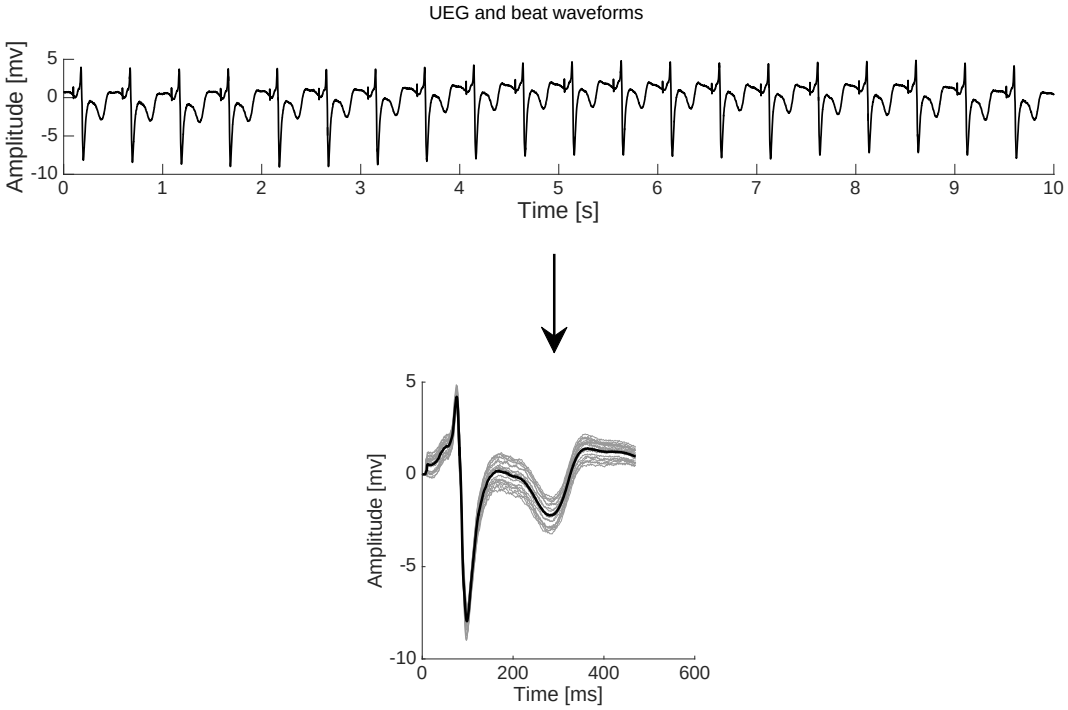

Figure 3.1: Extraction of the beat waveforms from the UEG. The black line in the lower plot represents the template waveform, constructed by averaging all individual waveforms.

3.1.1 Description of the new algorithm

Figure 3.2 depicts the proposed algorithm to process UEGs in four stages that perform the following functions: identification of the beat events, computation of heartbeat waveform template and selection of reliable beat waveforms, and identification of local ATs and RTs. The algorithm was written in Matlab and a graphical user-interface was designed to facilitate the process of testing.

3.1.1.1 Step 1: Detection of beat events

Electrical pacing of the heart creates a pacing artefact in the electrogram. A ”spike” can be detected by its restricted triangular transient morphology, which is normally clearly distinguishable from background activity. As shown in upper-left panel of Figure 3.3, the spike normally occurs just before the QRS-complex. Even if spikes are not detectable, it is still possible to identify heartbeats by identifying the sharp deflections of the QRS complexes. However, this method does not allow investigation of the dynamics of AT since they need to be referenced to the time at which the electrical stimulus is given.

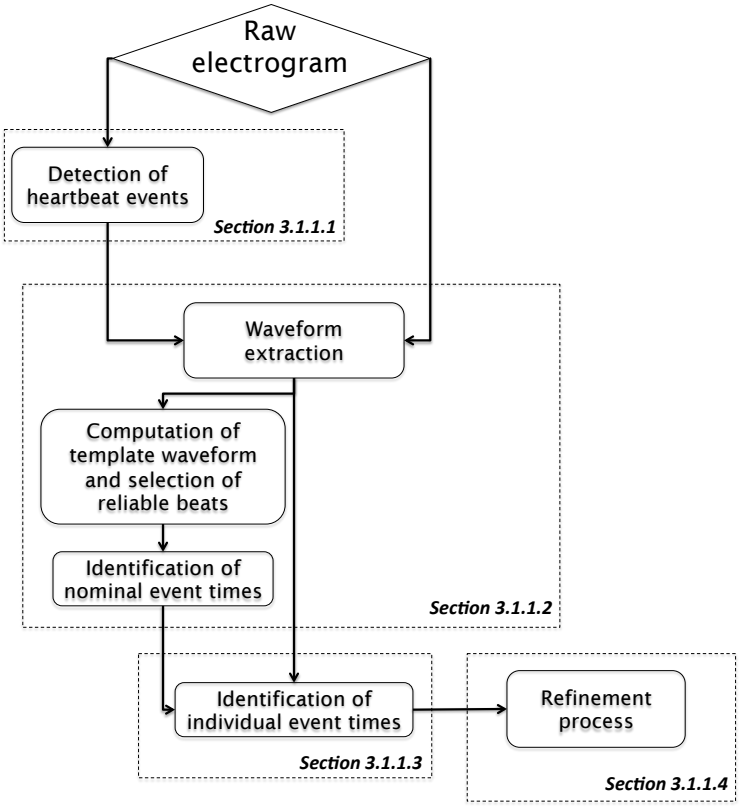

Figure 3.2: Flowchart of the proposed method for automated detection of activation and recovery times from raw electrograms. The electrogram is processed in four steps which are highlighted by the dashed boxes. The sections numbers shown in the lower-right corner of each box provide a detailed description of the processes involved in each step.

To identify spikes or QRS complexes, signals are filtered using a bandpass filter to enhance the spikes or QRS-complexes. Since the duration of spikes is expected to be shorter than the duration of QRS-complexes, the cut-off frequencies for spikes detection were set higher (50-150 Hz) compared to QRS detection (3-40 Hz). By limiting the high-pass frequency, the algorithm was prevented from picking up too much high frequency noise that may affect the detection.

Figure 3.3 provides a descriptive summary of the beat detection algorithm. Beat detection is an optimisation problem: the algorithm may skip beats when the threshold is set too high, whereas a threshold that is set too low may cause other components of the signal to be incorrectly marked as spike or QRS-complex. An optimal threshold was identified by taking the mean of the filtered signal + two times the standard deviation.

During experiments, heart rate is expected to occur usually below 160 beats per minute. Therefore, a beat interval limit of 375 ms was applied to further improve beat detection.

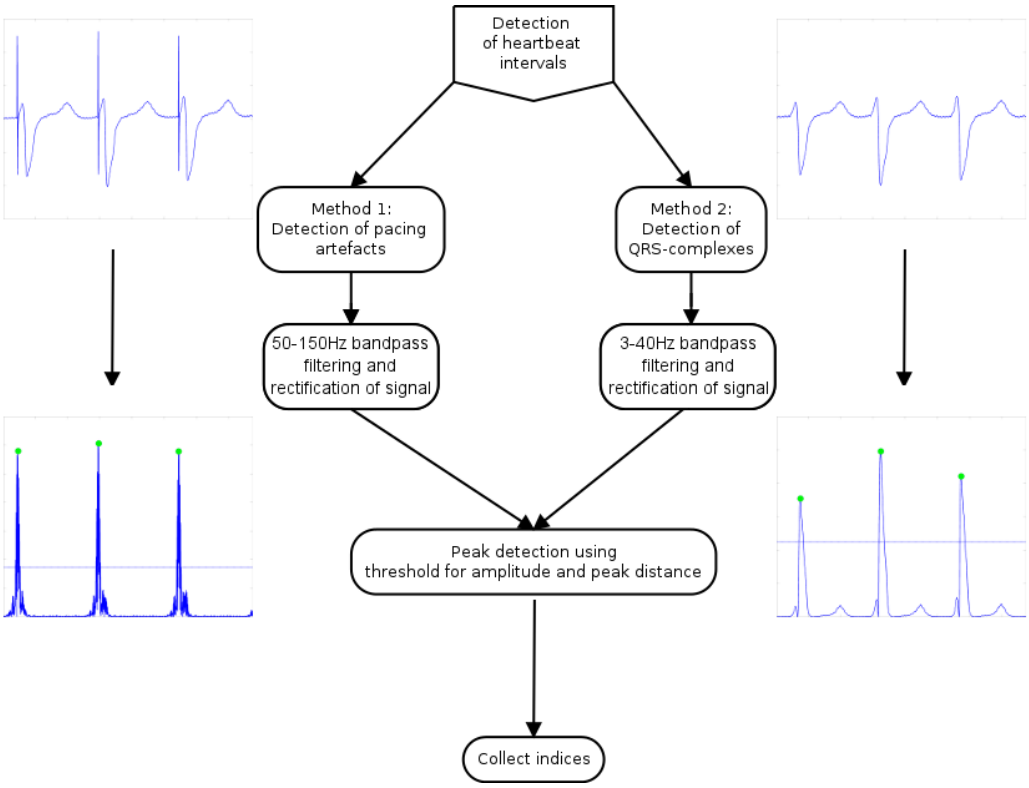

Figure 3.3: Flowchart of the beat detection algorithm by identification of pacing spikes or QRS complexes. Different bandpass filters were used between both methods for optimal detection.

3.1.1.2 Step 2: Computation of heartbeat waveform template and selection of reliable beat waveforms

Once the beat events are known, all heartbeats can be collected and aligned based on the spike or QRS-complex to compute the average or template waveform. Because the template waveform represents the expected behaviour of the UEG during a single heartbeat, it can be used to estimate which of the individual beats are reliable and which are not. This is achieved by calculating the correlation coefficient between each individual beat waveform and the template. A high correlation coefficient means that an individual waveform matches well with the template and can hence be assumed to be reliable. The effect of the different correlation thresholds to detect (un)reliable beats is illustrated in Figure 3.4, which shows a UEG trace with some unreliable beat waveforms (ectopic beats). A very low correlation threshold (0.2) causes some unreliable beats to be incorrectly classified as reliable (unreliable waveforms are marked with a 'X'), whereas a very high correlation threshold (0.9) results in rejection of reliable waveforms. A correlation threshold between 0.6 and 0.8 was found to offer an optimal threshold.

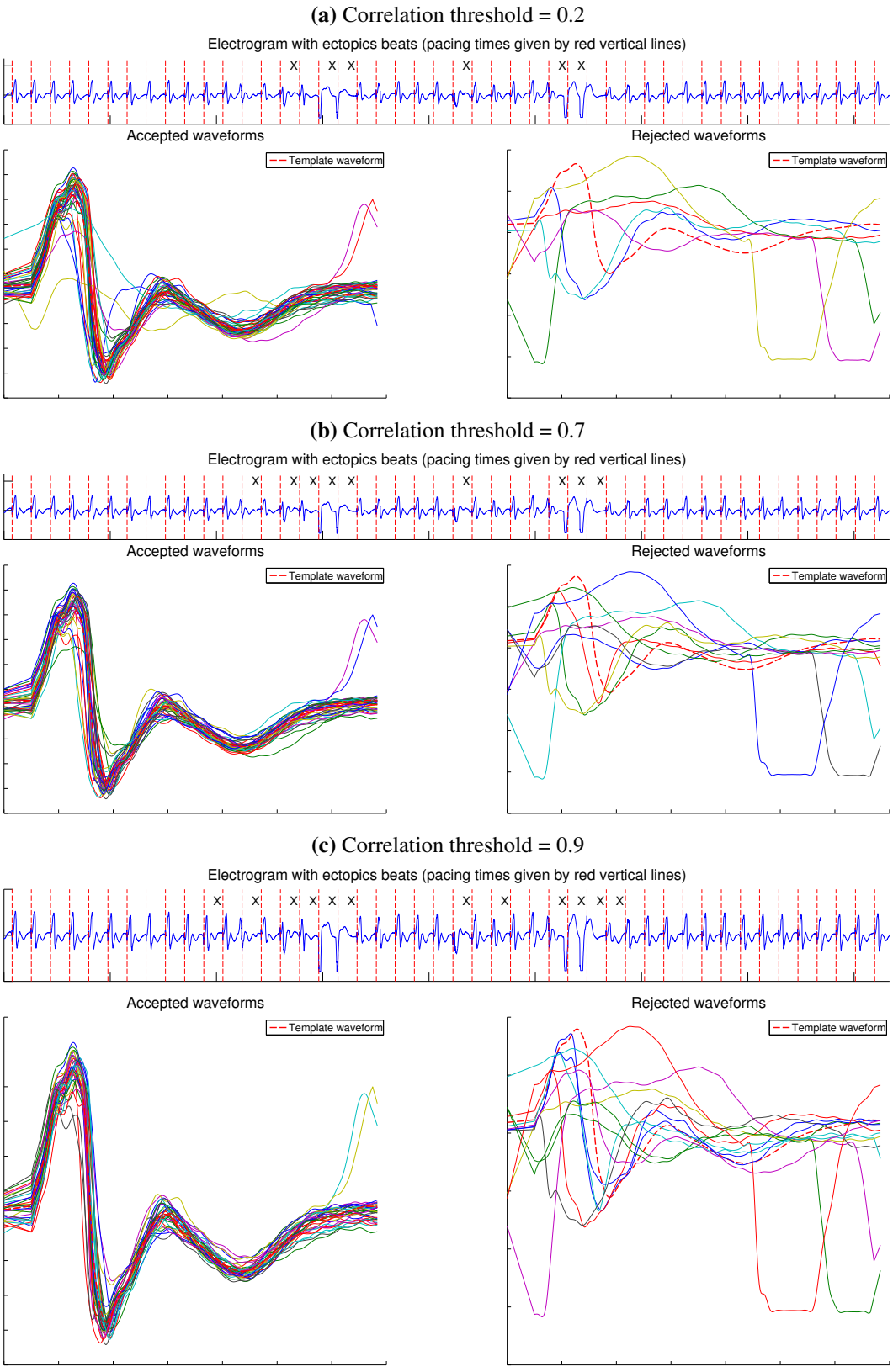

Figure 3.4: Extraction and classification of the QRST-waveforms from the electrogram for different correlation threshold. The rejected beats are marked with a 'X' mark in the electrogram recording. Low threshold accept ambigious beats, while a high threshold rejects beats that should be considered as normal activity.

3.1.1.3 Step 3: Identification of activation and recovery times

As explained previously in this section, the AT and RT derived from the template can be used to guide the identification of ATs and RTs from individual beats. The first step to achieve this is to determine the AT and RT from the template. To that end, a standard method is used which includes computation of the time derivative of the template waveform (dV/dt). The AT is measured as the time at which the derivative reaches its minimum. This point is computed in a section that covers the first third of the waveform, as this point corresponds to the steepest downslope in the action wave. The RT is then computed as the time at which dV/dt reaches a local maximum. This point is sought in a window that ranges from 120 to 400 ms after the activation time to cover most physiological RTs. After having established the nominal AT and RT, the algorithm is now able to refine to a much narrower window in which to search for ATs and RTs in the individual beats: the search window for AT was defined as the nominal AT $\pm$10 ms and RT was searched in a window of defined as the nominal RT $\pm$30 ms. The search window is larger to reflect the greater variability observed in RT (see Figure 3.5).

Filtering of the waveform is critical in the determination of the event times, especially the RT where the deflections are smaller, more gradual, hence more sensitive to noise. In agreement with previous experiences from Western and colleagues, signals are low-pass filtered at 150 Hz to detect activation and 30 Hz to detect repolarisation [11].

3.1.1.4 Step 4: Refinement process

The algorithm developed by Western allows the user to define the limits for AT and RT measurements. Although this method is useful to prevent detection of ATs and RTs in incorrect parts of the signal, it does not take into account physiological knowledge that AT and RT between consecutive beats can only vary within certain limits. As a result, physiological unrealistic changes may occur in AT and RT between beats even though limits were set to prevent detection of unrealistic AT and RT value. It was hypothesised that incorporating this knowledge into the quantification of the beat-to-beat variability of AT and RT could improve detection.

The presented algorithm has implemented a method to improve detection by identifying ATs and RTs that exceed the mean value of the 5 closest neighbouring beats by more than 12 ms. As illustrated in Figure 3.6, beats that exceed this beat-to-beat change are re-

analysed for the particular event time using a narrow search window defined by the mean event time of the 5 closest neighbouring beats $\pm$ 12 ms.

3.1.2 Development environment

The facilitate the development of the algorithms, a graphical-user interface was designed using Matlab. The upper panel of Figure 3.7 shows the wave inspection viewer: ATs and RTs are marked on the UEG signal and the lower graph window shows the corresponding ARI trend. The panel in the upper right of the window can be used to change the settings of the refinement algorithm discussed previous subsection. The settings interface is shown in the lower panel of Figure 3.7. The template waveform and search windows offer an intuitive way to visualise and adjust important parameters for the identification of AT and RTs.

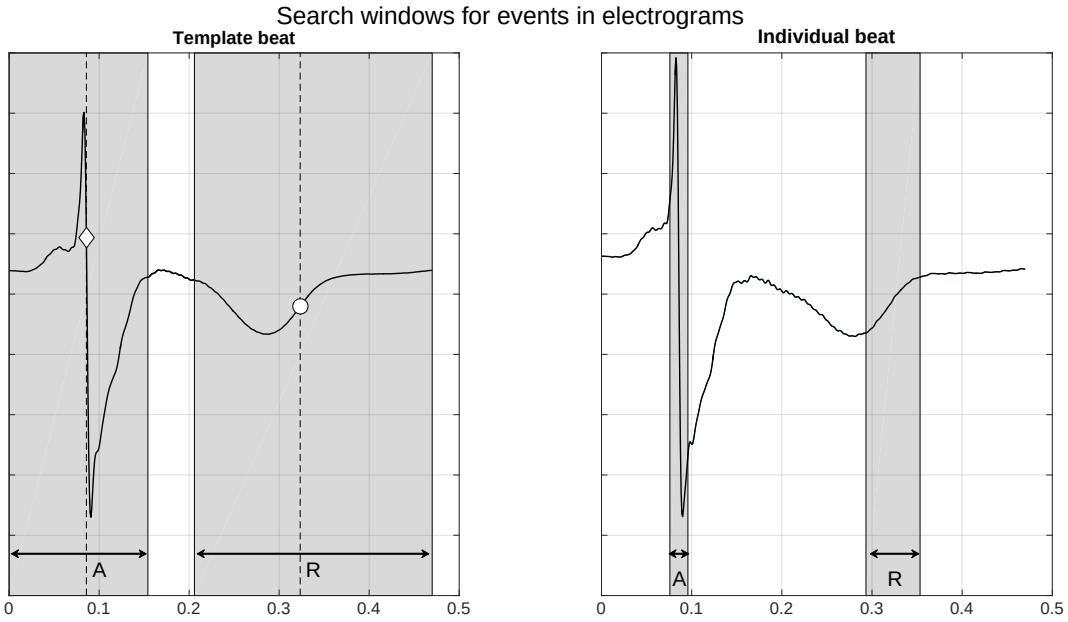

Figure 3.5: Identification of event times from the template waveform (left panel) and an individual waveform (right panel). The template waveform is used to detect the nominal event times using large search windows. The nominal event times then allow much narrower windows to be used for identification of event times in individual beats: activation time is defined as the nominal activation time $\pm$ 10 ms. Similarly, the search window for recovery times is defined as the nominal recovery time $\pm$ 30 ms.

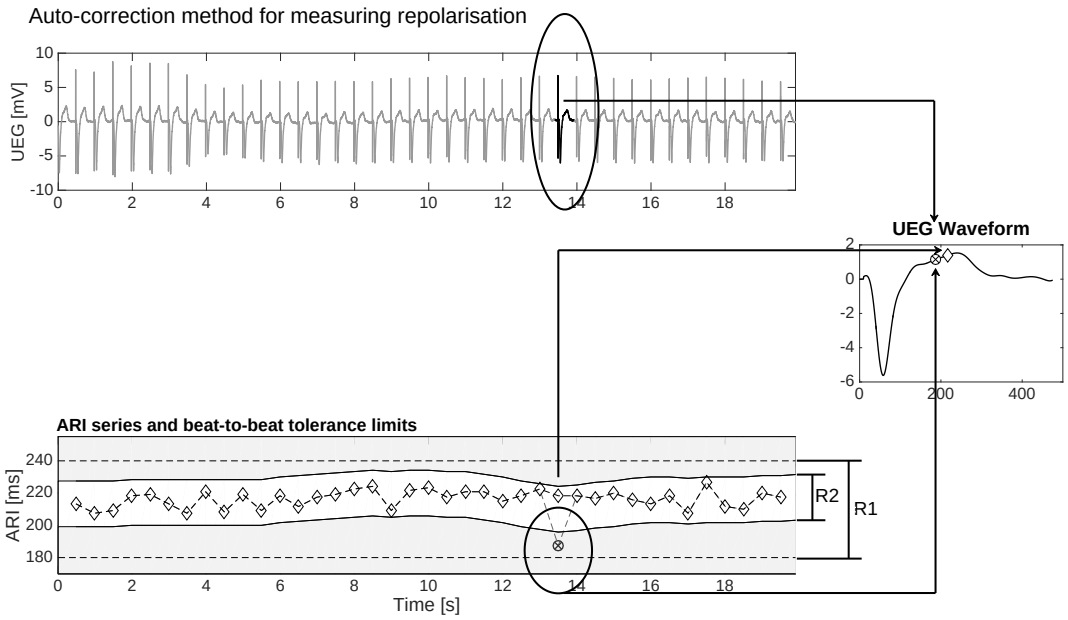

Figure 3.6: Automatic identification and correction of a repolarisation time. R1 represents the original search window to detect repolarisation times. However, this windows does not take into account that beat-to-beat changes are considered to be limited by physiology. Once an unrealistic beat-to-beat change in repolarisation time has been detected, the algorithm seeks to improve the estimation of repolarisation timing for this beat using a narrower search window (R2).

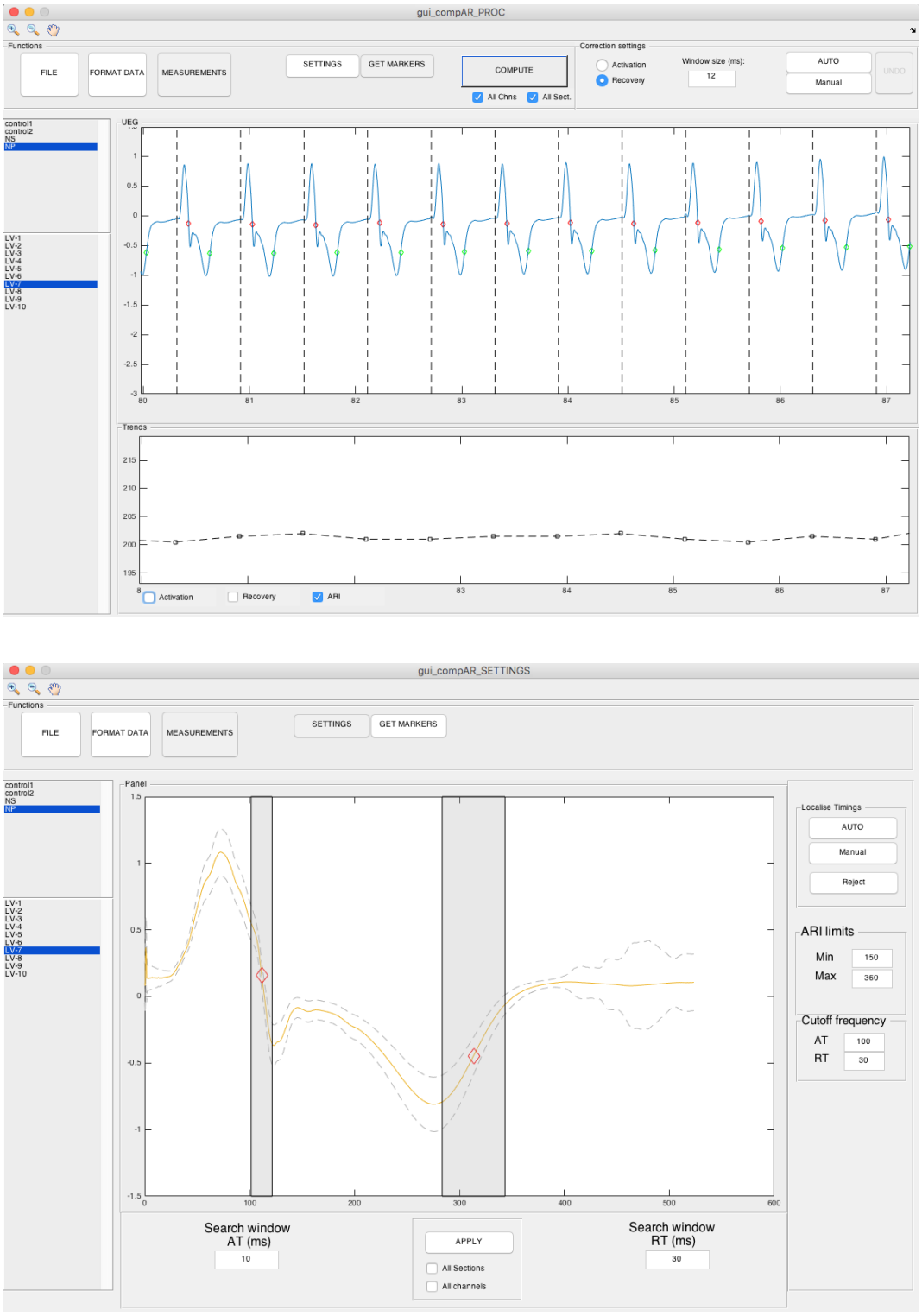

Figure 3.7: Graphical-user interface designed to facilitate testing of algorithms for UEG processing: interface of the settings window. Upper panel: waveform inspector, lower panel: settings window.

3.2 Investigation to determine the accuracy of UEG derived measurements

Fluctuations in ARI are typically small. For example, studies performed by Hanson et al. showed that the amplitude of ARI variations related to respiratory behaviour ranged from $0-26$ ms [10]. Combined with the fact the ARI measurements are sensitive to noise, it is important to know which levels of noise and filtering are acceptable such that ARI measurements are still meaningful. However, this has not been thoroughly investigated yet.

In addition to noise and signal artefacts, whether ARIs are meaningful or not also depends on the data acquisition. Fundamental in this process is the sampling rate at which UEG are recorded. In the clinic, different sampling rates are currently in use: for example, UEGs recorded from implantable pacemakers are often sampled around 500 Hz, while clinical recordings systems used in the catherisation laboratory often allow signals to be recorded at 1 or 2 kHz. It was hypothesised that low sampling rates could potentially affect measurements of ARI dynamics because of the limited time resolution. For example, it has been shown that measurements of ECG QT-variability were affected when using ECGs were sampled at low rates [55].

In order to evaluate the efficacy of the proposed refinements for ARI identification and the effects of noise, filtering and sample rate to ARI detection under controlled conditions, a study was designed and carried out using simulated electrograms. To that end, realistic UEG signals with predetermined ARI behaviour were generated and controlled degrees of noise and artefacts were added.

Research questions

In line with the aim of this chapter to improve detection of ARI dynamics, the following research questions were addressed in this section:

1. How does the accuracy of ARI measurements depends on signal quality, filtering and sampling rate of the electrogram?

2. Can the accuracy of ARI measurements be improved by using template electrogram waveform morphology to construct narrower search windows and detect ambiguous activity?

The workflow of the data processing is shown in Figure 3.8: UEGs were simulated

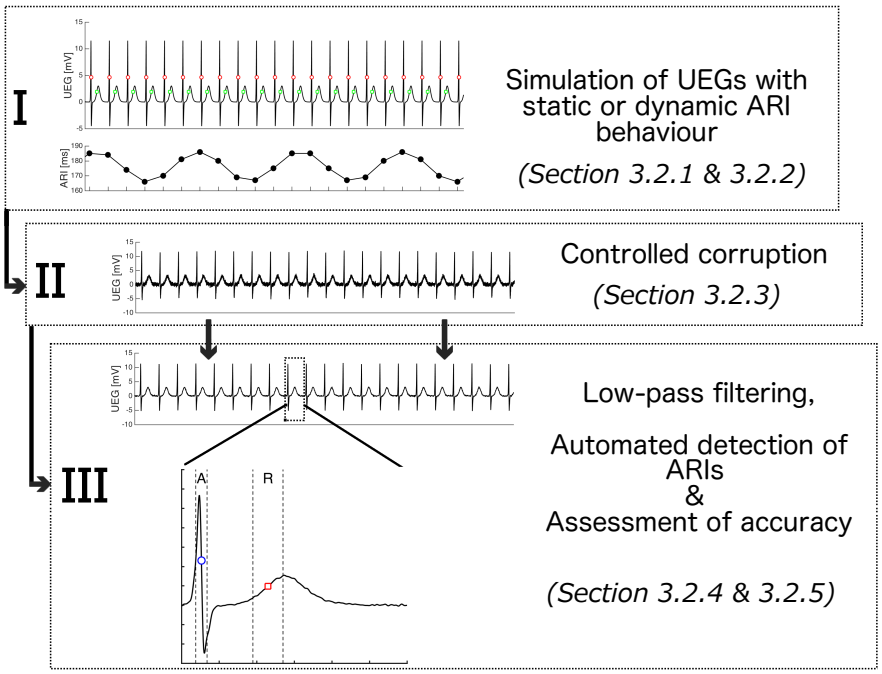

Figure 3.8: Workflow of data processing to investigate the accuracy of ARI measurements using simulated UEG signals. First, UEG signals with predetermined ARI behaviour were generated using synthetic action potentials (Section 3.2.1 & 3.2.2). Next, controlled degrees of noise and artefacts were added to affect the signal quality (Section 3.2.3). Signals were then low-passed filtered and analysed for ARIs using a standard method and the method that uses the template waveform to construct narrow search windows (Section 3.2.4). Finally, the accuracy of the ARI measurements was examined for each detection method (Section 3.2.5).

with predetermined ARI behaviour and then corrupted with realistic noise and artefacts to affect the signal quality. The contaminated UEGs were then analysed for ARIs using the proposed template method (Section 3.1.1) and a standard method. The accuracy of both methods was examined to determine the effect of signal quality on ARI detection and whether the template method with narrow search windows improved the ARI estimation.

3.2.1 Synthetic action potentials and unipolar electrograms

UEGs were generated using a theoretical model based on work of Potse and colleagues [37] discussed in Section 2.4.2.2. This model is described by Equation 2.3 and describes the UEG as the weighted difference between an inverted local transmembrane action potential (TAP) and a remote, position-independent signal. The definition is re-stated below:

$$S(x,t) = -\frac{g_i}{g_i + g_e}(V_m(x,t) - V_R(t)) \tag{3.1}$$

where $S(x,t)$ is the simulated UEG at position x and time t. For the simple model proposed by Potse, conductivities are assumed to be isotropic with $g_i/(g_i+g_e) = 0.25$ [37]. V_m describes the transmembrane potential during the action potential and is described in more detail below in Equation 3.2. The remote component V_R was computed as the average of all TAPs. Realistic transmembrane potentials of N = 257 sources (nodes) each located at a given point x on the epi- or endocardium, were obtained using an analytical expression proposed by Van Dam and colleagues [56] and used for simulation purposes in [57, 58]. This expression is defined as:

$$V_m(x,t) = \alpha(x)D(x,t)R(x,t) - V_0 \tag{3.2}$$

where $\alpha(x)$ is the amplitude and V_0 is the resting potential. $D(x,t)$ and $R(x,t)$ are two logistic functions that describe transmembrane potential during the depolarisation and repolarisation phase of the TAP, respectively:

$$D(x,t) = \frac{1}{1+e^{-\beta_D(t-\tau_D)}} \qquad R(x,t) = \frac{1}{1+e^{-\beta_R(t-\tau_R)}} \tag{3.3}$$

where β_D describes the upstroke of $V_m(x,t)$ during the depolarisation and β_R the downstroke during the repolarisation. Parameters τ_D and τ_R represent the depolarisation and repolarisation time, respectively. The APD is defined as τ_R - τ_D. Figure 3.9 shows how the TAP is constructed using the product of $D(x,t)$ and $R(x,t)$ in Equation 3.2.

Parameters β_D and β_R were obtained from a model of normal male heart and provided by ECGSIM software [59]. From the 257 available sources, 20 were selected to generated UEGs exhibiting a wide range of positive and negative T-wave morphologies. Figure 3.10 shows two transmembrane potentials ($V_m(t)$) obtained from two different locations x and the corresponding UEG waveforms. The red dashed line in panel A and B represents the remote component ($V_R(t)$). As shown in this figure, the UEG obtained from a source that repolarises relatively early with respect to the remote component (panel A) has a positive T-wave. Conversely, late repolarisation is reflected by a negative T-wave. This demonstrates that the designed method is capable to realistically simulate the basic concepts underlying the genesis of UEGs and that it is in agreement with the both theoretically and experimentally established relation between repolarisation and UEG T-wave morphology [36–38].

3.2.2 Patterns of repolarisation

The accuracy of ARI estimation was tested in simulated situations of steady-state periods of constant ARI and of ARI which was changing dynamically. Steady-state ARI series were generated to study the accuracy by means of trueness and precision of ARI estimations. Dynamic behaviour of ARI was achieved by artificial sinusoidal modulation of repolarisation (τ_R in Equation 3.3) uniformly for all nodes, resulting in sinusoidal modulation of the ARI. Dynamical patterns were used to study the ability to track the induced variability in the presence of noise as a function of modulation amplitude (2 ms, 5 ms and 10 ms) and frequency (0.1 Hz, 0.2 Hz and 0.3 Hz.). The chosen frequencies were chosen such they would cover the two most important cardiovascular rhythms: respiration and low-frequency Mayer wave activity (section 2.3.4, page 41).

3.2.3 Signal corruption

Two sources of corruption were applied to the UEG: uncorrelated interference noise and ambiguous activity. Interference noise was generated by white Laplacian distributed noise, which is assumed to give a good approximation of real electrogram noise [60, 61]. Ambiguous activity was introduced in every recording by replacing beats with simulated ectopic beats exhibiting abnormal ARIs. This was achieved by changing the activation (τ_D) and repolarisation times (τ_R) in Equation 3.3 for all nodes except the one that was recorded.

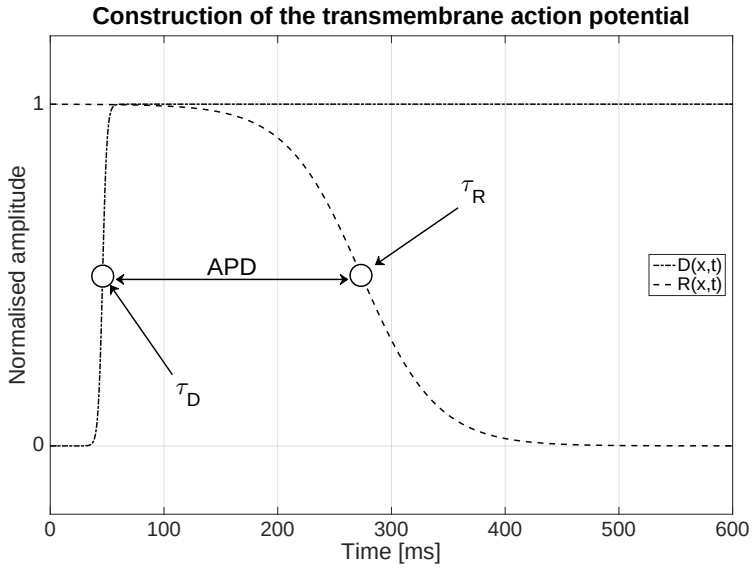

Figure 3.9: Construction of a synthetic transmembrane action potential ($V_m(x,t)$) using the product of $D(x,t)$ and $R(x,t)$ as defined in Equation 3.2). *APD = action potential duration. Parameters used:* $\beta_D = 0.53$, $\beta_R = 0.03$, $\tau_D = 46$, $\tau_R = 273$.

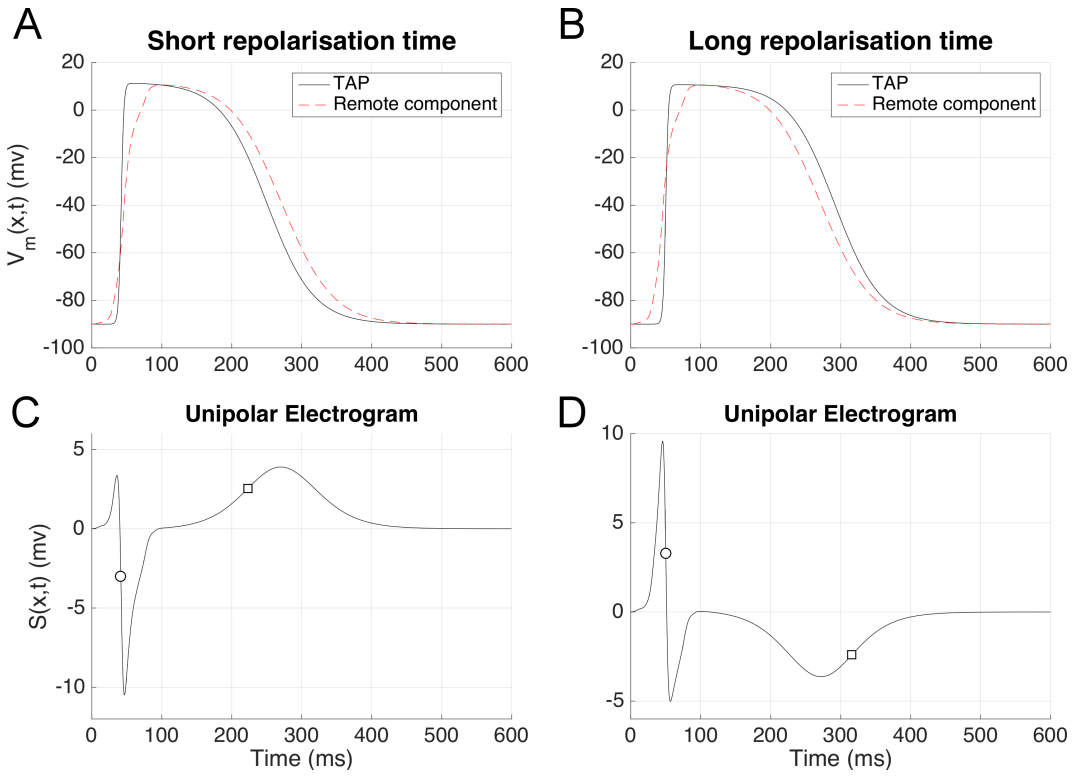

Figure 3.10: Construction of unipolar electrograms (UEGs) with the simple model (Eq. 3.1). Panel A and B show membrane potentials V_m (solid line) during the transmembrane action potential (TAP) from 2 different locations (A & B) and the location-independent remote component V_R (dashed line). Location A has a short repolarisation time, whereas B has a long repolarisation time. According to the simple model, the corresponding UEGs can then be computed as the difference between the remote component and the TAP, as shown in panel C and D. The circles represent the time of activation and squares the time of recovery. As predicted by the simple model, recovery occurs earlier in C than D.

This shifted the remote component, V_r, resulting in a dramatically changed UEG waveform for that particular beat.

3.2.4 Automatic detection of the activation recovery intervals

In order to quantify any performance improvement provided by the refinements to the new algorithm, data was analysed using a basic standard method and using the described method with narrow search windows based on the nominal AT and RT derived from the template UEG waveform. The basic method uses wide scanning windows: the window for activation covered the initial 20% of UEG waveform, which includes the QRS-complex, and the scanning window for the RT covered the remaining part of the waveform, which mainly includes the T-wave. Results obtained with the basic method were compared to the improvements presented in Section 3.1.1.2:

Strategy 1: Narrow search windows : Application of narrow search windows by first computing the nominal AT and RT from the template wavelet. The scanning window for AT was set at the nominal AT $\pm$ 20 ms and for RT at the nominal RT $\pm$ 50 ms.

Strategy 2: Narrow search windows + exclusion of unreliable beat waveforms : This strategy was an extension of the first strategy. The correlation threshold between the individual beats and the template beat was set at 0.6. Beat waveforms below this value were labelled as unreliable and excluded from analysis. The gaps introduced in the ARI-series were replaced by linear interpolation, but the ARI-series were omitted from analysis if more than 10% of the beats were excluded.

To examine the effect of filtering on the detection of repolarisation, the analysis was conducted using low-pass filter (4th order Butterworth filter) with cut-off frequencies ranging from 5 to 50 Hz.

3.2.5 Protocol and assessment of accuracy

Twenty different one-minute duration UEG recordings were generated. Recordings were then corrupted with unreliable activity by replacing 5 % of the beats with ectopic beats. Next, zero mean white Laplacian noise was added to the signals to obtain signal-to-noise ratios (SNRs) ranging from 0 to 40 dB. Repeated measurements were obtained by corrupting the recordings with 100 different, but equal powered, noise signals.

UEGs were sampled at three typical sampling frequencies: 500 Hz, 1 kHz and 2 kHz to determine the effect of sampling frequency on the accuracy of ARI measurements. As a result, large quantities of data needed to be analysed: a total of 3 million signals for each of the three sampling rates. Computations were therefore performed by UCL's high-powered-computing facility Legion.

When evaluating the accuracy of the estimated ARI series in steady-state conditions it is important to have a measure of the trueness (i.e. the deviation from the real value) and the precision. Trueness was measured as the mean absolute error (MAE), defined as:

$$MAE(y,\hat{y}) = \frac{1}{N}\sum_{i=0}^{N-1}|y_i - \hat{y}_i| \tag{3.4}$$

where y_i is the estimated ARI value and $\hat{y}_i$ the corresponding true ARI value. Precision

was quantified as the standard deviation of the ARI series. Because the steady-state conditions apply, there is no variability in ARI and consequently one would expect the standard deviation to be zero for maximum precision. Any higher value indicates ARI variability that has been introduced by measurement errors of AT and RT. As mentioned previously, signals were corrupted with 100 equally powered noise realisations to compute mean values for the trueness and precision.

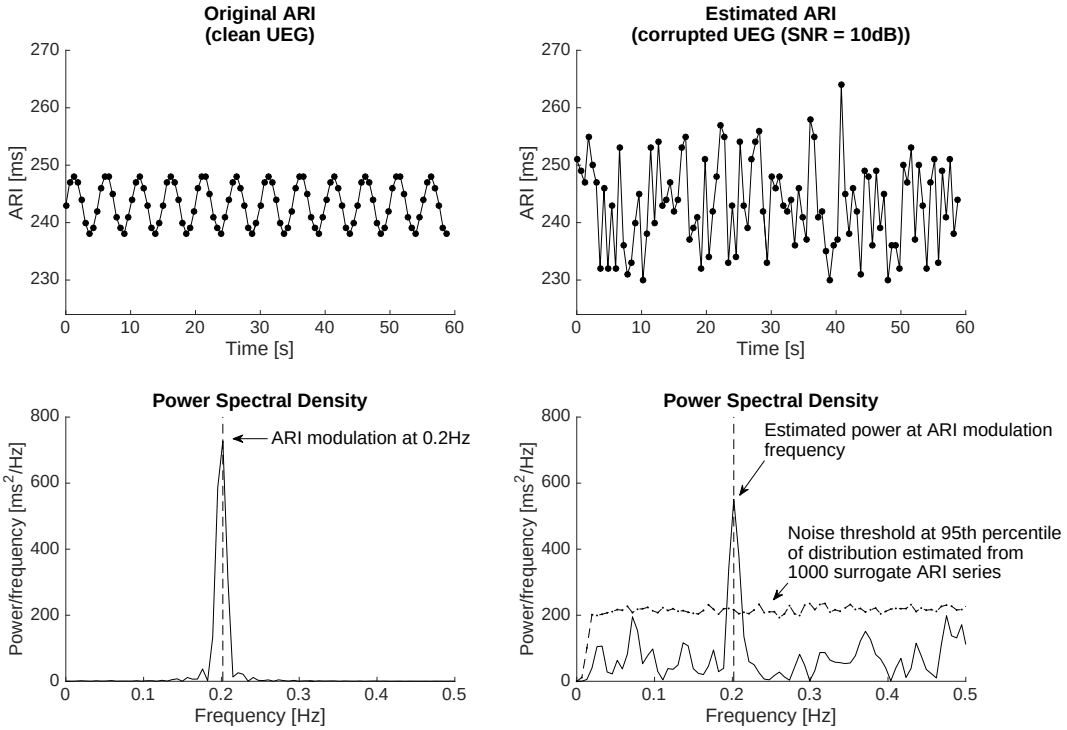

Figure 3.11: Evaluation of the accuracy of dynamic ARI estimates. ARI estimates were considered accurate when they were able to track the original induced sinusoidal ARI modulation. This was tested by computing the power of the estimated ARI series at the modulation frequency using the fast Fourier transform. To determine the significance of the power, surrogate data series were generated and their power at the modulation frequency was computed. The noise threshold was defined as the 95^{th} percentile of the surrogate power distribution. In this figure, the estimated ARIs after corrupting the UEG were still able to track the original induced 0.2 Hz modulation as the power exceeded the noise threshold.

To evaluate the accuracy of the dynamic ARI estimates, a spectral method was designed to qualify whether it was possible to track to original induced sinusoidal behaviour of ARI from the estimated ARI series obtained from corrupted UEGs. The method analyses the spectral content of the estimated ARI series and determines whether the amplitude of the frequency at which the original ARI series (before corruption) was modulated is significant.

This was achieved using surrogate data analysis that preserves the amplitude distribution, but destroys any correlation by shuffling the ARI samples in random order [62–65]. A solid noise floor was created by repeating this process 1000 times and taking the upper 95^{th} percentile of the obtained noise distribution. As illustrated in Figure 3.11, ARI estimates were considered accurate if their power at the ARI modulation frequency exceeded this noise threshold.

3.2.6 Results

3.2.6.1 Accuracy of steady-state ARI measurements

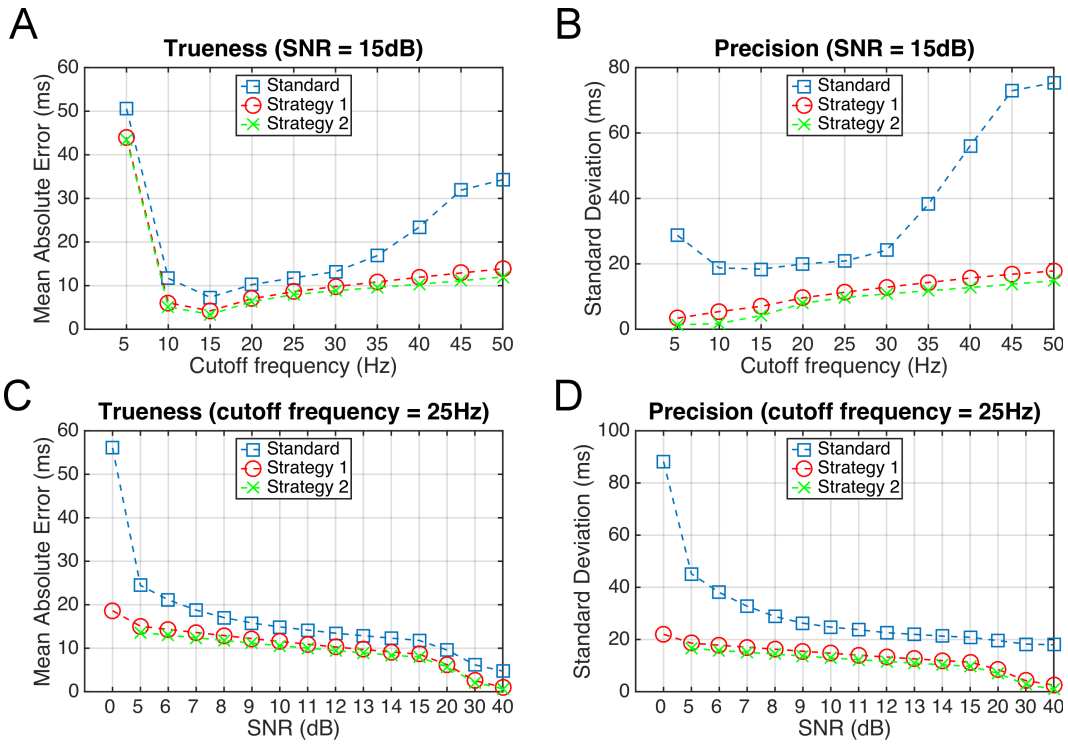

Figure 3.12: Accuracy of steady-state ARI measurements, expressed by trueness and precision, as function of low-pass filter cutoff frequency (panel A and B, signal-to-noise ratio (SNR) fixed at 15 dB) and signal quality (panel C and D, cutoff frequency fixed at 25 Hz). The blue square markers show the results for the standard method, red circles correspond to improvement method 1, and green crosses to improvement method 2. The data shows a clear trend between accuracy and cutoff frequency: except for the lowest frequency, increasing the cutoff frequency reduces the accuracy. Optimal filtering results were found for a cutoff frequency of 10 Hz. As predicted, the relation between SNR and accuracy showed also a clear trend. Both improvement methods improved the accuracy substantially, especially for high cutoff frequencies and low signal qualities. The sampling frequency of the UEGs was 1 kHz.

Figure 3.12 shows the trueness and precision of ARI estimates as a function of cutoff frequency for low pass filtering and signal quality for UEG signals sampled at 1 kHz. The blue square markers show the results for the standard method, while the results of the in-

vestigated improvement method are shown by the red circles (improvement method 1) and green crosses (improvement method 2). The effect of low-pass filtering is shown in Figure 3.12A and B. In panel A, it is shown that, with exception of the lowest cut-off frequency (5 Hz), the trueness gradually improves from (decrease of MEA) by decreasing the cutoff frequency. Also the precision of the measurements (panel B, lower is better), improve by selecting low cutoff frequencies. Note that the high precision obtained by lowest cut-off frequency was associated with a sudden reduction of trueness (high MAE in panel A). The effect of signal quality on trueness and precision is studied in Figure 3.12C and D. Both trueness and precision were found to improve for increasing signal quality.

Regarding the proposed improvement methods for measuring ARI, both proposed improvements resulted in a higher accuracy of steady-state ARI measurements, especially for low SNRs and high cutoff frequencies. As shown in Figure 3.12C and 3.12D, the trueness of ARI measurements obtained from UEG recordings with a typical SNR of 15 dB filtered at a cutoff frequency of 25 Hz using the basic method was 16.2 ms (range:12.2-29.0 ms). When the same signals were analysed using improvement 1 (narrow search window), the trueness was found to be improved to 12.7 ms (range: 6.0-15.5 ms). The trueness was further improved using improvement 2 (narrow search windows + exclusion of unreliable beats) to 11.6 ms (range:6.0-13.4 ms). Similar trends were observed for the precision of the measurements: 38.2 ms (range:26.8-58.5 ms) for the basic method, 17.3 ms (range:7.6-21.0 ms) for improvement 1, and 14.6 ms (range:7.6-16.9 ms) for improvement 2.

3.2.7 Accuracy of dynamic ARI measurements

Figure 3.13 shows accuracy of ARI measurements to track 0.2 Hz sinusoidal ARI oscillations with an amplitude of 5 ms as function of cutoff frequency for signals with a SNR of 15 dB (panel A) and signal quality for signals filtered at a cutoff frequency of 25 Hz (panel B). The blue square markers represent the standard method, red circles improvement 1, and green crosses improvement 2. The accuracy was expressed as the percentage of the 100 different noise realisations in which ARI modulation could be tracked. The analysed UEGs for this figure were sampled at 1 kHz. In panel A it is shown that the basic method was able to track ARI modulation in almost 45% of the available signals when using a cutoff frequency of 10 Hz. The general trend was that dynamic accuracy decreased with

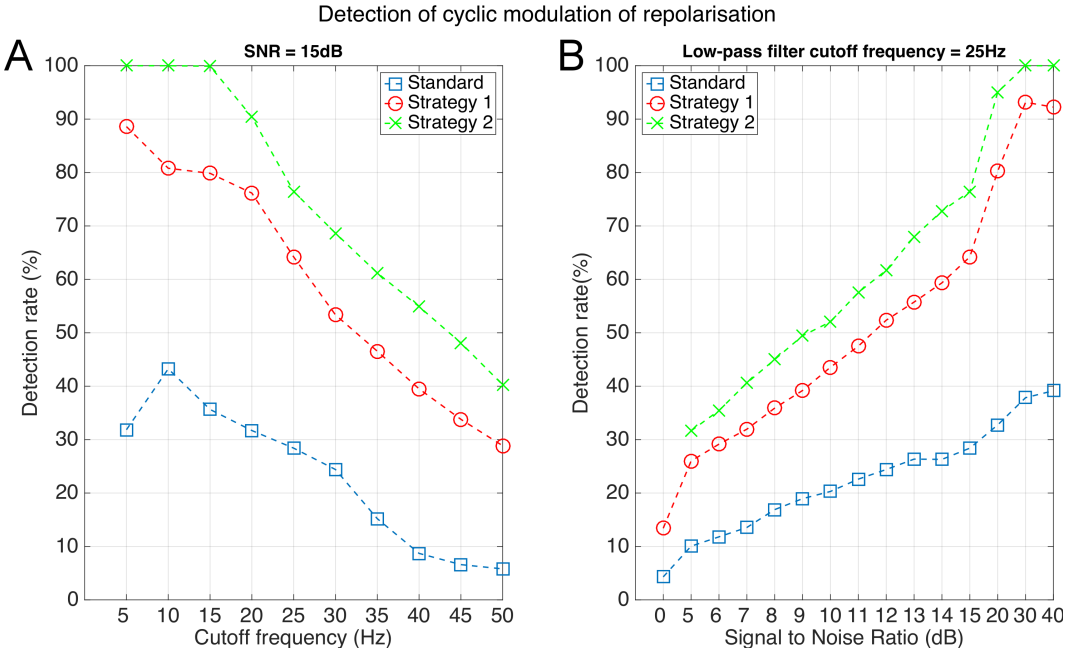

Figure 3.13: Accuracy of dynamic ARI measurements. Detection of f=0.2 Hz ARI modulation with 5 ms amplitude. The blue square markers show the results for the standard method, red circles correspond to improvement method 1, and green crosses to improvement method 2. Panel A: average detection rate across UEG recordings with a signal-to-noise-ratio (SNR) SNR of 15 dB as a function of low-pass cutoff frequency. At a cutoff frequency of 15 Hz, improvement method 2 achieved a detection rate of 100% compard to approximately 35% for the standard method. Panel B: detection rate plotted as a function of SNR using a fixed cutoff frequency of 25 Hz. Detection rate improved with increasing signal quality. Improvement method 2 provided the highest accuracy of the tested methods. UEGs analysed for this figure were sampled at 1 kHz.

increasing cutoff frequency for all the three measurement methods. Also the effect of signal quality was found to gradually improve the dynamic accuracy. Panel B shows an example for signals filtered at a cutoff frequency of 25 Hz.

Similar to the steady-state ARI results, the proposed improvement methods were found to improve the dynamic accuracy. Figure 3.13A shows that the maximum dynamic accuracy obtained with the basic method was less than 45%, whereas improvement 1 reached almost 90% and improvement 2 was able to identify the ARI modulation in all signals (100%) for cutoff frequencies of 15 Hz and lower. In Figure 3.13B, it is shown that the improvement performed better than the standard method for the full range of signals qualities, although no results were available for improvement method 2 at a SNR of 0dB, because too many beats ($>$ 10%) were defined as unreliable by the correlation method.

The recordings analysed for the examples in Figure 3.12 and 3.13 were sampled at 1 kHz. The final part of this study investigates the relationship between the accuracy of ARI measurements and the sampling frequency. Table 3.1 shows the detection rate for 0.2 Hz ARI oscillations of three different amplitudes as function of the sampling frequency. The SNR for this investigation was fixed at 15 dB and the cutoff frequency of the low-pass filter was 25 Hz. Accuracy improved by increasing the sample rate.

Amplitude	Fs = 500	Fs = 1kHz	Fs = 2 kHz
2 ms	12%	13%	15%
5 ms	36%	45%	58%
10 ms	84%	93%	98%

Table 3.1: Detection rate of 0.2 Hz ARI variations for different sampling frequencies and amplitudes.

3.2.8 Discussion

Noise and ectopic beats are ubiquitous in clinical recordings and affect the measurements of ARI. This study was set out to evaluate the significance of each potentially corrupting influence, as well as identifying the relative successfulness of different algorithms in identifying ARI in the presence of such noise and interference. Realistic UEGs were obtained by generating realistic transmembrane action potentials (TAPs) at cellular level using exponential equations previously proposed and established in [56]. The simulated TAPs were incorporated in the simple but intuitive model of Potse which has shown to provide a good description of the genesis of the UEG based on computational and clinical data [37]. The generated UEGs and its modulation by changing APD looked realistic and mimic UEG changes during APD modulation in a fundamental way. This allowed the accuracy of ARI measurements to be investigated for a wide range of UEG waveforms and ARI dynamics under controlled conditions, which is practically impossible to be achieved using physiological data.

Compared to the basic ARI detection method with large search windows, this study shows that the accuracy of ARI measurements was substantially improved using the two tested improvements (narrow search window and exclusion of unreliable beats). Also the filtering properties were found to affect the reliability of ARI measurements and maximum accuracy was obtained for a cutoff frequency of 10 Hz. It is perhaps surprising that the best results were found with such a low low-pass cutoff frequency. For example, Western

observed in real data that some aspects of ARI behaviour were obscured when using cutoff frequencies lower than 30 Hz [11]. This may indicate that in reality the changes in the T-wave during ARI modulation are more complex and may be attenuated when using a lower cutoff frequency. However, the current study was designed to allow investigation of ARI identifcation for a very broad range of situations under very controlled conditions at a fundamental level. It is possible to extend the study to more realistic but more variable human data, as found in [10, 66].

Regarding the signal quality, it was clear that lower SNRs made accurate estimation of ARI more difficult. For tracking ARI dynamics it is shown that using improvement strategy 2, it is possible to obtain reasonable results for signals with a SNR of 15 dB or more. This may be used to guide future measurements when considering measuring ARI dynamics. For example, ARI measurements obtained from of 0 dB recordings were in general not meaningful as they could not be used to identify the underlying ARI dynamics.

Regarding the effect of UEG sampling frequency on ARI detection: this study shows no important differences in accuracy between the tested sampling frequencies. This may suggest that compared to clinical electrophysiology recording systems, the lower sampling rates used in implantable cardioverter-defibrillators and pacemakers devices, does not notably affect detection of ARI oscillations. The results have been published in [67]

Chapter 4

Oscillatory behaviour of ventricular repolarisation with respiration and at low frequencies

4.1 Introduction

Oscillatory behaviour at the respiratory frequency and at approximately 0.1 Hz (often referred to as Mayer waves) are ubiquitous properties of the cardiovascular system and linked with cardiac autonomic regulation [9, 25, 30]. Since cardiac autonomic nerves are known to innervate the ventricular myocardium and to elicit changes in ion channels that are important for the action potential, it is possible that the ventricular action potential duration (APD) exhibits variability at both rhythms. If such behaviour would occur heterogeneously across the myocardium, then it could potentially increase the regional differences in repolarisation which may promote pro-arrhythmic conditions.

As discussed in Section 2.3.4, oscillations in ARI and blood pressure with respiration have been reported during controlled breathing independently of heart rate [10, 11]. Phase analysis has shown that the phase lags between respiration and systolic blood pressure (SBP) are different compared to activation recovery interval (ARI). The (causal) relationship between ARI, respiration and blood pressure has not been identified yet and and could aid our fundamental understanding of the mechano-electrical regulation of the heart, lungs and autonomic nervous system (ANS). Data from a pilot study in [11] suggests that the ANS is indeed involved in the genesis of respiratory-related ARI oscillations as pharmaceutical blockade of sympathetic activity caused a reduction of respiratory oscillations, however the group size was too small for robust statistical analysis. In addition, autonomic

outflow generated during consciously controlled breathing may differ substantially from natural breathing. The work in this chapter aims to address those gaps in our knowledge. Such knowledge could help to improve treatment and diagnostics of patients with respiratory disorders that are linked with arrhythmias.

Autonomic cardiac modulation during psychological stress

Independently of respiratory changes, heart rate and blood pressure are also modulated at a lower frequency associated with sympathetic stimulation, as explained in Section 2.3.3. Experiments involving emotions, have shown that psycholigical stress can increase the variability of heart rate and blood pressure at approximatetly 0.1 Hz [68, 69]. Since sympathetic nervers are known to innervate the myocardium and it was hypothesised that mental stress might also evoke or increase low frequency variability of cardiac repolarisation independent of heart rate. Such variation of repolarisation might increase the susceptibility to arrhythmogenesis and could be a possible mechanism by which psychological stress and sympathetic activity can destabilise cardiac electrophysiology. In previous work it was observed that mental stress was associated with changes in the T-wave of the ECG, suggesting that mental stress could indeed induce changes in repolarisation [69]. The work presented in this chapter attempts to investigate the extent to which low-frequency oscillations in repolarisation may occur by measuring ARIs from unipolar electrograms (UEGs) recorded at the cardiac tissue level in humans during mental arousal.

Research aim & questions

The aim of this chapter is two-fold: (1) to explore the origin of respiratory-related oscillations of APD in more detail, and (2) to identify if APD is also modulated at a lower frequency associated with sympathetic stimulation. Specifically, this chapter seeks to answer the following research questions:

1. What is the effect of sympathetic and parasympathetic blockers on the amplitude of respiratory-related ARI oscillations?

2. How are ARI, arterial blood pressure and respiration causally entangled?

3. Does respiratory modulation of ARI also occur during spontaneous breathing?

4. Does ARI exhibit low frequency oscillations synchronised with Mayer waves during psychological stress?

Answers to the proposed research questions are thought to lead to a better understanding of how electrophysiology is controlled by the autonomic nervous system.

4.2 Methods

Two sets of experimental data were used in this chapter. Both were originally obtained in the lab of Dr. Jaswinder Gill at St. Thomas' Hospital, London, between 2010 and 2012. The diagram shown in Figure 4.1 summarises the characteristics of the experimental data and the proposed analytical approaches to analyse the corresponding data.

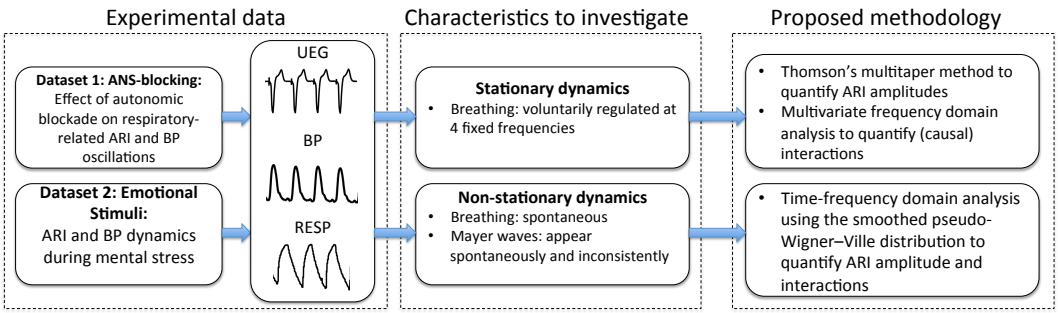

Figure 4.1: Workflow of the data processing for dataset 1 and 2.

UEGs were processed using the algorithm presented in the previous chapter. Cases in which the T-wave was indistinct or corrupt were removed from the analysis. Blood pressure recordings were analysed for systolic blood pressure (SBP) and the maximum rate of systolic pressure increase (dP/dt max) as a measure of myocardial contractility. The dP/dt max was used to evaluate the effect of the agents on blocking sympathetic activity as sympathetic blockade reduces the contractile force of the heart.

Any beats for which ARI or SBP measurement could not be determined were replaced by cubic spline interpolation between the surrounding beats, but series were rejected if these surrogate beats constituted more than 10% of the series.

4.2.1 Clinical recording protocols

Dataset 1: ANS-blocking: The first set of experimental data was used to investigate the effect of autonomic blockers on respiratory-related oscillations of APD and SBP. The experiment was performed in 10 apparently healthy patients with normal ventricular function

in the cardiac catheterisation suite before the routine clinical procedure for treatment of supraventricular arrhythmias. Four patients had paroxysmal atrial fibrillation, and six patients established atrial fibrillation. Cardioactive medications were discontinued for 5 days before the experiment to avoid their potential effect on the experimental results. UEGs were measured from two decapolar electrode catheters (St Jude Medical, St. Paul, MN; 6F Livewire Steerable Catheter model 401915 with 25-2 mm spacing, 35 mm total span). The catheters were inserted in the femoral vein and fed to the inside of the right and left ventricle. The left ventricle was reached by piercing the atrial septal wall. Arterial blood pressure was recorded invasively using a continuous-flush pressure transducer (Tru-Wave PX600F; Ed- wards Lifesciences, Irvine, CA) located in the femoral artery and breathing activity by measuring the chest circumference using a custom-adapted tension sensor (adapted from a RESPeRATE device; InterCure, New York, NY). During the experiment, subjects were instructed to breathe at different fixed frequencies during a control period in random order. The protocol was repeated following administration of sympathetic blocking agents (β-blockers (metroprolol)) and then following the subsequent addition of parasympathetic blockers (atropine). Heart rate was controlled throughout the experiment to prevent possible fluctuations of APD due to changes in heart rate. This was achieved by pacing from the right ventricular apex using a Biotronik (Berlin, Germany) stimulator (model UHS 3000). To avoid breakthrough intrinsic beats, the cycle length was set $>$20 beats/min faster than the intrinsic atrial fibrillation rate. The median cycle length was 500 ms. Recordings were made after a minimum adaptation period of 2 min of pacing. UEGs and arterial blood pressure recordings were sampled at 1200 Hz and breathing activity at 6 Hz. Details of the experiment have also been described in [70].

Dataset 2: Emotional Stimuli: The second set of experimental data was used to investigate short term variability of APD related to spontaneous breathing and Mayer waves. Data was obtained from 14 heart-failure patients who had an implanted bi-ventricular cardiac resynchronisation device suitable for recording UEGs from the left ventricle tissue (epicardial). The device had been implanted for at least 6 months prior to study and β-adrenergic blocking agents were discontinued for 5 days prior to the study. During the experiment, heart rate was kept constant by electrical pacing from the electrode in the right ventricle (endocardial) using the implanted pacing device. A finger cuff (Finometer pro, Finapres Medical

Systems B.V., Amsterdam, The Netherlands) was used to obtain non-invasive measurements of blood pressure. Breathing activity was measured using the same technique used in dataset 1. Blood pressure and breathing activity were recorded simultaneously and synchronised offline with the UEG data. To elicit and maintain increased sympathetic arousal during the experiment, subjects were exposed to psychological stress by watching three dramatic movie-clips of psychological horror film The Shining, whilst allowed to breathe freely. UEG recordings were sampled at 512 Hz, blood pressure at 1200 Hz and respiration at 6 Hz. The experiment has also been described in [66].

4.2.2 Spectral analysis methods

4.2.2.1 Dataset 1: ANS-blocking:

Amplitude estimation of respiratory-related ARI and SBP oscillations:

Breathing rate was controlled in the first dataset, which allowed analytical techniques that assume stationarity (traditional spectral analysis & (directed) coherence. To compute the amplitude of the ARI and SBP oscillations a spectral method need to be chosen that is as accurate as possible for this purpose. Importantly, the data series were relatively short, containing between 120 and 180 beats only, and although breathing was controlled, the breathing patterns were not sinusoidal. Both conditions are likely to cause spectral leakage (distribution of energy over multiple frequencies) which may underestimate the amplitude estimation. Multitaper spectral analysis is a powerful tool to analyse pseudo-stationary data and has shown to particularly more leakage-resistant compared to conventional spectral methods giving more precise estimates of the amplitude [71–73]. Also, the method is non-parametric, thus does not need the estimation of a model, which requires knowledge about the dynamics to be measured, which can be difficult when analysing unknown dynamics [74]. For these reasons the Thomson multitaper method was used . A multitaper spectrum is composed by the average of K direct spectral estimators [72]

$$\hat{S}^{(mt)} = \frac{1}{K}\sum_{K=0}^{K-1} \hat{S}_k^{(mt)}(f) \tag{4.1}$$

where $\hat{S}_k^{(mt)}(f)$ is a basic multitaper estimator given by:

$$\hat{S}_K^{(mt)}(f) = \Delta t \left| \sum_{t=1}^{N} h_{t,k} X_t e^{-i2\pi t \Delta t} \right|^2 \tag{4.2}$$

The choice of the number of tapers K represents the classical trade-off between spectral resolution and variance' properties of the spectral estimate. Four tapers were found to optimal results, in term of frequency resolution and spectral leakage. The peak amplitude was estimated inside a breathing frequency band, defined as the breathing frequency $\pm$ 10%, where the breathing frequency was defined as the peak-frequency in the spectrum of the respiratory signal.

Assessment of coupling and causality:

Causal interactions between ARI, systolic blood pressure (SBP), and respiration were studied according to a trivariate model presented in Figure 4.2. Given the fact that respiration is controlled by the human experimental subject, one would expect the causal influence of ARI and SBP on respiration to be negligible. However, it is still of interest to analyse these pathways to verify that the model agrees with this expectation; if the analysis did reveal variation in ARI or SBP to be apparently driving respiration, that could indicate the results of the model are unreliable.

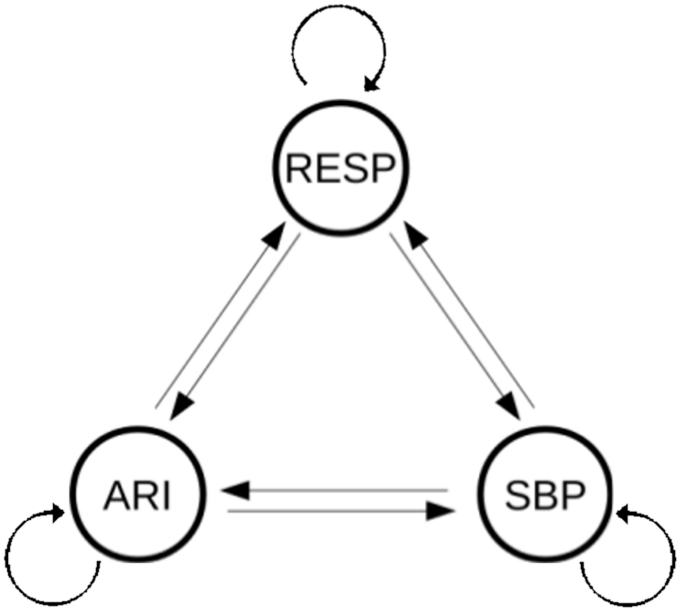

Figure 4.2: Schematic model of the theoretical interactions between respiration (RESP), systolic blood pressure (SBP) and activation recovery interval (ARI). The arrows indicate the possible causal interactions.

The impact of zero-lag correlations on the classic, strictly causal multivariate autoregressive (MVAR) representation of multiple series has been studied previously by Faes et al. [49]. It was shown that neglecting the presence of significant instantaneous interactions

may be detrimental for the estimation of causality. A solution to this problem was provided by Faes & Nollo who developed an extension of the MVAR process that takes into account the existence of instantaneous effects (i.e. effects for which the lag is smaller than the beat-to-beat interval) [49]. Both coupling and causality were measured by the coherence and directed coherence, as explained in Section 2.5.2. The direction (though not the strength) of the instantaneous transfer paths ($A(0)$ in Equation A.3) was *a-priori* determined by ordering the signal markers such that for each $j < i$, instantaneous effects are allowed from $y_j(n)$ to $y_i(n)$ ($a_{ij}(0)\neg 0$) but not from $y_i(n)$ to $y_j(n)$ ($a_{ji}(0) = 0$). This was achieved by sorting the markers in agreement with physiological considerations, thus with respect to their temporal order within each heart beat: respiration samples were taken at the timing of the pacing spikes, which is before the timing of activation in each electrogram, and thus ARI was measured after respiration. In this way, an 'instantaneous' causal pathway could theoretically only occur from respiration to ARI but not visa versa [47]. SBP was measured after ARI due to the pulse travel time from the ventricles down to the femoral artery, in which the pressure sensor was positioned.

Following standard practice, the model order of the autoregressive model was optimised according to the Akaike information criterion and the residuals were tested for whiteness and independence.

4.2.2.2 Dataset 2: Emotional Stimuli:

In contrast to the first dataset, in the second dataset, breathing is not controlled and varies with time. Furthermore, Mayer waves cannot be assumed to be stationary as they are known to appear and disappear spontaneously. To analyse time-varying dynamics, non-stationary approaches were used: The smoothed pseudo-Wigner-Ville distribution (SPWVD) was chosen to analyse the spectral content for breathing and Mayer waves, as it offers good localisation of spectral components (section 2.5.0.2).

The cardiac resynchronisation devices were capable of storing five separate recordings of 30 seconds duration which were downloaded off-line. Pre-processing of the data consisted of two steps. The first step concerns the construction of a continuous electrogram signal of approximately 100 seconds by 'stitching' the separate 30 s recordings. An overlap of approximately 5 seconds between consecutive recordings ensured that no 'gaps' would occur in the constructed signal trace. The second step was to synchronise the electrogram

signal with externally recorded blood pressure and respiration signals. At the time of the experiment, synchronisation spikes were introduced in a separate recording channel of the cardiac device by pressing a buzzer. These spikes were simultaneously recorded in another separate recording that was synchronised with respiration and blood pressure. Data from the cardiac device was then synchronised with the other recordings by alignment of the synchronisation spikes.

Tracking the respiratory frequency during spontaneous breathing

SPWVD of the respiratory signal was used to identify the instantaneous respiratory frequency, and to track changes in the respiratory frequency over the duration of the experiment. As discussed in Section 2.5.0.2 on page 57, interference terms were suppressed using the same exponential shaped kernel as used in [27], in which it was used to investigate respiratory and low-frequency variability in heart rate:

$$\phi(\tau,\upsilon) = exp\left\{-\pi\left[\left(\frac{\upsilon}{\upsilon_0}\right)^2 + \left(\frac{\tau}{\tau_0}\right)^2\right]^{2\lambda}\right\} \tag{4.3}$$

where τ_0 and υ_0 define the shape of the smoothing kernel along τ_0 (the degree of time filtering) and υ (the degree of frequency filtering). The parameter λ represents the size of the kernel's tails. In this case, the parameters were chosen as: v_0 = 0.046, τ_0 = 0.05, and λ = 0.3. in order to provide the most suitable combination of elimination of interference terms and an appropriate time-frequency resolution (11 s and 0.04 Hz respectively). The respiratory frequency was determined using the following method:

1. Computation of the time-frequency spectrum of the respiratory signal, as illustrated in Figure 4.3A and B.

2. The maximum amplitude was determined in the frequency band that is normally associated with spontaneous breathing (0.15-0.5 Hz) for each time bin.

3. The respiratory frequency band was then defined as the respiratory frequency $\pm$ the spectral resolution, which is defined as the width of amplitude spectrum at half the amplitude of the maximum peak, as shown in Figure 4.3C.

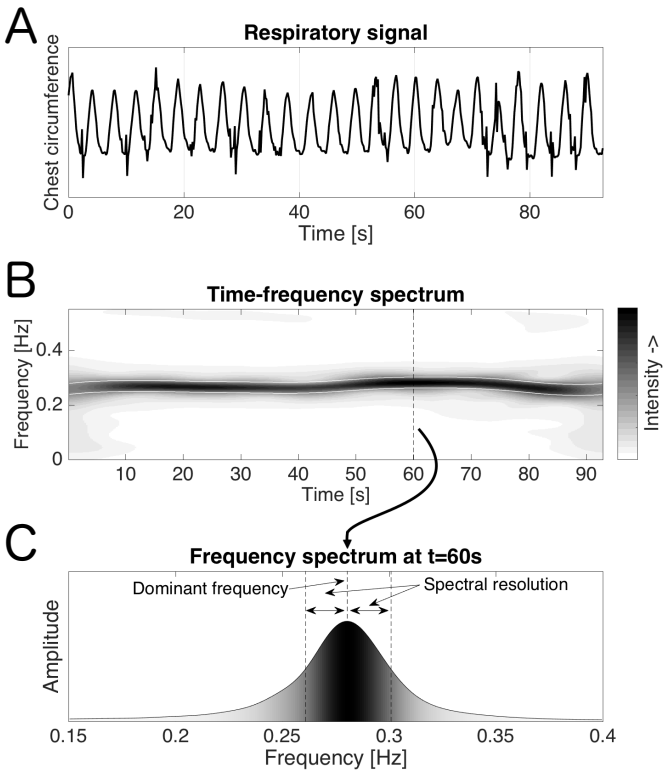

Figure 4.3: Method to detect the respiratory frequency band based on the smoothed pseudo-WignerVille distribution. (A): respiratory signal, (B): corresponding time-frequency spectrum, (C): Frequency distribution at t=60 s to illustrate that the respiratory frequency band was constructed as the frequency of maximum amplitude $\pm$ the frequency resolution.

Assessing relationship between Mayer-wave oscillations in blood pressure and low-frequency oscillations in ARI

To address the final research question, the first step is to identify whether there are periods in recordings when ARI exhibits significant (relative to the noise threshold) low-frequency oscillatory behaviour. Once these instances have been identified, then by studying the concurrence of low-frequency ARI oscillations and Mayer waves in blood pressure, one can investigate the relationship between both signals. During periods of concurrence, the coherence was measured to determine the significance of the coupling between both signals. The following method was applied to investigate this relationship:

1. The Mayer frequency band was defined as the maximum amplitude in a low frequency band (0.04-0.15Hz) $\pm$ the spectral resolution in the SPWV time-frequency spectrum of the blood pressure signal.

2. Sections in which the Mayer-band oscillation was significant were identified for both blood pressure and ARI.

3. Blood pressure and ARI sections were compared and categorised into four different conditions, depending whether Mayer waves were present or not (see Table 4.1).

Significant oscillations at the Mayer frequency

Condition	BP	ARI
1	✓	✓
2	✓	✗
3	✗	✓
4	✗	✗

Table 4.1: Categorisation of blood pressure and ARI intervals into the four possible conditions depending whether Mayer waves were present in BP and/or ARI measures.

4. Finally, the coupling between ARI and BP was studied for the sections in which both signals exhibited significant oscillations (condition 1) by estimating the significance of the time-frequency coherence at the Mayer frequency.

4.2.3 Surrogate data analysis for assessing the significance of ARI oscillations and coupling measures

The research question requires determining whether respiration and Mayer-band oscillation are significant in the presence of measurement noise. The magnitude of this variation is not constant between patients, nor between measurement sites so it is not appropriate to apply a simple magnitude-based threshold. Therefore a significance threshold must be determined for each recording against the background variation existing at the time. The method selected was determined using the surrogate data method [75]. This approach generates set of surrogate series from the original series by randomly shuffling their samples. The method is similar to the method used to evaluate the accuracy of the dynamic ARI estimates in Section 3.2.5 on page 84.

For dataset 1, surrogate data analysis was used to determine the significance of the amplitude of ARI and SBP oscillations. For each ARI and SBP signal, 1000 pairs of surrogate time series were generated and their amplitude at the respiratory frequency was determined using the same method used to analyse the original signal. The threshold for significance was then set at the 95^{th} percentile of the distribution of surrogate amplitudes. The amplitude of respiratory-related ARI and SBP oscillations were considered significant

when the amplitude exceeded this noise threshold.

For the analysis of dataset 2, surrogate data analysis was also used to determine the threshold for zero coherence, as each surrogate signal is completely uncorrelated with respect to the other original signal. For each ARI and SBP signal, an ensemble of 10,000 pairs of surrogate time series were generated to obtain a noise distribution of frequency and coherence values generated by surrogates. The threshold for zero coherence was set at the 95^{th} percentile of this noise distribution with the condition that any coherence value above this threshold is significant (i.e. both signals are coupled). As a result, this approach allows determining the significance of coherence spectra for each couple of signals as a function of time.

4.2.4 Statistical analysis

For dataset 1, mean dP/dt max and SBP values and the amplitudes of significant ARI and SBP oscillations were compared between control and autonomic blockade. The differences were tested for significance using two non-parametric tests: the two-tailed paired Wilcoxon signed-rank test for paired sample testing and the Friedman test and to decrease the probability of type I errors by multiple testing. Results for both tests were considered significant at $p < 0.05$.

4.3 Results

4.3.1 Dataset 1: The effect of autonomic blockade on respiratory-related oscillations in ARI and SBP

In total, 10 subjects were included, each having a median of 15 recording sites of sufficient quality for measurements. First, the effect of autonomic blockade was studied on the mean blood pressure indexes to determine whether the blocking agents produced a measurable effect on the cardiovascular system. Figure 4.4 shows the effect of β-blocker administration and subsequent addition of atropine on systolic blood pressure and dP/dt max. The Friedman test showed that the changes in dP/dt max were significantly for the tested conditions (control, β-blocker administration and subsequent addition of atropine): $p < 0.01$. SBP showed a tendency to decrease, but the measurements were not statistically different between the testing conditions ($p = 0.15$). Using paired sample testing, it was found that the dP/dt max was significantly reduced from 1271($\pm$646) at baseline to 930($\pm$433) mmHg/s

following administration of β-blocker; $p < 0.01$. Addition of atropine was associated with a further significant decrease of the mean dP/dt max from 930 ($\pm$ 433) (β-blocker) to 887 ($\pm$ 436) mmHg/s following administration of atropine; $p < 0.05$. Pairwise comparison of the mean SBP showed a tendency to decreased from baseline 133 ($\pm$21) to 128 ($\pm$ 25) mmHg following β-blocker; $p = 0.06$ and a significant decrease following administration of atropine from 128 ($\pm$ 25) (β-blocker) to 122 ($\pm$ 26) mmHg; p<0.05.

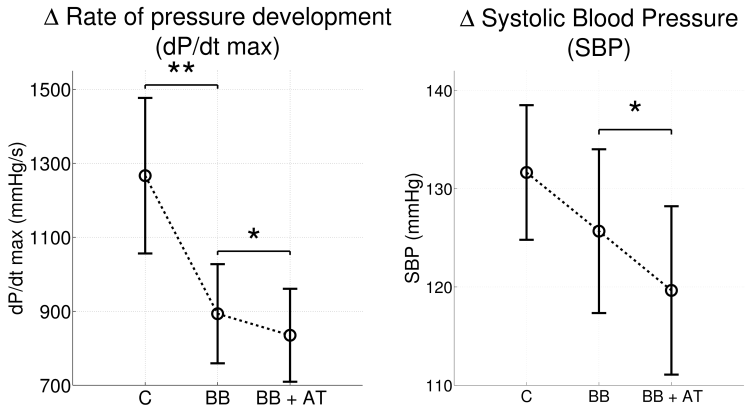

Figure 4.4: Effect of sympathetic and parasympathetic blockers on mean values of dP/dt max and systolic blood pressure (SBP). The Friedman test showed that there was a statistically significant effect of autonomic blockade on dP/dt max ($p < 0.01$), but not on SBP ($p = 0.15$). Further analysis using the paired sign rank test showed a significant reduction of dP/dt max following β-blockers (BB) compared to control (C) and SBP showed a trend of reduction. Subsequent administration of Atropine (BB+AT) resulted in a further significant decrease of both indexes. ($* = p < 0.05$, $** = p < 0.01$)

Spectral analysis revealed significant oscillations with respiration at all breathing frequencies. From the recordings sites of sufficient quality, the median number of electrodes showing significant ARI oscillations with respiration across all patients was 7. Figure 4.5 shows two examples of ARI and SBP signals exhibiting respiratory-related oscillations at 6 and 15 breaths/min.

Of the ARI oscillations which were calculated to be significant with respect to their individual noise thresholds, the peak-to-peak amplitude ranged from 1 to 16 ms. Figure 4.6 shows the average effect of autonomic blocking agents on the amplitude of respiratory-related oscillations in ARI and SBP. Panel A shows the amplitudes of ARI oscillations obtained from recording sides in both left (LV) and right ventricle (RV) combined. LV and RV ARI measurements are considered separately in panel C and D . Finally, panel B

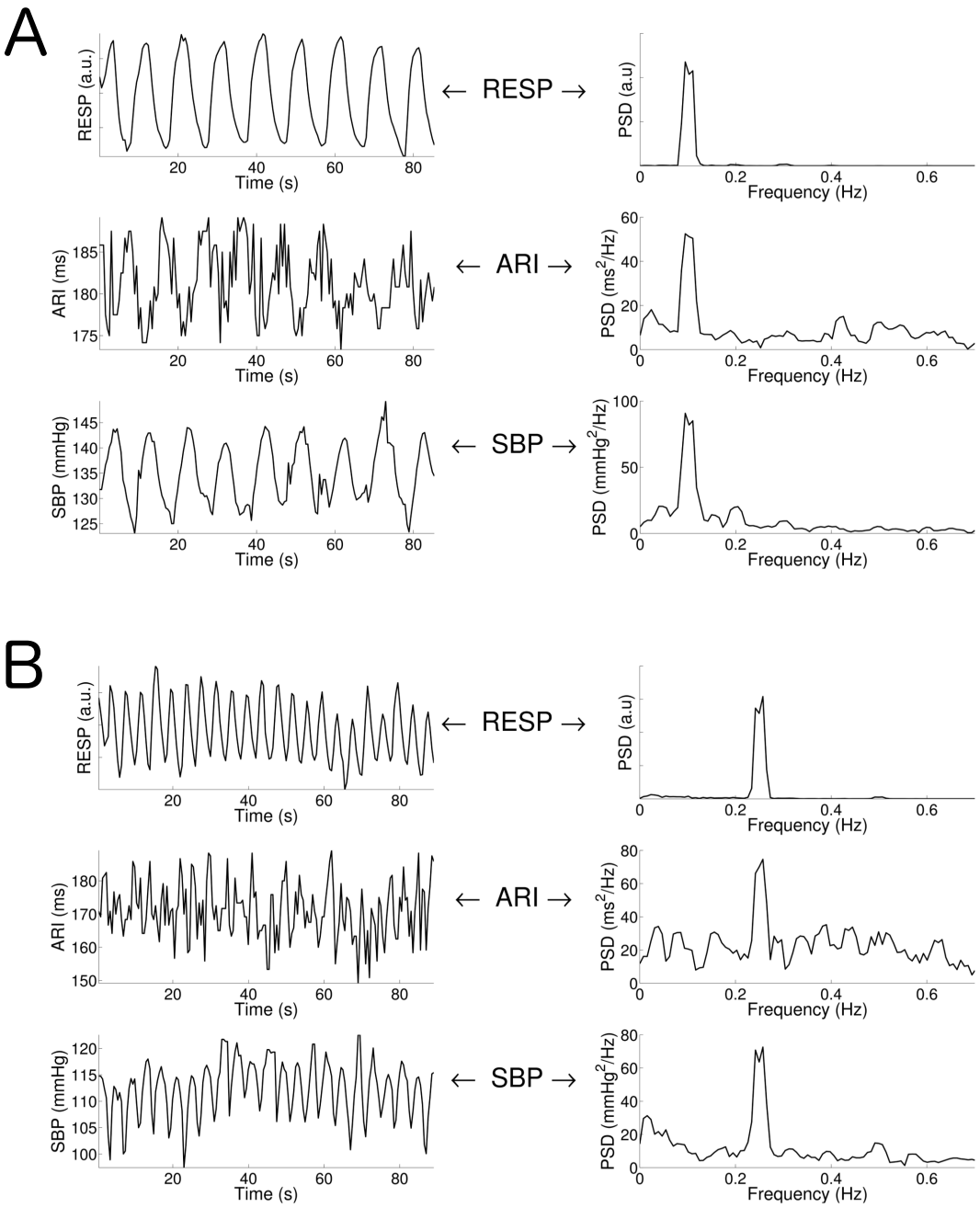

Figure 4.5: Examples of respiration (RESP), ARI and systolic blood pressure (SBP) signals during breathing at: (A) 0.1Hz (6 breaths/min) and (B) 0.25Hz (15 breaths/min). The time series are shown on the left and the corresponding power spectral density (PSD) plots are shown on the right. Both ARI and SBP clearly exhibit respiratory-related oscillations.

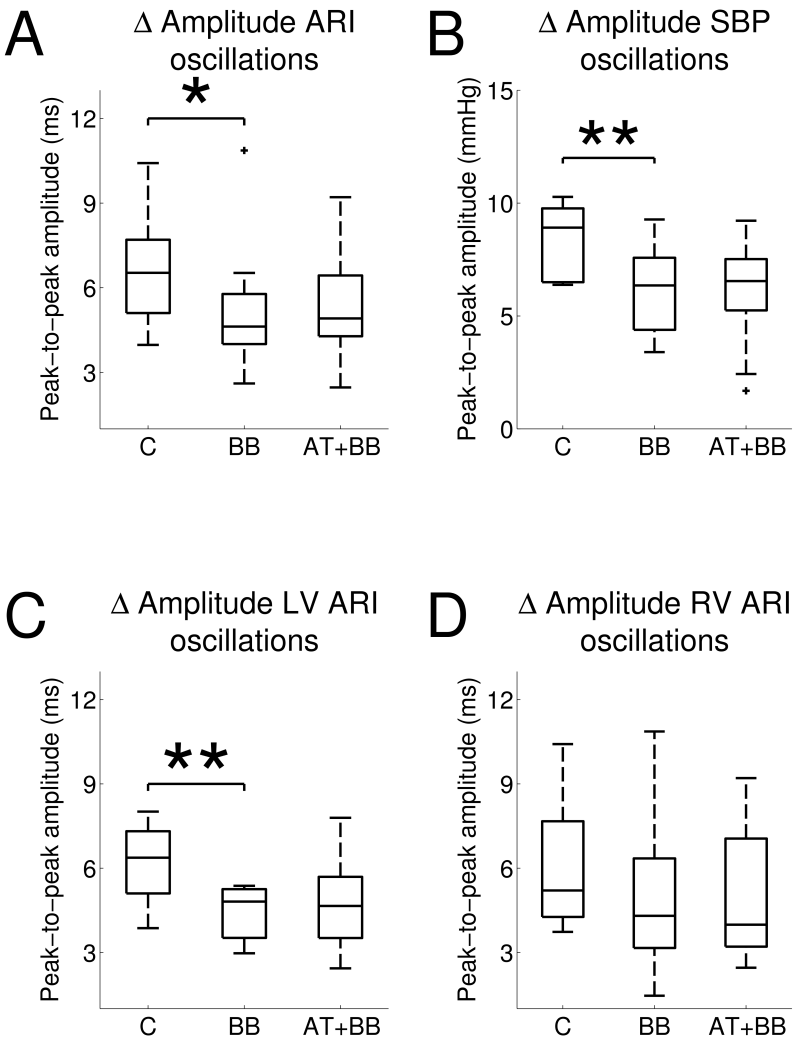

Figure 4.6: Mean peak-to-peak amplitudes of the ARI and systolic blood pressure (SBP) oscillations for three conditions: control (C), β-blocker (BB) and addition of atropine (BB+AT). The Friedman test for comparing multiple related samples showed that the amplitudes for both ARI and SBP oscillations were statistically different for the three conditions. The p-values corresponding to each panel are: A: $p < 0.05$, B: $p < 0.01$, C: $p < 0.05$, D: $p < 0.05$. Further analysis using the paired sign rank tests showed a significant reduction of the ARI and SBP amplitude following BB, except for ARI values taken from the right ventricle (RV). (LV = left ventricle, $* = p < 0.05$, $** = P < 0.01$)

represents the amplitude of SBP oscillations. The p-values of the Friedman test for each panel are: A: $p < 0.05$, B: $p < 0.01$, C: $p < 0.05$, D: $p < 0.05$. Regarding the pairwise testing: administration of β-adrenergic blocking agents reduced the average peak-to-peak amplitude of ARI oscillations: baseline: 6.6 ($\pm$ 1.9) vs. β-blocker: 5.1 ($\pm$ 2.4) ms; $p = 0.04$. As shown in Figure 4.6C and D, the results for the LV are: baseline: 6.2 ($\pm$ 1.4) vs. β-blocker: 4.4 ($\pm$ 1.0) ms; $p = 0.008$. The reduction in the RV was not statistically significant: baseline: 6.0 ($\pm$ 2.2) vs. β-blocker: 4.9 ($\pm$ 2.7) ms; $p = 0.2$. No further changes in the peak-to-peak amplitude were observed following addition of atropine. Regarding the SBP oscillations, the peak-to-peak amplitude ranged from 0.7 to 17.0 mmHg. As shown in Figure 4.6B, the average peak-to-peak amplitude was significantly reduced following administration of β-blocker: baseline: 8.4 ($\pm$1.6) vs. β-blocker: 6.2 ($\pm$ 2.0) mmHg; $p = 0.002$. Like oscillations of ARI, addition of atropine was not associated with any significant change.

4.3.2 Dataset 1: Characterisation of the causal interactions between respiration, blood pressure and ARI at controlled breathing

Using Dataset 1, where breathing frequency was controlled at one of 4 fixed rates, significant coherence (P<0.05) between ARI, SBP, and RESP at the breathing frequency was found in all subjects for all breathing frequencies. From all electrogram signals that exhibited significant oscillations in ARI at the respiratory frequency, 47% were found to be significantly coupled with respiration. The mean coherence values are shown in Figure 4.7. The mean coherence was not affected by the autonomic blocking agents: ARI $\leftrightarrow$ RESP: baseline: 0.76 ($\pm$ 0.12) vs. β-blocker: 0.76 ($\pm$ 0.12) vs. atropine: 0.75 ($\pm$ 0.11); ARI $\leftrightarrow$ SBP: baseline: 0.71 ($\pm$ 0.11) vs. β-blocker: 0.71 ($\pm$ 0.11) vs. atropine 0.71 ($\pm$ 0.11); SBP $\leftrightarrow$ RESP: baseline: 0.92 ($\pm$ 0.07) vs. β-blocker: 0.93 ($\pm$ 0.07) vs. atropine: 0.93 ($\pm$ 0.07).

The causal interactions between the example signals presented Figure 4.5B are plotted in Figure 4.8. For the example signal, respiration was found to be an important contributor to the oscillations observed in ARI, as the directed coherence is around 0.9, which means that 90% of the ARI signal power could be explained by the respiratory signal. Furthermore, the contribution of SBP to ARI was found to be negligible. As one would expect, ARI and SBP do not contribute to the power spectrum of the respiratory signal.

Figure 4.9 shows the mean directed coherences at the breathing frequency for baseline,

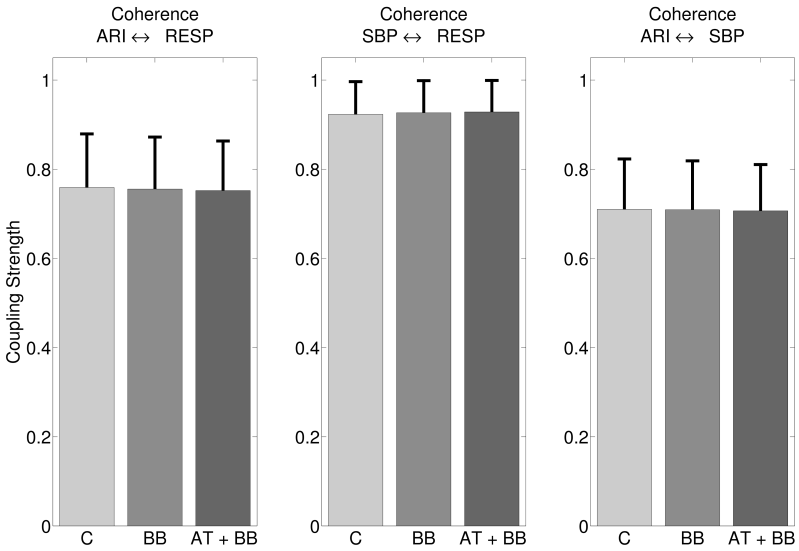

Figure 4.7: Mean coherences between the ARI, respiration (RESP) and systolic blood pressure (SBP) for control (C), β-blocker (BB) and addition of atropine (BB+AT).

β-blocker, and subsequent addition of atropine. The directed coherence RESP $\rightarrow$ ARI at the breathing frequency was 0.70 ($\pm$ 0.17), thus on average, 70% of the ARI signal power could be explained by the respiratory signal. While the coherence between ARI and SBP was found to be high, the directed coherence shows that the causal interactions from SBP $\rightarrow$ ARI was low: 0.07 ($\pm$ 0.06). The directed coherence RESP $\rightarrow$ SBP was found to be high: 0.70 ($\pm$ 0.17).

Administration of β-blockers reduced the directed coherence RESP $\rightarrow$ ARI significantly: baseline: 0.70 ($\pm$ 0.17) vs. β-blocker: 0.50 ($\pm$ 0.23); $P < 0.05$, whereas no effect was seen in RESP $\rightarrow$ SBP. The directed coherence SBP $\rightarrow$ ARI showed a tendency to increase but remained low: control: 0.07 ($\pm$ 0.06) vs. β-blocker: 0.12 ($\pm$ 0.07); p = 0.06. Subsequent addition of atropine did not result in any further changes of the causal interactions.

4.3.3 Dataset 2: ARI oscillations during spontaneous breathing

The effect of spontaneous breathing was investigated by analysing dataset 2. From the three movie-clips, recordings were available in 8/14, 13/14 and 14/14 of the subjects. In total, 33 ARI, 30 blood pressure, and 32 respiratory traces from 14 subjects were analysed. One electrogram signal was not analysed because of the presence of multiple ectopic beats and one respiratory recording was rejected because it did not show a clear respiratory component.

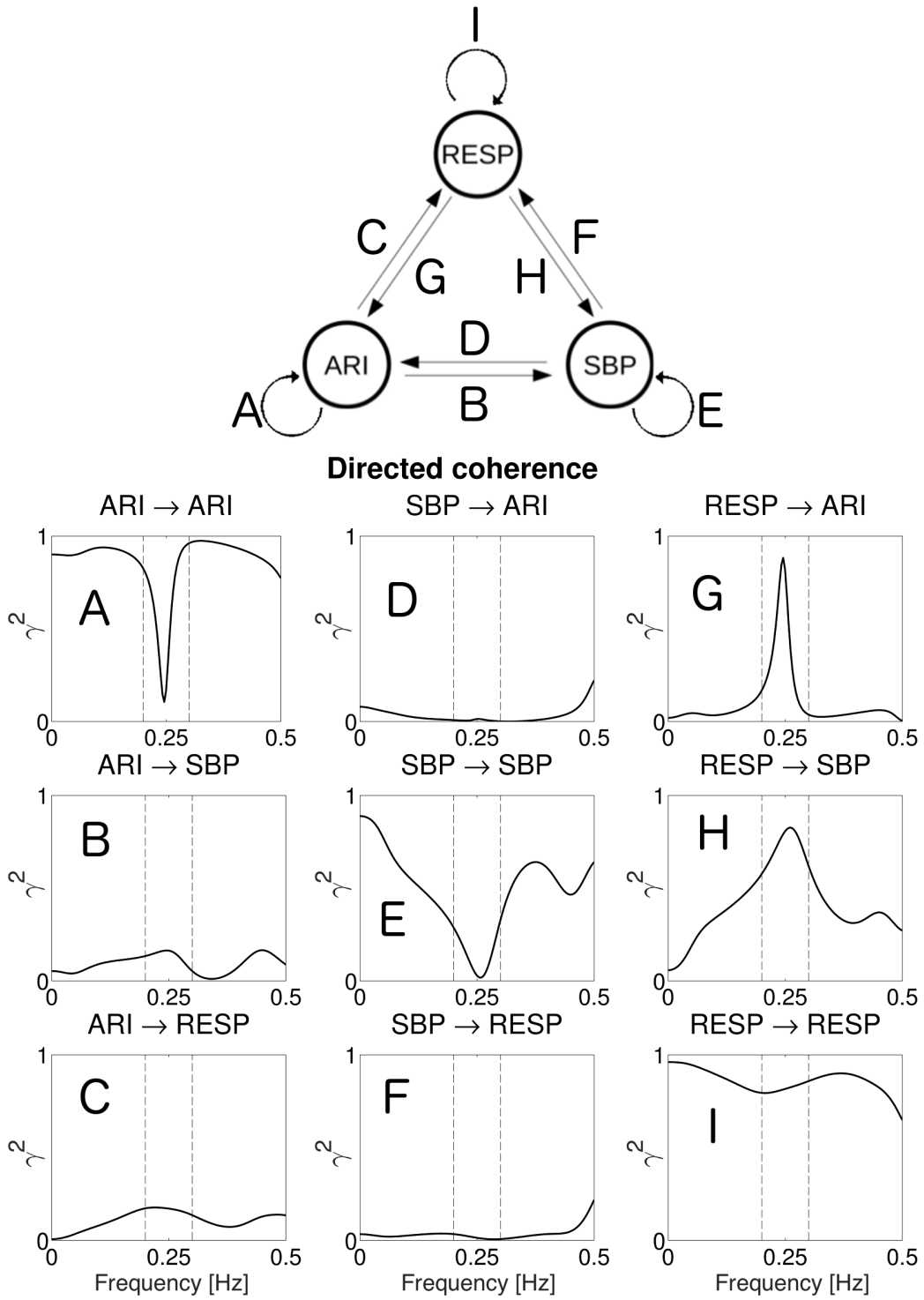

Figure 4.8: The directed coherences between the ARI, systolic blood pressure (SBP) and respiration (RESP) signals shown in Figure 4.5. Frequency band of respiration indicated by dashed lines (in this example controlled at 15 breaths/minute = 0.25 Hz). The diagram at the top shows again the graphical representation of the (theoretical) possible interactive pathways between all signals. The directed coherences are plotted below and show the decomposition of the power spectrum of each signal into contributions from itself and other signals. Note that respiration is an important contributor to the oscillations observed in ARI, while SBP is not. As expected, both ARI and SBP do not contribute the respiratory signal.

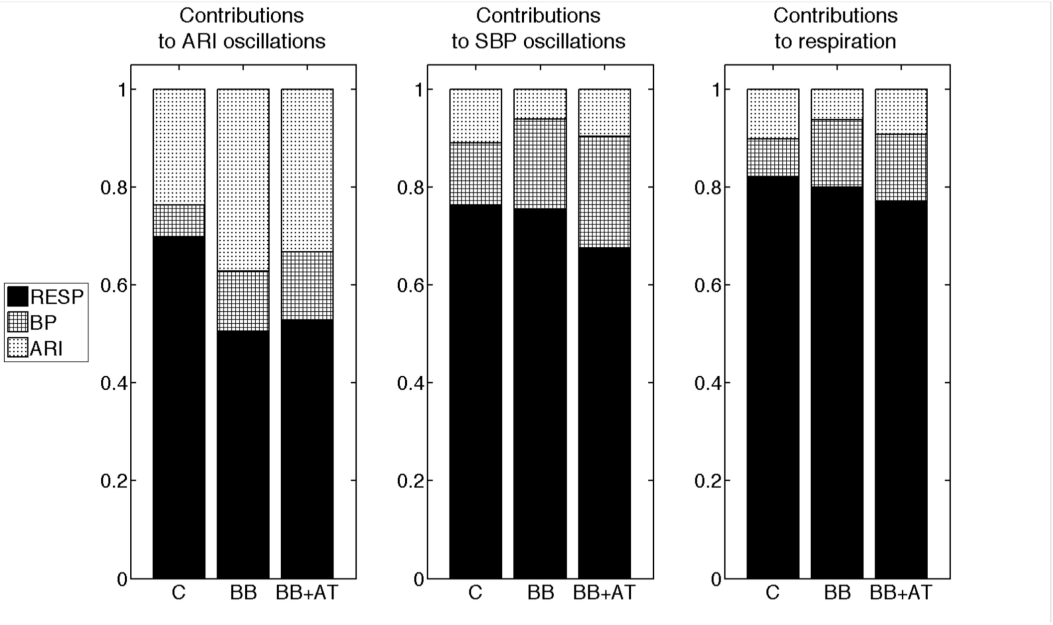

Figure 4.9: Bar graphs presenting the mean directed coherences for ARI, systolic blood pressure (SBP) and respiration (RESP) signals following control (C), β-blocking agents (BB) and addition of atropine (BB+AT). High directed coherence was found between respiration (RESP) and ARI, and RESP and systolic blood pressure (SBP). The directed coherence from RESP $\rightarrow$ ARI was significantly reduced following administration of β-blocker agents ($P < 0.05$). The directed coherence between SBP $\rightarrow$ ARI was low at all stages.

Significant ARI oscillations at the breathing frequency were observed in all subjects. The average peak-to-peak amplitude was 5 ms and ranged from 2.2 to 6.9 ms. The individual results are summarised in the left column of Table 4.2. Figure 4.10 shows an example of clear respiratory-related ARI oscillations during spontaneous breathing for the entire recording period. The corresponding time-frequency spectra (shown in the second row), show enhanced amplitude in the respiratory time-frequency band (green lines) indicating that the oscillations are related to respiration. The enhanced amplitude in the respiratory time-frequency band of the cross-spectral density suggest that both respiration and ARI are indeed correlated at the breathing frequency. Finally, the time-frequency coherence shows that the coupling between both signals is indeed statistically significant for the entire length of the recording. In other subjects, significant coherence occurred more intermittently, as shown in Table 4.2. The average coupling time covered approximately 43% of the recording length.

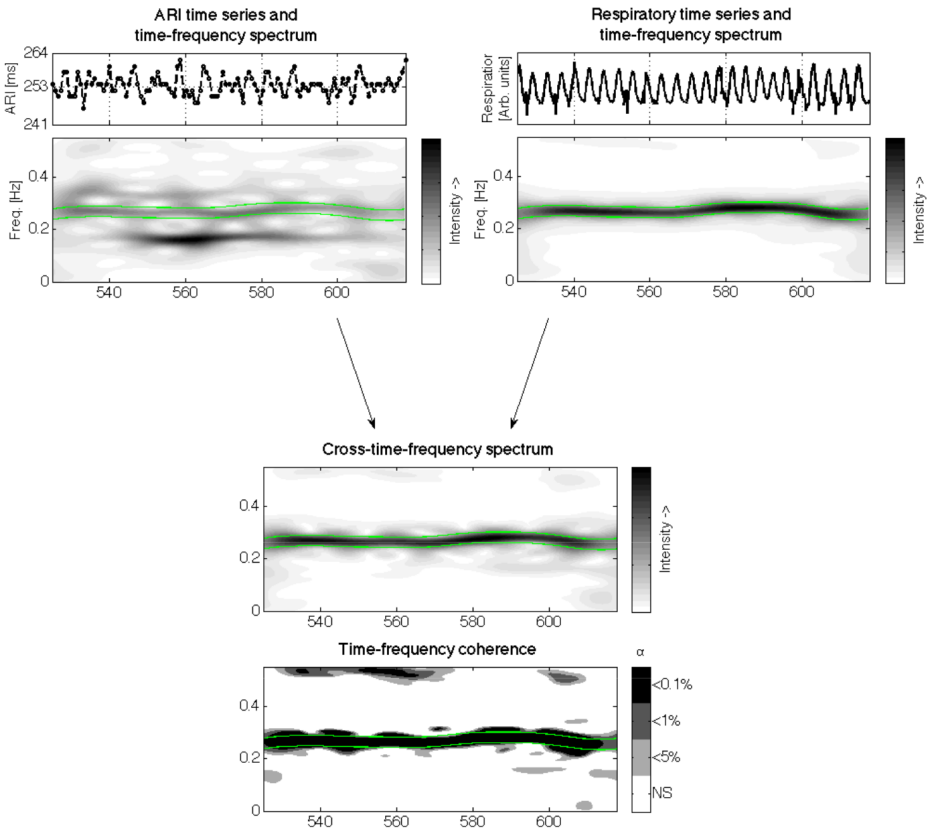

Figure 4.10: Investigation of the relationship between ARI and respiration in an example subject during spontaneous breathing. Top graphs shows the time-series of both ARI and respiration, with clear oscillations in the ARI signal. The corresponding time-frequency spectra are displayed in the second row and show that the amplitude of the ARI signal is indeed enhanced in the respiratory time-frequency band, defined by the green lines. The cross-time-frequency spectrum in the third row shows also enhanced amplitude in the time-frequency band, indicating a possible correlation between both signals at the breathing frequency. Finally, the lower figure shows the time-frequency coherence between both signals, with significant coherence at the breathing frequency for the entire duration of the recording.

Oscillatory behaviour of ARI

	Oscillations at breathing frequency			Oscillations at Mayer frequency		
subject	coupling	Amplitude (ms)	Duration (% of recording)	Coupling	Amplitude (ms)	Duration (% of recording)
1	+	5.7	9	-	-	-
2	+	2.3	57	-	-	-
3	+	3.5	27	-	-	-
4	+	6.9	40	-	-	-
5	+	3.9	61	-	-	-
6	+	3.6	42	+	5.5	19
7	+	4.4	95	-	-	-
8	+	3.5	36	-	-	-
9	+	2.7	52	+	2.9	8
10	+	2.2	34	+	5.4	33
11	+	5.2	21	+	3.6	66
12	+	4.4	16	-	-	-
13	+	2.8	68	X	9.2^{*}	X
14	+	2.4	42	+	3.4	18
Range		2.2-6.9	9-95		2.9-9.2	8-66
Mean $\pm$ SD		3.8 ± 1.4	43 ± 23		5.0 ± 2.3	29 ± 23

Table 4.2: Amplitude and duration of section exhibiting significant oscillatory behaviour at the respiratory and Mayer wave frequency. All subjects showed significant coupling with ARI and respiration. In 5 patients, significant coupling was also found between blood pressure Mayer waves and low frequency ARI oscillations. One patient, indicated by $*$ showed significant oscillations at a low-frequency not related to respiration. However, no blood pressure data was availble to determine the the coupling with Mayer waves.

4.3.4 Dataset 2: ARI oscillations at the Mayer-wave frequencies

Significant Mayer waves in blood pressure were observed in all subjects in whom blood pressure measurements were available (13/14 subjects). The amplitude of ARI oscillations at this frequency was statistically significant in 6 of these subjects (Table 4.2). The average peak-to-peak amplitude ranged from 2.9 to 9.2 ms. Figure 4.13 shows an example of 0.05 Hz oscillations in ARI with a maximum amplitude of 15ms during all three movie-clips.

Significant coupling between Mayer waves in blood pressure and low-frequency oscillations in ARI is shown in Figure 4.12. The top panel shows the time series of both signals: Mayer waves are clearly visible in the systolic blood pressure and also the ARI signal does show low frequency behaviour. The corresponding time-frequency spectra show that the ARI amplitude was enhanced in the Mayer wave frequency band. Also, the

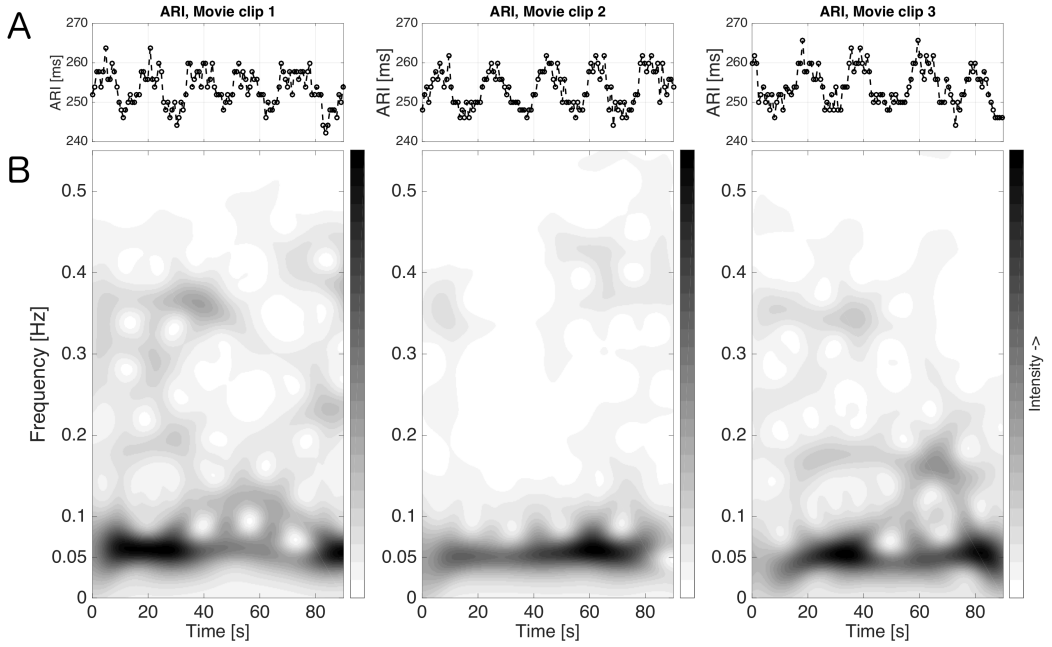

Figure 4.11: An example is shown for one subject illustrating ARI time series (A) oscillating with a peak-to-peak amplitude of 10 - 15 ms. The lower panels (B) show the corresponding time-frequency spectra. The spectra show an increased intensity at a frequency of 0.05 Hz.

cross time-frequency spectrum reveals the existence of correlation between Mayer waves and low-frequency behaviour of ARI. The time-frequency coherence spectrum shows that coupling between low-frequency ARI behaviour and Mayer waves in blood pressure was significant throughout 78% of the recording length. The mean coupling duration for all subjects was 29% of the recordings lengths.

Table 4.3 shows that on average, significant ARI oscillations in the Mayer frequency range were observed for 29% of the time when Mayer waves were present in blood pressure. Additional coupling analysis showed that the coherence between ARI and Mayer waves was significant for 75 to 100% of the durations of these sections. Individual results of the coupling analysis are shown in Table 4.2. In more than 90% of the time in which Mayer waves were absent, no significant ARI oscillations were observed. However, large sections were found in which Mayer waves were not accompanied by significant oscillations in ARI (71% of the time).

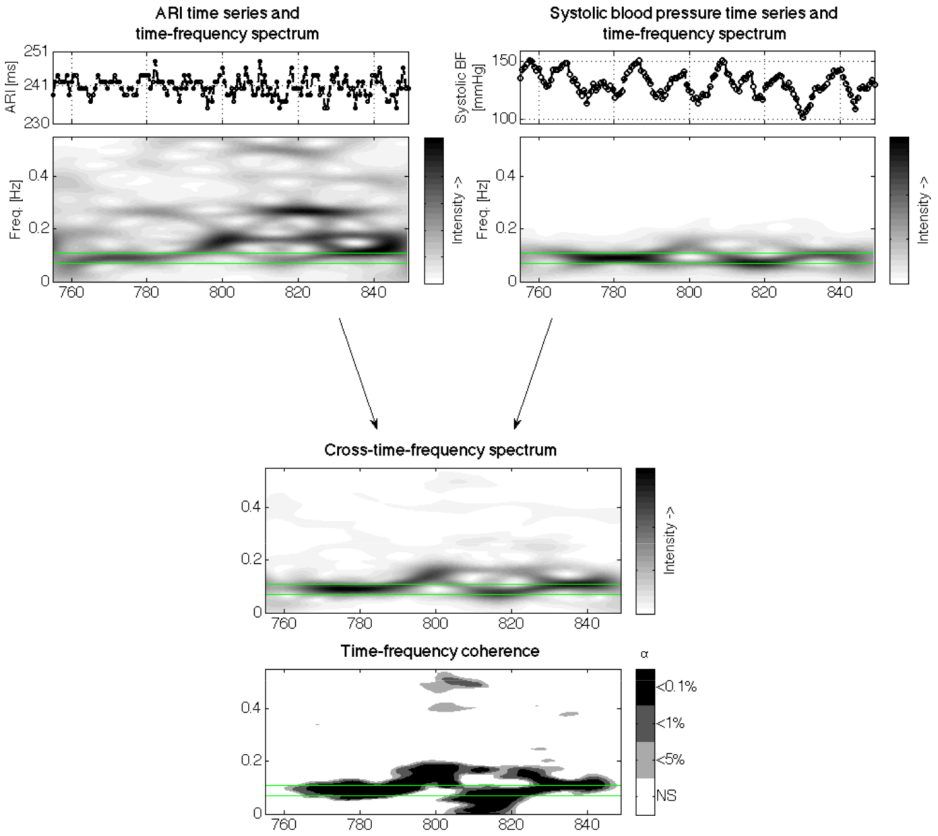

Figure 4.12: Investigation of the relationship between ARI and Mayer waves in an example subject. Top graphs shows the time-series of both ARI and systolic blood pressure (SBP). The corresponding time-frequency spectra are displayed in the second row with enhanced amplitude at the Mayer frequency band (green lines) in ARI. The cross-time-frequency spectrum is plotted in the third row and indicates correlation between both signals at the Mayer frequency. Finally, the lower figure shows that the time-frequency coherence between both signals is significant at the Mayer frequency for 78% of the recording duration.

	Mayer waves in blood pressure	
	Present	Absent
ARI oscillations significant	29%	8%
ARI oscillations not significant	71%	92%

Table 4.3: Concurrence between significant oscillations in ARI and Mayer waves in blood pressure. Values represent mean values across the subjects and were expressed as percentage of the recording period of the condition. For example, concurrence of Mayer waves and low-frequency oscillations in ARI was seen on average in 29% of the periods in which Mayer waves were present.

4.4 Discussion

Data from two previous experiments were used in this study to investigate respiratory and Mayer wave oscillations in ARI with the aim of examining the neural involvement in controlling cardiac electrophysiology.

4.4.1 Interpretation of ARI oscillations and their possible origins

Before discussing potential physiological mechanisms underlying the observed ARI oscillations, one should first carefully consider whether the observed oscillations did indeed reflect oscillatory behaviour of APD, or at least electrophysiology, or whether other (non-electrophysiological) mechanisms could also be attributable to the observations, like lead-field changes or other artefacts. Chapters 2 and 3 have demonstrated the potential for inaccuracy in measurement of activation and repolarisation times from electrograms, and how to identify and avoid such situations.

Regarding oscillations at the breathing frequency, changes in the electrical field around recording leads could indeed occur as a result of respiratory motion as already discussed in the work of Western [11]. Evidence of cyclic baseline wander was observed in the isoelectrical segments of some electrograms. However, in the present analysis, artefacts are unlikely to be wholly responsible for ARI oscillations as the amplitude of the oscillations was significantly reduced following administration of β-blockers. Compared to the work of Western in [11], autonomic blockade was tested in a larger population of 10 subjects, allowing robust statistical testing. The profound effect of autonomic nervous blocking agents on mean blood pressure indices shown in Figure 4.4 provide strong evidence that the blockers were indeed causing inhibition of autonomic activity.

Another novel observation in this work is the phenomenon of ARI oscillations related to Mayer waves. Similar to respiratory oscillations, two important question arise from this observation: 1) Are the oscillations indeed electrophysiological in origin? 2) Can the underlying changes in ARI be truthfully interpreted as changes in APD, or are other electrophysiological changes responsible for the oscillatory behaviour?

In contrast to respiration, it is not possible that the influence of cyclical chest movement could have led to the observation of Mayer Waves, since these are at separate frequencies.

However, Mayer waves are known to modulate the vasomotor tone, that might affected left ventricular afterload. As a result, the end-systolic volume may cyclically change thereby inducing changes in the lead field. Bleich studied the effect in the ECG by changing the volume of the left ventricle and did indeed notice that it affect the amplitude of the QRS waveform [76]. This effect is known as the Brody effect. The UEG waveform could be affected in a similar manner affecting the ARIs. Figure 4.13 helps to understand how the UEG waveform changes for the minimum and the maximum ARI observed in one Mayer wave cycle of one subject. As can been seen from the graph, Mayer wave changes in ARI are mainly due to changes in repolarisation rather than activation. Because the Brody effect is not expected to play a major role during the repolarisation phase, it is likely that the low-frequency oscillations of ARI are at least partly electrophysiological in origin.

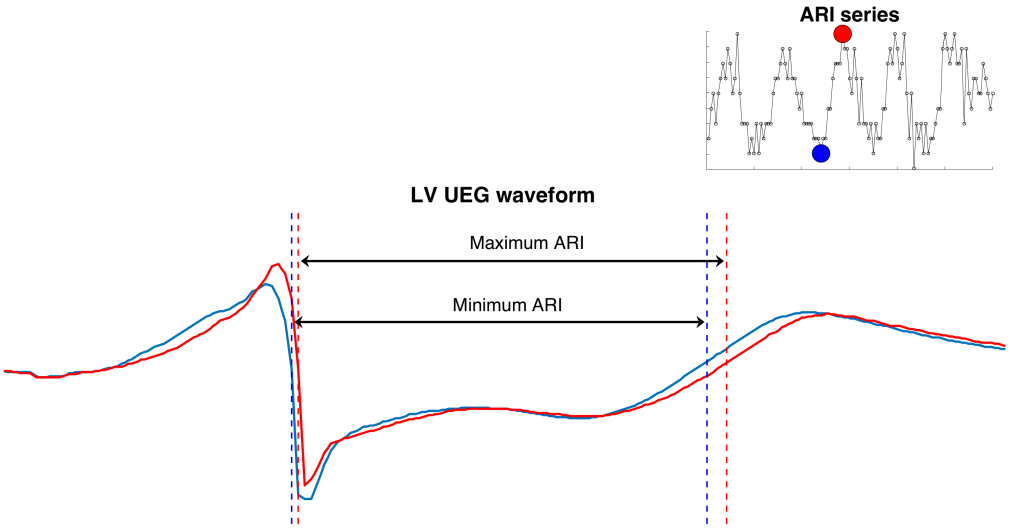

Figure 4.13: Two unipolar electrograms from the left ventricle (same electrode) at the peak and trough of 0.05 Hz ARI oscillations (see Fig. 4.11), aligned according to the pacing time. Local activation and recovery timings are marked with the vertical lines. Changes in ARI seems to be mainly driven by caused changes in repolarisation time.

Figure 4.13 is also useful to determine whether the underlying changes in ARI are related to local changes in APD. For example, the morphology of the activation wave stays roughly the same, which confirms that the spatiotemporal distribution of activation does not change significantly. Hence, changes in activation are likely to represent local behaviour. It can also be seen that the T-wave is shifted slightly to the right when when the ARI is prolonged. It is therefore likely that the change in ARI indeed represent changes in APD caused by changes of local repolarisation.

4.4.2 Interpretation of the interactions between ARI, respiration and blood pressure

Following this conclusion that it is likely that ARI oscillations at the respiratory and Mayer frequency can (at least partly) be interpreted as true oscillations in electrophysiology and APD, one can further focus at the possible driving mechanisms by investigation of the underlying interactions:

Amplitude changes of ARI oscillations related to administration of autonomic blockers: Reduction in the amplitude of ARI oscillations after autonomic blockade suggests a link between autonomic activity and oscillatory behaviour. This reasoning is supported by the fact that breathing was controlled, which makes it unlikely that the effects were due to changes in respiratory behaviour. The observation that additional administration of atropine did not result in additional changes of the magnitude of ARI oscillations (see Figure 4.6), seems to suggest that ARI oscillations are mainly driven by a sympathetic activity. However, because all subjects were already affected by β-blockers before receiving atropine *, it is not possible to determine the independent effect of atropine the autonomic nervous activity and subsequently ARI oscillations in this study.

Multivariate autoregressive (MVAR) analysis to characterise coupling and causality: The coherence and causality analysis using the MVAR model, reveal a strong causal interaction from respiration to ARI but not from blood pressure to ARI, suggesting a direct driving mechanisms of respiration on electrophysiology. However, the results should be interpreted within the limit of a linear model and does not exclude a more complex involvement of blood pressure as part of a causal chain in the generation ARI oscillation. It could still be possible that changes in intraventricular pressure induce regional changes in cardiac strain that could in turn cause ARI oscillations via the mechano-electric feedback pathway [77, 78]. In that case, blood pressure changes, which only partially reveals heterogeneous cardiac strain, may still be involved in the generation of ARI oscillations without necessarily exhibiting a linear interaction with them.

Time-frequency coherence: In the absence of direct neural recordings, studying interactions and coupling between Mayer waves and ARI can be a useful alternative to find deter-

*necessarily this order due to safety concerns of avoiding possible tachycardia

mine its contribution in the genesis of ARI oscillations. Independent time and frequency filtering using the smoothed pseudo Wigner-Ville distribution (SPWVD) has found to be useful in many biomedical applications for accurate tracking of dynamics in time. In this study, significant time-frequency coherence was found between respiration and ARI at the breathing frequency, and Mayer waves and ARI at a lower frequency, usually around 0.1 Hz. As discussed in Section 2.5.0.2, the reliability and physical meaning of these coherence estimates depends critically on the reduction of interference terms. Inspection of the coherence estimates in this study confirmed that the coherence estimates were bounded between 0 and 1, which implies that interference terms had successfully been attenuated to insignificant levels. To study the physical meaning of the coherence, surrogate data test applied successfully to improve the interpretation of the coherence spectra (i.e. whether signals were coupled or not).

4.4.3 Underlying mechanisms

Oscillatory behaviour with respiration: Several possible mechanisms explaining APD oscillations at the respiratory frequency in subjects with normal ventricles have been discussed in Section 2.3.4. This study contributes to the possible mechanisms as follows: a reduction of the amplitude of respiratory-related ARI oscillations following administration of the β-blocker, and the further reduction following atropine, confirmed preliminary results reported by Western [11], who found a similar trend in a small group of 5 subjects. Computation of the coherence provided more information about the origin of the oscillatory behaviour: significant coupling at the respiratory frequency between respiration, ARI and SBP suggest that the respiratory-related behaviour between ARI and SBP share common rhythms. Similar results were reported by studies focussing on respiratory-sinus arrhythmia, showing significant coherence between respiration, RR variability (variability in heart rate) and SBP during rest [27, 79]. Detection of coupling contributes to a better understanding of the underlying interactions between ARI, respiration and SBP by detecting the presence or absence of interactions between the processes. Causality analysis performed in this work constitutes an eligible approach to characterise the interdependence between these processes and showed that strong causal interaction from respiration to ARI, but not from SBP to ARI as shown in Figure 4.9.

As already cautioned, the results should be interpreted within the limit of a linear model and does not exclude a more complex involvement of blood pressure in the generation ARI

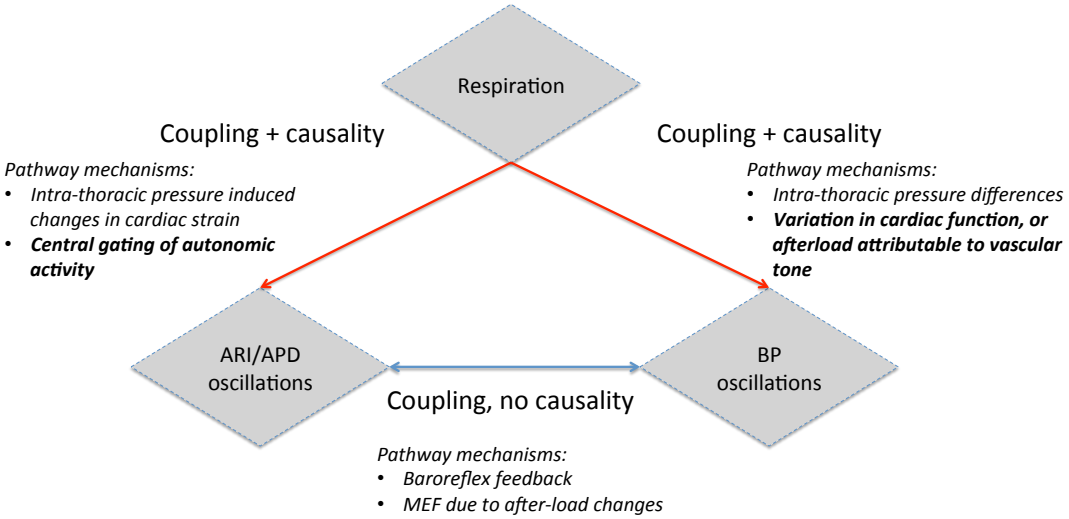

Figure 4.14: Possible pathways of ARI and BP oscillations and corresponding underlying mechanisms. Analysis of magnitude, coupling and causality of ARI oscillations indicate that ARI oscillations are likely to be driven by respiration via a direct pathway, which is more consistent with the explanation that APD oscillations are driven by autonomic activity from respiratory networks than by feedback from the blood pressure (baroreflex).

oscillation. However, combined with the findings of the phase relationship between ARI and SBP by Hanson et al. in [10], this might argue against a important role of the baroreflex feedback in generating ARI oscillations. The results of the amplitude and causality analysis can be best explained using a mechanism comprising central gating of autonomic neural traffic by central respiratory networks [80]. For example as a result of brainstem interactions [81] or entrained by cortical activity [82]. Respiratory gating manifests as an increase in the sympathetic outflow to the hearts and a decrease in parasympathetic during respiration [83]. As described on page 39, sympathetic activity can directly affect the ion channels on the cardiac membrane causing shortening the ventricular APD. Consequently, phasic modulation of sympathetic activity may result in oscillatory behaviour of APD. Figure 4.14 summarises the possible mechanism underlying ARI oscillations and how the findings of this chapter contributed to this.

Oscillatory behaviour at low frequencies: The presence of significant coupling between ARI and systolic blood pressure at low-frequencies during mental stress suggests that both signals may be driven by a common source. This suggestion is supported by the lack of significant low-frequency ARI oscillations in the absence of blood pressure oscillations (Table 4.3). Because electrogram and blood pressure data were off-line synchronised, the experimental model was less reliable for investigating phase relationships between low-

frequency oscillations in ARI and SBP. The phase relationship could however reveal important information about the causal interactions between ARI and SBP. As discussed in Section 2.3.4 on page 41, the precise mechanism underlying of the blood pressure Mayer waves is still subject of debate, but is believed to result from oscillatory behaviour of the vasomotor tone resulting in cyclic variation of vascular resistance [25, 30]. Two candidate mechanisms considered on the nature of Mayer waves are: pacemaker-like activity of an oscillator in the brain versus oscillatory responses to hemodynamic changes. Either of the above mechanisms could be associated with periodic autonomic outlfow to the ventricular myocardium and a direct effect on the ventricular APD. Figure 4.15 shows how low-frequency modulation of sympathetic nerve activity could affect APD and how this process is correlated to blood pressure waves caused by dynamic changes in vasomotor activity. Although significant coupling suggests that low-frequency oscillations in ARI and SBP are driven by similar mechanisms, it does not necessarily mean that both processes are also modulated by nervous activity. Importantly, it has been shown that myocardial stretch produced by volume or pressure can also lead to significant electrophysiological changes [77, 84]. This is phenomenon is known as mechano-electric feedback and may also contribute to low-frequency APD behaviour when APD is modulated secondary to the periodic mechanical stimuli accompanying the Mayer wave oscillations in blood pressure. For example, the changes of the vasomotor tone during Mayer waves may affect the cardiac afterload (the pressure against which the heart must work to eject blood during contraction). This may result in changes in myocardial stretch and thus mechano-electric feedback. As mentioned previously, analysis of the phase relationship is important to further investigate the consistency of this explanation.

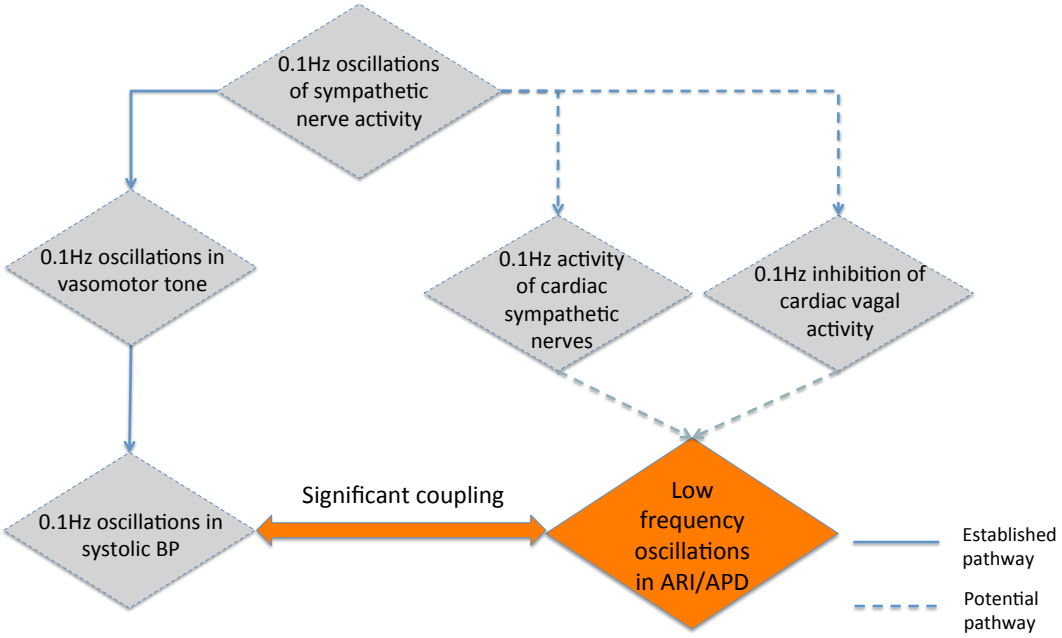

Figure 4.15: Significant coupling between Mayer waves in blood pressure and low-frequency oscillations in ARI may indicate that 0.1 Hz oscillations in sympathetic nerve activity also modulate APD.

Chapter 5

Carotid sinus stimulation and ventricular APD

The results presented in the previous chapter suggest that the ventricular action potential duration (APD) is subject to autonomic regulation related to respiratory behaviour and blood pressure Mayer waves. The validity of this postulation could be further explored by demonstrating that periodic behaviour of APD can be induced by rhythmic activation of the autonomic nervous system (ANS). To that end, this final chapter describes a time and a spectral analysis technique combined with the design and assessment of a physiological test-bed for periodic autonomic stimulation. In investigating this concept, one should take into account the physiological nature of how nervous input is generated. Although artificial stimulation of the nerves leading to the heart may be useful for characterising their influence, it does not necessary reflect the physiology of the heart's neural control mechanisms. Instead, stimulation of the mechanisms that regulate the autonomic outflow to the heart would provide more physiological insight into the interplay between the ANS and cardiac electrophysiology.

As explained in section 2.3, ANS activity to the heart is reflexively altered to keep blood pressure in balance. Stretch receptors (known as baroreceptors) originating in the carotid sinus bifurcation in the neck play a pivotal role in this process by supplying barosensory information of the arterial system. Because these receptors are sensitive to stretch, they can also be stimulated non-invasively by applying an external pressure on the carotid region of the neck. The pressure neck chamber is a well-established method to deliver neck pressure and has played an important role in a long line of experiments to investigate carotid

baroreflex control of heart rate, blood pressure and sympathetic nerve activity [85–89]. However, less is known about the influence of the carotid baroreflex on ventricular APD has not been investigated. Since sympathetic nerves are also known to innervate ventricular myocardium, and elicit changes to important components of the cardiac APD, this work hypothesises that the carotid baroreceptor reflex can also affect cardiac APD.

Main research question and aim

The aim of this work is to investigate the effect of carotid baroreceptor reflex on ventricular APD by applying periodic stimulation of the carotid baroreceptors. The work addresses the following research question:

- Can ARI be influenced by periodic stimulation of the carotid baroreceptor at the Mayer wave (0.1 Hz) frequency?

Accordingly, the first part of this chapter covers the concept of baroreceptor stimulation, the experimental protocol and the design of a neck pressure chamber for use in the catheterisation laboratory of the hospital. The second part of the chapter concerns investigating the efficacy of this hardware, and associated analysis processes. The method is investigated in several human subjects, providing unique pilot results which demonstrate significant changes in ventricular APD associated with baroreceptor stimulation.

The workflow of the data processing is shown in Figure 5.1. Invasive blood pressure and electrogram measurements were taken from the patient during periodic carotid baroreceptor stimulation by a neck pressure chamber (Section 5.2). The recordings were then analysed for ARI and systolic blood pressure (SBP) values and the influence of carotid baroreceptor stimulation on these indices was assessed using a time and a spectral method. The time method measured the average response of ARI and SBP to carotid stimulation as function of the stimulation time, whereas the spectral method was used to estimate the ARI and SBP amplitudes at the stimulation frequency (Section 5.3.2). Surrogate data analysis was applied to determine the noise threshold for both methods. Measurements that exceeded this threshold were considered statistical significant (Section 5.3.2).

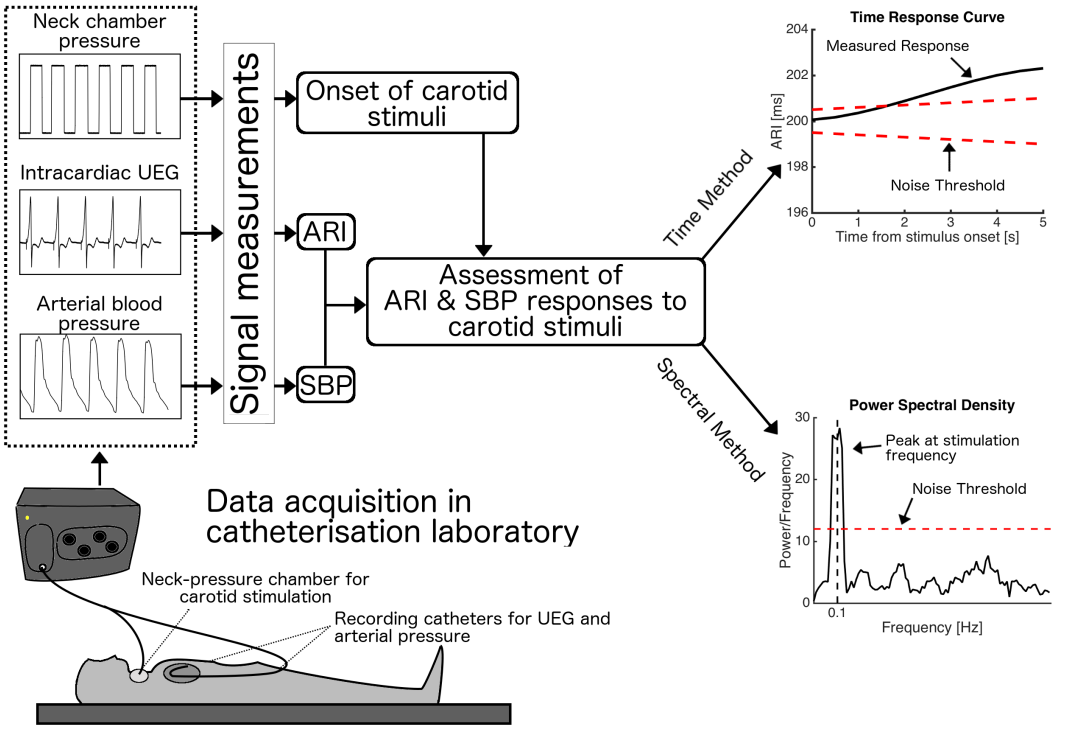

Figure 5.1: Workflow of data processing to investigate the effect of periodic carotid baroreceptor stimulation on activation recovery interval (ARI) and systolic blood pressure (SBP). The influence of carotid baroreceptor stimulation on ARI and SBP was investigated using a time method and a spectral method.

5.1 Characteristics of carotid baroreceptor stimulation

The baroreceptors in the carotid sinus are quantitatively the most important for regulating arterial pressure and are located just above the carotid artery bifurcation at the level of the superior border of the thyroid cartilage. Carotid baroreceptors normally respond to beat-to-beat changes in arterial pressure that change in the stretch in the vessel wall. Since the carotid baroreceptors are located relatively close to the skin, it is also possible to stimulate them by changing the transmural pressure using the neck pressure chamber [88]. To that end, the carotid region and surrounding anatomical structures in the neck are sealed. Application of either suction (partial vacuum) or pressure inside the chamber causes changes in the transmural pressure. As illustrated in Figure 5.2, application of neck suction (NS) increases the transmural pressure causing dilatation of the carotid sinus. This is sensed by the baroreceptors in the vessel wall which respond by increasing their electrical firing, equivalent to what would happen when the arterial pressure is increased. The activity of the receptors is transmitted via the carotid sinus nerves to central terminals (synapses) in the

brainstem that transmit this information to neurons within the solitary nucleus. The brain reflexively responds by reducing sympathetic and (reciprocal) increasing parasympathetic outflow to the heart and blood vessels to reduce heart rate, contractility and vasomotor tone in an attempt to reduce the increased wall stretch. Note that the opposite effect occurs by applying neck pressure (NP) which reduces transmural pressure and consequently baroreceptor firing. The brainstem responds reflexively by increasing sympathetic and reducing parasympathetic activity.

Periodic stimulation of the carotid baroreceptor

Previous work by Bath et al. has shown that the application of sinusoidal NS at a low frequency similar to Mayer waves induced cyclical changes in sympathetic nerve activity, blood pressure, and heart rate [90]. Although sympathetic activity was estimated by measuring the sympathetic outflow to muscles, which may not necessarily reflect the sympathetic activity outflow to the heart, the changes in heart rate make it highly likely that also the autonomic outflow to the heart was modulated. As discussed in Section 2.3.2, sympathetic activity shortens APD and parasympathetic prolongs APD. It was therefore hypothesised that rhythmic stimulation of the carotid sinus at the Mayer wave frequency could result period changes in ventricular APD. As illustrated in Figure 5.3, periodic application of NP would result in periodic modulation of sympathetic activity causing periodic shortening of APD. In the presented work, both NP and NS were considered and their influence on ventricular APD was investigated separately.

Intensity of the stimulus

Previous work has shown that the change in heart rate induced by NS or NP is proportional to the intensity of stimulus [85, 91]. Pressures of 60 mmHg below (NS) or above (NP) ambient pressure has shown to adequately activate the carotid sinus arterial baroreceptors by means of heart rate without causing discomfort for the subject [85, 91]. Therefore this study sought to apply an additional 60 mmHg pressure during NP periods and to apply suction reducing the pressure at the neck surface by 60 mmHg during NS.

Asymmetry of the carotid baroreflex

Carotid baroreceptors are located in the left and right carotid sinus. The influence of each side on the heart is slightly different, and is probably related to differences in nerve innervation between the right and left side innervation of the heart [86, 91]. For example, stimu-

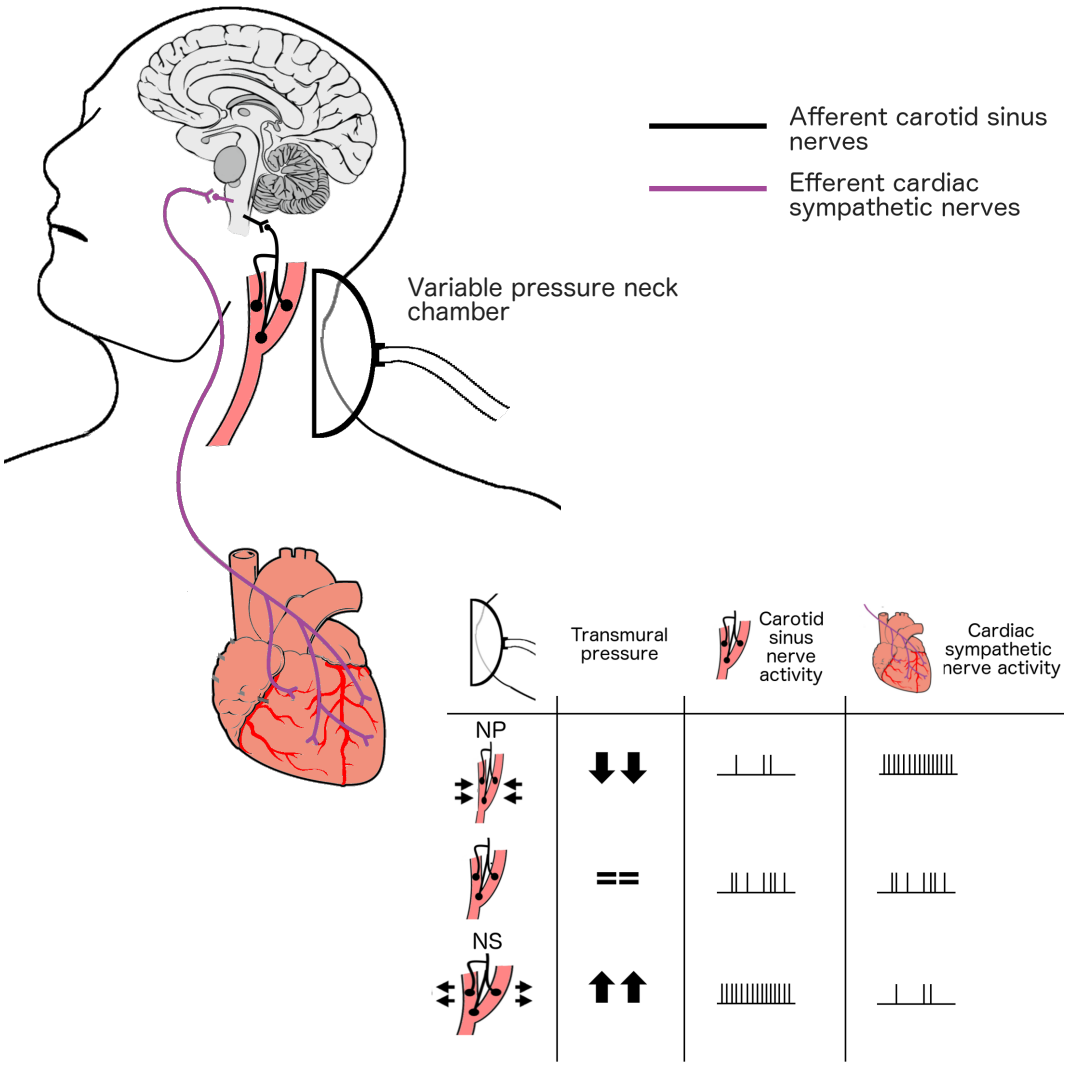

Figure 5.2: A schematic illustration of the neural responses to alterations in carotid transmural pressure produced by neck pressure (NP) and neck suction (NS). The carotid baroreflex is designed to correct alterations in blood pressure sensed by the carotid baroreceptor. NP mimics a hypotensive stimulus by lowering the carotid transmural pressure, which reduces the carotid sinus nerve firing. The reduced input to the brainstem causes an increase in sympathetic nerve activity to the heart. The opposite effect can be achieved by producing NS.

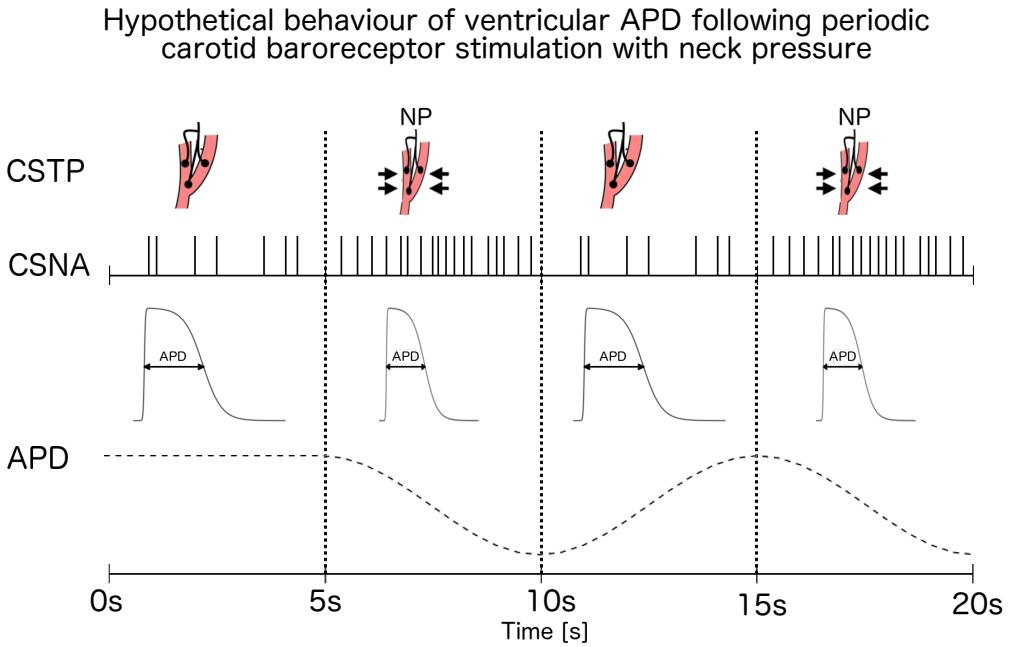

Figure 5.3: Hypothetical behaviour of APD following carotid stimulation with neck pressure (NP). CSTP: carotid sinus transmural pressure, CSNA: cardiac sympathetic nerve activity.

lation of the left carotid sinus has shown to be predominantly influence contractility of the heart (inotropic), whereas right carotid stimulation mainly affects heart rate (chronotropic) [86, 91, 92]. Since contractility is related to the calcium handling of the myocytes (Figure 2.5, on page 37), one may suspect the APD is most affected by stimulation of the left carotid baroreceptor.

5.2 Design of a neck chamber device for carotid baroreceptor stimulation

Pressure neck chamber devices are not widely available and the device used in this work was designed from scratch. In literature, two concepts of neck chambers exist: neck collars, that fully cover the whole neck, and the (paired) pressure capsules, that need to be positioned in the anatomical area of each carotid locus [88]. The preferred configuration for this study is the pressure capsules method, due to its practical advantages over neck collars:

- Offering more comfort for the subject and less likely to introduce anxiousness that might affect the measurements.
- Better vacuum and pressure seal: no need for different collar sizes to tailor different neck sizes

- Device dimensions are smaller which is desired given the limited accessibility to the subject in the catherisation laboratory environment

The most important disadvantage of the chosen device concept is that it needs accurate positioning of the capsule. Incorrect positioning will affect the pressure transmitted to the carotid sinus region, which reduces the magnitude of the stimulus.

A schematic overview of the designed device is presented in Figure 5.4. Using a three way valve, the neck chamber is linked to either atmospheric pressure or vacuum/pressure produced by a pump. The neck-side of the pressure chamber was provided with a cushioned rim to form an airtight seal with the skin. This solution worked well for NS, but mainly because the device draws itself actively against the neck. However, NP lifted the capsule from the neck, causing substantial air leakage and loss of applied pressure. This problem was solved by putting a latex rubber membrane inside the cushioned rim that is pushed outwards against the skin when applying NP. The designed equipment is shown on right-hand side of Figure 5.5. Compared to a conventional neck collar system, the device dimensions are much smaller.

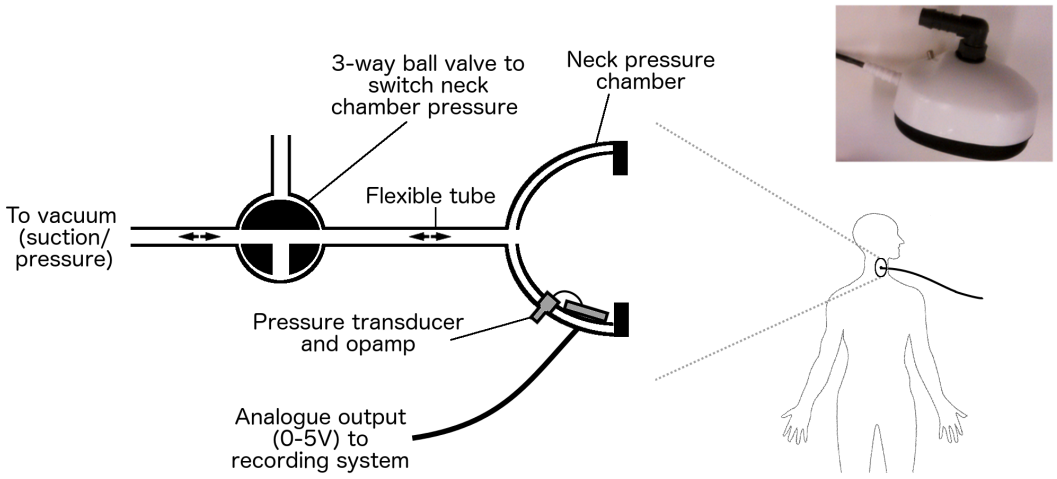

Figure 5.4: Schematic overview of the developed neck pressure chamber. The pressure inside the chamber was recorded using the analogue output. Top right: A photograph of the chamber cup.

5.2.1 Pilot study

Before conducting the experiments, a prototype of the device was tested on a healthy volunteer to ensure it was properly functioning. The baroreceptor was stimulated at a 0.1 Hz

Figure 5.5: Neck chamber devices: Left: conventional neck collar device that fully covers the neck. The size of the designed device (right) is substantially smaller and is essential for usage in the clinical environment.

rhythm by applying square wave stimulation patterns (5 seconds on, 5 seconds off) for a 2 min period. NS and NP were tested separately at relative pressure of -60 and +60 mmHg respectively. The ECG was recorded in synchronous with the neck chamber pressure. The ECG recordings were analysed offline to obtain heart periods. Heart period behaviour was analysed for NS and NP to evaluate the effect of stimulation. Figure 5.6 shows pressure and RR-interval (the interval between successive beats) values obtained during NP (panel A and C) and NS (panel B and D). The pressure values in Panel A and B are plotted superimposed and are aligned at stimulus onset (t = 0 s) and show a good degree of consistency across the repeated stimuli. Panel C and D show clear trends in the RR-interval following NS and NP. Similar to literature findings, the RR-interval was shortened following NP, and prolonged following NS by approximately 75 ms. Regarding the magnitude of the response, the reported magnitude in literature shows some variability. In [93] an average response of 200 ms was found in 8 subjects using a very similar device for a stimulus of $\pm$ 40 mmHg, but during bilateral stimulation, which is known to evoke a stronger response [91]. Although responses are subject dependent, it may have happened that the neck chamber did not fully covered the locus of the carotid sinus.

Despite the low magnitude of the response compared to literature findings, the results of this test suggest that the device is capable to stimulate the carotid baroreceptors and thus to affect the autonomic nerve outflow to the heart in this subject.

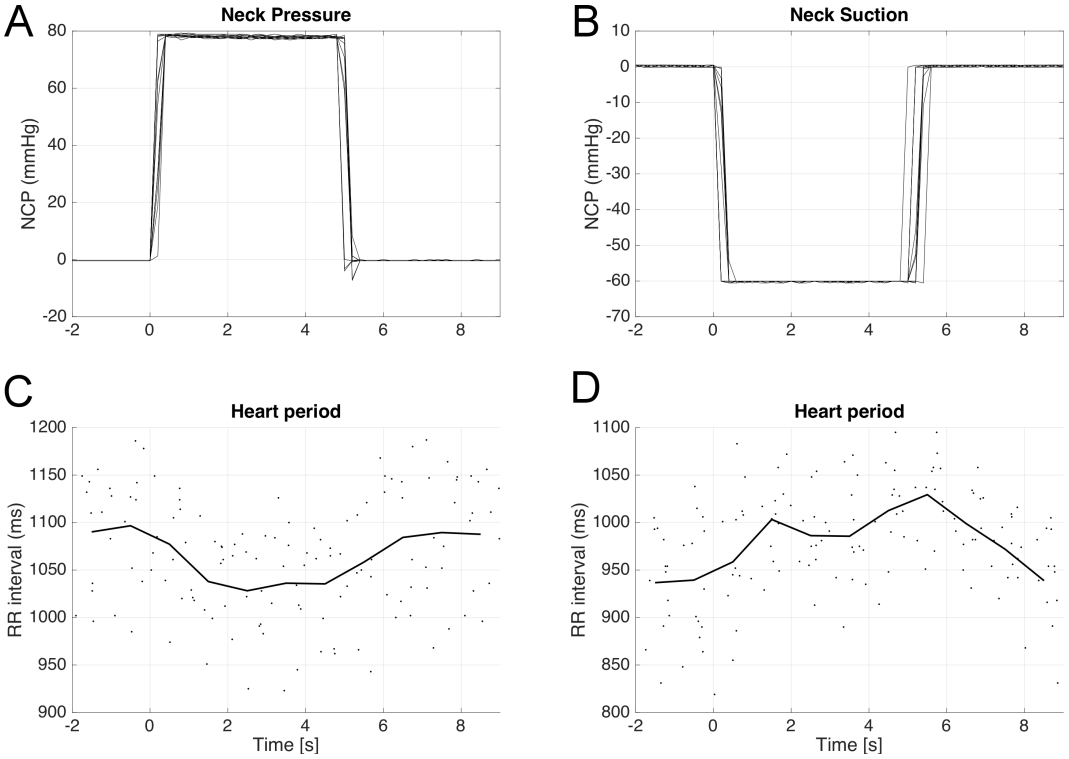

Figure 5.6: All RR interval responses of a healthy volunteer to 2-min applications of 60mmHg neck suction (NS) and neck pressure (NP) for 5 seconds (NP in this pilot study was approx. 75 mmHg; in the subsequent study it was controlled to 60 mmHg). Panel A and B show the super imposed pressure curves for NP (A) and NS (B). Pressure curves were aligned at stimulus onset (t = 0 s). Panel C and D show each heart beat interval plotted as a function of the interval between the stimulus onset and termination (t = 5 s). The trend of both responses is clear: the beat-to-beat interval is shortened during NP and prolonged during NS by approximately 75 ms.

5.3 Methods

The physiological studies to investigate the effect of carotid stimulation on ventricular APD were conducted in the cardiac catheterisation suite at the Barts Heart Centre, London. All subjects were in the unsedated state after the routine treatment for supra-ventricular tachycardias and had normal ventricular function and were otherwise apparently healthy. Since the data collection was incorporated into the clinical procedures, invasive electrogram recordings could be made without exposing the patient to any additional risk.

Ethical approval for the study was granted by the Bart's Hospital Ethics Committee and conformed to the standards set by the declaration of Helsinki (latest revision: 59th WMA General Assembly). Informed consent was obtained in writing from all the subjects.

The study was designed to investigate the effect of baroreceptor stimulation during

pacing and normal sinus rhythm: Pacing at a fixed cycle length allowed investigation of the effect on APD independently of heart rate variation, whereas sinus rhythm allowed quantification of heart rate changes to evaluate the efficacy of the stimuli using standard indexes of baroreceptor function reported in literature.

5.3.1 Baroreceptor stimuli

To reduce the risk of potential adverse effects of cerebral blood pressure changes, the experiment was limited to unilateral stimulation of the left carotid sinus. Stimulation of the left side was considered more interesting than the right side for the following reasons:

- Left-sided carotid baroreceptors are responsible to a greater degree for inotropic reaction, which strongly depends on the calcium regulation of the myocytes. Increased influx of Ca^{2+} enhances the contractile force of the myocytes, but also affects phase 2 of the APD (see Figure 2.5 on page 37). In contrast, stimulation of the right side has shown to be more chronotropic, which is regulated by cells in the SA and AV-node, and not the ventricle [91, 92].

- Work performed in the previous chapter showed that the amplitude of respiratory-related oscillations of ARI were significantly reduced following β-blocker in the left ventricle but not the right, which may suggests that the effects of sympathetic stimulation is more apparent in the left ventricle.

To stimulate the carotid baroreceptor, the designed enclosed neck capsule was placed carefully in position to cover the anatomical area expected to surround the left carotid sinus. NS and NP were produced by opening the three-way valve similar to that shown in Figure5.4, causing an abrupt change of the neck chamber pressure from atmospheric pressure to either -60 mmHg sub-atmospheric (NS) or +60 mmHg super-atmospheric (NP) pressure. Periodic NS/NP was generated by opening the valve fully for a period of 5 seconds, then shutting fully for 5 seconds causing a square pressure pattern. Stimulation was not synchronised with breathing or the cardiac cycle.

5.3.2 Measurements

Synchronous measurements were made of the UEG, ECG, femoral arterial blood pressure, and the pressure in the capsule: the neck chamber pressure (NCP). UEGs were measured using two decapolar electrode catheters (St Jude Medical, St. Paul, MN; 4F/5F Livewire Steerable Catheter with 2-5-2 mm spacing, 35 mm total span). One electrode catheter was

introduced from the femoral vein into the coronary sinus and positioned on the anterior to the epicardial wall in the apex-base orientation. Measurements were taken from the four most distal electrodes of this electrode, from which it could be stated with certainty that they were located at the left ventricle. The other electrode catheter was introduced into the right ventricle and positioned on the anterior septal wall in a base-apex orientation. All recording electrodes were referenced to the Wilson central terminal.

Data analysis Data was sampled at 2 kHz using a Bard EP Lab System (Bard Inc., Lowell, MA, USA). Ventricular APDs at each recording site were estimated from the UEG by measuring ARIs using the developed algorithm, described in Chapter 3. Arterial blood pressure recordings were analysed for systolic blood pressures (SBP) to assess haemodynamic responses. To establish evenly sampled series, any beats for which ARI or SBP measurement could not be determined were replaced by cubic-spline interpolation.

ARI and SBP behaviour during NS and NP was investigated using a time and a spectral method: The time method involves construction of the average response pattern to stimulation, whereas the spectral method was used to quantify and compare the spectral content at the 0.1 Hz stimulation frequency. Ectopic and spurious activity were removed and replaced by cubic interpolation. Signals were rejected if surrogate beats constituted more than 10% of the series. Both methods are described in more detail below.

Characterisation of ARI and blood pressure response patterns The purpose of applying pattern analysis is to characterise the ARI and SBP responses to NS and NP. This was achieved by obtaining a graphical portrayal of the pattern of ARI and SBP changes in the 5 seconds period immediately following the stimulus onset. Compared to the spectral method, an important advantage of this method is that it allows detailed investigation of the temporal behaviour of ARI and SBP in response to the stimulus. In addition to providing amplitude information, pattern analysis also characterises possible non-linearities and circumvents the assumption that the changes are sinusoidal.

Response patterns were generated for the left and right ventricle by computing the average ARI from the available recordings sites. The process is described in Figure5.7: panel A shows simulated ARI series during 0.1 Hz application of NS (panel B). The figure in Panel C shows all ARI values plotted as dots and sorted with respect to the timing of

the stimuli. To determine the trend, a pattern was generated using a 3rd order polynomial function based on the least-square error between model and data points.

A surrogate data method was then developed and implemented to investigate the significance of this pattern. As shown in Figure 5.6D, random ARI series were obtained by computing the pattern after randomly reshuffling the ARI values. This process was repeated 5000 times to obtain 5000 surrogate patterns. From the corresponding pattern distribution, the upper and lower 5th percentile were used to determine the significance threshold as a function of time. Figure5.6F shows the corresponding thresholds of the surrogate distribution computed at t=1 s and t=4 s after the stimulus onset. Finally, the thresholds were used to investigate the significance of the pattern obtained from the real data. A trend was considered significant if it exceeded this threshold. For the particular example of Figure5.6, it is shown in panel E that the measured response is significantly difference from the noise band from 1-5 seconds after the stimulus onset.

Spectral response quantification The same spectral method as used in Section 4.2.2.1 to measure the amplitude of respiratory oscillations was applied in this study to determine the amplitude of ARI and SBP data in the 0.1 Hz($\pm$ 10%) frequency band. The significance of the amplitude was determined using spectral surrogate data analysis, similar to what has been described in Section 3.2.5). The upper 95th percentile of the distribution was taken as $P<0.05$ significance threshold based on $N = 500$ surrogates. The amplitude and the number of electrodes exhibiting significant ARI oscillations were compared between control, NS and NP.

5.3.3 Experimental protocol

As mentioned previously, carotid baroreceptor stimulation was carried out during ventricular pacing and sinus rhythm. Pacing was established using a Biotronik (Berlin, Germany) model UHS 3000 stimulator, at the right ventricular apex using the two most distal electrodes of the decapolar recording catheter at a pulse width of 2 ms and stimulus strength of 2 diastolic threshold at a minimum cycle length sufficient to maintain capture (median 600 ms). Since APD depends on the cycle length and needs to adapt when commencing ventricular pacing at a fixed rate, an adaptation period of approximately 2 minutes [94] was implemented. Carotid stimulation was first applied during clamped heart rate. A two-minute control period was applied in absence of any carotid stimulation to obtain the neces-

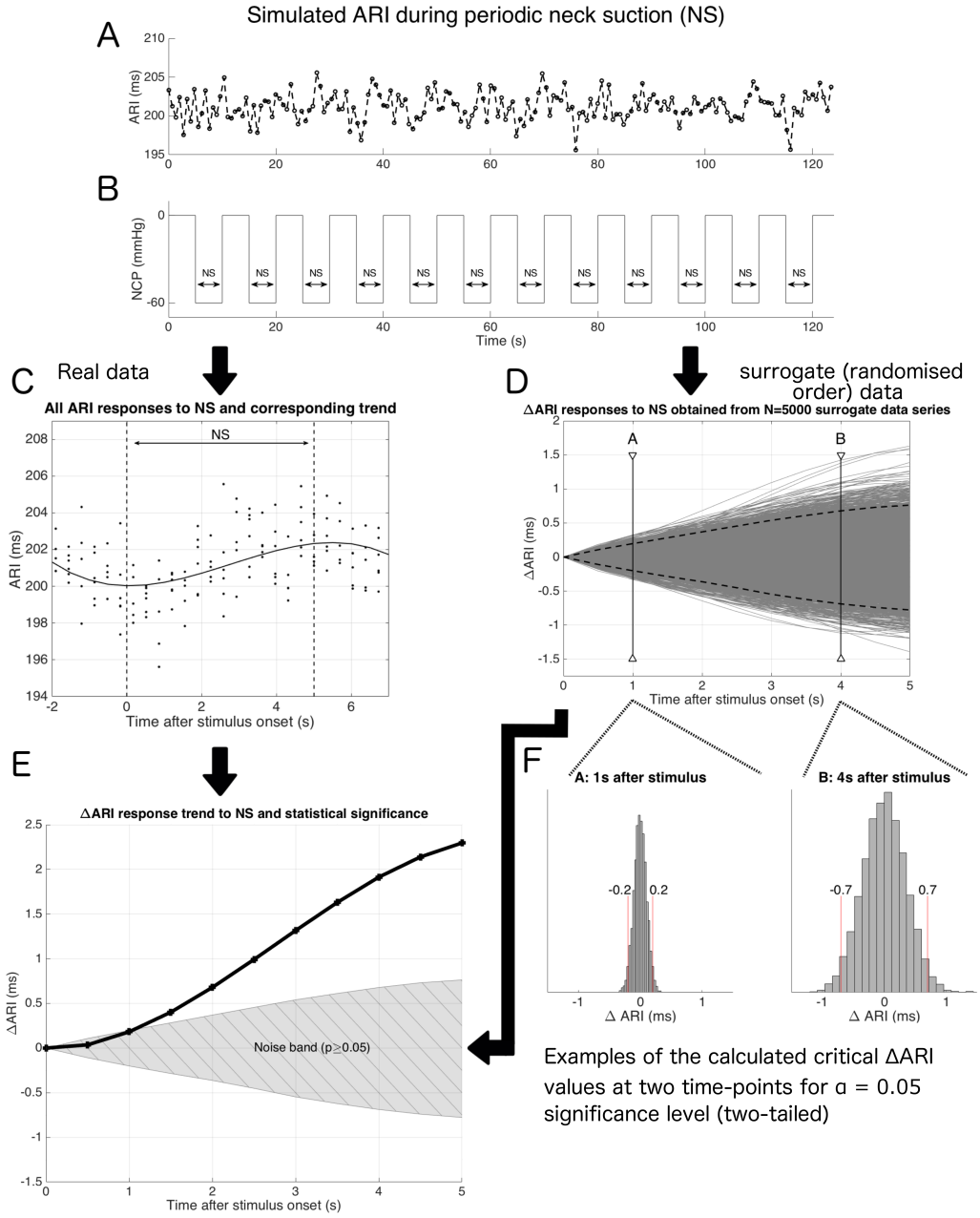

Figure 5.7: Illustration of the used method to determine a signal trends to neck suction (NS) or neck pressure (NP) and to assess their significance based on surrogate data analysis. In this example, the response of simulated ARI data to NS is considered. Panel E: The measured response shows a statistically significantly difference from the noise band from 1-5 seconds. NCP = neck chamber pressure.

sary baseline information to compare against. For the experiment, it was important to keep the pacing frequency constant to avoid inducing APD changes due by changing the cycle length. An additional one-minute control period was implemented between NS and NP to change in apparatus configuration from pressure to suction. After NP stimulation was finished, pacing was turned off and the experimental protocol was repeated during sinus rhythm, starting again with a 2-minute control period. However, the NP period was now applied before NS. This reversal was partly to counter for order-effects in the experiment and partly a practical consideration to avoid a change in apparatus configuration. The time-line of study protocol is presented in Figure5.8.

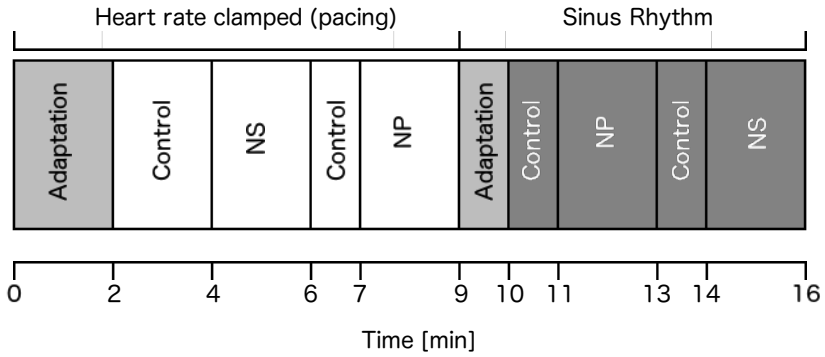

Figure 5.8: Time line of the study protocol. NS = Neck Suction, NP = Neck Pressure.

5.4 Results

Patients were able to wear the pressure cuffs in supine position on the lab table of the catherisation laboratory, which would not have been feasible with the available equipment of a whole-neck-collar (Figure 5.5). The process of applying the equipment on patients was easy and did not cause any discomfort and it took generally less than one minute to apply. The output of the pressure transducer in the neck chamber was checked for every experiment and the pressure transducer was found to be reliable for detecting the required gauge pressures of -60 (NS) and +60 mmHg (NP). The calibration graph of the pressure sensor is given in Appendix B.

The feasibility of the presented method to activate the autonomic nervous system to modulate ARI was investigated in 7 subjects. Neck chamber pressure recordings were available in 5 patients. The effect of carotid stimulation in the two remaining patients was assessed using the spectral method only, as this technique does not need temporal align-

ment of ARI and SBP signals with baroreceptor stimuli. Control data was rejected for one patient, because surrogate beats constituted more than 10% of the total beats. Remaining NS and NP data was analysed using the pattern method only, as this method only uses the surrogate method to compare against.

5.4.1 ARI and blood pressure response patterns

Construction of the example response patterns obtained from one patient is illustrated in Figure 5.9. In this figure the changes in ARI and SBP following the application of neck suction are shown, aligning each period so that onset of suction is at t=0s. The resultant superimposed pattern was obtained by computing the polynomial function of the collective values. The ARI response patterns are shown in Figure 5.9A and B for the left and right ventricle respectively. Both patterns show a clear trend of prolongation, especially for left ventricular ARI with an increase of 2 ms. The SBP response shows a clear reduction of 6 mmHg as shown in Figure 5.9C.

The significance of the response patterns of NS and NP for the patient shown in Figure 5.9 is assessed in Figure 5.10. Panel A shows the ARI patterns for NS obtained from the left ventricle (triangles) and right ventricle (squares). The dashed lines represent the significance thresholds derived from the surrogate data analysis. Response patterns obtained for NS were found to exceed this threshold for both left and right ventricular ARI. Also the trend in SBP (panel C) was found to clearly exceed the significance threshold. In contrast, the changes in ARI and SBP during NP remained within the noise thresholds, indicating that the changes of the real data were not statically different from the changes generated by the surrogate data.

Table5.1 shows the results of patterns analysis for each patients. Responses were quantified for their maximum amplitude and significance. Significant changes for ARI and SBP were found in 1 subjects during NS. Note that the maximum response in RV ARI and SBP subject 3 during NP were large, but not significant.

5.4.2 Spectral analysis of 0.1 Hz variability

The results of the spectral method are presented in Table 5.2. Except for first subject, all subjects showed already significant ARI variability at the 0.1 Hz frequency during the control period at multiple recording sides. The mean maximum peak-to-peak amplitude

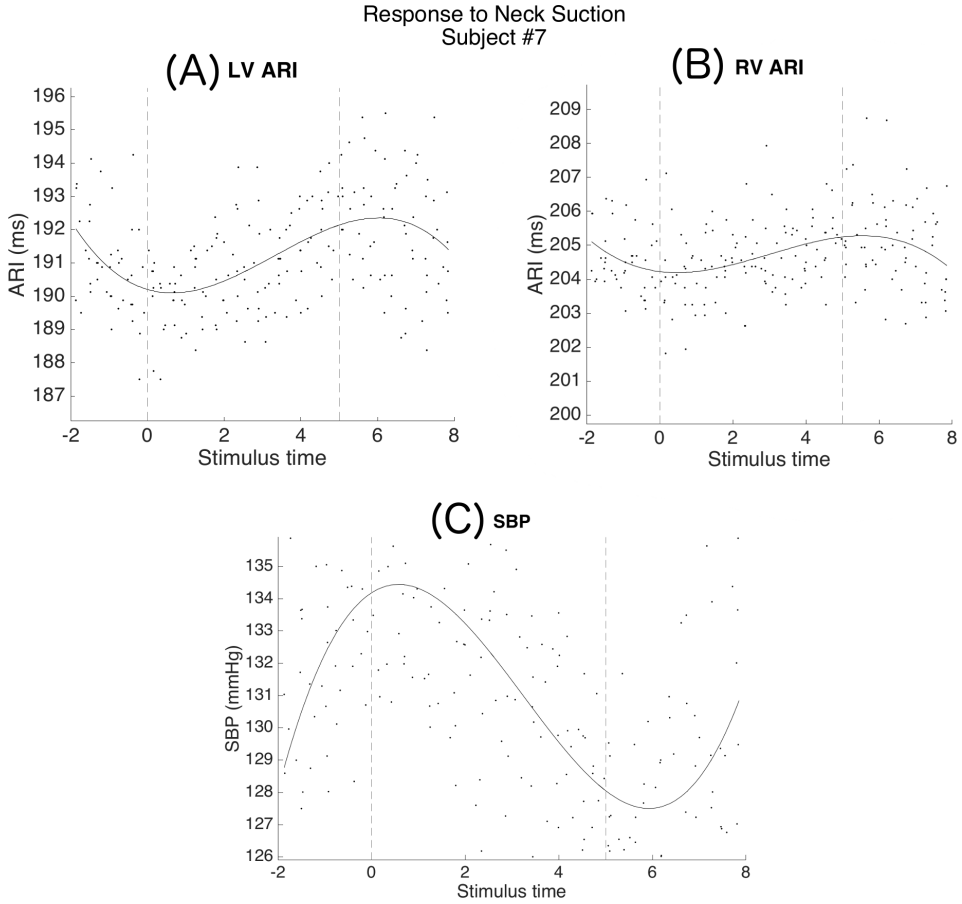

Figure 5.9: Example data showing activation recovery interval (ARI, panel A & B) and systolic blood pressure (SBP, panel C) patterns in response to 0.1-Hz neck suction (NS) for one subject. From the average ARI time series, each ARI value was plotted as function of the stimulation period with t=0 s the onset of the 5 second stimulation period. The resultant superimposed pattern was obtained by computing the polynomial function of the collective values based on the least-square error method. The SBP pattern was extracted in a similar fashion.

Maximum response in ARI (ms) and SBP (% of mean SBP)to NS and NP

	NS			NP		
Subject	LV ARI	RV ARI	SBP	LV ARI	RV ARI	SBP
2	0.1	0.1	0	-0.4	-0.6	-3
3	- -	- -	- -	0.2	1.9	-10
4	-0.2	0.1	-2	0.3	-0.3	3
5	0.3	0.1	- -	-0.1	-0.1	- -
7	**1.0***	**2.0***	**-6***	0.2	0.2	-1
AVG	0.3	0.6	-3	0	0.2	-3

Table 5.1: Average responses in ARI (ms) and SBP (mmHg) to 5 s applications of NS and NP. Significant response trends ($p < 0.05$) are indicated by *. No significant results were responses were found for NP.

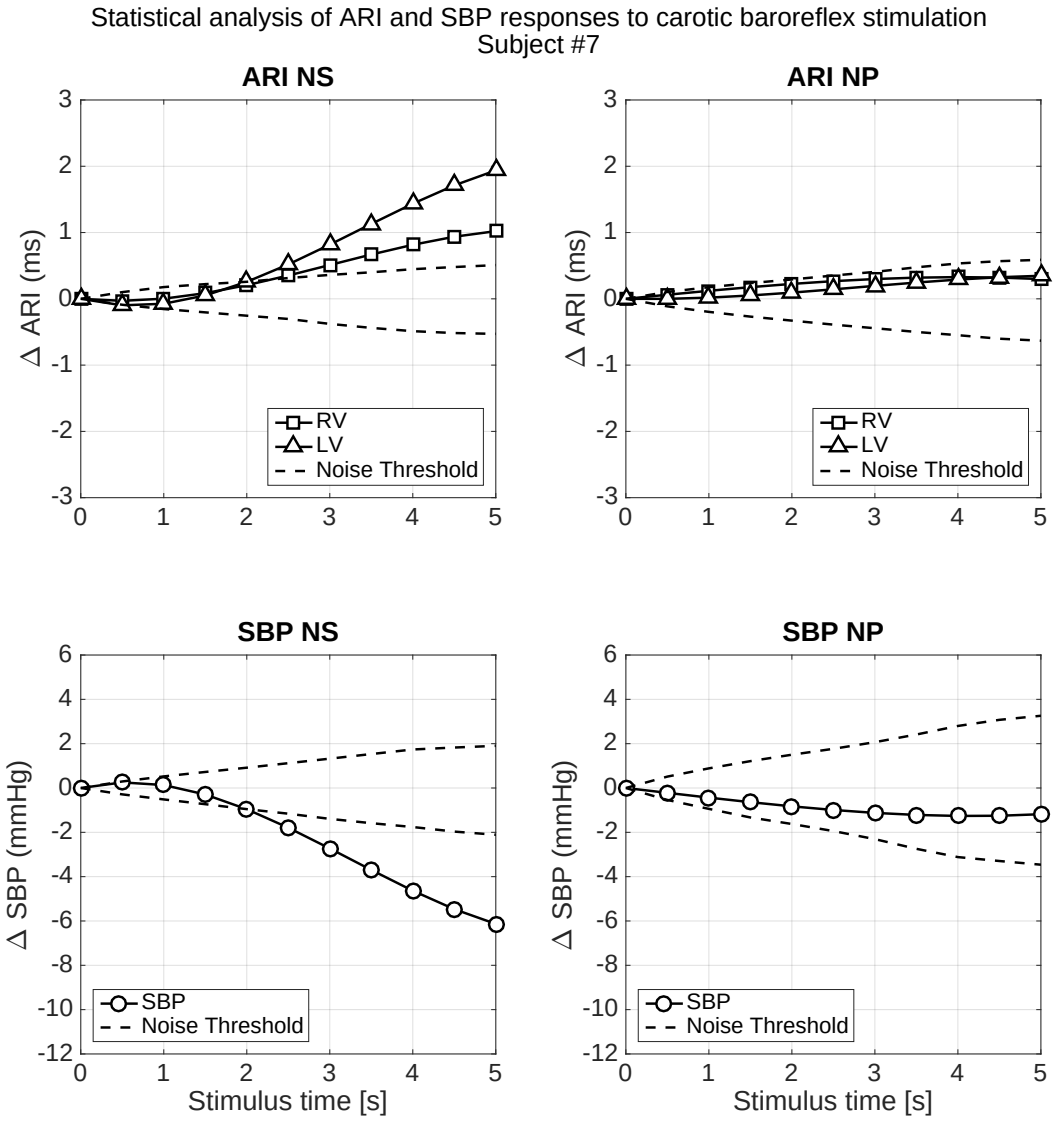

Figure 5.10: Statistical assessment of activation recovery interval (ARI) and systolic blood pressure (SBP) trends following carotid baroreceptor stimulation in subject 7. Trends in left and right ventricular (LV,RV) ARI, and SBP exceeded the noise threshold for neck suction (NS), but not for neck pressure (NP). The results therefore suggest that ARI and SBP in this subject were influenced by NS, but not NP.

during control was 4.8 ± ms). For both NS the maximum peak-to-peak amplitude showed a trend do decrease compared to baseline: from 4.8 ± 3.7 ms to 2.6 ± 1.5 ms and 2.7 ± 1.7 ms, respectively. For SBP, no clear differences in peak-to-peak amplitude were observed between control, NS and NP.

Oscillatory behaviour of ARI and SBP at 0.1Hz

Subject	# of electrodes rejected	# of electrodes with significant oscillations			Peak-to-peak amplitude of largest ARI oscillation (ms)			Amplitude of SBP oscillation (mmHg)		
		C	NS	NP	C	NS	NP	C	NS	NP
1	2	0	0	-	1.2	0.8	-	0	0	-
2	2	5	3	4	4.5	1.1	2.0	2	1	1
3	-	-	-	-	-	-	-	-	-	-
4	5	8	6	10	10.9	4.1	4.8	4	4	5
5	3	4	2	0	2.8	2.9	0.8	-	-	-
6	7	6	5	4	7.7	4.5	4.7	2	2	2
7	0	9	10	9	2.2	2.4	1.4	2	2	3
AVG		5.3	4.3	5.4	4.8	2.6	2.7	2	2	3

Table 5.2: Analysis of the maximum peak-to-peak amplitude and significance of 0.1 Hz oscillations in activation recovery interval (ARI) and systolic blood pressure (SBP) during control (C), neck suction (NS) and neck pressure (NP). Subject 3 was omitted from analysis due to due too excessive ectopic beats ($> 10\%$) during control.Significant variability at the 0.1 Hz frequency was already observed during control. The maximum peak-to-peak amplitude for ARI oscillations seem to be reduced during NS and NP compared to control.

5.4.3 Baroreceptor stimulation during sinus rhythm

Responses in heart-beat interval to NS and NP were available for three of the five subjects for which NCP recordings were available (# 2, 3, and 4). None exceed the significant threshold. As shown previously in Table 5.1, the ARI trends of these particular subjects did not vary significantly during ventricular pacing either.

5.5 Discussion

The aim of this chapter was to demonstrate that rhythmic activation of the ANS causes rhythmic modulation of the APD. The designed equipment allowed periodic stimulation of the carotid baroreceptors at 0.1 Hz and was able to provide physiological evidence that ARI underwent periodic changes during periodic application of NS. The existence of such baroreflex related modulation of ventricular electrophysiology, independent of heart rate, is

a novel observation. The statistical significance of ARI and SBP changes were investigated using a surrogate data method that was specifically designed for this project.

The equipment and signal processing tools used in this study allowed more detailed investigations of the inter-relationship between the carotid baroreflex and ventricular APD. The size of the neck chamber device was substantially smaller than traditional neck chamber arrangements and is essential for usage in the clinical environment where the patient is in supine position with limited abilities to change position. Despite the minimal dimensions, this study shows that it still allowed meaningful interpretation of the indexes of baroreceptor control.

To optimally transfer NS and NP to the carotid baroreceptors, it is essential that the device is put as close as possible to the baroreceptors [95]. Insignificant modulation of ARI might be related to suboptimal positioning, as these subjects did not show any changes in heart rate when NS and NP were applied during sinus rhythm. Apart from this, the lack of heart rate response might also be explained by functional asymmetry in carotid reflexes. For example, Tafil-Klawe showed that The maximal response of the RR interval (heart beat interval) was significantly greater during right sided than during left sided stimulation [91].

To ensure that neck chambers are placed in the correct position, each carotid artery can be first palpated and the overlying skin marked, as performed by Raine [93].

Another observation was that the subject showing significant ARI changes during NS, did not show any significant variability during NP. This might be explained by the difference in methods to apply NS and NP. In contrast to NS, NP is transferred to the skin using a latex membrane that is pushed against the skin. Because the membrane is elastic and the distance to the skin minimal, it was assumed that the pressure needed to shift the membrane is negligible during stimulation. A potential problem of this design is that the stimulation of the surrounded skin may be less homogeneous compared to NS. As a result, the pressure is not transmitted directly to the carotid sinus. Raine used a similar technique for applying NP, demonstrated the the method was useful for studying baroreceptor control on heart rate and blood pressure [93]. Because the pressure cups of the device are relatively small, it is recommended for future studies to remove the membrane and keep the capsules in place manually when applying NP in order to obtain a homogeneous distribution of the applied pressure.

5.5.1 Methodological considerations

In this work, two methods were used to quantify the ARI and SBP behaviour during NS and NP: the first method characterises the changes in ARI and blood pressure by computing the response pattern, whereas the second method applies spectral analysis to quantify the variability at the stimulation frequency (0.1 Hz). Importantly, in this study the spectral method failed to observe modulation of ARI related to NS. Compared to the pattern analysis method, an important difference is that pattern analysis allows ARI and SBP changes to be tracked as a function of NS and NP. This allows more detailed assessment of the temporal relationship. For example, the spectral method does not take into account the phase relationship with the chamber pressure signal and any 0.1 Hz oscillations.

Statistical significance was tested by means of a surrogate data approach. A major advantage of this method is that it allows construction of a significance threshold based on the intrinsic features of the signals [75]. This allows to reduce the likelihood of attributing a significant amplitude. For example, as shown in Table 5.1, the change in SBP of subject 3 is relatively large, but not significant. Apparently, this signal already contains a high level of variability by itself (an intrinsic feature). This causes the significance threshold of this signals to be higher than other signals. This example clearly indicates the important advantage of the surrogate method to determine the significance threshold, as a fixed threshold for all subjects might have resulted in a wrong interpretation of the data.

Two related questions to this topic are: (1) were the ARI and SBP responses indeed caused by stimulation of the carotid baroreflex, or is some other effect responsible? and (2) do changes in the measured ARI represent changes in electrophysiology?

5.5.2 Are the ARI and SBP responses caused by baroreceptor stimulation?

Figure 5.9 shows that the ARI changes during NS are synchronised with the stimuli, which strongly suggest that the observed ARI behaviour was induced by NS. Theoretically, it is possible that spontaneous Mayer waves co-occurred during NS, but this highly unlikely as this would require Mayer waves to be exactly synchronised with the stimuli.

Another possible confounding factor may be respiration. Although it is unlikely that the subject was breathing at 0.1 Hz throughout the 2-min stimulation period, the subject could have unconsciously adapted breathing behaviour to NS stimuli. For example, NS

might have induced (unconsciously) a brief breath-pause during the onset of each stimulus as a response to the (unfamiliar) force of the neck suction. As discussed in the previous chapter, respiratory behaviour may induce ARI changes via different pathways, including artefacts. Due to limitations of the clinical environment, it was not possible to recording of respiratory behaviour in this study, however, the spectral analysis of ARI and BP measurements revealed clear oscillations around 0.25 Hz in ARI and SBP suggesting that breathing was not disturbed during NS. In addition, the ARI and SBP measurements in Figure 5.9 show a gradual increase until the end of the 5-s stimulation period, whereas a short breath hold would have been more likely to have introduced a short and not a gradual response. Consequently, this potential caveat can not be fully excluded with confidence, but does not seem to be fully compatible with the observations either. The results therefore suggest that that ARI and SBP were indeed modulated by NS in this subject. Further studies are needed to validate this finding, but this is beyond the scope of this PhD research.

5.5.3 Do changes in the measured ARI represent changes in electrophysiology?

The scrutiny which was applied in the previous chapter regarding the physiological meaning of ARI measurements, one should critically analyse whether these changes in measured ARI values during NS can be truthfully interpreted as changes in APD, or whether some other process changed the electrogram waveform morphology. In the previous chapter, differences were found in how the UEG waveforms changed during low-frequency breathing and mental stress. Figure 5.11 expands this analysis by compares both UEG waveforms(top: 0.1 Hz respiration, middle: mental stress) with the UEG waveforms observed during NS in subject 7 of this study (bottom). The black traces represent the UEG waveforms recorded during the maximum ARI of a low-frequency oscillation and the grey traces show the waveform during the minimum ARI within the same modulation cycle. In this example, the variations in local activation times were more substantial than recovery for respiration, whereas mental stress (Mayer waves) and baroreceptor stimulation were associated with variations in recovery times. This suggest that the changes in APD are caused by direct modulation of local repolarisation rather than remote changes in conduction velocity, similar to APD changes observed during mental stress, which are assumed to be coupled to Mayer waves. The UEG waveforms obtained during this study therefore seem to confirm that ARI changes indeed reflect changes in repolarisation.

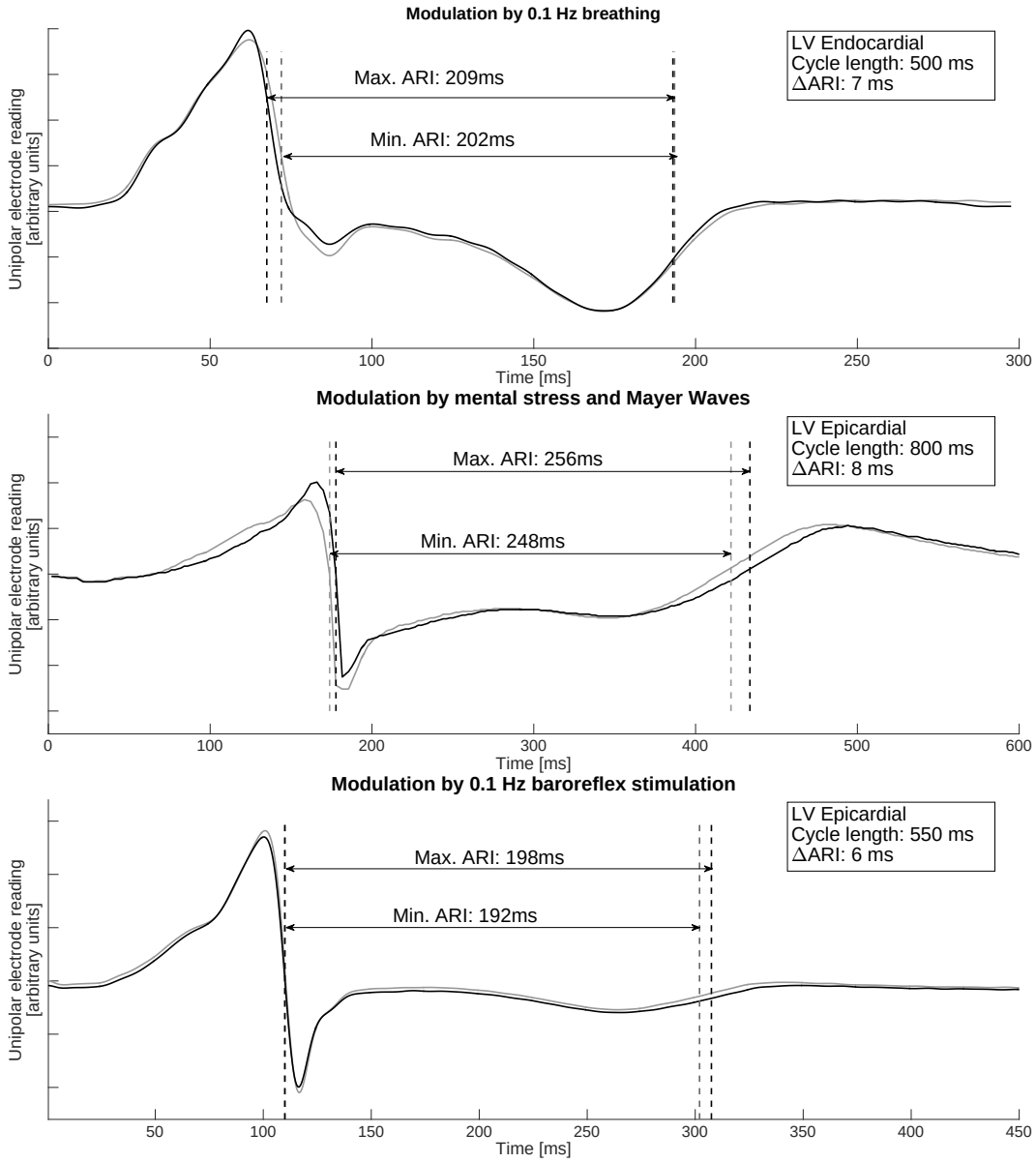

Figure 5.11: Example plots showing unipolar electrogram (UEG) morphologies recorded in the left ventricle (LV) during low-frequency modulation of ARI. Each panel shows two single beat UEG traces, the black waveform corresponds to the maximum ARI value and the gray waveform corresponds to the minimum ARI value within one low-frequency modulation cycle. Low-frequency modulation was related to 0.1 Hz breathing (top panel), mental stress (middle panel) and baroreceptor stimulation (lower panel). Each waveform pair was aligned based on the pacing artefact. The vertical lines in each graph represent the measured times of local activation and recovery. The traces suggest that low frequency ARI modulation may occur via different mechanisms. For respiration, ARI modulation was associated the timing of local activation, whereas mental stress and baroreceptor stimulation were found to be more related to modulation of local recovery in this example.

5.5.4 Underlying mechanisms & implications for cardiac stability

It is well known that spatial and temporal heterogeneities in APD may facilitate arrhytmogenesis [5–8]. A shown in Figure 5.10, the ARI changes during NS were slightly larger in the left ventricle, which may indicate an increase of regional differences in repolarisation. Although the differences were small, it could still reflect a possible mechanism of how ANS activity can increase the heterogeneity in repolarisation between the left and right ventricle and possibly promote pro-arrhythmic conditions. Further research will have to elucidate whether this effect was a result of unilateral application of NS. For example, Furlan and colleagues already reported different responses in heart rate to unilateral sinusoidal NS, which also suggests that ANS response to carotid baroreflex activation is lateralised [86]. This is important to know, because lateralised carotid baroreflex regulation may also occur under natural conditions. For example, unilateral atheroscleroses causes stiffness of one of the carotid arteries that may affect the stretch receptors of the carotid baroreflex (i.e. there are less able to stretch, hence providing less input). For an alternative explanation, one should realise that ARI from the right ventricle was measured from the endocardium (inner wall of the heart), while the left ventricular measurements were obtained from the epicardium (outer wall of the heart). It is well known that both regions can respond different to changes in ANS. For example, Finlay and colleagues showed that Mental stress induces significant changes between ARIs measured from the endo- and epicardium [96].

To summarise, the results in this study demonstrate that the application rhythmic baroreflex stimulation and ARI pattern analysis has potential to yield new insights into fundamental relationships between local cardiac electrophysiology and autonomic (baroreflex) regulation.

Chapter 6

Conclusions

6.1 Summary of achievements

The aim of this thesis was to provide more insight into the autonomic control mechanisms that exist to control and regulate the local electrical behaviour of the heart. The main reason to focus on the local electrical activity is that the risk of sudden cardiac death is strongly linked to the spatio-temporal patterns of local electrophysiological parameters. Since malfunctions of the autonomic control mechanisms are an important cause of death, it is important to understand the inter-relationship between both facets. To that end, this thesis presents novel extensions to improve existing methods for inferring nervous input to the heart using invasive measurements of cardiac electrical activity. These methods were used to analyse existing data and to design and conduct a new clinical experiment

The action potential duration (APD) is a fundamental property of the electrical behaviour of cardiac cells and is related to the strength and duration of their mechanical contraction. APDs of the cardiac tissue can be estimated by measuring activation and recovery intervals (ARIs) from intracardiac unipolar electrograms (UEGs). However, analysis of this data is challenging and involves identifying small changes in measured parameters in the presence of noise and uncertainty. In this work, new contributions have been made to improve the automatic detection of ARIs to enable the handling of large sets of experimental or simulated data. Such data sets are required in the experimental investigation of neural modulation of cardiac activity. The reliability of ARI measurements was improved in this work by using knowledge of the physiological variation of APD to create a template for typical behaviour and identifying variations from that pattern. This was integrated in an automated processing software suite, including graphical user interfaces, and incorporating

new algorithmic processes to extract ARI measurements from large volumes of physiological data.

Signal processing research in Chapter 3 presented results quantifying how the extraction of physiological measurements of cardiac electrical activity from the raw electrical waveform depend on signal quality and filter configuration. Many researchers have sought to refine the reliability and accuracy of these physiological measurements, but here for the first time a simulation study was carried out to investigate the effect of noise and filtering on the identification of activation and recovery times from unipolar electrograms (UEGs). In this study, special emphasis was put on the accuracy of measurements of dynamic ARI behaviour. To evaluate the accuracy of these measurements, a surrogate data hypothesis testing method was developed, which generates an ensemble of artificial surrogate ARI series that are both like the original ARI series, but do not exhibit any dynamic behaviour. If the real series were not significantly different from the surrogate series, then one may reject the hypothesis that the measured series exhibit dynamic behaviour. It was found that the two main algorithmic processes designed to improve the reliability of ARI estimations improved the detection of ARI dynamics from less than 45%, to 100% in recordings with low signal quality.

These novel tools and algorithms were used to investigate existing experimental data which had been acquired prior to this PhD project. The surrogate data hypothesis testing method was applied to determine the significance of the ARI oscillations and showed significant oscillations with respiration in all subjects. It was found that the amplitude of these oscillations was significantly reduced following pharmaceutical manipulation of neural activity, suggesting that sympathetic activity is involved in the modulation of ARI variability with respiration. While it could not be fully excluded that ARI oscillations are due to respiratory motion artefacts in the UEG, the pharmaceutical effects strongly suggest that the oscillations are at least in part reflect modulation of electrophysiology. The driving mechanisms of respiratory-related ARI oscillations were further investigated by studying the interrelationship between ARI, systolic blood pressure (SBP) and respiration using analytical techniques to measure coupling and causality. Results showed that ARI and systolic blood pressure (SBP) were all coupled at the respiratory frequency, but directed coherence measure pointed out that information flow was mainly from respiration to ARI, suggesting

that respiratory reflexes are involved in the genesis of ARI oscillations rather than a feedback mechanism that responds to blood pressure changes. The results were published in the American Journal of Physiology [70].

These recordings implemented a controlled-breathing protocol to ensure a fixed, known breathing frequency which increased the confidence of the results and allowed the use of classical frequency-domain techniques which assume steady-state oscillation. The situation of spontaneous breathing was also studied, however this required non-stationary time-frequency analysis to track non-stationary ARI behaviour related to spontaneous breathing. The smoothed-pseudo-Wigner-Ville distribution (SPWVD) was identified as the most reliable and precise time-frequency method. Computation of the time-frequency coherence showed that ARI was significantly coupled in time with respiration during natural breathing. This is a novel finding that strongly suggest that respiratory-related behaviour of APD and BP are driven by a common source during natural breathing. It also links normal respiratory related activity and repolarisation and could be a potential pathway that explains how disorders of respiratory behaviour or increased sensitivity of cardiac cells can lead to destabilisation of the repolarisation process which may have consequences in the context of arrhythmogenesis.

Low frequency oscillations of blood pressure at approximately 0.1 Hz is another autonomic rhythm known and related to the organisation of sympathetic nerve activity. Because APD is sensitive to autonomic modulation, it was hypothesised that low-frequency oscillations at approximately 0.1 Hz, termed Mayer waves, could also affect the behaviour of APD. Time-frequency coherence analysis demonstrated significant coupling of Mayer waves and low-frequency oscillations observed in ARI in data during mental stress, which suggests that ARI oscillations are driven by the same mechanisms as Mayer waves. However, a good control period was lacking in this study, which would have been useful to confirm whether Mayer waves were enhanced during mental stress. In the future, direct recordings of nerve activity would be useful to further investigate whether low-frequency oscillations are caused by direct autonomic modulation or by processes like mechanical electrical feedback. These results are published in [66].

Finally, a clinical experiment was designed and conducted to test whether the 0.1 Hz oscillations could be autonomically mediated. A device was designed for rhythmic 0.1 Hz

stimulation of the baroreceptors in an attempt to periodically modulate sympathetic outflow to the heart. Response curves were obtained and a surrogate data method was designed to assess their significance. Although a small number of patients was included, this thesis presents for the first time evidence of significant modulation for the stimulation method to reduce sympathetic activity.

6.2 Plans and suggestions for future work

The work described in this thesis might be extended in terms of further validation of the developed methods and experimental findings.

The group of Prof. Axel Bauer has focussed on non-invasive measurements of low-frequency oscillations of repolarisation. Based on the findings of the mental stress study presented in this thesis [66], they proposed a new non-invasive marker to track low-frequency repolarisation dynamics from the surface ECG. This marker, termed periodic repolarisation dynamics (PRD) was found to be a predictor of mortality in survivors of acute MI and patients undergoing exercise testing [97, 98].

Stimulation of the control mechanisms of the ANS is not limited to carotid baroreceptor stimulation. Alternatively, Leuenberger et al. showed the rhythmic handgrip exercise also resulted in rhythmic modulation of sympathetic activity, heart rate and blood pressure [99]. Implementation of the analytical tools developed in Chapter 5 combined with further techniques for autonomic stimulation might help to obtain a deeper understanding of the effect of ANS activity on localised cardiac activity.

Apart from investigating the influence of respiratory and low-frequency related effects on ventricular APD, the tools developed for UEG analysis can also enable future investigations on the influence of other autonomic manifestations. For example, perturbations in heart rate after a premature ventricular contraction are caused by an autonomic reflex as a result of the brief disturbance in the arterial blood pressure (low amplitude of the premature beat, high amplitude of the following normal beat). It is likely that this typical behaviour of ANS activity can also induce temporal and regional changes in cardiac activity. The magnitude of these perturbations has shown to be a strong predictor sudden cardiac death. It would therefore be of interest to investigate how these autonomic changes may increase the heart's vulnerability to arrhythmias. Tools developed in Chapter 5 to assess the significance of ARI changes could help to assess the significance of the observed behaviour.

Incorporated in the on-board software on clinical electrophysiology recording sys-

tems, the UEG processing tools offer the opportunity for live mapping of repolarisation dynamics which would be arguably more useful than purely activation mapping for identification of critical re-entry circuits. In addition, implementation of causality analysis and time-frequency coherence to examine the interactions between systolic blood pressure, respiration and ARI could reveal clinically relevant information, for example coupling and causality values may be used to monitor or detect abnormal autonomic functioning.

Appendix A

Causality and coupling in MVAR processes

The proposed multivariate autoregressive (MVAR) framework to measure causality is based on the definition of causality proposed by Granger [100]. According to Granger causality, if a signal Y_1 "Granger-causes" (or "G-causes") a signal Y_2, then past values of Y_1 should contain information that helps predict Y_2 above and beyond the information contained in past values of Y_2 alone.

Generalising to a multivariate approach, we can denote $Z_j = \{Y_l | l = 1,...,M, i \neq j\}$ as the set of the past values of all processes except y_j, then direct causality from y_j to y_i, $y_j \rightarrow y_i$, exists if the prediction of $y_i(n)$ based on Z_j and Y_j is better than the prediction of $y_i(n)$ solely based on Z_j. Causality from y_j to y_i, $y_j \Leftrightarrow y_i$ exists if a cascade of direct causality relations $y_j \rightarrow y_m ... \rightarrow y_i$ occurs for at least one value m in the set $(1,...,M)$.

$$\gamma_{ij}(f) = \frac{\sigma H_{ij}}{\sqrt{\sum_{m=1}^{M} \sigma^2 |H_{im}(f)|^2}} \tag{A.1}$$

The multivariate processes (Y) are represented as the output of a linear shift invariant filter:

$$Y(t) = \sum_{k=-\infty}^{\infty} H(k)U(t-k) \tag{A.2}$$

where U is a vector of M zero-mean input processes and H is the MxM filter matrix, also called transfer matrix. Notions of causality and coupling are formalised in the context of a MVAR representation. The MVAR model of the multivariate processes $(Y(t))$ is defined as:

$$Y(t) = \sum_{k=1}^{p} A(k)Y(t-k) + U(t) \tag{A.3}$$

where p is the model order, which represents the maximum lag used to quantify interactions. $A(k)$ contains the coefficients of the model, where the i, j element of $A(k)$, $a_{ij}(k)$, quantifies the causal linear interaction effect occurring at lag k from y_j to y_i. In other words, Y_2 G-causes Y_1 if the coefficient a_{12} is significantly different from zero. The coupling and causality relations are found in the off-diagonal elements of $A(k)$. $U(t)$ is the input process and assumed to be composed of white noise.

The spectral representation of a MVAR process is derived considering the FT of the representations A.2 and A.3, which yield $Y(f) = H(f)U(f)$ and $Y(f) = A(f)Y(f) + U(f)$. The transfer and coefficient matrix are defined in the frequency domain as:

$$H(f) = \sum_{k=-\infty}^{\infty} H(k)e^{-i2\pi fkT} \qquad \text{(A.4)} \qquad A(f) = \sum_{k=1}^{p} A(k)e^{-i2\pi fkT} \qquad \text{(A.5)}$$

From A.2 and A.3 it can been seen that the coefficient and transfer matrices are linked by: $H(f) = [I - A(f)]^{-1} = \bar{A}^{-1}$. The same is true when deriving the corresponding frequency domain estimates of coupling and causality. The cross spectral density matrix, which we will call S and P, are inverse related:

$$S(f) = H(f)\Sigma H^*(f), \;\; P(f) = \bar{A}^*(f)\Sigma^{-1}\bar{A}(f) \qquad \text{(A.6)}$$

In these expressions, the asterisk denotes the conjugate transpose, Σ is the covariance matrix of the residuals U and H is the transfer matrix. Because we assume U to be white noises means that the signals are uncorrelated even at lag zero, thus the covariance matrix reduces to the diagonal matrix $\Sigma = diag(\sigma^2)$, and its inverse $\Sigma^{-1} = diag\left(\frac{1}{\sigma^2}\right)$ which is diagonal as well with σ^2 as the variance. Under this assumption, we can write the cross spectrum as:

$$S_{ij}(f) = \sum_{m=1}^{M} \sigma_m^2 H_{im}(f)H_{im}^*(f), \;\; P_{ij}(f) = \sum_{m=1}^{M} \frac{1}{\sigma_m^2}\bar{A}_{mi}^*(f)\bar{A}_{mj}(f) \qquad \text{(A.7)}$$

This expression is particular useful because it allows us to decompose the frequency domain measures of coupling and direct coupling, which expresses the directional information from one process to another. Using the spectral expressions we can compute the coherence:

$$\Gamma_{ij}(f) = \frac{h_i(f)\Sigma h_j^*(f)}{\sqrt{h_i(f)\Sigma h_i^*(f)}\sqrt{h_j(f)\Sigma h_j^*(f)}} \tag{A.8}$$

Substituting A.7 in this expression results in:

$$\Gamma_{ij}(f) = \sum_{m=1}^{M} \frac{\sigma_m H_{im}}{\sqrt{S_{ii}}} \frac{\sigma_m H_{jm}^*}{\sqrt{S_{jj}}} = \sum_{m=1}^{M} \gamma_{im}(f)\gamma_{jm}^*(f) \tag{A.9}$$

The last term contains the so-called directed coherence (DC), in this particular case the coherence from y_j to y_i:

$$\gamma_{ij}(f) = \frac{\sigma H_{ij}}{\sqrt{\sum_{m=1}^{M} \sigma^2 |H_{im}(f)|^2}} \tag{A.10}$$

The squared DC $|\gamma_{ij}(f)|^2$ measures the normalised coupling strength, being 0 in the absence of directed coupling and 1 in the presence of full coupling. The coupling strength from y_j to y_i as the normalised proportion of $S_{ii}(f)$ which is due to y_j that is transferred from u_j via the transfer function $H_{ij}(f)$, located in the nominator of the equation.

Appendix B

Pressure Sensor Calibration

An EPCOS AK2 series pressure sensor was used to measure the neck chamber pressure. The output of the sensor was measured for pressures ranging from -70 to +70 mmHg (-9.3 +9.3 kPa) with respect to atmospheric pressure using a U-tube manometer. The voltage readings as function of the gauge pressure are plotted in Figure B.1.

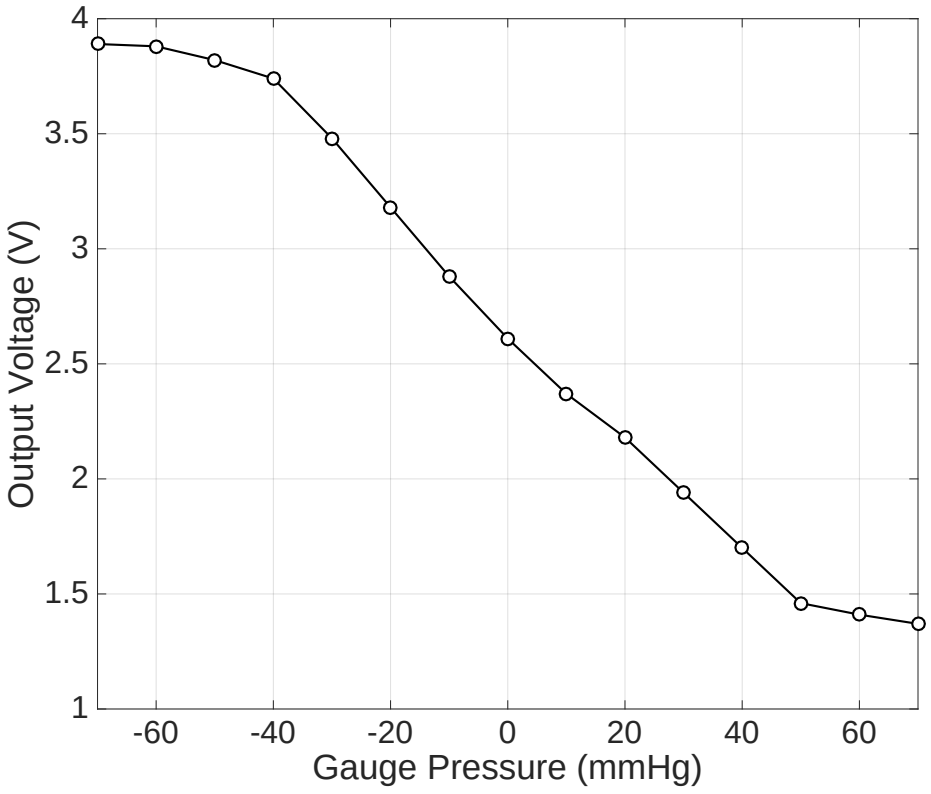

Figure B.1: Voltage output of the used EPCOS AK2 series pressure sensor for different gauge pressures.

Appendix C

Peer-Reviewed Journal Publications

Am J Physiol Heart Circ Physiol 309: H2108–H2117, 2015.
First published October 16, 2015; doi:10.1152/ajpheart.00560.2015.

Effect of autonomic blocking agents on the respiratory-related oscillations of ventricular action potential duration in humans

Stefan van Duijvenboden,[1] Ben Hanson,[1] Nick Child,[2] Michele Orini,[3] Christopher A. Rinaldi,[2] Jaswinder S. Gill,[2] and Peter Taggart[3]

[1]*Department of Mechanical Engineering, University College London, London, UK;* [2]*Department of Cardiology, Guy's and St. Thomas's Hospital, London, UK; and* [3]*Institute of Cardiovascular Science, University College London, London, UK*

Submitted 22 July 2015; accepted in final form 14 October 2015

van Duijvenboden S, Hanson B, Child N, Orini M, Rinaldi CA, Gill JS, Taggart P. Effect of autonomic blocking agents on the respiratory-related oscillations of ventricular action potential duration in humans. *Am J Physiol Heart Circ Physiol* 309: H2108–H2117, 2015. First published October 16, 2015; doi:10.1152/ajpheart.00560.2015.—Ventricular action potential duration (APD) is an important component of many physiological functions including arrhythmogenesis. APD oscillations have recently been reported in humans at the respiratory frequency. This study investigates the contribution of the autonomic nervous system to these oscillations. In 10 patients undergoing treatment for supraventricular arrhythmias, activation recovery intervals (ARI; a conventional surrogate for APD) were measured from multiple left and right ventricular (RV) endocardial sites, together with femoral artery pressure. Respiration was voluntarily regulated and heart rate clamped by RV pacing. Sympathetic and parasympathetic blockade was achieved using intravenous metoprolol and atropine, respectively. Metroprolol reduced the rate of pressure development (maximal change in pressure over time): 1,271 (± 646) vs. 930 (± 433) mmHg/s; $P < 0.01$. Systolic blood pressure (SBP) showed a trend to decrease after metoprolol, 133 (± 21) vs. 128 (± 25) mmHg; $P = 0.06$, and atropine infusion, 122 (± 26) mmHg; $P < 0.05$. ARI and SBP exhibited significant cyclical variations ($P < 0.05$) with respiration in all subjects with peak-to-peak amplitudes ranging between 0.7 and 17.0 mmHg and 1 and 16 ms, respectively. Infusion of metoprolol reduced the mean peak-to-peak amplitude [ARI, 6.2 (± 1.4) vs. 4.4 (± 1.0) ms, $P = 0.008$; SBP, 8.4 (± 1.6) vs. 6.2 (± 2.0) mmHg, $P = 0.002$]. The addition of atropine had no significant effect. ARI, SBP, and respiration showed significant coupling ($P < 0.05$) at the breathing frequency in all subjects. Directed coherence from respiration to ARI was high and reduced after metoprolol infusion [0.70 (± 0.17) vs. 0.50 (± 0.23); $P < 0.05$]. These results suggest a role of respiration in modulating the electrophysiology of ventricular myocardium in humans, which is partly, but not totally, mediated by β-adrenergic mechanisms.

respiration; cardiac electrophysiology; β-adrenergic blockade; parasympathetic blockade

NEW & NOTEWORTHY

Ventricular action potential repolarization is critical to electrical stability and arrhythmogenesis. Oscillations at the respiratory frequency were investigated in humans by combining endocardial electrophysiological recordings, controlled respiration with adrenergic blocking agents. Results are consistent with a partial role of the sympathetic nervous system combined with additional mechanisms, possibly involving mechano-electric feedback.

Address for reprint requests and other correspondence: P. Taggart, Institute of Cardiovascular Science, Univ. College London, Paul O'Gorman Bldg., 72 Huntley St., London WC1E 6BT, UK (e-mail: p.taggart@ucl.ac.uk).

DYNAMIC CHANGES IN ACTION potential duration (APD) are a critical component of many fundamental electrophysiological properties. Alterations of the normal time course of APD are a key factor in arrhythmogenesis (25, 34, 51, 54). Elucidation of the multiple mechanisms that underlie modulation of ventricular repolarization is, therefore, an important challenge. Ventricular APD has recently been observed to exhibit oscillations related to respiration in humans with healthy ventricles (18, 19). The mechanism is as yet undetermined.

Several considerations suggest the possibility of a role of the autonomic nervous system in respiratory-related ventricular APD oscillations. Heart rate is well known to exhibit cyclical variation with the respiratory cycle, known as respiratory sinus arrhythmia, usually attributed to waxing and waning of autonomic input to the sinus node (1, 2, 4, 9, 31). Ventricular myocardium is now known to receive substantial vagal as well as sympathetic innervation (7), raising the possibility of cyclical autonomic influence in the ventricle. Both sympathetic and vagal stimulation may modulate ventricular APD (30, 32, 35, 43, 50, 55). Respiration is known to gate the timing of autonomic motor neurone firing such that inspiration is associated with an increase in sympathetic and decrease in parasympathetic nerve activity (8, 16, 28), again suggesting the possibility of respiratory-related autonomic modulation of ventricular APD. In the present study, therefore, we sought to examine the contribution of autonomic nervous system to respiratory-related ventricular APD oscillations in humans in vivo.

We have collected a unique database including activation recovery intervals (ARIs) measured from unipolar electrograms as a conventional surrogate for ventricular APD (5, 21, 33, 40, 53) from multiple right and left ventricular endocardial sites, femoral arterial blood pressure, and respiration (chest movement), in humans with healthy ventricles. Respiratory rate was controlled and heart rate clamped by ventricular pacing to avoid confounding effects due to the cycle length dependency of APD. Autonomic blocking agents were administered intravenously to selectively study the contribution of sympathetic and parasympathetic modulation of respiratory-related oscillations of APD. We hypothesized that autonomic blocking agents would reduce the amplitude of the oscillations if autonomic input is indeed involved. To further investigate the mechanisms underlying respiratory-related APD oscillations, multivariate frequency domain analysis was used to characterize the causal interactions between APD, respiration, and blood pressure. In addition, phase analysis was implemented to investigate the oscillatory behavior of APD in the left and right ventricle.

  ISSN 0363-6135.

METHODS

Ethical approval. The study was approved by the ethics committee of Guy's and Thomas′ Hospitals and conformed to the standards set by the Declaration of Helsinki (latest revision: 59th World Medical Association General Assembly). All patients gave written, informed consent.

Subjects. Studies were performed in 10 patients (8 males, 2 females, aged 48–68, median 54) during the course of routine clinical radiofrequency ablation procedures for atrial fibrillation. Four patients had paroxysmal atrial fibrillation, and six patients established atrial fibrillation. All patients had normal ventricular function and were otherwise apparently healthy. No subject was known to have ventricular scar or disordered conduction due to bundle branch abnormality. The studies were conducted in the cardiac catheterization suite at St Thomas′ Hospital before the routine clinical procedure in the unsedated state as described previously (20, 45). Cardio-active medications were discontinued for 5 days before the study.

Measurements. Synchronous measurements were made of the unipolar electrogram (UEG), femoral arterial blood pressure, and respiration (chest movement).

UEGs were measured using two decapolar electrode catheters (St Jude Medical, St. Paul, MN; 6F Livewire Steerable Catheter model 401915 with 2–5-2 mm spacing, 35 mm total span). One electrode catheter was introduced from the femoral vein into the left ventricle (via an atrial trans-septal approach) and positioned on the inferoposterior endocardial wall in a base-apex orientation. The other electrode catheter was introduced into the right ventricle and positioned on the anterior septal wall in a base-apex orientation. The electrode arrays were positioned over the mid- and lower third of the LV and RV endocardial wall. Both electrodes were referenced to a large skin surface electrode (100 × 150 mm) on the abdomen at the level of the naval such that distance to each individual electrode was considered to be approximately equal. The position of the recording and pacing electrodes are shown in Fig. 1*A*. Cine imaging fluoroscopy was used to verify secure positioning of the catheters throughout the cardiac and respiratory cycles. This has previously been established in detail for catheters in these positions (19).

Arterial blood pressure was measured from a femoral artery with a continuous-flush pressure transducer system (Tru-Wave PX600F; Edwards Lifesciences, Irvine, CA). The subject's breathing cycle was monitored using a custom-constructed tension sensor fixed to a freely expandable band placed around the chest/abdomen (adapted from a RESPeRATE device; InterCure, New York, NY). The optimum location for each subject was chosen as the site of maximum circumferential strain during normal breathing.

Controlled respiration. To identify respiratory-related oscillations of ARI and SBP, subjects were instructed to breathe at four fixed rates (6, 9, 15, and 30 breaths/min) for 90 s each, in random order. This was achieved with the aid of a large video monitor with a 19-inch diagonal backlit screen mounted in easy line of site, on which was displayed a computer-generated animated visual display representing lung volume, which cycled at the required breathing rate (implemented in LabVIEW software; National Instruments, Austin, TX). Patients were instructed to breath at the same rate as the movement of the cursor on the screen. This was practiced before study commencement.

Protocol. Subjects were paced from the right ventricular apex using a Biotronik (Berlin, Germany) stimulator (model UHS 3000) at 2× diastolic threshold and 2 ms pulse width, at a cycle length >20 beats/min faster than the intrinsic AF rate (median, 500 ms) to avoid breakthrough intrinsic beats and counteract the expected increase in intrinsic rate post atropine. A 2-min period of adaptation to the paced cycle length was applied before starting the controlled breathing

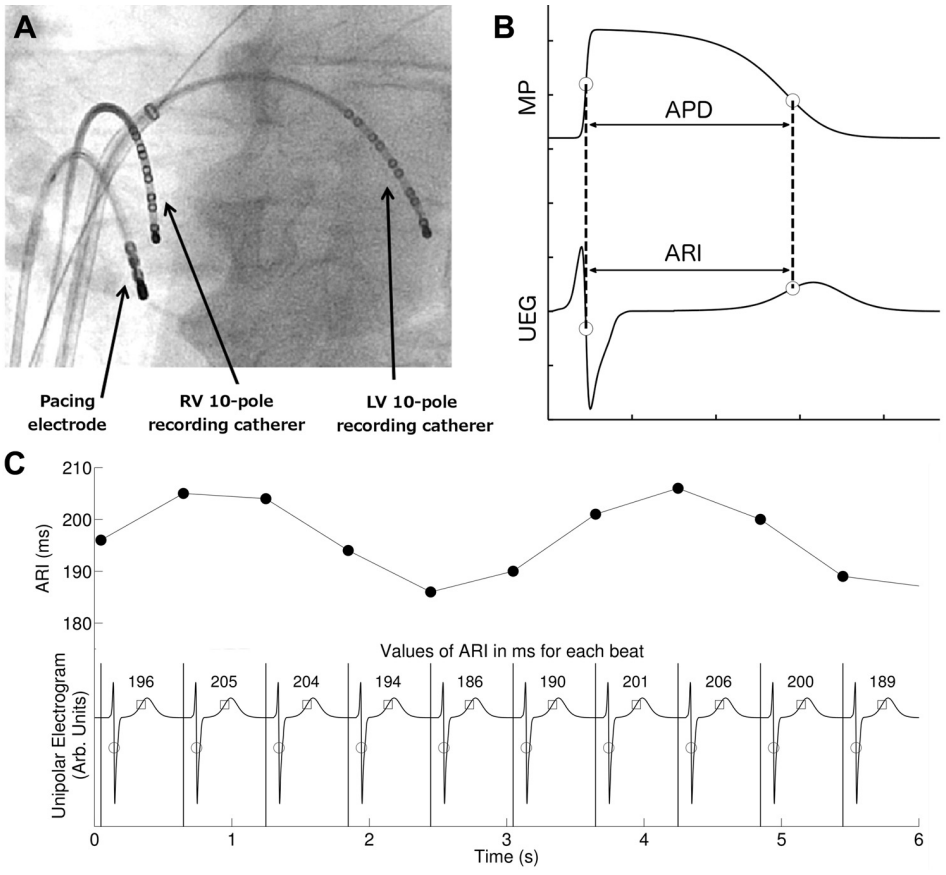

Fig. 1. Electrophysiological measurements. *A*: fluoroscopic image showing the position of the two 10-pole recording catheters located in the left ventricle (LV) and right ventricle (RV). *B*: diagrammatic representation of the relationship between the unipolar electrogram (UEG) and the intracellular ventricular transmembrane potential (MP) during an action potential (AP) showing that the activation recovery interval (ARI) corresponds to the action potential duration (APD). *C*: example of ARI measurements of the local UEG: times of activation are marked with circles [minimal change in volume over time (dv/dt_{min}) of the QRS] and repolarization with squares [maximal change in volume over time (dv/dt_{max}) of the T wave]. The interval between the 2 points is the ARI, and values for each beat are shown in milliseconds. *Top*: corresponding ARIs plotted as function of time.

protocol. First, a control period was established with the breathing protocol performed in absence of any autonomic blocking agents. The subject then received metoprolol at a dose sufficient to reduce the intrinsic heart rate by >10 beats/min (iv; dose range, 2–10 mg), and after ~10 min for equilibration the breathing protocol was repeated. Finally, the subjected was given atropine at a dose sufficient to increase the intrinsic heart rate >10 beats/min faster than the starting heart rate (iv; dose range, 600–1200 μg), and the breathing protocol was once again repeated. During the experiment, electrograms, blood pressure, and respiration were recorded synchronously.

Data analysis. Electrogram, blood pressure, and respiration recordings were sampled at 1,200 Hz (Ensite 3000; Endocardial Solutions) and analyzed offline. Ventricular APDs at each recording site were estimated from the UEG by measuring activation-recovery intervals (ARIs) using the Wyatt method (53). This method has been validated in theoretical, computational, and experimental studies (5, 21, 33, 40, 52). According to this method, activation is measured at the moment of minimum dV/d*t* of the QRS complex of the UEG (5, 21, 33, 40, 53) and repolarization at the moment of maximum dV/d*t* of the T-wave. The relationship between APD and ARI is illustrated in Fig. 1*B*. In this work, ARI was measured semi-automatically using a custom algorithm written in MATLAB (Matlab Mathworks). Heuristic-based screening was used to identify and discount any cases where the T-wave was indistinct or corrupt.

Blood pressure recordings were analyzed for systolic blood pressure (SBP) and the maximum rate of systolic pressure increase (dP/dt_{max}) as a measure of myocardial contractility. To establish evenly sampled series, any beats for which ARI or SBP measurement could not be determined were replaced by linear interpolation between the surrounding beats. If these surrogate beats constituted more than 10% of any series, the series was rejected.

Amplitude estimation of respiratory-related ARI and SBP oscillations. The peak-to-peak amplitude of respiratory-related ARI and SBP oscillations, hereinafter referred to as oscillations, was estimated in the frequency domain using the Thomson's multitaper method with three Slepian tapers (48). This method was used because of its robustness against noise. The power inside a breathing frequency band, defined as the breathing frequency ± 10%, was measured and then converted to amplitude, which is half the peak-to-peak amplitude. The ARI and SBP peak-to-peak amplitude was measured in milliseconds and millimeters of mercury, respectively. The breathing frequency was defined as the peak frequency in the power spectrum of the respiratory signal.

Surrogate data analysis was used to establish a threshold to test whether ARI oscillations were significant. Surrogate data series were created by random permutations of the signal such that the amplitude distribution remained intact, but the original (oscillatory) behavior was destroyed (14). For each signal, 1,000 surrogate series were generated and their corresponding spectra were computed. The threshold function for significance was then determined for each frequency bin as the upper 95th percentile of the surrogate distribution. ARI oscillations were considered significant if the power at the breathing frequency exceeded this threshold ($P < 0.05$). Recording sites that showed significant oscillations were selected for further analysis to investigate the effect of autonomic drugs on the amplitude of the oscillations.

Assessment of coupling and causality. Interactions between ARI, SBP, and respiration (RESP) were characterized in the frequency domain. Coupling was studied by means of coherence, which quantifies the coupling strength between two signals as a function of frequency. The coherence attains a value between 0, indicating absence of coupling, and 1, indicating full coupling. Directed coherence was used to infer causality. Intuitively, the directed coherence represents the fraction of the power spectrum of a signal due to another signal through direct or indirect pathways. This measure of causality is grounded on the notion of Granger causality, stating that a process is causal to another if the prediction of the second is improved by incorporating the knowledge of the first (13). In this work, both coherence and directed coherence are formulated in the framework of an extended linear multivariate autoregressive (MVAR) model proposed (11–13). This model takes into account both instantaneous and lagged effects. The MVAR model is defined in Appendix A. Definitions for coherence and directed coherence are provided in Appendix B. The coefficients of the (multivariate) model were estimated using the least-squares approach with a fixed model order of 10. The resulting residuals of the trivariate model were tested for white noise and independence.

Phase relationship between ARI oscillations in the left and right ventricle. The phase relationship between left and right ventricular ARI oscillations was studied by computing the mean phase lags for the left and right ventricle recording sites. The lag was measured using the Thomson's multitaper cross-power spectrum computed to determine the phase at the breathing frequency using three tapers (23).

Recordings sites were included only if the signal exhibited significant amplitude and coherence at the breathing frequency. The relationship was then investigated by subtracting the mean phase from the left and right ventricle.

Statistical analysis. For all subjects, mean values obtained for dP/dt_{max}, SBP, amplitude of ARI, and SBP oscillations and the (directed) coherence measures were averaged across the four respiratory rates. The effect of β-blocker and atropine infusion was then investigated by comparing control and β-adrenergic blocking (BB) values and BB and BB + atropine (AT) values using the two-tailed paired Wilcoxon signed-rank test for statistical significance. Results were considered significant at $P < 0.05$.

RESULTS

The effect of autonomic blocking agents on blood pressure. Figure 2 shows the effect of autonomic inhibitors on mean blood pressure indexes. After administration of β-adrenergic blocking agents (metoprolol), the mean dP/dt_{max} was significantly decreased [1,271 (± 646) vs. 930 (± 433) mmHg/s; $P < 0.01$]. The mean SBP showed a tendency to decrease [baseline 133 (± 21) vs. metoprolol 128 (± 25) mmHg; $P = 0.06$]. Addition of atropine was associated with a further significant decrease of the mean dP/dt_{max} [930 (± 433) vs. 887 (± 436) mmHg/s; $P < 0.05$]. The mean SBP showed also a significant decrease following the addition of atropine: 128 (± 25) vs. 122 (± 26) mmHg; $P < 0.05$.

Significant ARI and SBP oscillations were observed in all subjects at all breathing frequencies in 61% and 92% of the available recordings, respectively.

Two examples of ARI and SBP time series during paced breathing at 6 and 15 breaths/min are shown in Fig. 3. In both cases, ARI and SBP exhibit oscillatory behavior at the breathing frequency.

The peak-to-peak amplitude of ARI oscillations was ranging from 1.0 to 16.0 ms (left ventricle, 1.0–12.9 ms; right ventricle, 1.0–16.0 ms). The effect of autonomic blocking agents on the mean peak-to-peak amplitude of respiratory-related ARI and SBP oscillations is shown in Fig. 4. After administration of β-adrenergic blockers, the mean ARI peak-to-peak amplitude decreased [6.6 (± 1.9) vs. 5.1 (± 2.4) ms; $P = 0.04$; Fig. 4*A*]. The main effect was in the left ventricle, which showed a significant reduction in peak-to-peak amplitude [6.2 (± 1.4) vs. 4.4 (± 1.0) ms; $P = 0.008$; Fig. 4*C*]; in the right ventricle the differences were not statistically significant [6.0 (± 2.2) vs. 4.9 (± 2.7) ms; $P = 0.2$; Fig. 4*D*]. Addition of atropine did not result in any further changes of the ARI peak-to-peak amplitude in both left and right ventricle.

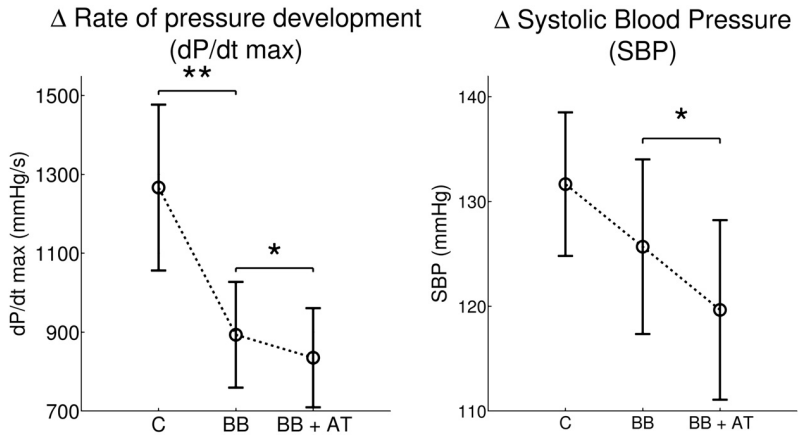

Fig. 2. *Left*: maximum rate of systolic pressure increase (dP/dt_{max}) was significantly reduced after administration of the β-adrenergic blocking (BB) agent metoprolol. Subsequent addition of atropine (AT) was associated with a further small but significant reduction. *Right*: systolic blood pressure (SBP) showed no significant change following metoprolol but a significant reduction following the addition of atropine. Error bars indicate SE. C, control. $*P < 0.05$; $**P < 0.01$.

The peak-to-peak amplitude of SBP oscillations was ranging from 0.7 to 17.0 mmHg. The mean peak-to-peak amplitude of SBP oscillations showed a significant reduction following the administration of β-adrenergic blockers [8.4 (± 1.6) vs. 6.2 (± 2.0) mmHg; $P = 0.002$; Fig. 4*B*]. Subsequent addition of atropine was not associated with any significant change [6.2 (± 2.0) vs. 6.0 (± 2.4) mmHg; $P = 0.8$].

In the LV the absolute ARI shows a tendency to increase at the sites where ARIs were measured after administration of the β-blocker: control, 189 ms (± 25 ms), β-blocker: 191 ms (± 23 ms); this would be consistent with a reduced sympathetic action on APD. Subsequent atropine administration shortened ARI to 189 (± 20 ms), consistent with reduced parasympathetic restraint on residual sympathetic tone resulting in APD shortening.

Assessment of the interactions between ARI, SBP, and respiration. Significant coherence ($P < 0.05$) was detected between ARI, SBP, and RESP, significant in all subjects. The coherence was significant in 47% of the ARI signals. Figure 5 shows the mean coherences between ARI, SBP, and RESP. For example, Fig. 5, *left*, shows that the mean coherence (coupling strength) between ARI and RESP was strong, being 0.76 on a scale of 0 to 1. The mean coherence was not affected by the administration of autonomic inhibitors: ARI ⇔ RESP: 0.76 (± 0.12) vs. 0.76 (± 0.12) vs. 0.75 (± 0.11); ARI ⇔ SBP: 0.71 (± 0.11) vs. 0.71 (± 0.11) vs. 0.71 (± 0.11); SBP ⇔ RESP: 0.92 (± 0.07) vs. 0.93 (± 0.07) vs. 0.93 (± 0.07) for control, β-blocker, and subsequent addition of atropine.

The results of the directed coherence analysis are presented in Fig. 6. Figure 6*A* shows a graphical representation of the (theoretical) possible interactive pathways between all processes. The directed coherence describes the coherence according to the direction of information transmission by measuring the relative power contributions for all processes (ARI, SBP, and respiration). Figure 6*B* shows the mean directed coherence at the breathing frequency during control, β-blocker, and subsequent addition of atropine. Regarding the observed ARI oscillation, during control, the directed coherence from respiration to ARI (RESP ⇒ ARI) was 0.70 (± 0.17), which means that, at the breathing frequency, on average, 70% of the ARI signal power could be explained by the respiratory signal.

In contrast, the directed coherence from SBP to ARI (SBP ⇒ ARI) was found to be marginal: SBP ⇒ ARI: 0.07 (± 0.06), indicating that the causal interaction from SBP to ARI was weak.

High directed coherence was also found from respiration to SBP (RESP ⇒ SBP): 0.70 (± 0.17), whereas, as expected, the directed coherence from ARI to SBP (ARI ⇒ SBP) was low: 0.11 (± 0.05).

After administration of β-adrenergic blockers, the directed coherence from respiration to ARI was significantly reduced: 0.70 (± 0.17) vs. 0.50 (± 0.23), $P < 0.05$. The directed coherence from SBP to ARI showed a tendency to increase, but remained very small: SBP ⇒ ARI: 0.07 (± 0.06) vs. 0.12 (± 0.07), $P = 0.06$.

Regarding SBP oscillations, RESP ⇒ SBP was not affected by β-blocker: 0.76 (± 0.17) vs. 0.75 (± 0.11), $P = 0.9$. When compared with RESP ⇒ SBP, ARI ⇒ SBP was very small during both control and β-blocker: 0.11 (± 0.05) and 0.06 (± 0.06), respectively ($P < 0.05$). Subsequent addition of atropine did not result in any further changes of the directed coherences (RESP ⇒ ARI, SBP ⇒ ARI, RESP ⇒ SBP, and ARI ⇒ SBP).

Investigation of the phase of left and right ventricular ARI oscillations. The phase lag between respiration and ARI was investigated for left and right ventricular recordings. During control, on average, ARI oscillations in the LV lagged behind RV oscillations: the mean relative phase difference was statically different from 0: 37 (± 46) dgr, $P < 0.05$. The phase difference did not change after administration of β-blocker: 37 (± 46) vs. 17 (± 45) dgr, $P = 0.6$. However, the phase difference was not statically significant from 0 anymore ($P = 0.2$). Addition of atropine was not associated with additional changes: 17 (± 45) vs. −4 (± 78), $P = 0.7$. Various phase differences between RV and LV were observed between subjects. Figure 7 shows an example of LV and RV ARI signals that are approximately in phase (Fig. 7, *left*) and in anti-phase (Fig. 7, *right*).

DISCUSSION

The duration of the ventricular action potential plays a crucial role in maintaining electrical stability and in arrhythmogenesis. Oscillations of APD in ventricular myocardium have recently been shown to occur at the frequency of respiration in human subjects (18, 19). To investigate the underlying mechanism, we have used infusion of autonomic blocking agents together with causal coherence analysis in subjects with

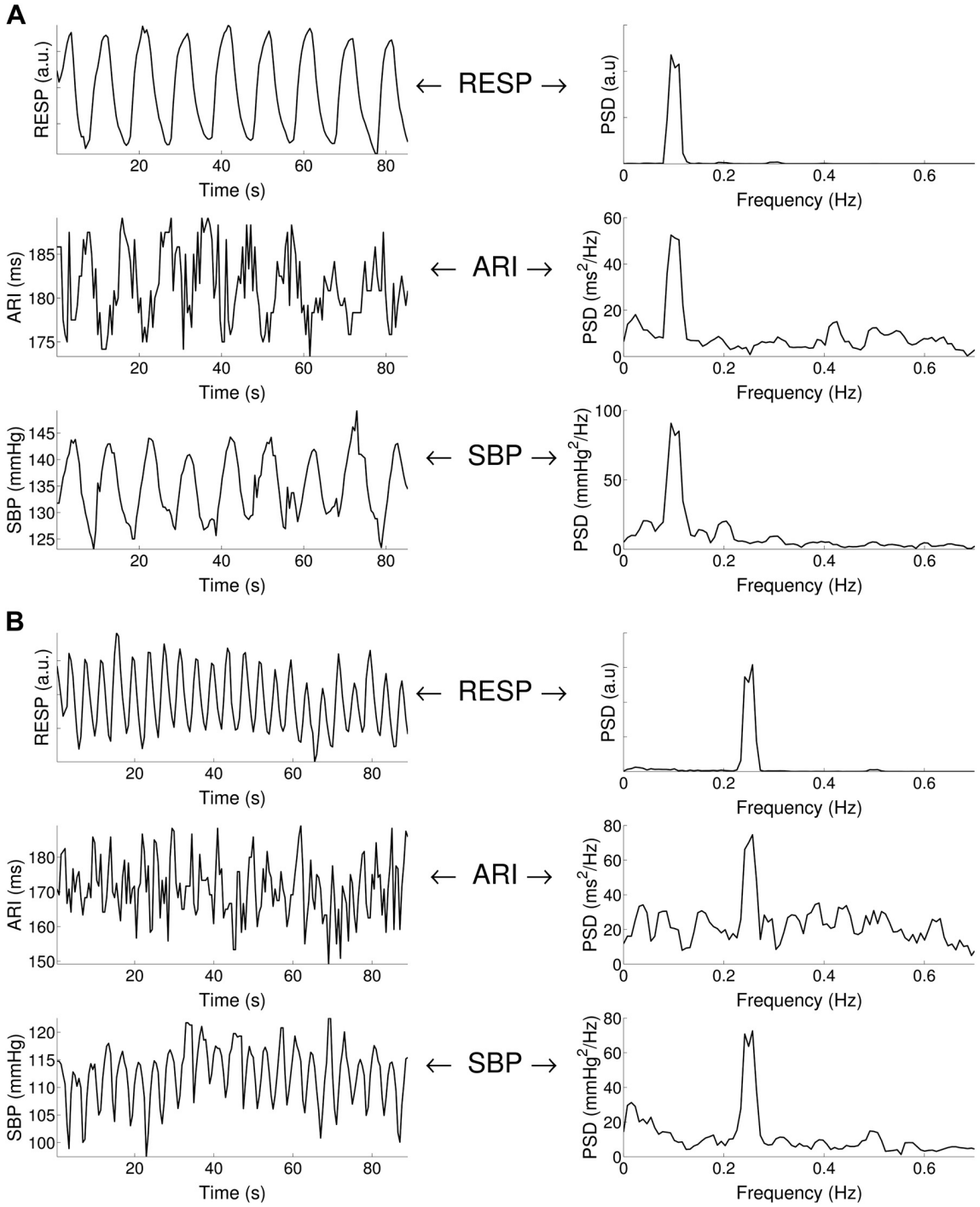

Fig. 3. Respiratory-related ARI and SBP oscillations. *A*: example of ARI, SBP, and respiration (RESP) recordings for 0.1 Hz (6 breaths/min) breathing. Cyclical variation was observed in both ARI and SBP at the breathing frequency. PSD, power spectral density. *B*: example of ARI, SBP, and RESP recordings for 0.25 Hz (15 breaths/min) breathing. Cyclical variation was observed in both ARI and SBP at the breathing frequency.

healthy ventricles while recording a measure of ventricular endocardial APD using catheter electrodes, SBP, and respiration. The main findings were as follows: *1*) we confirmed the presence of oscillations in APD and SBP at each of four controlled respiratory frequencies: 6, 9, 15, and 30 breaths/min; *2*) the β-adrenergic blocking agent metoprolol resulted in a decrease in the amplitude of APD oscillation; *3*) IV administration of atropine following metoprolol was without effect on LV or RV ARI oscillation amplitude; *4*) coherence analysis showed a significant linear coupling between respiration, APD, and SBP at the breathing frequency; *5*) analysis of the directed coherence showed a high directed coherence from respiration to APD and from respiration to SBP. β-Adrenergic blockade reduced the contribution of respiration to APD oscillations.

Methodological considerations. The unipolar signal recorded using the multipolar catheters as used here (St. Jude

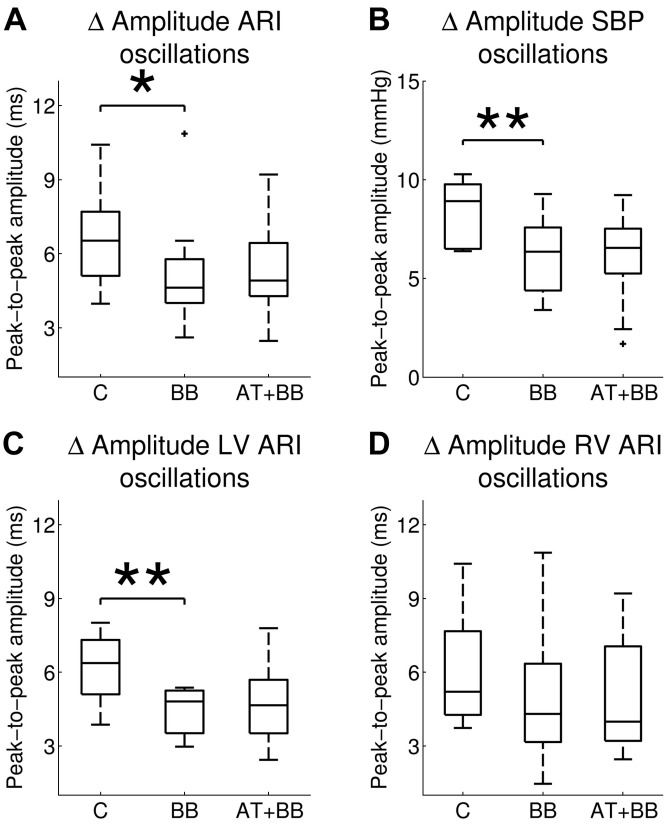

Fig. 4. Mean values of peak-to-peak amplitude of respiratory-related oscillations of ARI and SBP during control (C), following administration of β-adrenergic blocking (BB) agents and after subsequent addition of atropine (AT + BB). After administration of β-blockers, the amplitude of LV ARI and SBP oscillations were significantly reduced, and a trend to reduction was seen for RV ARI oscillations. $*P < 0.05$; $**P < 0.01$.

Medical) has been extensively validated as a true representation of the local endocardial activity, and the derived ARI measure as representative of the local APD (5, 40, 53), and has been further validated in the context of the protocol used in the present study (52). Respiratory frequency was well controlled by the subjects, but we did not measure tidal volume, arterial P_{CO2}, and pH, which may affect APD. However, we measured blood gasses and discussed this issue in a previous communication and concluded that any possible influence would be small (19). In these studies autonomic blockade was not complete. The dosage of metoprolol and atropine was titrated on an individual patient basis to achieve a target change in heart rate. This is a regime used in the clinical scenario where complete blockade is avoided as the border between complete blockade and overdose is narrow and unpredictable. As a result, we cannot exclude the possibility that the level of blockade may have affected our results. It is well known that there is regional variation in parasympathetic innervation, which is greatest at the base and decreases toward the apex, as well as epicardial to endocardial differences. The electrode arrays were located over the mid- and lower third of each ventricle where stable recordings are best obtained. It is possible, therefore, that a response to atropine occurred in the more basal regions, which we did not detect.

APD oscillations-mechanisms. We are at present unaware of any reported observations on the effect of autonomic blocking agents on the respiratory-related oscillations of ventricular APD. Respiration physically alters membrane potentials of sympathetic and parasympathetic preganglionic motoneurones and thereby continuously modulates sympathetic neuronal and vagal motorneurone activity over a wide range of frequencies (8), both of which are known to modulate APD (30, 32, 35, 50, 55). Our results show a reduction in respiratory-related ARI oscillation following administration of the β-blocking agent metoprolol with further reduction following atropine, suggesting a role for autonomic nerve activity. One possibility is a baroreflex-mediated effect on the autonomic modulation of individual myocytes and hence APD in response to cyclic variation in the hemodynamics during the respiratory cycle. Although the exact relation between cardiopulmonary hemodynamics and right and left ventricular pressure-volume relations has been the subject of debate, a general consensus is that during inspiration the fall in intrathoracic pressure results in increased filling of the right heart with increased right ventricular stroke volume. The increased pleural pressure increases left ventricular afterload and together with the increased right ventricular volume result in reduced stroke volume during inspiration (17, 24, 26, 41, 49). In RR interval studies, it has been shown that the influence of SBP variability on RR variability was high during rest (36–39). The methodology used in this work did not reveal a strong causal interaction from SBP to ARI respiratory oscillations (Fig. 6). This should be interpreted within the limit of a linear model and does not exclude a more complex involvement of blood pressure in the generation ARI oscillation. For example, a change in intraventricular pressure may induce regional changes in cardiac strain that could in turn cause ARI oscillations via the mechano-electric feedback pathway (44, 46). Therefore, blood pressure changes, which only partially reveals heterogeneous cardiac strain, may be involved in the generation of ARI oscillations without necessarily exhibiting a linear interaction with them.

Another possible mechanism is central gating of autonomic neural traffic by central respiratory networks (15), arising as a result of brainstem interactions (6) or entrained by cortical activity during controlled breathing (10). We could not exclude the possibility that the cardioselective β-adrenergic blocking agent metoprolol we used, being moderately lipophilic and therefore capable of passing the blood brain barrier, could have exerted a central effect.

Parasympathetic activity decreases during inspiration and, therefore, could potentially influence APD by the ACh-activated K^+ current IK, ACh, now recognized as being widely represented in ventricular myocardium (7). In the present study the administration of atropine after β-blockade induced no further effect on the amplitude of the ARI oscillations, suggesting no significant involvement of this current.

The β-adrenergic signaling cascade involves phosphorylation of a number of target proteins, and it is at present unclear as to whether the time constants of the phosphorylation/dephosphorylation process would be capable of following the breathing frequencies used in the present study. An alternative possibility is that sympathetic activity may act indirectly by interacting by modulating mechano-electric coupling (MEC).

MEC whereby changes in myocardial fiber stretch/strain alter the electrophysiology (29, 44, 46) has been shown to be substantially enhanced by β-adrenergic blocking agents (22), and therefore the reduction in the oscillation of APD that we

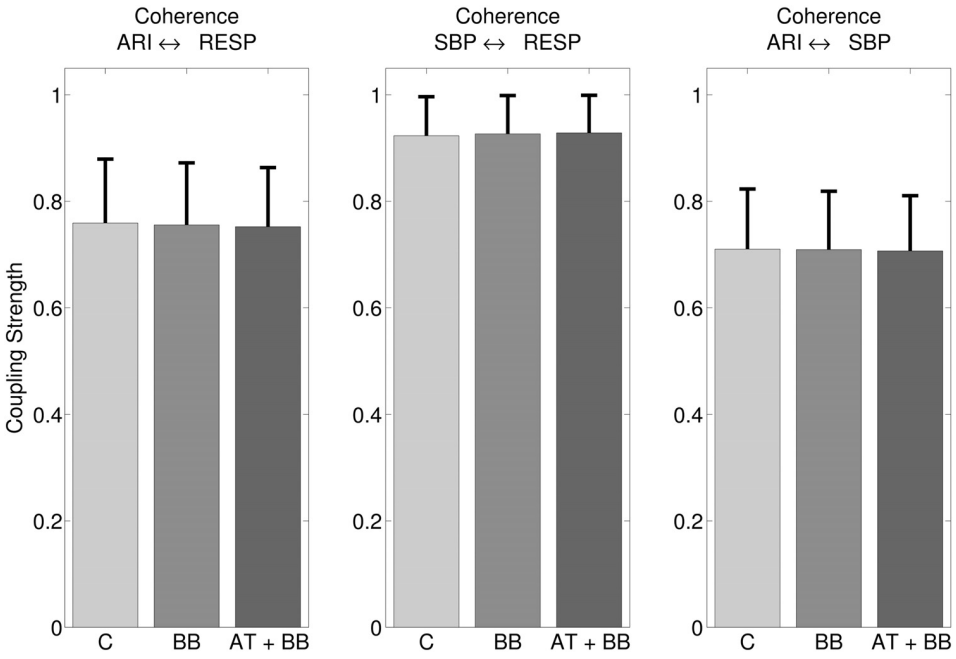

Fig. 5. Mean coherence measures the coupling strength between ARI and respiration (*left*), between SBP and RESP (*middle*), and between ARI and SBP (*right*). Significant coherence was detected in all subjects and was unaffected after administration of autonomic blocking agents.

observed after administration of metoprolol would be consistent with MEC as an underlying mechanism. The effects of MEC on APD are complex depending on the nature and timing of the mechanical perturbation (3, 27, 42, 47). In general increased stretch tends to shorten APD. Increased fiber length increases the affinity of Troponic C for calcium, which slows calcium release from TnC resulting in a reduced calcium transient, decreased NaCa exchange current, and APD shortening. Increased fiber shortening results in a decreased affinity of TnC for calcium, faster calcium release, an increased calcium transient, increased inward NaCaX, and APD prolongation. In addition stretch-activated channels either shorten or lengthen APD dependent on the timing of the stretch relative to the reversal potential (~ -30 mv), such that early stretch shortens and late stretch lengthens APD. Thus the overall effect is likely to be a complex function of whichever mechanism is dominant. As described above, during inspiration LV stroke volume decreases, which would be expected to reduce stretch and fiber excursion, whereas opposite effects would be expected in the RV. The marked variability that we observed in phase of ARI oscillations that we observed between endocardial left ventricular free wall and right ventricular septum would be consistent with such a mechanism. Discordant ARI oscillations in the LV and RV increased the regional ARI differences between LV and RV. We observed that the dispersion of ARI (APD) between left and right ventricle could increase up to ~40 ms when ARI oscillations reached their peak in the RV and its trough in the LV at the same time. Because ARI is a component of total repolarization and regional differences in repolarization are important in arrhythmias based on reentry, the cyclical variation in dispersion of ARI due to respiration may contribute to the conditions for reentry to occur.

Conclusion

The dynamics of ventricular repolarization play a critical role in maintaining electrical stability. We have investigated the role of the autonomic nervous system in generating oscillations in ventricular APD at the respiratory frequency in humans with healthy ventricles. Ventricular APD and SBP exhibited oscillations at each of four controlled respiratory frequencies. The β-adrenergic blocking agent metoprolol partly but not completely reduced the APD oscillation. The addition of a parasympathetic blocking agent (atropine) was without any additional effect. Directed coherence as a measure of causality indicated respiration rather than (femoral artery) SBP as a major cause of APD oscillation. β-Adrenergic blockade reduced the contribution of respiration to APD oscillations. The results are consistent with a role of the sympathetic nervous system combined with an additional mechanism.

APPENDIX A: MULTIVARIATE AUTOREGRESSIVE MODEL

In this study, ARI, SBP, and RESP are a joint multivariate zero-mean process: $Y(n) = [y_{ARI}(n), y_{SBP}(n), y_{RESP}(n)]^T$. Here, ARI is numbered as process 1, SBP is process 2, and RESP is process 3. The set was described as a multivariate autoregressive (MVAR) process defined as:

$$Y(n) = \sum_{k=1}^{p} A(k)Y(n-k) + U(n)$$

where p is the model order, A(k), k = 1, ..., p, are the 3×3 matrices containing the coefficients $a_{ij}(k)$ that describe the linear interaction at lag k from $y_j(n\text{-}k)$ to $y_i(n)$ (i,j = 1,2,3), and $U(n) = [u_1(n), u_2(n), u_3(n)]^T$ is a vector of zero-mean white noise processes with diagonal covariance matrix $\sum_U$. This strictly causal model representation (k>0) cannot describe zero-delay correlations among the observed series Y, which are thus explained by correlations among the input noises U. To overcome this problem, series Y can be described including instantaneous effects [$y_i(n)$ to $y_j(n)$] into the interactions allowed by the model as proposed by Faes and Nollo (12). This is achieved by extending the MVAR process:

$$Y(n) = \sum_{k=0}^{p} B(k)Y(n-k) + W(n)$$

Like U(n), $W(n) = [w_1(n), w_2(n), w_3(n)]^T$ is a vector of uncorrelated processes with diagonal covariance matrix $\sum_W$. Instantaneous

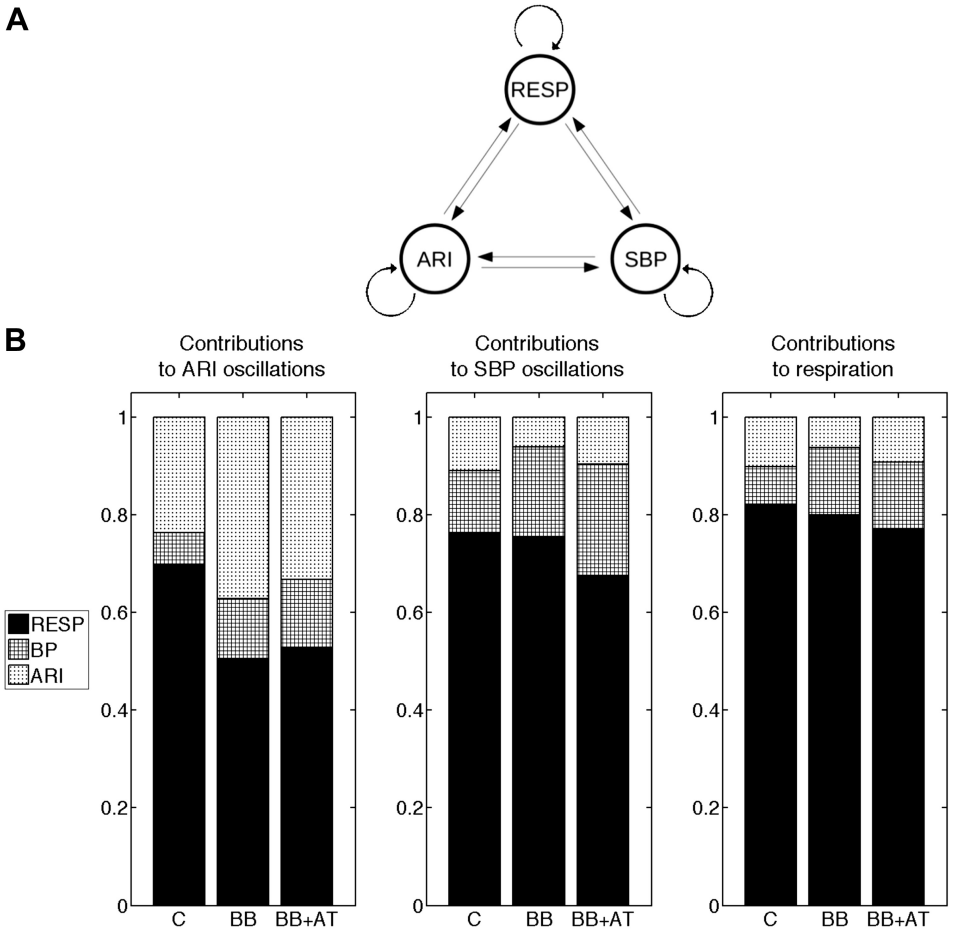

Fig. 6. Assessment of the causal interactions between respiration (RESP), ARI, and SBP. *A*: possible (theoretical) interactive pathways between all processes. *B*: for all processes the mean relative power contributions related to all processes (the directed coherence) at the breathing frequency. Black quantifies the contribution of respiration; densely hatched represents SBP and lightly hatched ARI. The directed coherence was measured during control (C), following administration of β-adrenergic blocking (BB), and subsequent addition of atropine (BB + AT). For example, during control, the directed coherence from respiration to ARI (*left*) is 0.70, indicating that respiration explains 70% of ARI signal power at the breathing frequency. Administration of β-blocker agents significantly reduced the contribution of respiration to respiratory-related oscillations of activation recovery intervals ($P < 0.05$).

effects are modelled in the form of the coefficients $b_{ij}(0)$ of the matrix B(0). B(0) is a lower triangular matrix with null diagonal and can only be solved by imposing a priori knowledge of the structure of instantaneous causation, i.e., the time-series have to be ordered in a way that instantaneous effects are allowed from one process to another but not vice versa. The instantaneous effects were ordered based on information of the physiological system: respiration was measured before ARI and before SBP due to the pulse transit time and the time delay between electrical and mechanical activation.

APPENDIX B: DEFINITIONS OF SPECTRA, COHERENCE, AND DIRECTED COHERENCE FOR MVAR MODELS

The spectral representation of the MVAR process is derived considering the Fourier transform of the MVAR process:

$$Y(f) = B(f)Y(f) + W(f)$$

The transfer function that links input and output is the inverse of the coefficients of B:

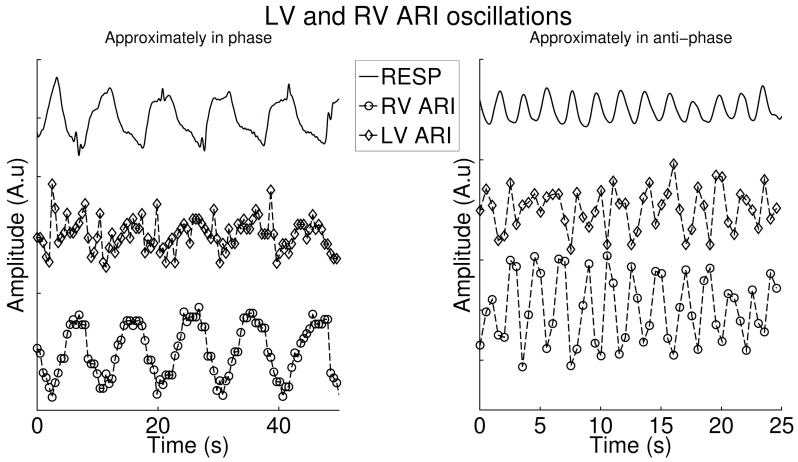

Fig. 7. Two examples of oscillations in the RV and LV. *Right*: example in which both oscillations are approximately in phase. *Left*: example in which the oscillations are approximately in anti-phase. Note the different time scales for clarity.

$$H(f) = \left[I - B(f)\right]^{-1}$$

where I is the identity matrix. The spectral matrix is then defined as:

$$S(f) = H(f) \wedge H^{H}(f)$$

where the superscript H stands for the Hermitian transpose and $\wedge$ is the covariance matrix. Its compact form is written as:

$$Sij(f) = h_i(f) \wedge h_j(f)$$

Under the assumption that the input white noises are uncorrelated, their covariance matrix $\wedge$ reduced to the diagonal matrix $\wedge = diag(\sigma_i^2)$, where σ_i^2 is the variance of w_i.

S can be factorized in:

$$S_{ij}(f) = \sum_{m=1}^{3} \sigma_m^2 H_{im}(f) H_{jm}^{*}(f)$$

The coherence between y_i and y_j is defined as:

$$\Upsilon_{ij}(f) = \frac{S_{ij}(f)}{\sqrt{S_{ii}(f) S_{jj}(f)}}$$

$$\Upsilon_{ij}(f) = \frac{h_i(f) \sum h_j^{H}(f)}{\sqrt{h_i(f) \sum h_i^{H}(f)} \sqrt{h_j(f) \sum h_j^{H}(f)}} = \sum_{m=1}^{3} \frac{\sigma_m H_{im}(f)}{\sqrt{S_{ii}(f)}} \frac{\sigma_m H_{jm}^{*}(f)}{\sqrt{S_{jj}(f)}} = \sum_{m=1}^{3} \gamma_{im}(f) \gamma_{jm}^{*}(f)$$

The last term contains the so-called directed coherence. The directed coherence (γ) from y_i to y_j is defined as:

$$\gamma_{ij}(f) = \frac{\sigma_j H_{ij}(f)}{\sqrt{\sum_{m=1}^{3} \sigma_m^2 \left| H_{im}(f) \right|^2}}$$

APPENDIX C: METHODOLOGICAL CONSIDERATIONS FOR FREQUENCY DOMAIN MEASURES OF CAUSALITY

For this study, respiration was required to be voluntarily controlled, and the tidal change voluntarily adjusted to suit the wide range of rates, thus avoiding hyper- or hypoventilation. By controlling the respiratory frequency, we endeavored to maximize stationarity of respiratory modulation of APD. Estimation of the amplitude using the power spectra are, therefore, likely to have produced the average frequency content of the ARI and SBP signal over the entire recording time of 90 s. To provide a good representation of the frequency content, Thomson's multitaper spectra were used to estimate the amplitude of ARI and SBP oscillations. When compared with the Fourier Transform, this method reduces the amplitude estimation bias by obtaining multiple estimates from the same sample and averaging over all the tapered spectra (48). The cyclical variation of ARI and SBP was quantified as peak-to-peak amplitude, since this measure represents the absolute changes in APD.

Frequency domain measures of causality have been used previously to investigate causal interactions between spontaneous variability of the heart period (RR interval), SBP, and the respiratory flow (36, 39). To the best of our knowledge, our work is the first application in studying cardiorespiratory interactions between ventricular endocardial APD, SBP, and RESP. In this work, we used a MVAR model that describes both lagged and instantaneous effects as proposed by Faes and colleagues (12, 38, 39). The use of a strictly causal MVAR models to describe multiple time series with zero-lag correlations may lead to incorrect estimates of the lagged effects and thus to erroneous causality inferences.

MEC is the process by which mechanical forces on the myocardium can alter its electrical properties (3, 27, 29, 42, 47). In contrast with the baroreceptor reflex, MEC may act almost instantaneously (i.e., before arrival of the next heart beat). Consequently, to achieve a full description of the correlation structure of the observed signals, we used an extended MVAR model that combines both instantaneous and lagged effects. When neglecting instantaneous effects, we discovered cross-correlation between the residuals, indicating that causality measures would have been adversely affected when excluding instantaneous effects (12, 13). The analysis showed that the directed coherence from ARI to RESP and from SBP to RESP was (very) low, which corresponds to our expectations, since these pathways do not have any physiological meaning. With respect to nonparametric methods, MVAR analysis presents the advantage of infer directionality and causality through the parameterization of the mutual interactions between processes (37).

GRANTS

S. van Duijvenboden is supported by the UCL Impact bursary scheme. M. Orini is supported by the IEF-2013 Marie Curie Fellowship. B. Hanson is in receipt of a grant from the UK Medical Research Council MRC Project Grant (Ref G0901819).

DISCLOSURES

No conflicts of interest, financial or otherwise, are declared by the author(s).

AUTHOR CONTRIBUTIONS

Author contributions: S.v.D. analyzed data; S.v.D., B.H., M.O., and P.T. interpreted results of experiments; S.v.D. prepared figures; S.v.D., M.O., and P.T. drafted manuscript; S.v.D., B.H., N.C., M.O., C.A.R., J.G., and P.T. edited and revised manuscript; S.v.D., N.C., M.O., and P.T. approved final version of manuscript; B.H., M.O., J.G., and P.T. conception and design of research; B.H., N.C., and J.G. performed experiments.

REFERENCES

1. **Anon.** Heart rate variability: standards of measurement, physiological interpretation, and clinical use. Task Force of the European Society of Cardiology and the North American Society of Pacing and Electrophysiology. *Circulation* 93: 1043–1065, 1996.
2. **Anrep G, Pascual W, Rossler R.** Respiratory variations of the heart rate. I—The reflex mechanism of the respiratory arrhythmia. *Proc R Soc Lond B Biol Sci* 119: 191–217, 1936.
3. **Calaghan S, Belus A, White E.** Do stretch-induced changes in intracellular calcium modify the electrical activity of cardiac muscle? *Prog Biophys Mol Biol* 82: 81–95, 2003.
4. **Cohen MA, Taylor JA.** Short-term cardiovascular oscillations in man: measuring and modelling the physiologies. *J Physiol* 542: 669–683, 2002.
5. **Coronel R, de Bakker JM, Wilms-Schopman FJ, Opthof T, Linnenbank AC, Belterman CN, Janse MJ.** Monophasic action potentials and activation recovery intervals as measures of ventricular action potential duration: experimental evidence to resolve some controversies. *Heart Rhythm* 3: 1043–1050, 2006.
6. **Dergacheva O, Griffioen KJ, Neff RA, Mendelowitz D.** Respiratory modulation of premotor cardiac vagal neurons in the brainstem. *Respir Physiol Neurobiol* 174: 102–110, 2010.
7. **Dobrzynski H, Janvier NC, Leach R, Findlay JB, Boyett MR.** Effects of ACh and adenosine mediated by Kir3.1 and Kir34 on ferret ventricular cells. *Am J Physiol Heart Circ Physiol* 283: H615–H630, 2002.
8. **Eckberg DL.** The human respiratory gate. *J Physiol* 548: 339–352, 2003.
9. **Eckberg DL.** Point: counterpoint: respiratory sinus arrhythmia is due to a central mechanism vs. respiratory sinus arrhythmia is due to the baroreflex mechanism. *J Appl Physiol (1985)* 106: 1740–1742, 2009.
10. **Evans KC.** Cortico-limbic circuitry and the airways: insights from functional neuroimaging of respiratory afferents and efferents. *Biol Psychol* 84: 13–25, 2010.
11. **Faes L, Erla S, Porta A, Nollo G.** A framework for assessing frequency domain causality in physiological time series with instantaneous effects. *Philos Trans A Math Phys Eng Sci* 371: 20110618, 2013.
12. **Faes L, Nollo G.** Extended causal modeling to assess Partial Directed Coherence in multiple time series with significant instantaneous interactions. *Biol Cybern* 103: 387–400, 2010.
13. **Faes L, Nollo G.** Multivariate frequency domain analysis of causal interactions in physiological time series. In: *Biomedical Engineering, Trends in Electronics, Communications and Software*, edited by Laskovski A. InTech, 2011, chapt. 2, p. 403–428.

14. **Faes L, Pinna GD, Porta A, Maestri R, Nollo G.** Surrogate data analysis for assessing the significance of the coherence function. *IEEE Trans Biomed Eng* 51: 1156–1166, 2004.
15. **Gilbey MP.** Entrainment of sympathetic rhythms. In: *Primer on the Autonomic Nervous System*, edited by Robertson P. St. Louis: Graph World Publishing Services, 2004, p. 147–150.
16. **Gilbey MP, Jordan D, Richter DW, Spyer KM.** Synaptic mechanisms involved in the inspiratory modulation of vagal cardio-inhibitory neurones in the cat. *J Physiol* 356: 65–78, 1984.
17. **Guz A, Innes J, Murphy K.** Respiratory modulation of left ventricular stroke volume in man measured using pulsed Doppler ultrasound. *J Physiol* 393: 499–512, 1987.
18. **Hanson B, Child N, Van Duijvenboden S, Orini M, Chen Z, Coronel R, Rinaldi CA, Gill JS, Gill JS, Taggart P.** Oscillatory behavior of ventricular action potential duration in heart failure patients at respiratory rate and low frequency. *Front Physiol* 5: 414, 2014.
19. **Hanson B, Gill J, Western D, Gilbey MP, Bostock J, Boyett MR, Zhang H, Coronel R, Taggart P.** Cyclical modulation of human ventricular repolarization by respiration. *Front Physiol* 3: 379, 2012.
20. **Hanson B, Sutton P, Elameri N, Gray M, Critchley H, Gill JS, Taggart P.** Interaction of activation-repolarization coupling and restitution properties in humans. *Circ Arrhythm Electrophysiol* 2: 162–170, 2009.
21. **Haws CW, Lux RL.** Correlation between in vivo transmembrane action potential durations and activation-recovery intervals from electrograms. Effects of interventions that alter repolarization time. *Circulation* 81: 281–288, 1990.
22. **Horner S, Murphy C, Coen B, Dick D.** Sympathomimetic modulation of load-dependent changes in the action potential duration in the in situ porcine heart. *Cardiovasc Res* 32: 148–157, 1996.
23. **Huybers P.** *Matlab Scripts* (Online). http://www.people.fas.harvard.edu/~phuybers/Mfiles/ [July 2015].
24. **Innes J, De Cort S, Kox W, Guz A.** Within-breath modulation of left ventricular function during normal breathing and positive-pressure ventilation in man. *J Physiol* 460: 487–502, 1993.
25. **Kanaporis G, Blatter LA.** The mechanisms of calcium cycling and action potential dynamics in cardiac alternans. *Circ Res* 116: 846–856, 2015.
26. **Karam M, Wise RA, Natarajan T, Permutt S, Wagner H.** Mechanism of decreased left ventricular stroke volume during inspiration in man. *Circulation* 69: 866–873, 1984.
27. **Kohl P, Bollensdorff C, Garny A.** Effects of mechanosensitive ion channels on ventricular electrophysiology: experimental and theoretical models. *Exp Physiol* 91: 307–321, 2006.
28. **Kollai M, Koizumi K.** Cardiovascular reflexes and interrelationships between sympathetic and parasympathetic activity. *J Auton Nerv Syst* 4: 135–148, 1981.
29. **Lab MJ.** Mechanosensitive-Mediated Interaction, Integration, and Cardiac Control. *Ann N Y Acad Sci* 1080: 282–300, 2006.
30. **Levy MN.** Sympathetic-parasympathetic interactions in the heart. *Circ Res* 29: 437–445, 1971.
31. **Malliani A.** *Principles of cardiovascular neural regulation in health and disease*. Boston: Springer Science & Business Media, 2000.
32. **Martins JB, Zipes DP.** Effects of sympathetic and vagal nerves on recovery properties of the endocardium and epicardium of the canine left ventricle. *Circ Res* 46: 100–110, 1980.
33. **Millar CK, Kralios FA, Lux RL.** Correlation between refractory periods and activation-recovery intervals from electrograms: effects of rate and adrenergic interventions. *Circulation* 72: 1372–1379, 1985.
34. **Nearing BD, Verrier RL.** Progressive increases in complexity of T-wave oscillations herald ischemia-induced ventricular fibrillation. *Circ Res* 91: 727–732, 2002.
35. **Ng GA, Brack KE, Patel VH, Coote JH.** Autonomic modulation of electrical restitution, alternans and ventricular fibrillation initiation in the isolated heart. *Cardiovasc Res* 73: 750–760, 2007.
36. **Nollo G, Faes L, Porta A, Antolini R, Ravelli F.** Exploring directionality in spontaneous heart period and systolic pressure variability interactions in humans: implications in the evaluation of baroreflex gain. *Am J Physiol Heart Circ Physiol* 288: H1777–H1785, 2005.
37. **Orini M, Bailón R, Laguna P, Mainardi LT, Barbieri R.** A multivariate time-frequency method to characterize the influence of respiration over heart period and arterial pressure. *EURASIP J Adv Signal Process* 2012: 1–17, 2012.
38. **Orini M, Valenza G, Citi L, Barbieri R.** Tetravariate point-process model for the continuous characterization of cardiovascular-respiratory dynamics during passive postural changes. In: *Computing in Cardiology (CinC)*, 2012. IEEE, 2012, p. 273–276.
39. **Porta A, Furlan R, Rimoldi O, Pagani M, Malliani A, Van De Borne P.** Quantifying the strength of the linear causal coupling in closed loop interacting cardiovascular variability signals. *Biol Cybern* 86: 241–251, 2002.
40. **Potse M, Vinet A, Opthof T, Coronel R.** Validation of a simple model for the morphology of the T wave in unipolar electrograms. *Am J Physiol Heart Circ Physiol* 297: H792–H801, 2009.
41. **Robotham JL, Rabson J, Permutt S, Bromberger-Barnea B.** Left ventricular hemodynamics during respiration. *J Appl Physiol Respir Environ Exerc Physiol* 47: 1295–1303, 1979.
42. **Solovyova O, Katsnelson L, Konovalov P, Kursanov A, Vikulova N, Kohl P, Markhasin V.** The cardiac muscle duplex as a method to study myocardial heterogeneity. *Prog Biophys Mol Biol* 115: 115–128, 2014.
43. **Stramba-Badiale M, Vanoli E, De Ferrari GM, Cerati D, Foreman RD, Schwartz PJ.** Sympathetic-parasympathetic interaction and accentuated antagonism in conscious dogs. *Am J Physiol Heart Circ Physiol* 260: H335–H340, 1991.
44. **Taggart P.** Mechano-electric feedback in the human heart. *Cardiovasc Res* 32: 38–43, 1996.
45. **Taggart P, Sutton P, Chalabi Z, Boyett MR, Simon R, Elliott D, Gill JS.** Effect of adrenergic stimulation on action potential duration restitution in humans. *Circulation* 107: 285–289, 2003.
46. **Taggart P, Sutton P, John R, Swanton H.** Monophasic action potential recordings during acute changes in ventricular loading induced by the Valsalva manoeuvre. *Br Heart J* 67: 221–229, 1992.
47. **Taggart P, Sutton P, Kohl P, Sachs F, Franz M.** *Load dependence of ventricular repolarization. Cardiac Mechano-electric Feedback and Arrhythmias From Pipette to Subject*. From Pipette to Subject (2nd ed.), edited by Kohl P, Sachs F, Franz MR. Philadelphia: Elsevier, 2011, p. 269–273.
48. **Thomson DJ.** Spectrum estimation and harmonic analysis. *Proc IEEE Sens* 70: 1055–1096, 1982.
49. **Toska K, Eriksen M.** Respiration-synchronous fluctuations in stroke volume, heart rate and arterial pressure in humans. *J Physiol* 472: 501–512, 1993.
50. **Vaseghi M, Lux RL, Mahajan A, Shivkumar K.** Sympathetic stimulation increases dispersion of repolarization in humans with myocardial infarction. *Am J Physiol Heart Circ Physiol* 302: H1838–H1846, 2012.
51. **Weiss JN, Garfinkel A, Karagueuzian HS, Nguyen TP, Olcese R, Chen PS, Qu Z.** Perspective: a dynamics-based classification of ventricular arrhythmias. *J Mol Cell Cardiol* 82: 136–152, 2015.
52. **Western D, Hanson B, Taggart P.** Measurement bias in activation-recovery intervals from unipolar electrograms. *Am J Physiol Heart Circ Physiol* 308: H331–H338, 2015.
53. **Wyatt RF, Burgess MJ, Evans AK, Lux RL, Abildskov JA, Tsutsumi T.** Estimation of ventricular transmembrane action potential durations and repolarization times from unipolar electrograms. *Am J Cardiol* 47: 488, 1981.
54. **Xie Y, Grandi E, Puglisi JL, Sato D, Bers DM.** β-Adrenergic stimulation activates early afterdepolarizations transiently via kinetic mismatch of PKA targets. *J Mol Cell Cardiol* 58: 153–161, 2013.
55. **Yamakawa K, So EL, Rajendran PS, Hoang JD, Makkar N, Mahajan A, Shivkumar K, Vaseghi M.** Electrophysiological effects of right and left vagal nerve stimulation on the ventricular myocardium. *Am J Physiol Heart Circ Physiol* 307: H722–H731, 2014.

frontiers in
PHYSIOLOGY

ORIGINAL RESEARCH ARTICLE
published: 28 October 2014
doi: 10.3389/fphys.2014.00414

Oscillatory behavior of ventricular action potential duration in heart failure patients at respiratory rate and low frequency

Ben Hanson[1], Nick Child[2], Stefan Van Duijvenboden[1], Michele Orini[3], Zhong Chen[2], Ruben Coronel[4], Christopher A. Rinaldi[2], Jaspal S. Gill[5], Jaswinder S. Gill[2] and Peter Taggart[3]*

[1] Department of Mechanical Engineering, University College London, London, UK
[2] Cardiovascular (Imaging) Department, King's College London, London, UK
[3] Institute of Cardiovascular Science, University College London, London, UK
[4] Department of Experimental Cardiology, Academic Medical Center, Amsterdam, Netherlands
[5] Division of Medicine, University College London, London, UK

Edited by:
Sami Noujaim, Tufts University School of Medicine, USA

Reviewed by:
David Filgueiras-Rama, Centro Nacional de Investigaciones Cardiovasculares, Spain
Ed White, University of Leeds, UK

***Correspondence:**
Peter Taggart, Department of Cardiovascular Sciences, The Heart Hospital, Westmoreland Street, London W1G8PH, UK
e-mail: peter.taggart@uclh.nhs.uk

Oscillations of arterial pressure occur spontaneously at a frequency of approximately 0.1 Hz coupled with synchronous oscillations of sympathetic nerve activity ("Mayer waves"). This study investigated the extent to which corresponding oscillations may occur in ventricular action potential duration (APD). Fourteen ambulatory (outpatient) heart failure patients with biventricular pacing devices were studied while seated upright watching movie clips to maintain arousal. Activation recovery intervals (ARI) as a measure of ventricular APD were obtained from unipolar electrograms recorded from the LV epicardial pacing lead during steady state RV pacing from the device. Arterial blood pressure was measured non-invasively (Finapress) and respiration monitored. Oscillations were quantified using time frequency and coherence analysis. Oscillatory behavior of ARI at the respiratory frequency was observed in all subjects. The magnitude of the ARI variation ranged from 2.2 to 6.9 ms (mean 5.0 ms). Coherence analysis showed a correlation with respiratory oscillation for an average of 43% of the recording time at a significance level of $p < 0.05$. Oscillations in systolic blood pressure in the Mayer wave frequency range were observed in all subjects for whom blood pressure was recorded ($n = 13$). ARI oscillation in the Mayer wave frequency range was observed in 6/13 subjects (46%) over a range of 2.9 to 9.2 ms. Coherence with Mayer waves at the $p < 0.05$ significance level was present for an average of 29% of the recording time. In ambulatory patients with heart failure during enhanced mental arousal, left ventricular epicardial APD (ARI) oscillated at the respiratory frequency (approximately 0.25 Hz). In 6 patients (46%) APD oscillated at the slower Mayer wave frequency (approximately 0.1 Hz). These findings may be important in understanding sympathetic activity-related arrhythmogenesis.

Keywords: action potential duration, Mayer wave, respiration, oscillation, ARI

INTRODUCTION

Oscillatory activity is a ubiquitous property of autonomic nerves innervating the heart, and is considered by some to facilitate synchronization of nerve traffic and hence potentiate the response. Oscillations at a low frequency of approximately 0.1 Hz, known as Mayer waves, occur in arterial pressure coupled with synchronous sympathetic efferent nerve activity and are exaggerated during enhanced sympathetic activity (Julien, 2006; Malpas, 2010). The mechanism of these systolic blood pressure oscillations is thought to involve sympathetic modulation of peripheral vascular resistance and the baroreflex response, although their exact relationship remains to be determined (Julien, 2006; Malpas, 2010). Since sympathetic nerves are known to innervate ventricular myocardium, and elicit changes in the potassium and calcium channels, both of which are important components of the cardiac action potential, it is possible that oscillations in APD may also occur at this slower frequency (Zipes and Jalife, 1999; Workman, 2010; Taggart et al., 2011; Shen and Zipes, 2014). Such time-varying and regional oscillation of APD could have important implications for arrhythmogenesis, since beat to beat variability in APD has been associated with ventricular arrhythmogenesis and sudden cardiac death (Nearing and Verrier, 2002; Thomsen et al., 2007; Qu et al., 2010; Heijman et al., 2013; Xie et al., 2014). We have previously reported oscillations of ventricular action potential duration (APD) in humans occurring at free and voluntarily-controlled respiratory frequencies (Hanson et al., 2012). These data in subjects whose heart rate was paced at a fixed rate indicated that the variability in APD was independent of respiration-induced changes in heart rate. However, to the authors' knowledge, variation of APD in synchronization with Mayer waves has not been reported.

In order to study this relationship we recruited patients with heart failure in whom a biventricular pacing resynchronization device had been implanted. This enabled ambulatory recording of electrophysiology to be made directly from the left ventricular epicardium. As mental stress is known to enhance Mayer wave oscillations in blood pressure (Lucini et al., 2002), we devised a protocol whereby subjects were studied while watching emotionally-charged movie clips to elicit and maintain a state of arousal. A unipolar electrogram (UEG) was recorded from an epicardial electrode of the device and activation-recovery intervals (ARI) were obtained as a surrogate measure of APD. We observed oscillatory behavior of APD (ARI) in synchrony with respiration and blood pressure Mayer waves.

MATERIALS AND METHODS

Ethical approval: The study was approved by the local Ethics Committee (Ref: 05/Q0702/89) and conformed to the standard set by the Declaration of Helsinki (latest revision: 59th WMA General Assembly). Written informed consent was obtained from all subjects.

SUBJECTS AND PROTOCOL

Studies were performed in 14 ambulatory (outpatient) subjects with heart failure (all male, age 48–80 (**Table 1**). All subjects were undergoing treatment via implanted bi-ventricular cardiac resynchronization devices, which had been implanted for at least 6 months prior to study. Beta-adrenergic blocking agents were discontinued for 5 days prior to the study. Recordings were made with the subjects seated upright and stationary, facing a large display screen (approximately 1 m diagonal width, at a distance of 2.2 m) wearing over-the-ear headphones in a quiet room with dimmed lighting. To elicit and maintain heightened arousal of the sympathetic nervous system throughout the duration of the investigation, subjects were presented with excerpts containing dramatic sequences from the psychological horror film "The Shining" (Kubrick, 1980). Three excerpts were chosen, allowing three physiological recordings as described in Section Physiological Recordings. This study did not attempt to identify physiological changes in response to the specific stimuli, which are highly subjective.

Table 1 | Subject characteristics.

Subject	Age (years)	Gender	Diagnosis	NYHA Class	Ejection fraction (%)
1	77	M	NICM	2	23
2	67	M	NICM	2	30
3	69	M	IHD	1	35
4	77	M	IHD	3	30
5	61	M	IHD	2	55
6	63	M	NICM	2	45–50
7	63	M	IHD	1	45
8	68	M	IHD	2	40
9	67	M	NICM	1	37
10	80	M	IHD	2	40
11	72	M	NICM	2	65
12	80	M	NICM	1	60–65
13	48	M	NICM	2	39
14	59	M	IHD	1	49
Range	48–50			1–3	23–65
Mean ± *SD*	68 ± 9				42 ± 12

IHD, Ischemic heart disease; NICM, non-ischemic cardiomyopathy.

PHYSIOLOGICAL RECORDINGS

APD is strongly dependent on the interval between beats, which fluctuates over a wide range of frequencies from 0 up to half the heart beat frequency (i.e., every other beat); in this study, that confounding variation was isolated by maintaining the subjects' heart rate at a constant rate by right ventricular pacing (Hanson et al., 2012; Child et al., 2014), using their implanted pacing device. The pacing rate was chosen as a minimum rate sufficient to maintain continuous capture. Recordings were made after a minimum adaptation period of 2 min of pacing.

The implanted cardiac resynchronization device was also used to record unipolar electrograms from the left ventricular epicardial lead, sampled at 512 Hz. For a comparison between the unipolar electrogram and monophasic action potential. The devices used in this study were able to store five separate recordings of 30 s duration; a continuous recording of approximately 100 s was constructed by overlapping the 30 s recordings. Activation-recovery intervals (ARI) were measured from the time of minimum dV/dt of the electrogram QRS complex, representing local activation time, to the time of maximum dV/dt of the subsequent T-wave, representing local repolarization time (Wyatt et al., 1981; Haws and Lux, 1990; Coronel et al., 2006; Potse et al., 2009). The time resolution of ARI measurements was 1.95 ms (1/512 Hz). Ectopic beats occurred infrequently (median 0.68% of beats across all recordings) and were removed from analysis together with the successive beat. Afterwards, linear interpolation was applied to fill in missing ARI values (Task Force of the European Society of Cardiology and the North American Society of Pacing and Electrophysiology, 1996). Recordings in which ectopic beats comprised more than 10% of the total number of beats were rejected from the analysis (only 1 recording in this study).

Breathing activity was recorded by measuring chest circumference: a custom-adapted tension sensor (adapted from a RESPeRATE device, InterCure Inc., New York, NY, USA) fixed to an expandable elastic band was placed around the subject's abdomen. Tension in the elastic band was directly proportional to circumference, and hence inspiration. The signal was digitized and sampled at 6 Hz.

Arterial blood pressure was measured non-invasively using a finger cuff (Finometer pro, Finapres Medical Systems B.V., Amsterdam, The Netherlands). The signal was digitized and sampled at 1 kHz. Systolic blood pressure for each beat was computed as the maximum blood pressure measured from the pressure waveform using a script written in MATLAB (Mathworks, Inc., Natick, MA, USA).

These physiological recordings were synchronized using a short-duration electrical "spike" signal which was recorded across all measurement systems.

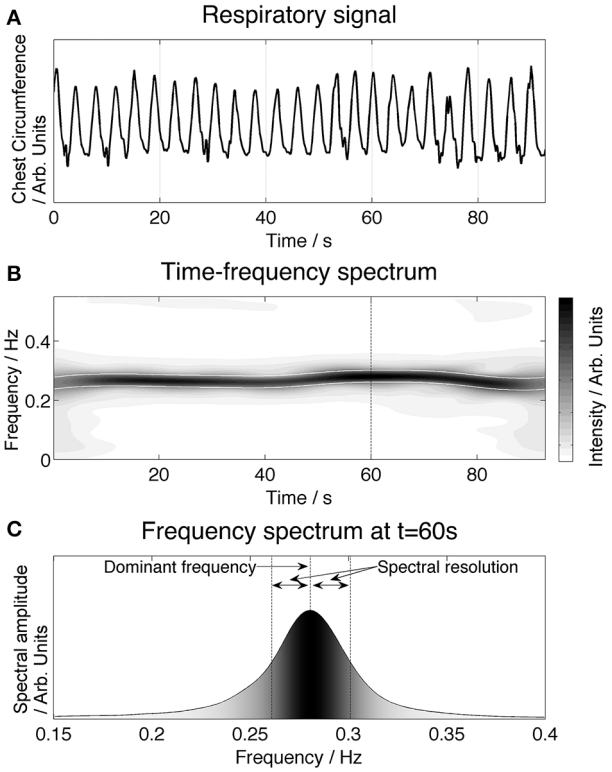

FIGURE 1 | Illustration of time-frequency analysis of the respiratory signal and the definition of the respiratory frequency band. The upper panel **(A)** shows the time series of the respiratory signal. The corresponding time-frequency spectrum is presented in the middle panel **(B)**. The intensity of a specific frequency is given by the grayscale (white: low intensity, black: high intensity). An enhanced frequency band is clearly visible at the respiratory frequency (approximately 0.28 Hz in this example). The frequency spectrum **(C)** provides a cross-section of the time-frequency plot at 60 s, shown by a dashed line in **(B)**. The respiratory frequency band is defined by taking the maximum amplitude frequency ± the spectral resolution.

ANALYSIS OF DATA

Respiratory frequency oscillation

To quantify the respiratory frequency over the duration of the recordings we applied time-frequency analysis, which computes the frequency spectrum as a function of time. In **Figure 1**, the upper panel **(A)** shows the time series of the respiration signal. In the middle panel **(B)**, the time-frequency representation is shown: the horizontal axis represents time, the vertical axis gives the frequency and the amplitude is visualized by the grayscale. A high intensity (dark color) band is found around the respiratory frequency (approximately 0.28 Hz). The lower panel (C) demonstrates how the respiratory frequency band is defined as the dominant frequency ± the spectral resolution inside a high frequency band (0.15–0.5 Hz).

The time-frequency method used in this study is based on Cohen's class of quadratic time-frequency distributions, the smoothed pseudo-Wigner-Ville distribution (SPWVD). Previous research has demonstrated that this method provides good temporal and frequency resolution and is suitable to study cardiovascular interactions (Orini et al., 2012a). The spectral resolution depends on the SPWVD smoothing function, and was defined by the width of the smoothing function at the level of 50% of the maximum amplitude (**Figure 1C**).

To test whether ARI was oscillating with respiration, we evaluated if the ARI and respiration signals were coupled at the respiratory frequency. Coupling was studied using time-frequency coherence, Equation 1:

$$\gamma(t,f) = \frac{|S_{xy}(t,f)|}{\sqrt{S_{xx}(t,f)S_{yy}(t,f)}} \gamma(t,f) \in [0,1] \quad (1)$$

where: $\gamma(t,f)$ quantifies the strength of the linear coupling between signals x and y at time, t, and frequency, f. The strength of the coupling is defined between 0 (absence of correlation) and 1 (complete correlation). S_{xx} and S_{yy} are the time-frequency (TF) spectra of the x and y respectively (from the autocorrelation of each signal), and S_{xy} is the cross-time-frequency spectrum, which is the TF spectrum of the cross-correlation between x and y. The cross-correlation evaluates the similarity between the two signals.

Mayer-wave frequency oscillation

In the second part of the analysis, the ARI signals were examined for oscillations at Mayer-wave frequencies. The relationship between Mayer waves in blood pressure and slow oscillations in ARI was studied as follows:

1. First, the blood pressure signals (BP) were analyzed for presence of Mayer waves. Mayer waves were assumed to be present in the signal if the average frequency spectrum contained a significant peak (see following Section Determination of Statistical Significance) in the low frequency band (0.04–0.15 Hz). The Mayer frequency was then defined as the peak-frequency ± the spectral resolution of the average frequency spectrum.
2. Time intervals were identified in which oscillatory behavior in ARI and/or blood pressure was statistically significant at the Mayer frequency.
3. The obtained intervals were categorized into the four possible conditions depending whether Mayer waves were present in BP and/or ARI measures:

Condition	BP	ARI
1	×	×
2	×	✓
3	✓	×
4	✓	✓

✓ Presence of Mayer waves in the signal; × Absence of Mayer waves.

A final step was applied in condition 4: to investigate whether the Mayer-wave oscillations in BP and ARI were significantly coupled. This was assessed by the TF coherence method described previously.

Determination of statistical significance

To determine the average peak to peak amplitude of the significant ARI oscillations we computed the amplitude spectrum and measured the peak at the respiratory and Mayer frequency.

The time frequency spectra contain components of signals across the frequency range, including some measurement noise, and it is important to identify whether the magnitudes of oscillations at respiratory and Mayer wave frequencies are significant in comparison to the noise. The method involves creating surrogate data (Faes et al., 2004): the samples of the measured signals were randomly shuffled to create a surrogate signal having the same important features at equal magnitudes while being completely uncoupled. This process was repeated 10,000 times to obtain a distribution of time frequency spectra and time frequency coherence values created by random. Consequently, the values of the real data signals were assumed to be significant if they exceeded a threshold set at the 100(1-α) percentile of the noise distribution, where α is the significance level of the statistical test. In this study, the threshold for significance was set at $\alpha = 5\%$.

RESULTS

Due to the challenging logistics of recording from multiple measurement systems concurrently it was not possible to achieve complete recordings in every instance, however recordings were obtained from 8/14, 13/14, and 14/14 subjects for the three recording periods, respectively. One electrophysiological recording was not analyzed because of the presence of multiple escape—un-paced—beats. One respiratory recording was rejected because it did not show a clear respiratory component. In one subject blood pressure measurements were not obtainable. A total of 33 ARI, 30 blood pressure, and 32 respiratory traces obtained from 14 subjects were analyzed. The average paced heart rate was 85 bpm.

ARI OSCILLATIONS AT RESPIRATORY FREQUENCY

All patients showed significant ARI oscillation at the respiratory frequency (**Table 2**). The average ARI peak to peak differences per patient were between 2.2 and 6.9 ms and averaged 5 ms. **Figure 2** shows an example in which ARI oscillations at the respiratory frequency were observed during the entire recording period. The two uppermost plots, **Ai** and **Bi** show the time series of ARI and respiration respectively. The ARI exhibits cyclical variation at a frequency similar to the respiratory pattern, notably in the absence of respiratory sinus arrhythmia since the heart rate is paced (at 80 bpm in this case). Plots **Aii** and **Bii** show the corresponding time-frequency spectra. The ARI time-frequency spectrum shows an enhanced amplitude (higher intensity) at the respiratory frequency band (approximately 0.25 Hz) indicating that the ARI is oscillating at this frequency for the duration of the recording (in addition to transitory oscillations at other frequencies). The cross-time-frequency spectrum (plot C) shows a high intensity inside the respiratory frequency band which demonstrates a correlation between ARI and respiration at the respiratory frequency. The time-frequency coherence analysis (plot D) shows that the coupling between ARI and respiration is statistically significant at the respiratory frequency for the whole length of the recording. In all other subjects coupling between ARI and respiration occurred intermittently during the recordings. The average coupling time was about 43% of the total recording time for each subject.

Table 2 | Oscillatory behavior of ARI.

	Oscillations at respiratory frequency			Oscillations at Mayer frequency		
Subject	**Coupling**	**Amplitude, ms**	**Duration, % of total recording**	**Coupling**	**Amplitude, ms**	**Duration, % of total recording**
1	+	5.7	9	–	–	–
2	+	2.3	57	–	–	–
3	+	3.5	27	–	–	–
4	+	6.9	40	–	–	–
5	+	3.9	61	–	–	–
6	+	3.6	42	+	5.5	19
7	+	4.4	95	–	–	–
8	+	3.5	36	–	–	–
9	+	2.7	52	+	2.9	8
10	+	2.2	34	+	5.4	33
11	+	5.2	21	+	3.6	66
12	+	4.4	16	–	–	–
13	+	2.8	68	X	9.2*	X
14	+	2.4	42	+	3.4	18
Range		2.2–6.9	9–95		2.9–9.2	8–66
Mean ± SD		3.8 ± 1.4	43 ± 23		5.0 ± 2.3	29 ± 23

*In all subjects, ARI showed oscillations at the respiratory frequency. In 6 subjects we observed significant slow oscillatory behavior in the Mayer frequency range, which was coupled in 5 subjects with Mayer waves in blood pressure (BP not available in 6th subject). The amplitude quoted is the average peak to peak amplitude over the total duration of oscillation for each subject. Duration represents the total period for which oscillation was both of significant magnitude ($p < 0.05$) and coupled to oscillation in BP, expressed as a fraction of the total duration of the three recording periods. SD, standard deviation; x, data not available. *, Blood pressure recordings not available; –, no significant oscillation recorded; +, coupling significant at $p < 0.05$.*

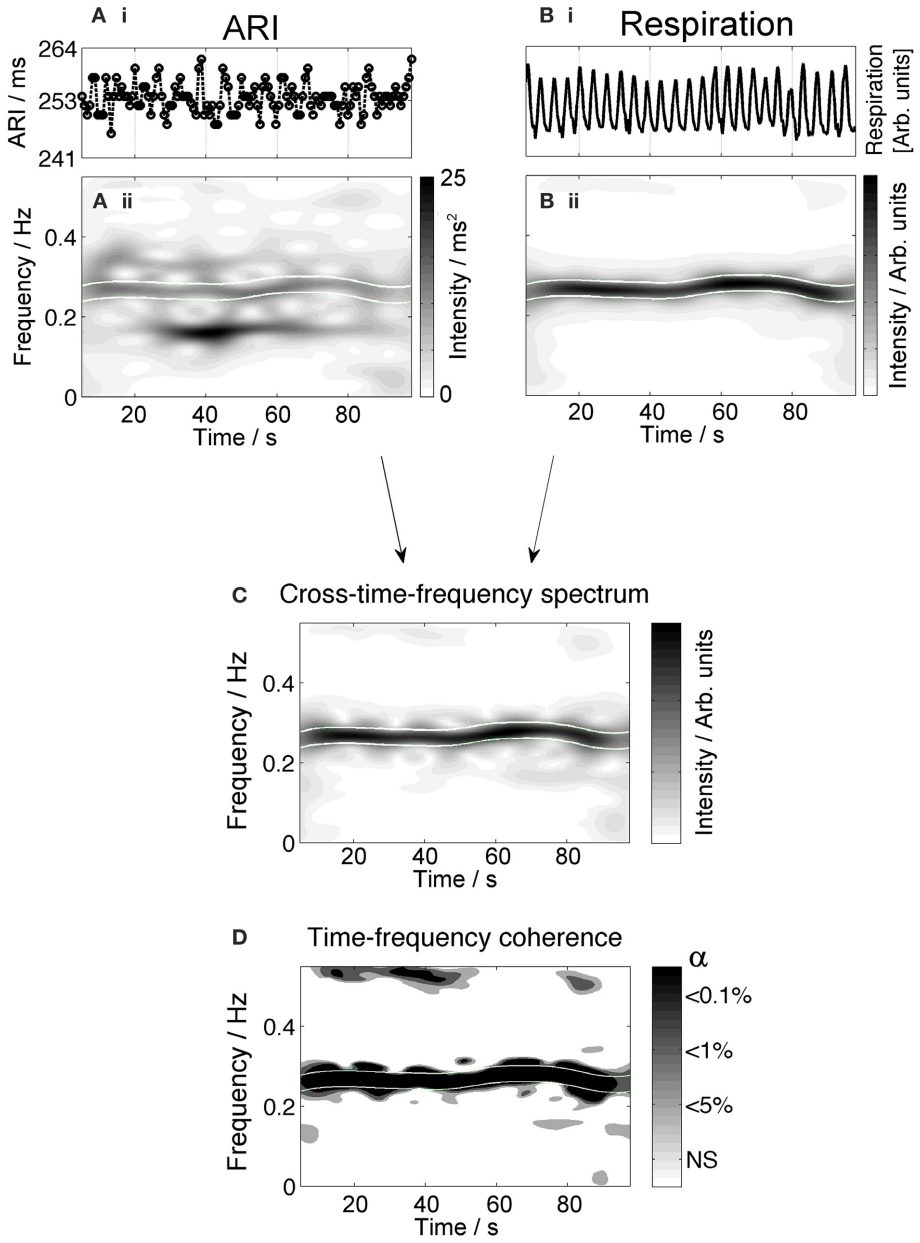

FIGURE 2 | Example plot showing oscillations in the ARI signal at the respiratory frequency. The top graphs **(Ai,Bi)** show the time series of ARI and respiration. The corresponding time-frequency spectra are plotted below, **(Aii,Bii)**. The high intensity band in the time-frequency spectrum of the respiratory signal **(Bii)** represents the frequency of the respiratory signal (approximately 0.25 Hz). High intensity is also seen in the ARI time-frequency plot **(Aii)** in this frequency band. Oscillation is also present at other frequencies and times across the spectrum. The cross time- frequency spectrum **(C)** shows that the ARI and respiratory signal are correlated at the respiratory frequency and the other variations in each signal are not correlated. The results of coherence analysis in the lower panel **(D)** show the coherence at the respiratory frequency is significant at $p < 0.001$, indicating that both signals are coupled at this frequency. *NS* = not significant.

ARI OSCILLATIONS AT MAYER-WAVE FREQUENCIES

Significant Mayer waves were observed in all patients in whom blood pressure recordings were available, (13/14). Oscillatory behavior—of ARI at the Mayer wave frequency was observed in 6/13 (46%) of subjects (**Table 2**). The average peak to peak ARI differences ranged from 2.9 to 9.2 ms between subjects. An example is shown in **Figure 3** in which ARI oscillates at a frequency of 0.05 Hz and has a maximum peak-to-peak amplitude of approximately 15 ms.

Synchronization of low-frequency oscillations in ARI and Mayer waves is shown in **Figure 4**. **Figures 4Ai,Bi** show the time series of ARI and systolic blood pressure with clearly-visible waves in the blood pressure occurring at a 10 s period. The time frequency spectrum of this signal, **Figure 4Bii**, shows

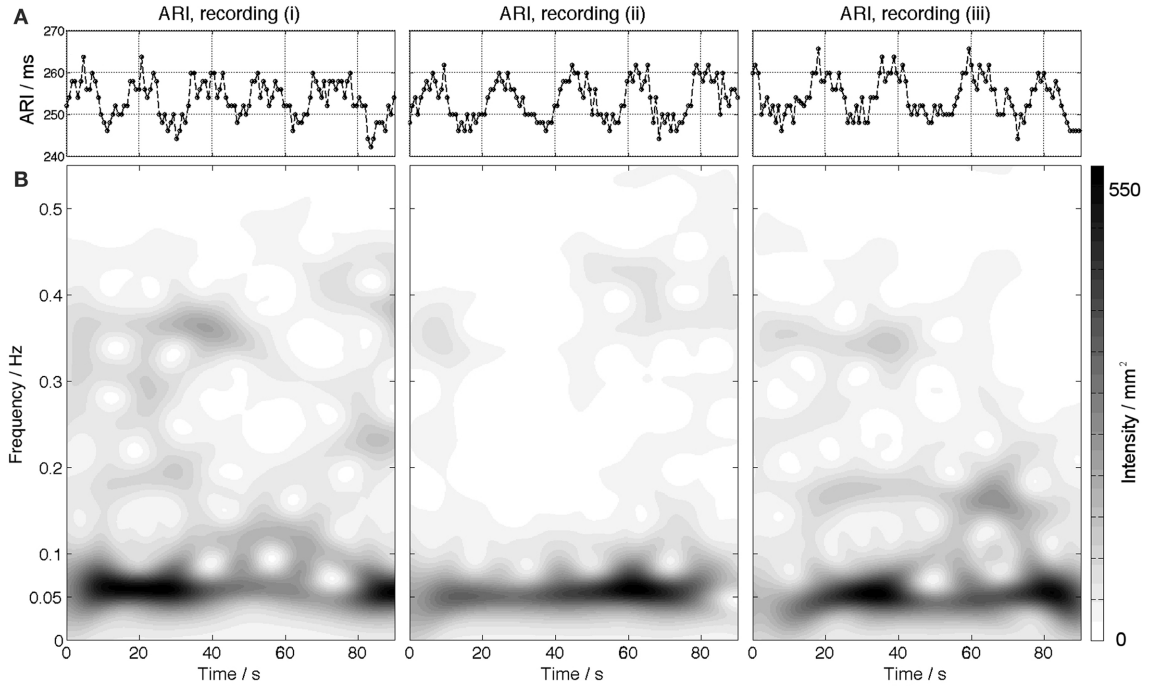

FIGURE 3 | An example is shown for one subject illustrating ARI time series (A) oscillating with a peak-to-peak amplitude of 10–15 ms. The lower panels **(B)** show the corresponding time-frequency spectra. The spectra show an increased intensity at a frequency of 0.05 Hz.

a high intensity at 0.1 Hz. The ARI time-frequency spectrum **Figure 4Aii** also shows increased intensity at 0.1 Hz. The cross-time-frequency spectrum, **Figure 4C**, confirms a correlation between ARI and systolic blood pressure at this frequency. Finally, coherence analysis shown in the lower panel, **Figure 4D**, demonstrates that the slow oscillations in ARI are significantly coupled with oscillations in systolic pressure, throughout 78% of the recording time (average: 66% over all 3 recordings for this subject, summarized in **Table 2**).

When Mayer waves were present in BP, significant ARI oscillations in the Mayer frequency range were observed an average of 29% of the time, across all recordings and patients. On occasions when oscillations of ARI and systolic pressure were both present, they were coupled at the significance level of $p < 0.05$ for 75–100% of the duration of the oscillatory period. When Mayer waves were absent in blood pressure, there were some instances of significant ARI oscillations in the Mayer frequency range; across all recordings and patients this occurred for 8% of the time. Data for all patients are summarized in **Table 2**.

There was no relation between ejection fraction (EF) or heart failure class and the occurrence of slow oscillating behavior in ARI that was correlated with Mayer waves. However, five of the six patients that showed slow oscillating behavior had non-ischemic cardiomyopathy and only 1 had ischemic heart disease (IHD). None of the other patients with IHD showed these slow oscillations.

DISCUSSION

Ambulatory heart failure patients exhibited oscillation of left ventricular epicardial APD (measured as ARI) at two main frequencies. Oscillations in APD were present for all subjects at the respiratory frequency which were strongly correlated with respiration. Oscillations in APD were also present at a slower frequency (approximately 0.1 Hz) in a proportion of subjects which were coupled with systolic blood pressure oscillations. These APD oscillations were independent of beat to beat interval, which was constant (paced).

Ventricular activation exhibits cyclical variation such that the interval between heartbeats varies with the respiratory cycle, increasing with expiration and decreasing with inspiration, known as respiratory sinus arrhythmia (Anrep et al., 1936; Cohen and Taylor, 2002; Eckberg, 2009). It was recently reported that ventricular APD (measured as ARI) also varies cyclically with respiration (Hanson et al., 2012). This study in subjects with normal ventricles examined 10 left and 10 right ventricular endocardial sites at breathing frequencies of 6, 9, 12, 15, and, 30 breaths per min. Cyclical variation of APD at the respiratory frequency was observed with maximum magnitudes over a range from 0 to 26 ms. The present observations corroborate the existence of APD oscillations in humans and extend the findings to ambulatory patients with heart failure.

Oscillations in arterial pressure have long been known to occur at a frequency slower than respiration, known as Mayer waves (Mayer, 1876; Julien, 2006; Malpas, 2010). The present results demonstrate for the first time measurements of ventricular APD oscillations at the frequency range of the known Mayer wave oscillations, which were observed in a paced, heart-failure human model. Although commonly occurring at a frequency of approximately 0.1 Hz, Mayer waves occur over a fairly wide range of frequencies spanning the range of 0.03 to 0.15 Hz

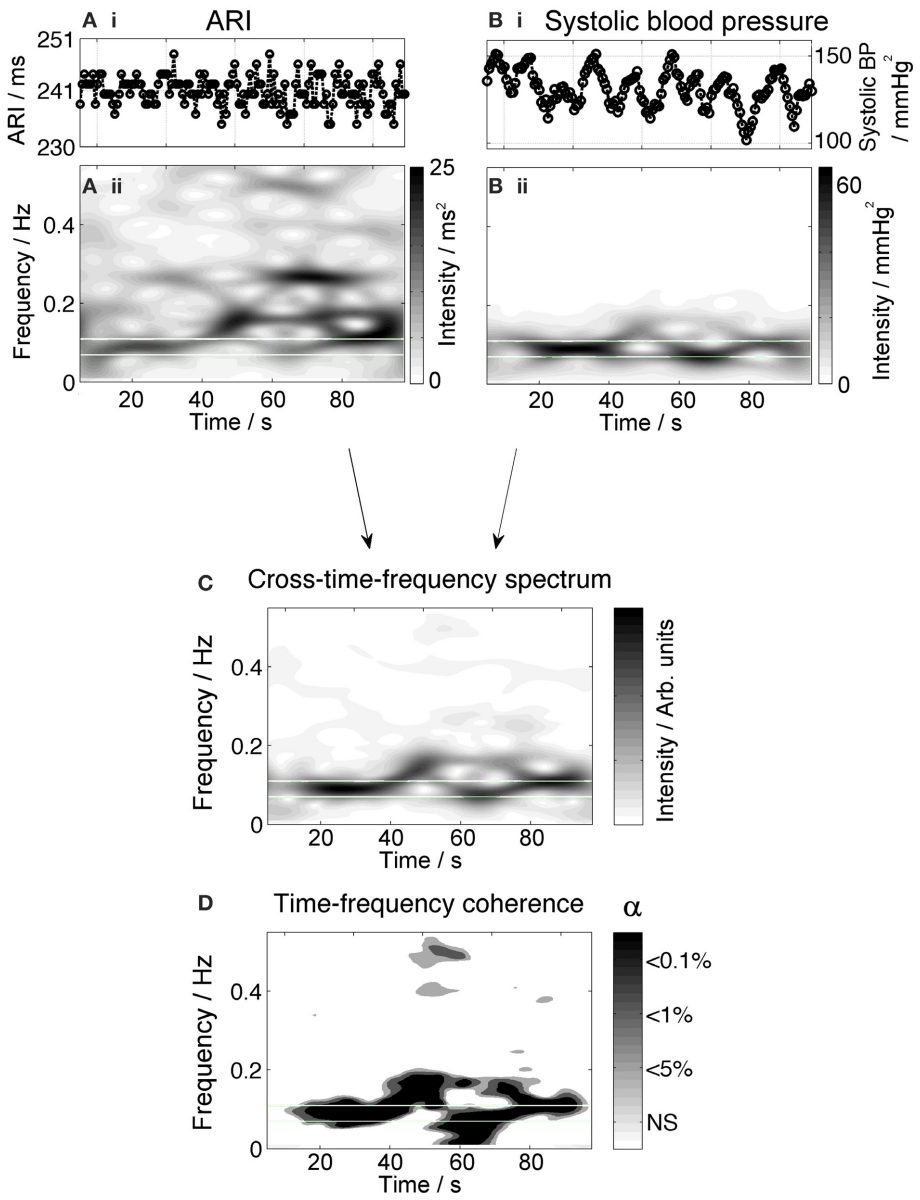

FIGURE 4 | Example measurements from one subject showing oscillatory behavior of ARI at the Mayer frequency. The upper panels **(Ai,Bi)** show the time series of ARI and blood pressure, respectively. Blood pressure shows prominent oscillation with a 10-s period; ARI shows oscillation at this rate as well as variation at higher frequencies. The corresponding time-frequency spectra, **(Aii,Bii)**, show high-intensity bands highlighting the presence of waves at a Mayer wave frequency (0.1 Hz). The cross time-frequency spectrum **(C)** demonstrates that the ARI and blood pressure are correlated at the Mayer frequency and not at other frequencies of oscillation. The results of coherence analysis in the lower panel **(D)** show the coherence at the respiratory frequency is significant at $p < 0.001$, indicating that both signals are coupled at this frequency over most of the recording.

(Cohen and Taylor, 2002). The frequency range of the slow oscillations we observed was 0.04 to 0.12 Hz.

EXPERIMENTAL MODEL

The methodology employed in this study was novel: the study was designed to enable measurements of epicardial ventricular APD in ambulatory humans during a period of enhanced emotional arousal. The left ventricular pacing electrode of the biventricular pacing device enables recordings to be made of UEGs from the epicardium, while steady-state pacing was maintained from the right ventricular electrode in order to isolate changes in ARI (APD) from cycle length-dependent effects.

Mayer oscillations are associated with oscillations of sympathetic nervous tone (Cevese et al., 2001; van de Borne et al., 2001): these subjects were studied while seated in an upright position which is known to facilitate sympathetic activation. Sympathetic activity may have been further exaggerated in this heart failure patient group, whose hemodynamic function is less than normal, particularly during the pacing strategy employed in this experiment. Emotional arousal was enhanced by the use of movie

excerpts which are considered to be among the most-powerful stimuli to elicit affective responses in the laboratory setting (Westermann et al., 1996; Schaefer et al., 2010). In this study we made no attempt to investigate how oscillatory APD behavior changes in response to different degrees of stress and tranquility, which is a highly-subjective measurement, but focussed on establishing the existence of these phenomena under conditions likely to enhance their presence.

The time frequency coherence method applied in this study accounts for the time-varying nature (non-stationarity) of the oscillations in ARI, systolic blood pressure and respiration signals. It has been demonstrated recently that the Cohen's class distributions used for this study can be used to reliably quantify the dynamic interactions between cardiovascular signals, such as heart rate variability, BP and respiration (Orini et al., 2012a,b). The statistical significance of the time frequency coherence was assessed by using surrogate data analysis to establish the "noise floor" of the recordings to determine the confidence interval. Subsequently it was demonstrated that oscillations in ARI and BP showed significant coupling at the respiratory rate and at Mayer wave frequencies with significance levels reaching $p < 0.001$ for periods.

In this study, we examined whether slow oscillatory behavior in both APD and blood pressure was present or absent at the same time. The results suggest that if Mayer waves are absent in blood pressure, oscillations in APD at the Mayer wave frequency are also likely to be absent. On the other hand, when Mayer waves were observed in blood pressure, they were sometimes but not always accompanied by coupled oscillations in APD. It should be noted that since APD variation may be heterogeneous, it is possible that APD oscillation was present in ventricular regions which were not captured by the single-site epicardial recording used here (see Limitations).

UNDERLYING MECHANISMS

At the respiratory frequency

These results support a relationship between respiration and electrophysiology, demonstrating significant coupling between oscillation in ARI and BP with respiration. A previous study employed a constant-rate breathing protocol to observe rate-dependence and phase relationships (Hanson et al., 2012); in this study there was natural variation in each subject's breathing rate and statistical coupling was retained. We have previously proposed and discussed in some detail several possible mechanisms as underlying the APD oscillations seen at the respiratory frequency in subjects with normal ventricles (Hanson et al., 2012). In brief: One possibility is mechano-electric feedback whereby changes in ventricular load alter the electrophysiology (Kohl et al., 2006; Taggart and Sutton, 2011). Respiration results in a cyclical change in ventricular filling and hence in myocardial loading conditions (Guz et al., 1987). Furthermore, these effects are more pronounced when cycle length is maintained constant by constant pacing as was the case in the present study (Innes et al., 1987). Previous studies in humans have shown that altering ventricular loading alters ventricular APD over a range comparable to that seen in the present study (Taggart and Sutton, 2011). Two other mechanisms which have been proposed to account for respiratory related oscillations of sinus node firing could be operative (Task Force of the European Society of Cardiology and the North American Society of Pacing and Electrophysiology, 1996; Malliani, 2000; Cohen and Taylor, 2002; Eckberg, 2009; Karemaker, 2009). The baroreflex mechanism attributes fluctuations in RR interval to baroreflex-induced fluctuations in vagal activity in response to respiration induced changes in stroke volume (de Boer et al., 1987; Innes et al., 1993). An alternative mechanism is central gating of autonomic drive to the myocardium by central respiratory networks (Spyer and Gilbey, 1988; Dergacheva et al., 2010). In this heart failure model we observed similar magnitudes of variation in ARI as those observed in normal ventricles (Hanson et al., 2012), however this was only a single-point measurement and it is likely that ARI variation was heterogeneous across the myocardium as previously observed. Multi-site mapping is recommended to identify whether diseased ventricles exhibit a higher-degree of local heterogeneity in ARI as a result of respiratory-related variation.

At Mayer-wave frequencies

The presence of significant coupling between ARI and systolic blood pressure suggests the possibility that both signals may be driven by a common source. That possibility is further supported by occurrences of significant oscillations at Mayer frequencies in ARI in the absence of oscillations in BP, and vice-versa. The data do not wholly support a model of ARI oscillation being dependent on BP oscillation, nor vice-versa. The experimental model was not able to identify phase relationships between oscillations in ARI and BP since the periods of oscillation and coupling varied and steady-state oscillation was not observed. Mayer wave oscillations on systolic blood pressure are generated by oscillations of sympathetic tone (Cevese et al., 2001; van de Borne et al., 2001). Two mechanisms have been proposed to explain their consistent frequency. One theory attributes the rhythmicity of Mayer waves to pacemaker-like activity of an oscillator in the brainstem or spinal cord region generating sympathetic nerve activity. An alternative theory proposes that Mayer waves are oscillatory responses to hemodynamic changes and governed by the magnitude of the hemodynamic change and the sensitivity of the sympathetic limb of the baroreflex (for review see Julien, 2006 and Malpas, 2010). The mechanism underlying the synchronous slow oscillations in APD has yet to be determined. Either of the above mechanisms could be associated with phasic autonomic input to the ventricular myocardium and a direct effect on the cellular electrophysiology. Our study does not allow discrimination between the two possibilities. Mechano-electric feedback may play a role whereby the APD oscillations are secondary to the phasic mechanical stimuli accompanying the oscillations in systolic pressure. In patients with heart failure the myocardial stress may be different to that in normal hearts because of altered diastolic stiffness. Further work is recommended to elucidate the mechanisms.

LIMITATIONS

In this study, it was not possible to pace and record from the same lead due to electrical interference, hence the RV was paced and LV sensed. This pacing protocol may have significantly affected

the haemodynamic efficiency. In our previous study frequency in subjects with normal ventricles, we observed that the presence and magnitude of APD oscillation on the endocardium at the respiratory was inhomogeneous (Hanson et al., 2012). However, the electrophysiological measurements in the present study were obtained from single site recordings on the left ventricular epicardium, and therefore we cannot comment on whether the oscillatory behavior we observed on APD was a local or generalized phenomenon. In our previous study in which blood pressure was recorded directly from the aorta, we performed phase analysis between BP and APD; this was not possible in the present study owing in part to the technical limitations of the non-invasive system (Finometer pro, Finapres Medical Systems B.V., Amsterdam, The Netherlands). Intra-arterial measurements were precluded in this set-up as they were not appropriate for this ambulatory patient group. The question as to whether slow wave APD oscillations are confined to heart failure patients or also occur in normal subjects cannot be addressed at the present time owing to the inability to perform comparable intracardiac electrophysiology measures in normal subjects.

IMPLICATIONS

In general, oscillatory behavior of APD such as APD alternans or beat to beat APD variability, reflect repolarization instability and an increased susceptibility to arrhythmogenesis (Nearing and Verrier, 2002; Thomsen et al., 2007; Qu et al., 2010; Heijman et al., 2013; Xie et al., 2014). It remains to be determined whether the APD oscillation we observed, particularly at the slower frequencies, represents simply a benign enhancement of normal physiology or whether it represents a destabilization of the repolarization process which may have consequences in the context of arrhythmogenesis.

AUTHOR CONTRIBUTIONS

Ben Hanson, Peter Taggart, Nick Child and Jaswinder Gill conceived and designed the experiments. All authors took responsibility in collecting, analyzing and interpreting the data, with particular individual input in the following areas: electrophysiology (Peter Taggart), analysis (Stefan Van Duijvenboden), experimentation (Nick Child). All authors contributed to drafting or revising the manuscript and all authors approved the final version of the manuscript.

ACKNOWLEDGMENTS

Prof. Taggart and Dr. Hanson are part-supported by a grant from the UK Medical Research Council (G0901819). Dr. Gill received funding from the Academic Health Sciences Centre for research activity time. Dr. Child is supported by an educational grant from St. Jude Medical.

REFERENCES

Anrep, G. V., Pascual, W., and Rossler, R. (1936). Respiratory variations of the heart rate. I.-The reflex mechanism of the respiratory arrhythmia. *Proc. R. Soc. Lond. B* 119B, 191–217. doi: 10.1098/rspb.1936.0005

Cevese, A., Gulli, G., Polati, E., Gottin, L., and Grasso, R. (2001). Baroreflex and oscillation of heart period at 0.1 Hz studied by alpha-blockade and cross-spectral analysis in healthy humans. *J. Physiol. (Lond.)* 531(Pt 1), 235–244. doi: 10.1111/j.1469-7793.2001.0235j.x

Child, N., Hanson, B., Bishop, M., Rinaldi, C. A., Bostock, J., Western, D., et al. (2014). Effect of mental challenge induced by movie clips on action potential duration in normal human subjects independent of heart rate. Circ. Arrhythm. Electrophysiol. 15, 2014. doi: 10.1161/CIRCEP.113.000909

Cohen, M. A., and Taylor, J. A. (2002). Short-term cardiovascular oscillations in man: measuring and modelling the physiologies. *J. Physiol. (Lond.)* 542(Pt 3), 669–683. doi: 10.1113/jphysiol.2002.017483

Coronel, R., de Bakker, J. M., Wilms-Schopman, F. J., Opthof, T., Linnenbank, A. C., Belterman, C. N., et al. (2006). Monophasic action potentials and activation recovery intervals as measures of ventricular action potential duration: experimental evidence to resolve some controversies. *Heart Rhythm* 3, 1043–1050. doi: 10.1016/j.hrthm.2006.05.027

de Boer, R. W., Karemaker, J. M., and Strackee, J. (1987). Haemodynamic fluctuations and barorefex sensitivity in humans. A beat to beat model. *Am. J. Physiol.* 253, H680–H689.

Dergacheva, O., Griffioen, K. J., Neff, R. A., and Mendelowitz, D. (2010). Respiratory modulation of premotor cardiac vagal neurons in the brainstem. *Respir. Physiol. Neurobiol.* 174, 102–110. doi: 10.1016/j.resp.2010.05.005

Eckberg, D. L. (2009). Point:counterpoint: respiratory sinus arrhythmia is due to a central mechanism vs. respiratory sinus arrhythmia is due to the baroreflex mechanism. *J. Appl. Physiol.* 106, 1740–1742. doi: 10.1152/japplphysiol.91107.2008

Faes, L., Pinna, G. D., Porta, A., Maestri, R., and Nollo, G. (2004). Surrogate data analysis for assessing the significance of the coherence function. *IEEE Trans. Biomed. Eng.* 51, 1156–1166. doi: 10.1109/TBME.2004.827271

Guz, A., Innes, J. A., and Murphy, K. (1987). Respiratory modulation of left ventricular stroke volume in man measured using pulsed Doppler ultrasound. *J. Physiol. (Lond.)* 393, 499–512.

Hanson, B., Gill, J., Western, D., Gilbey, M. P., Bostock, J., Boyett, M. R., et al. (2012). Cyclical modulation of human ventricular repolarization by respiration. *Front. Physiol.* 3:379. doi: 10.3389/fphys.2012.00379

Haws, C. W., and Lux, R. L. (1990). Correlation between *in vivo* transmembrane action potential durations and activation-recovery intervals from electrograms. Effects of interventions that alter repolarization time. *Circulation* 81, 281–288. doi: 10.1161/01.CIR.81.1.281

Heijman, J., Zaza, A., Johnson, D. M., Rudy, Y., Peeters, R. L., Volders, P. G., et al. (2013). Determinants of beat-to-beat variability of repolarization duration in the canine ventricular myocyte: a computational analysis. *PLoS Comput. Biol.* 9:e1003202. doi: 10.1371/journal.pcbi.1003202

Innes, J. A., De Court, S. C., Kox, W., Guz, A. (1993). Within-breath modulation of left venrtricular function during normal breathing and positive-pressure ventilation in man. *J. Physiol.* 460, 487–502.

Innes, J. A., Mills, C. J., Noble, M. I. M., Murphy, K., Pugh, S., Shore, A. C., et al. (1987). Validation of beat-by-beat pulsed Doppler measurements of ascending aortic blood velocity in man. *Cardiovasc. Res.* 21, 72–80. doi: 10.1093/cvr/21.1.72

Julien, C. (2006). The enigma of Mayer waves: facts and models. *Cardiovasc. Res.* 70, 12–21. doi: 10.1016/j.cardiores.2005.11.008

Karemaker, J. M. (2009). Counterpoint: respiratory sinus arrhythmia is due to the baroreflex mechanism. *J. Appl. Physiol.* 106, 1742–1743. doi: 10.1152/japplphysiol.91107.2008a

Kohl, P., Bollensdorff, C., and Garny, A. (2006). Effects of mechanosensitive ion channels on ventricular electrophysiology: experimental and theoretical models. *Exp. Physiol.* 91, 307–321. doi: 10.1113/expphysiol.2005.031062

Kubrick, S. (Director). (1980). *The Shining* [DVD]. Warner Home Video, 2001.

Lucini, D., Norbiato, G., Clerici, M., and Pagani, M. (2002). Hemodynamic and autonomic adjustments to real life stress conditions in humans. *Hypertension* 39, 184–188. doi: 10.1161/hy0102.100784

Malliani, A. (2000). *Principles of Cardiovascular Neural Regulation in Health and Disease*. Boston, MA: Kluwer Academic Publishers.

Malpas, S. C. (2010). Sympathetic nervous system overactivity and its role in the development of cardiovascular disease. *Physiol. Rev.* 90, 513–557. doi: 10.1152/physrev.00007.2009

Mayer, S. (1876). Studien zur Physiologie des Herzens und der Blutgefässe. Sitz. Kaiser. Akad. Wiss. 74, 281–307.

Nearing, B. D., and Verrier, R. L. (2002). Progressive increases in complexity of T-wave oscillations herald ischemia-induced ventricular fibrillation. *Circ. Res.* 91, 727–732. doi: 10.1161/01.RES.0000038887.17976.33

Orini, M., Bailon, R., Mainardi, L. T., Laguna, P., and Flandrin, P. (2012a). Characterization of dynamic interactions between cardiovascular signals by time-frequency coherence. *IEEE Trans. Biomed. Eng.* 59, 663–673. doi: 10.1109/TBME.2011.2171959

Orini, M., Laguna, P., Mainardi, L. T., and Bailon, R. (2012b). Assessment of the dynamic interactions between heart rate and arterial pressure by the cross time-frequency analysis. *Physiol. Meas.* 33, 315–331. doi: 10.1088/0967-3334/33/3/315

Potse, M., Vinet, A., Opthof, T., and Coronel, R. (2009). Validation of a simple model for the morphology of the T wave in unipolar electrograms. *Am. J. Physiol. Heart Circ. Physiol*. 297, 792–801. doi: 10.1152/ajpheart.00064.2009

Qu, Z., Xie, Y., Garfinkel, A., and Weiss, J. N. (2010). T-wave alternans and arrhythmogenesis in cardiac diseases. *Front. Physiol.* 1:154. doi: 10.3389/fphys.2010.00154

Schaefer, A., Nils, F., Sanchez, X., and Phillippot, P. (2010). Assessing the effectiveness of a large database of emotion eliciting films: a new tool for emotion researchers. *Cogn. Emot.* 24, 1153–1172. doi: 10.1080/02699930903274322

Shen, M. J., and Zipes, D. P. (2014). Role of the autonomic nervous system in modulating cardiac arrhythmias. *Circ. Res.* 114, 1004–1021. doi: 10.1016/SO140-6736(14)61303-9

Spyer, K. M., and Gilbey, M. P. (1988). Cardiorespiratory interactions in heart-rate control. *Ann. N.Y. Acad. Sci*. 533, 350–357. doi: 10.1111/j.1749-6632.1988.tb37263.x

Taggart, P., Boyett, M. R., Logantha, S., and Lambiase, P. D. (2011). Anger, emotion, and arrhythmias: from brain to heart. *Front. Physiol.* 2:67. doi: 10.3389/fphys.2011.00067

Taggart, P., and Sutton, P. (2011). "Load dependence of ventricular repolarisation," in *Cardiac Mechano-Electric Feedback and Arrhythmias. From Pipette to Subject*, *2nd Edn.*, eds P. Kohl, F. Sachs, and M. R. Franz (Philadelphia, PA: Elsevier), 269–723.

Task Force of the European Society of Cardiology and the North American Society of Pacing and Electrophysiology, N. (1996). Heart rate variability: standards of measurement, physiological interpretation and clinical use. *Circulation* 93, 1043–1065. doi: 10.1161/01.CIR.93.5.1043

Thomsen, M. B., Oros, A., Schoenmakers, M., van Opstal, J. M., Maas, J. N., Beekman, J. D., et al. (2007). Proarrhythmic electrical remodelling is associated with increased beat-to-beat variability of repolarisation. *Cardiovasc. Res.* 73, 521–530. doi: 10.1016/j.cardiores.2006.11.025

van de Borne, P., Rahnama, M., Mezzetti, S., Montano, N., Porta, A., Degaute, J. P., et al. (2001). Contrasting effects of phentolamine and nitroprusside on neural and cardiovascular variability. *Am. J. Physiol. Heart Circ. Physiol*. 281, H559–H565. Available online at: http://ajpheart.physiology.org/content/281/2/H559.article-info

Westermann, R. S. K., Stahl, G., Hesse, F. W. (1996). Relative effectiveness and validity of mood induction procedures: a meta-analysis. *Eur. J. Soc. Psychol*. 26, 557–580.

Workman, A. J. (2010). Cardiac adrenergic control and atrial fibrillation. *Naunyn Schmiedebergs Arch. Pharmacol*. 381, 235–249. doi: 10.1007/s00210-009-0474-0

Wyatt, R. F., Burgess, M. L., Evans, A. K., Lux, R. L., Abildskov, J. A., and Tsutsu, T. (1981). Estimation of ventricular transmembrane action potential durations and repolarization times from unipolar electrograms. *Am. J. Cardiol.* 47:488. doi: 10.1016/0002-9149(81)91028-6

Xie, Y., Izu, L. T., Bers, D. M., and Sato, D. (2014). Arrhythmogenic transient dynamics in cardiac myocytes. *Biophys. J.* 106, 1391–1397. doi: 10.1016/j.bpj.2013.12.050

Zipes, D. P., and Jalife, J. (1999). *Cardiac Electrophysiology. From Cell to Bedside*, *5th Edn.* Philadelphia, PA: Saunders (W.B.) Co Ltd.

Conflict of Interest Statement: The authors declare that the research was conducted in the absence of any commercial or financial relationships that could be construed as a potential conflict of interest.

Received: 05 August 2014; accepted: 07 October 2014; published online: 28 October 2014.

*Citation: Hanson B, Child N, Van Duijvenboden S, Orini M, Chen Z, Coronel R, Rinaldi CA, Gill JS, Gill JS and Taggart P (2014) Oscillatory behavior of ventricular action potential duration in heart failure patients at respiratory rate and low frequency. Front. Physiol. **5**:414. doi: 10.3389/fphys.2014.00414*

This article was submitted to Cardiac Electrophysiology, a section of the journal Frontiers in Physiology.

References

[1] J. M. Morgan, "Sudden cardiac death: opportunities for prevention," *Heart*, vol. 92, pp. 721–723, oct 2005.

[2] D. P. Zipes and H. J. J. Wellens, "Sudden Cardiac Death," *Circulation*, vol. 98, pp. 2334–2351, nov 1998.

[3] P. J. Schwartz, A. M. Brown, A. Malliani, and A. Zanchetti, eds., *Neural Mechanisms in Cardiac Arrhythmias*. New York: Raven Press, 1978.

[4] P. Taggart, M. R. Boyett, S. Logantha, and P. D. Lambiase, "Anger, emotion, and arrhythmias: from brain to heart.," *Frontiers in physiology*, vol. 2, no. October, p. 67, 2011.

[5] R. H. Clayton and A. V. Holden, "Dispersion of cardiac action potential duration and the initiation of re-entry: a computational study.," *Biomedical engineering online*, vol. 4, p. 11, feb 2005.

[6] R. H. Clayton and P. Taggart, "Regional differences in APD restitution can initiate wavebreak and re-entry in cardiac tissue: a computational study.," *Biomedical engineering online*, vol. 4, p. 54, sep 2005.

[7] B. D. Nearing and R. L. Verrier, "Modified moving average analysis of T-wave alternans to predict ventricular fibrillation with high accuracy.," *Journal of applied physiology (Bethesda, Md. : 1985)*, vol. 92, pp. 541–9, feb 2002.

[8] J. Han and G. K. Moe, "Nonuniform Recovery of Excitability in Ventricular Muscle," *Circulation Research*, vol. 14, pp. 44–60, jan 1964.

[9] P. E. Rapp, "Why are so many biological systems periodic?," *Progress in neurobiology*, vol. 29, no. 3, pp. 261–73, 1987.

[10] B. Hanson, J. Gill, D. Western, M. P. Gilbey, J. Bostock, M. R. Boyett, H. Zhang, R. Coronel, and P. Taggart, "Cyclical modulation of human ventricular repolarization by respiration.," *Frontiers in physiology*, vol. 3, no. September, p. 379, 2012.

[11] D. Western, *Bioelectric Signal Analysis to Expose Nervous Control of the Human Heart*. PhD thesis, University College London, 2012.

[12] R. H. Clayton and P. Taggart, "Regional differences in APD restitution can initiate wavebreak and re-entry in cardiac tissue: a computational study.," *Biomedical engineering online*, vol. 4, p. 54, sep 2005.

[13] D. P. Zipes and J. Jalife, *Cardiac electrophysiology : from cell to bedside*. Philadelphia (Pa.): Saunders, 2009.

[14] J. M. Morgan, A. D. Cunningham, and E. Rowland, "Relationship of the effective refractory period and monophasic action potential duration after a step increase in pacing frequency.," *Pacing and clinical electrophysiology : PACE*, vol. 13, pp. 1002–8, aug 1990.

[15] W. F. Boron and E. L. Boulpaep, *Medical Physiology*. Elsevier Health Sciences, 2008.

[16] D. P. Zipes and M. Rubart, "Neural modulation of cardiac arrhythmias and sudden cardiac death.," *Heart rhythm*, vol. 3, pp. 108–13, jan 2006.

[17] M. Rubart and D. P. Zipes, "Mechanisms of sudden cardiac death.," *The Journal of clinical investigation*, vol. 115, pp. 2305–15, sep 2005.

[18] G. N. Tseng, R. B. Robinson, and B. F. Hoffman, "Passive properties and membrane currents of canine ventricular myocytes.," *The Journal of general physiology*, vol. 90, pp. 671–701, nov 1987.

[19] M. Stramba-Badiale, E. Vanoli, G. M. De Ferrari, D. Cerati, R. D. Foreman, and P. J. Schwartz, "Sympathetic-parasympathetic interaction and accentuated antagonism in conscious dogs.," *The American journal of physiology*, vol. 260, pp. H335–40, feb 1991.

[20] N. Takahashi and D. P. Zipes, "Vagal modulation of adrenergic effects on canine sinus and atrioventricular nodes.," *The American journal of physiology*, vol. 244, pp. H775–81, jun 1983.

[21] K. Yamakawa, E. L. So, P. S. Rajendran, J. D. Hoang, N. Makkar, A. Mahajan, K. Shivkumar, and M. Vaseghi, "Electrophysiological effects of right and left vagal nerve stimulation on the ventricular myocardium.," *American journal of physiology. Heart and circulatory physiology*, vol. 307, pp. H722–31, sep 2014.

[22] P. J. Schwartz, "The rationale and the role of left stellectomy for the prevention of malignant arrhythmias.," *Annals of the New York Academy of Sciences*, vol. 427, pp. 199–221, 1984.

[23] U. Wilbert-Lampen, D. Leistner, S. Greven, T. Pohl, S. Sper, C. Völker, D. Güthlin, A. Plasse, A. Knez, H. Küchenhoff, and G. Steinbeck, "Cardiovascular events during World Cup soccer.," *The New England journal of medicine*, vol. 358, pp. 475–83, jan 2008.

[24] R. A. DeSilva, R. L. Verrier, and B. Lown, "The effects of psychological stress and vagal stimulation with morphine on vulnerability to ventricular fibrillation (VF) in the conscious dog.," *American heart journal*, vol. 95, pp. 197–203, feb 1978.

[25] M. a. Cohen and J. A. Taylor, "Short-term cardiovascular oscillations in man: measuring and modelling the physiologies.," *The Journal of physiology*, vol. 542, pp. 669–83, aug 2002.

[26] D. L. Eckberg, "Point:counterpoint: respiratory sinus arrhythmia is due to a central mechanism vs. respiratory sinus arrhythmia is due to the baroreflex mechanism.," *Journal of applied physiology (Bethesda, Md. : 1985)*, vol. 106, pp. 1740–2; discussion 1744, may 2009.

[27] M. Orini, R. Bailón, L. T. Mainardi, P. Laguna, and P. Flandrin, "Characterization of dynamic interactions between cardiovascular signals by time-frequency coherence.," *IEEE transactions on bio-medical engineering*, vol. 59, pp. 663–73, mar 2012.

[28] R. Furlan, A. Porta, F. Costa, J. Tank, L. Baker, R. Schiavi, D. Robertson, A. Malliani, and R. Mosqueda-Garcia, "Oscillatory patterns in sympathetic neural discharge and

cardiovascular variables during orthostatic stimulus.," *Circulation*, vol. 101, pp. 886–92, feb 2000.

[29] H. M. Stauss, R. Mrowka, B. Nafz, A. Patzak, T. Unger, and P. B. Persson, "Does low frequency power of arterial blood pressure reflect sympathetic tone?," *Journal of the autonomic nervous system*, vol. 54, pp. 145–54, aug 1995.

[30] C. Julien, "The enigma of Mayer waves: Facts and models.," *Cardiovascular research*, vol. 70, pp. 12–21, apr 2006.

[31] R. Negoescu, S. Wolf, and S. Porges, "THM power in the spectrum of the QT interval: a refined clue to the force of ventricular contraction in man," in *[1993] Proceedings of the Twelfth Southern Biomedical Engineering Conference*, pp. 117–119, IEEE, 1993.

[32] A. S. Gami, S. M. Caples, and V. K. Somers, "Sleep-Disordered Breathing and Arrhythmias," in *Cardiac Electrophysiology: From Cell to Bedside*, pp. 1087–1093, Elsevier, 2014.

[33] M. J. Janse, R. Coronel, T. Opthof, E. A. Sosunov, E. P. Anyukhovsky, and M. R. Rosen, "Repolarization gradients in the intact heart: transmural or apico-basal?," *Progress in biophysics and molecular biology*, vol. 109, pp. 6–15, may 2012.

[34] M. S. Spach, R. C. Barr, G. A. Serwer, J. M. Kootsey, and E. A. Johnson, "Extracellular potentials related to intracellular action potentials in the dog Purkinje system.," *Circulation research*, vol. 30, pp. 505–19, may 1972.

[35] R. F. Wyatt, "Comparison of estimates of activation and recovery times from bipolar and unipolar electrograms to in vivo transmembrane action-potential durations," in *IEEE Transactions On Biomedical Eengineering*, pp. 22–25, 1980.

[36] C. W. Haws and R. L. Lux, "Correlation between in vivo transmembrane action potential durations and activation-recovery intervals from electrograms. Effects of interventions that alter repolarization time.," *Circulation*, vol. 81, pp. 281–8, jan 1990.

[37] M. Potse, A. Vinet, T. Opthof, and R. Coronel, "Validation of a simple model for the morphology of the T wave in unipolar electrograms.," *American journal of physiology. Heart and circulatory physiology*, vol. 297, pp. H792–801, aug 2009.

[38] R. Coronel, J. M. T. de Bakker, F. J. G. Wilms-Schopman, T. Opthof, A. C. Linnenbank, C. N. Belterman, and M. J. Janse, "Monophasic action potentials and activation recovery intervals as measures of ventricular action potential duration: experimental evidence to resolve some controversies.," *Heart rhythm*, vol. 3, pp. 1043–50, sep 2006.

[39] C. K. Millar, F. A. Kralios, and R. L. Lux, "Correlation between refractory periods and activation-recovery intervals from electrograms: effects of rate and adrenergic interventions.," *Circulation*, vol. 72, pp. 1372–9, dec 1985.

[40] M. Chinushi, M. Tagawa, H. Kasai, T. Washizuka, A. Abe, H. Furushima, and Y. Aizawa, "Correlation between the effective refractory period and activation-recovery interval calculated from the intracardiac unipolar electrogram of humans with and without dl-sotalol treatment.," *Japanese circulation journal*, vol. 65, pp. 702–6, aug 2001.

[41] D. Geselowitz, "On the theory of the electrocardiogram," *Proceedings of the IEEE*, vol. 77, pp. 857–876, jun 1989.

[42] D. Western, B. Hanson, and P. Taggart, "Measurement bias in activation-recovery intervals from unipolar electrograms.," *American journal of physiology. Heart and circulatory physiology*, vol. 308, pp. H331–8, feb 2015.

[43] H. Akaike, "A new look at the statistical model identification," *IEEE Transactions on Automatic Control*, vol. 19, pp. 716–723, dec 1974.

[44] D. E. Mager, M. M. Merritt, J. Kasturi, L. R. Witkin, M. Urdiqui-Macdonald, J. J. Sollers, M. K. Evans, A. B. Zonderman, D. R. Abernethy, and J. F. Thayer, "Kullback-Leibler clustering of continuous wavelet transform measures of heart rate variability.," *Biomedical sciences instrumentation*, vol. 40, pp. 337–42, 2004.

[45] M. Orini, *Time-Frequency Analysis for the Dynamic Quantification of the Interactions Between Signals Related To the Cardiovascular System*. PhD thesis, University of Zaragoza, 2012.

[46] M. Orini, P. Laguna, L. T. Mainardi, and R. Bailón, "Assessment of the dynamic interactions between heart rate and arterial pressure by the cross time-frequency analysis.," *Physiological measurement*, vol. 33, pp. 315–31, mar 2012.

[47] L. Faes and G. Nollo, "Multivariate Frequency Domain Analysis of Causal Interactions in Physiological Time Series," in *Biomedical Engineering, Trends in Electronics, Communications and Software*, pp. 403–428, InTech, jan 2011.

[48] L. Faes, S. Erla, A. Porta, and G. Nollo, "A framework for assessing frequency domain causality in physiological time series with instantaneous effects.," *Philosophical transactions. Series A, Mathematical, physical, and engineering sciences*, vol. 371, p. 20110618, aug 2013.

[49] L. Faes, A. Porta, and G. Nollo, "Testing Frequency-Domain Causality in Multivariate Time Series," *IEEE Transactions on Biomedical Engineering*, vol. 57, pp. 1897–1906, aug 2010.

[50] B. F. ROBINSON, S. E. EPSTEIN, G. D. BEISER, and E. BRAUNWALD, "Control of Heart Rate by the Autonomic Nervous System: Studies in Man on the Interrelation Between Baroreceptor Mechanisms and Exercise," *Circulation Research*, vol. 19, pp. 400–411, aug 1966.

[51] B. P. Imholz, G. A. van Montfrans, J. J. Settels, G. M. van der Hoeven, J. M. Karemaker, and W. Wieling, "Continuous non-invasive blood pressure monitoring: reliability of Finapres device during the Valsalva manoeuvre.," *Cardiovascular research*, vol. 22, pp. 390–7, jun 1988.

[52] B. P. Imholz, J. J. Settels, A. H. van der Meiracker, K. H. Wesseling, and W. Wieling, "Non-invasive continuous finger blood pressure measurement during orthostatic stress compared to intra-arterial pressure.," *Cardiovascular research*, vol. 24, pp. 214–21, mar 1990.

[53] N. Child, B. Hanson, M. Bishop, C. A. Rinaldi, J. Bostock, D. Western, M. Cooklin, M. O'Neil, M. Wright, R. Razavi, J. Gill, and P. Taggart, "Effect of mental challenge induced by movie clips on action potential duration in normal human subjects independent of heart rate.," *Circulation. Arrhythmia and electrophysiology*, vol. 7, pp. 518–23, jun 2014.

[54] D. Western, P. Taggart, and B. Hanson, "Real-time feedback of dynamic cardiac repolarization properties.," *Conference proceedings: Annual International Confer-*

ence of the IEEE Engineering in Medicine and Biology Society. IEEE Engineering in Medicine and Biology Society. Annual Conference, vol. 2010, pp. 114–7, aug 2010.

[55] M. Baumert, M. Schmidt, S. Zaunseder, and A. Porta, "Effects of ECG sampling rate on QT interval variability measurement," *Biomedical Signal Processing and Control*, vol. 25, pp. 159–164, mar 2016.

[56] P. M. van Dam, T. F. Oostendorp, A. C. Linnenbank, and A. van Oosterom, "Non-invasive imaging of cardiac activation and recovery.," *Annals of biomedical engineering*, vol. 37, pp. 1739–56, sep 2009.

[57] M. Orini, L. Citi, B. M. Hanson, P. Taggart, and P. D. Lambiase, "Characterization of the causal interactions between depolarization and repolarization temporal changes in unipolar electrograms," in *Computing in Cardiology 2013*, pp. 719–722, sep 2013.

[58] R. Sassi, L. T. Mainardi, and S. Cerutti, "Amplitude of Dominant T-Wave Alternans assessment on ECGs obtained from a biophysical model.," *Conference proceedings : ... Annual International Conference of the IEEE Engineering in Medicine and Biology Society. IEEE Engineering in Medicine and Biology Society. Annual Conference*, vol. 2011, no. 8, pp. 5872–5, 2011.

[59] A. van Oosterom and T. F. Oostendorp, "ECGSIM: an interactive tool for studying the genesis of QRST waveforms.," *Heart (British Cardiac Society)*, vol. 90, pp. 165–8, feb 2004.

[60] J. Martinez and S. Olmos, "A robust T wave alternans detector based on the GLRT for Laplacian noise distribution," in *Computers in Cardiology*, pp. 677–680, IEEE, 2003.

[61] A. Mincholé, E. Pueyo, J. F. Rodríguez, E. Zacur, M. Doblaré, and P. Laguna, "Quantification of restitution dispersion from the dynamic changes of the T-wave peak to end, measured at the surface ECG.," *IEEE transactions on bio-medical engineering*, vol. 58, pp. 1172–82, may 2011.

[62] L. Faes, G. D. Pinna, A. Porta, R. Maestri, and G. Nollo, "Surrogate data analysis for assessing the significance of the coherence function.," *IEEE transactions on bio-medical engineering*, vol. 51, pp. 1156–66, jul 2004.

[63] A. Porta, R. Furlan, O. Rimoldi, M. Pagani, A. Malliani, and P. van de Borne, "Quantifying the strength of the linear causal coupling in closed loop interacting cardiovascular variability signals.," *Biological cybernetics*, vol. 86, pp. 241–51, mar 2002.

[64] M. Duarte and D. Sternad, "Complexity of human postural control in young and older adults during prolonged standing.," *Experimental brain research*, vol. 191, pp. 265–76, nov 2008.

[65] L. Faes, G. Nollo, and R. Antolini, "Investigating the level of significance of the coherence function in cardiovascular variability analysis," in *Computers in Cardiology 2001. Vol.28 (Cat. No.01CH37287)*, pp. 481–484, IEEE, 2001.

[66] B. Hanson, N. Child, S. Van Duijvenboden, M. Orini, Z. Chen, R. Coronel, C. A. Rinaldi, J. S. Gill, J. S. Gill, and P. Taggart, "Oscillatory behavior of ventricular action potential duration in heart failure patients at respiratory rate and low frequency.," *Frontiers in physiology*, vol. 5, no. October, p. 414, 2014.

[67] S. van Duijvenboden, M. Orini, P. Taggart, and B. Hanson, "Accuracy of measurements derived from intracardiac unipolar electrograms: A simulation study," in *2015 37th Annual International Conference of the IEEE Engineering in Medicine and Biology Society (EMBC)*, vol. 2015-Novem, pp. 76–79, IEEE, aug 2015.

[68] D. Lucini, G. Norbiato, M. Clerici, and M. Pagani, "Hemodynamic and autonomic adjustments to real life stress conditions in humans.," *Hypertension (Dallas, Tex. : 1979)*, vol. 39, pp. 184–8, jan 2002.

[69] P. Taggart, P. Sutton, C. Redfern, V. N. Batchvarov, K. Hnatkova, M. Malik, U. James, and A. Joseph, "The effect of mental stress on the non-dipolar components of the T wave: modulation by hypnosis.," *Psychosomatic medicine*, vol. 67, no. 3, pp. 376–83, 2005.

[70] S. van Duijvenboden, B. Hanson, N. Child, M. Orini, C. A. Rinaldi, J. S. Gill, and P. Taggart, "Effect of autonomic blocking agents on the respiratory-related oscillations of ventricular action potential duration in humans.," *American journal of physiology. Heart and circulatory physiology*, vol. 309, pp. H2108–17, dec 2015.

[71] D. Thomson, "Spectrum estimation and harmonic analysis," *Proceedings of the IEEE*, vol. 70, no. 9, pp. 1055–1096, 1982.

[72] D. J. Thomson, "Multitaper analysis of nonstationary and nonlinear time series data," *Nonlinear and nonstationary signal processing*, pp. 317–394, 2000.

[73] A. F. B. Bernardo, L. C. M. Vanderlei, and D. M. Garner, "HRV Analysis: A Clinical and Diagnostic Tool in Chronic Obstructive Pulmonary Disease," *International Scholarly Research Notices*, vol. 2014, pp. 1–6, 2014.

[74] R. Takalo, H. Hytti, and H. Ihalainen, "Tutorial on univariate autoregressive spectral analysis.," *Journal of clinical monitoring and computing*, vol. 19, pp. 401–10, dec 2005.

[75] L. Faes, A. Porta, R. Cucino, S. Cerutti, R. Antolini, and G. Nollo, "Causal transfer function analysis to describe closed loop interactions between cardiovascular and cardiorespiratory variability signals," *Biological Cybernetics*, vol. 90, no. 6, pp. 390–399, 2004.

[76] H. L. Bleich, E. S. Boro, and P. C. Voukydis, "Effect of Intracardiac Blood on the Electrocardiogram," *New England Journal of Medicine*, vol. 291, pp. 612–616, sep 1974.

[77] P. Taggart, P. Sutton, M. Lab, M. Runnalls, W. O'Brien, and T. Treasure, "Effect of abrupt changes in ventricular loading on repolarization induced by transient aortic occlusion in humans.," *The American journal of physiology*, vol. 263, pp. H816–23, sep 1992.

[78] P. Kohl and U. Ravens, "Cardiac mechano-electric feedback: past, present, and prospect.," *Progress in biophysics and molecular biology*, vol. 82, no. 1-3, pp. 3–9, 2003.

[79] A. Porta, F. Aletti, F. Vallais, and G. Baselli, "Multimodal signal processing for the analysis of cardiovascular variability.," *Philosophical transactions. Series A, Mathematical, physical, and engineering sciences*, vol. 367, pp. 391–409, jan 2009.

[80] M. P. Gilbey, "Entrainment of Sympathetic Rhythms," in *Primer on the Autonomic Nervous System*, pp. 147–149, Elsevier, 2012.

[81] O. Dergacheva, K. J. Griffioen, R. A. Neff, and D. Mendelowitz, "Respiratory modulation of premotor cardiac vagal neurons in the brainstem.," *Respiratory physiology & neurobiology*, vol. 174, pp. 102–10, nov 2010.

[82] K. C. Evans, "Cortico-limbic circuitry and the airways: insights from functional neuroimaging of respiratory afferents and efferents.," *Biological psychology*, vol. 84, pp. 13–25, apr 2010.

[83] D. L. Eckberg, "The human respiratory gate," *The Journal of Physiology*, vol. 548, no. 2, pp. 339–352, 2003.

[84] M. Franz, "Mechano-electrical feedback," *Cardiovascular Research*, vol. 45, pp. 263–266, jan 2000.

[85] D. L. Eckberg, M. S. Cavanaugh, A. L. Mark, and F. M. Abboud, "A simplified neck suction device for activation of carotid baroreceptors.," *The Journal of laboratory and clinical medicine*, vol. 85, pp. 167–73, jan 1975.

[86] R. Furlan, A. Diedrich, A. Rimoldi, L. Palazzolo, C. Porta, L. Diedrich, P. A. Harris, P. Sleight, I. Biagioni, D. Robertson, and L. Bernardi, "Effects of unilateral and bilateral carotid baroreflex stimulation on cardiac and neural sympathetic discharge oscillatory patterns.," *Circulation*, vol. 108, pp. 717–23, aug 2003.

[87] P. J. Fadel, S. Ogoh, D. M. Keller, and P. B. Raven, "Recent insights into carotid baroreflex function in humans using the variable pressure neck chamber.," *Experimental physiology*, vol. 88, pp. 671–80, nov 2003.

[88] V. L. Cooper and R. Hainsworth, "Carotid baroreflex testing using the neck collar device," *Clinical Autonomic Research*, vol. 19, pp. 102–112, apr 2009.

[89] D. L. Eckberg, "Adaptation of the human carotid baroreceptor-cardiac reflex.," *The Journal of physiology*, vol. 269, pp. 579–89, aug 1977.

[90] E. Båth, L. E. Lindblad, and B. G. Wallin, "Effects of dynamic and static neck suction on muscle nerve sympathetic activity, heart rate and blood pressure in man.," *The Journal of physiology*, vol. 311, pp. 551–64, feb 1981.

[91] M. Tafil-Klawe, F. Raschke, and G. Hildebrandt, "Functional asymmetry in carotid sinus cardiac reflexes in humans," *European Journal of Applied Physiology and Occupational Physiology*, vol. 60, no. 5, pp. 402–405, 1990.

[92] M. N. Levy, M. L. Ng, and H. Zieske, "Functional distribution of the peripheral cardiac sympathetic pathways.," *Circulation research*, vol. 19, pp. 650–61, sep 1966.

[93] N. M. Raine and N. T. Cable, "A simplified paired neck chamber for the demonstration of baroreflex blood pressure regulation.," *The American journal of physiology*, vol. 277, pp. S60–6, dec 1999.

[94] M. R. Franz, C. D. Swerdlow, L. B. Liem, and J. Schaefer, "Cycle length dependence of human action potential duration in vivo. Effects of single extrastimuli, sudden sustained rate acceleration and deceleration, and different steady-state frequencies.," *Journal of Clinical Investigation*, vol. 82, pp. 972–979, sep 1988.

[95] R. G. Querry, S. A. Smith, M. Strømstad, K. Ide, N. H. Secher, and P. B. Raven, "Anatomical and functional characteristics of carotid sinus stimulation in humans.," *American journal of physiology. Heart and circulatory physiology*, vol. 280, pp. H2390–8, may 2001.

[96] M. C. Finlay, P. D. Lambiase, R. Ben-Simon, and P. Taggart, "Effect of mental stress on dynamic electrophysiological properties of the endocardium and epicardium in humans.," *Heart rhythm*, vol. 13, pp. 175–82, jan 2016.

[97] K. D. Rizas, T. Nieminen, P. Barthel, C. S. Zürn, M. Kähönen, J. Viik, T. Lehtimäki, K. Nikus, C. Eick, T. O. Greiner, H. P. Wendel, P. Seizer, J. Schreieck, M. Gawaz, G. Schmidt, and A. Bauer, "Sympathetic activity-associated periodic repolarization dynamics predict mortality following myocardial infarction.," *The Journal of clinical investigation*, vol. 124, pp. 1770–80, apr 2014.

[98] K. D. Rizas, W. Hamm, S. Kääb, G. Schmidt, and A. Bauer, "Periodic Repolarisation Dynamics: A Natural Probe of the Ventricular Response to Sympathetic Activation," *Arrhythmia & Electrophysiology Review*, vol. 5, no. 1, p. 31, 2016.

[99] U. A. Leuenberger, S. Mostoufi-Moab, M. Herr, K. Gray, A. Kunselman, and L. I. Sinoway, "Control of skin sympathetic nerve activity during intermittent static handgrip exercise.," *Circulation*, vol. 108, pp. 2329–35, nov 2003.

[100] C. Granger, "Testing for causality," *Journal of Economic Dynamics and Control*, vol. 2, pp. 329–352, jan 1980.